Methodology and tools for the optimization of the PEM fuel cell break-in procedure

Fabian van der Linden

To cite this version:

Fabian van der Linden. Methodology and tools for the optimization of the PEM fuel cell break-in procedure. Electric power. Université Bourgogne Franche-Comté, 2022. English. NNT : 2022UBFCD036 . tel-04041460

HAL Id: tel-04041460
https://theses.hal.science/tel-04041460v1
Submitted on 22 Mar 2023

THESE DE DOCTORAT DE L'ETABLISSEMENT UNIVERSITE BOURGOGNE FRANCHE-COMTE

PREPAREE A L'UNIVERSITE DE FRANCHE-COMTE

Ecole doctorale n°37

Sciences Pour L'Ingénieur et Microtechniques

Doctorat de spécialité : Génie Electrique

Par

Van Der Linden Fabian

Methodology and tools for the optimization of the PEM fuel cell break-in procedure

Méthodologie et outils pour l'optimisation de la procédure de rodage de pile à combustible PEM

Thèse présentée et soutenue à Belfort, le 10 novembre 2022

Composition du Jury :

Mme. Didierjean Sophie	Professeure des Universités, Université de Lorraine	Rapportrice
M. Chatenet Marian	Professeur des Universités, INP Grenoble	Rapporteur
M. Venet Pascal	Professeur des Universités, Université Lyon 1	Président du jury
M. Vacquier Christophe	Senior Expert, Symbio	Examinateur
Mme. McCay Katie	Docteure, Research Scientist SINTEF	Examinatrice
M. Morando Simon	Docteur, diagnosis and prognosis specialist, Symbio	Encadrant de thèse
Mme. Pahon Elodie	Maitre de conférences, UTBM	Codirectrice de thèse
M. Bouquain David	Professeur des Universités, Université de Franche-Comté	Directeur de thèse

“The life and soul of science is its practical application”.
Lord Kelvin

Acknowledgements

Since the entire manuscript is written in English, so is the acknowledgements section (I am not a big fan of “Frenglish”, sorry).

First, I would like to express my gratitude to the members of the jury. Thank you, Prof. Pascal Venet, for having accepted to chair the jury, as well as Prof. Sophie Didierjean and Prof. Marian Chatenet for having evaluated this manuscript. I also thank Christophe Vacquier and Dr. Katie McCay for reviewing my work.

My deepest appreciation and respect go to my thesis supervisors.

To my PhD director, Prof. David Bouquain, thank you for having supervised and provided regular feedback on my work, despite your busy schedule. I really enjoyed working with you, always in a good mood and with very enlightening discussions. It was impressive to see that despite your obligations as professor and vice-director of the laboratory, you still managed to find time to be fully involved in the experimental tests. I really hope we can work together again in the future, for example to supervise a new thesis.

I would also like to thank my co-director at the FClab, Dr. Elodie Pahon, for all the guidance and expertise you brought to this thesis. As you recently mentioned, it is quite amazing that I attended your thesis defence in 2015 and that 7 years later, you attended mine as a member of the jury. Beyond your technical knowledge, I have always admired your kindness and generosity, with notable moments such as when you brought me a birthday gift when I was your intern, and when you prepared full Christmas packages for your colleagues. The FClab is lucky to have you.

To my other co-supervisor, Dr. Simon Morando, thank you for your fuel cell lectures, and the long discussions we had about PEMFC degradations and their relationship to break-in. I also really enjoyed the many laughs we had at Faurecia and Symbio. A special mention to the bat that accompanied us to the lab during our first fuel cell tests (may Corona rest in peace). The era of "sbiritude" has sadly finally come to an end. That said, I am sure we will continue to have interesting scientific but also non-work-related talks in the years to come.

Katie, I also want to thank you for the amazing time I had working with you for a month at Sintef, Norway. And let's never forget the record time our team set to solve the Trondheim escape game (also thanks to Josi)! Thanks also to Nicolas Autrusson (Symbio), Prof. Nadia Steiner (FClab) and Dr. Kyrre Sundseth (Sintef) for the organization and support. Without you all, the exchange would probably not have taken place.

There are so many colleagues (who have often become friends) whom I would like to thank, that it would not fit in one paragraph, but I will do my best.

First of all, I would like to thank all the PhD students and other FClab employees: Damien (the kebab/game night bro), Meziane (the crazy tinder/beer guy), Jeremy (the car talk/coffee break companion), Corey (du nord), Santiago (el jefe), Romain (the ambassador), Flavie (the madeleine girl), Sudnya (the great cook), Agnès (the almost 2000), Léo (my best student, don’t tell Gauthier), Gauthier (my best student, don’t tell Léo), Fatimatou & Clotilde (cifre rpz), Raphaël (the 1001 equations guy), Laurence & Silviya (the best problem solvers), Pierre (grandpa), Bruno (the budget chief)... The same goes for the people from Symbio: Kevin, Julien, Iona, Nicolas, Emilien, ... (there are literally too many of you to thank you all individually, as I don't want my manuscript to be 200 pages long). Thank you all for the great atmosphere you created at work, and outside of work (let's face it, mostly at the pub where we spent quite some time together, whether I'm talking about Belfort or Lyon). I wish you all the best. You rock.

And finally, a heartfelt thank you to my family, close friends, and my girlfriend, Julie, for always being there for me. This is going to sound a bit cheesy, but I would never have been able to finish this manuscript if it wasn’t for your love and support.

Titre : Méthodologie et outils pour l'optimisation de la procédure de rodage de pile à combustible PEM

Mots clés : Pile à combustible PEM, Rodage, Activation, Conditionnement, Optimisation de procédure

Résumé : La pile à combustible à membrane échangeuse de protons (PEMFC) est une alternative zéro émission au moteur à combustion interne. Suite à son assemblage final, une PEMFC doit être « rodée » ou « activée ». Ce processus est essentiel pour élever et stabiliser les performances de la pile autour d'une valeur seuil reproductible. L'activation d'une PEMFC est coûteuse (besoins en équipements et en hydrogène) et chronophage, la rendant ainsi incompatible avec une production de masse. L'objectif de cette thèse est d'apporter des solutions permettant de réduire la durée et le coût de rodage de la pile à combustible.

La phase d'activation de PEMFC est un sujet de recherche relativement nouveau. Ainsi, un état de l'art approfondi fut d'abord réalisé afin de mieux comprendre les principes physiques du rodage, et les méthodes associées. Activer une cellule consiste principalement à hydrater le polymère, à désorber les impuretés de la surface du catalyseur et à ouvrir des pores dans la couche catalytique.

A partir de ces connaissances, deux outils numériques furent développés. Le premier est un modèle analytique qui simule la procédure d'activation de la membrane, afin de remplacer des essais expérimentaux coûteux. Le second est un outil de diagnostic du rodage, visant à mesurer « l'état d'activation » de la pile à combustible.

Grâce à ces outils numériques et de l'état de l'art, des procédures de rodage optimisées furent proposées et testées sur différents stacks à grande surface. Chacun de ces protocoles a été optimisé selon un ou plusieurs critères, qui sont : cinétique de rodage, coût de réactifs, et durabilité de la pile à combustible. Le protocole phare de cette thèse, une combinaison de sous-alimentations cathodiques et de fonctionnement en flux inverse, est considéré comme le meilleur compromis entre tous ces critères. Par rapport aux protocoles conventionnels, il permet de fortement réduire le temps de rodage et le coût des réactifs, tout en conservant la durabilité de pile et en améliorant sa morphologie.

Title: Methodology and tools for the optimization of the PEM fuel cell break-in procedure

Keywords: PEM fuel cell, Break-in, Activation, Conditioning, Procedure optimization

Abstract: The proton exchange membrane fuel cell (PEMFC) is an emission-free alternative to the internal combustion engine. Following its final assembly, a PEMFC must be "broken-in" or "activated'. This process is essential to elevate and stabilize the stack performance to a reproducible threshold value. Activating a fuel cell stack is costly (machinery and fuel related) and time-consuming. It is therefore currently not adapted for mass-production. The objective of this thesis is to provide solutions to reduce the duration and cost of the fuel cell break-in process.

The PEMFC activation phase is a relatively novel research topic. Therefore, an in-depth state-of-the-art has firstly been carried out to gather a deeper understanding of the break-in physical principles, and the associated activation methods. Activating a cell mainly consists of hydrating the polymer, desorbing impurities from the catalyst surface, and opening pores within the catalyst layer.

From this knowledge, two numerical tools have been developed. One is an analytical model which simulates the ionomer activation procedure, to replace costly experimental applications. The other is a break-in diagnosis tool, to monitor the "state-of-activation" of the fuel cell.

Armed with these numerical tools and the state-of-the-art research, optimized break-in procedures have been proposed and tested on various large surface stacks. Each of these protocols is designed to be optimized along one or more of the following criteria: break-in kinetics, reactant cost, and fuel cell durability. The flagship protocol of this thesis, – a combination of cathode starvations and reverse flow operation – is considered as the best compromise between all criteria. Compared to conventional protocols, it strongly reduces the break-in time and reactant cost whilst conserving stack durability and improving its morphology.

Contents

List of figures

List of tables

General introduction

Our society is currently facing an era in which the effects of human activity on the Earth's climate are becoming significant and undeniable. Weather patterns are affected at profound and unprecedented levels, as they are becoming more extreme and unstable (heavy rainfall, heat waves, etc.), leading to increasingly frequent natural disasters (wildfires, floods, etc.) [1]. The global temperature increase could also soon cause crises such as food insecurity (drying out of soil) [2], and waves of population migration (rising sea level) [3]. Such a major disruption of the climate, along with its consequences, highlights the necessity to bring down greenhouse gas emissions. Without a sharp decline in emissions by 2030, global warming will exceed 1.5°C before the end of the century, leading to irreversible losses of the most fragile ecosystems, as well as to successive crises [4]. This decade is therefore decisive to mitigate the effects of climate change, for which action must immediately be taken. This drastic reduction of our emissions is one of the most complex challenges that our society must solve and requires collective efforts throughout various fields.

To tackle global warming, many alternative "green" renewable energy generation/storage/conversion systems have recently emerged [5]. The transport sector is one of the main targets for climate change mitigation, as alone it accounts for 28% of the global energy demand, and is a significant source of CO_2 emissions [6]. This has led to a new transport revolution, in the form of electrification of the personal and commercial vehicle fleets. These electric vehicles (EVs) must include compact energy storage and conversion systems, capable of delivering sufficient power and containing enough energy to compete with internal combustion engines (ICEs). For now, two electrochemical devices are mainly targeted to collectively fulfill these requirements. They are the lithium-ion battery (LIB) and proton exchange membrane fuel cell (PEMFC), which are both complementary and essential solutions. The Battery Electric Vehicle (BEV), which has reached mass-production levels in the light mobility sector, has proven to be efficient, whilst providing an acceptable charging time and range. However, the limited specific energy ($Wh.kg^{-1}$) of LIBs makes them unsuitable for heavy duty transport. For this application, the PEMFC technology, combined with its external fuel source (hydrogen tank), is preferable. Fuel Cell Electric Vehicles (FCEVs) also have other advantages over BEVs in terms of refueling time, dependence on specific minerals, and recycling.

The need to democratize FCEVs to fully electrify the fleet (especially for the heavy-duty sector) is clear. Previously, achieving this goal was impossible due to the PEMFC durability, material cost, and performance not meeting the FCEV specification targets [6]. These major obstacles are however progressively starting to be overcome, thanks to intensive research that took place over the last decades. Ever since the production of viable and durable FCEVs has become a recent attainable goal, the technology has been a focal point for industrial players. However, one main hurdle towards economically viable mass production of PEMFCs currently remains, which is its elevated manufacturing cost. Indeed, industrial investment in FCEVs has been set in motion with the help of political inclinations and public funding, as cost parity with traditional internal combustion engines has not yet been reached [7]. To truly achieve long term economically viable FCEV production, the fuel cell manufacturing process must also further be optimized.

One relatively costly aspect of a fuel cell production line is its "break-in" or "activation" process, which is carried out right after the final fuel cell assembly [8]. This process is essential to elevate and stabilize the stack performance to a reproductible threshold value, and takes place on an "activation bench", where it must produce electricity for multiple hours. In a mass manufacturing scenario (for example 500,000 systems per year), the break-in process accounts for over 5% of the total stack manufacturing machinery cost [9]. Worse still, these calculations do not include support infrastructure, buildings and installation, whose cost increase with the parallelization of manufacturing lines (which is essential to reach a high production rate).

Symbio, a joint venture between Faurecia and Michelin, is one of the leading industrial players aiming to rapidly achieve economically viable fuel cell production. This French automotive supplier plans to produce more than 200,000 fuel cell systems per year by 2030, which would place it among the largest PEMFC manufacturers in the world. As mentioned earlier, economically viable fuel cell mass production remains difficult at present, partly due to the cost of its activation step. It is in this context that the present thesis, funded by the research and innovation branch of Symbio and co-supervised by the FEMTO-ST institute, was born.

The global objective of this thesis is to optimize the PEM fuel cell break-in procedure, and more specifically, **to reduce its duration and cost**. Induced by the will of industrial players such as Symbio to mass produce PEMFCs, the general interest for the fuel cell activation step and the efforts taken towards its optimization have only recently emerged. In other words, the fuel cell break-in procedure is a novel research topic. This thesis therefore presents a relatively broad research subject ("Methodology and tools for the optimization of the PEM fuel cell break-in procedure"). That said, to center the study towards a finite number of specific goals, and to maintain a common thread, **the perimeter of this manuscript has been narrowed to three main goals.**

The first objective of this thesis consists of providing a review of the physical principles and mechanisms that affect fuel cell activation, as well as the existing break-in methods. Gathering a broader and better understanding of the fundamentals of fuel cell activation is vital, as the research towards break-in in the literature currently remains sparse and incongruent. Having a comprehensive list of all the existing break-in methodologies is also essential as a basis for creating new optimized activation protocols.

The second ambition of this research plan is to develop numerical tools capable of simulating or monitoring the fuel cell activation process. As each experimental break-in application requires one freshly assembled fuel cell stack, simulating certain activation procedures could replace costly trial-and-error applications. Similarly, with an advanced numerical break-in characterization tool, the quality and the amount of information provided per experiment would be improved.

Finally, based on the information gathered by the two previous objectives, **the third goal** is to develop and propose optimized fuel cell break-in procedures for the automotive grade Symbio fuel cell stacks. Compared to conventional processes, these novel protocols will ideally accelerate the break-in kinetics, at a reduced reactant cost, without any compromise on fuel cell durability.

This manuscript is divided in four distinct chapters. The chapters are arranged chronologically in relation to the work carried out over the last three years and categorized according to the above-mentioned list of objectives.

Chapter 1 commences with a brief introduction to the PEM fuel cell and its activation procedure. This is followed by a comprehensive state-of-the-art on the physical principles of fuel cell break-in. Next, all the activation methods provided by the literature, as well as the existing break-in characterization tools are listed and analysed.

In chapter 2 the development and validation process of an analytical cell water transport model is presented, which is then adapted to be representative of a PEMFC that is being activated. Its main goals are to obtain a better understanding of fuel cell behavior during break-in, and provide an ionomer activation simulation tool, capable of replacing costly trial-and-error experimental applications.

Chapter 3 focuses on the development process of a novel non-intrusive diagnosis tool, whose goal is to monitor the evolution of the break-in process, during its application. Creating such a diagnostic tool requires the provision of specific databases. The novel experiments used to form this essential data are also detailed in this chapter.

In chapter 4, the main new optimized fuel cell break-in protocols developed for the Symbio stacks are presented, along with associated experimental applications, and data analysis. This analysis is performed using the theoretical knowledge of chapter 1 and by applying the numerical tools presented in chapters 2 and 3. Chapter 4 also includes a study of the impact of each activation procedure on the durability of the stack.

Chapter 1: State of the art regarding Proton Exchange Membrane Fuel Cell Break-in

1 Introduction to Proton Exchange Membrane Fuel Cells and Break-in process

1.1 Introduction to Proton Exchange Membrane Fuel Cells

Fuel cells are electrochemical energy converters which are fed with reactants that are provided by an external source. They are capable of continuously producing current over large time periods, depending on the fuel storage system capacity. Multiple fuel cell technologies exist. They are categorized primarily by the kind of electrolyte they employ, and have different fuel requirements and operating conditions. Among these converters, one has suitable characteristics for clean mobility applications (e.g. fast start-up, low temperature operation, high volumetric power density, high efficiency, type of fuel). This is the low temperature Proton Exchange Membrane Fuel Cell (PEMFC) supplied with hydrogen and air, which is the centred technology of this thesis. The schematic diagram below introduces the PEMFC components and operating principles.

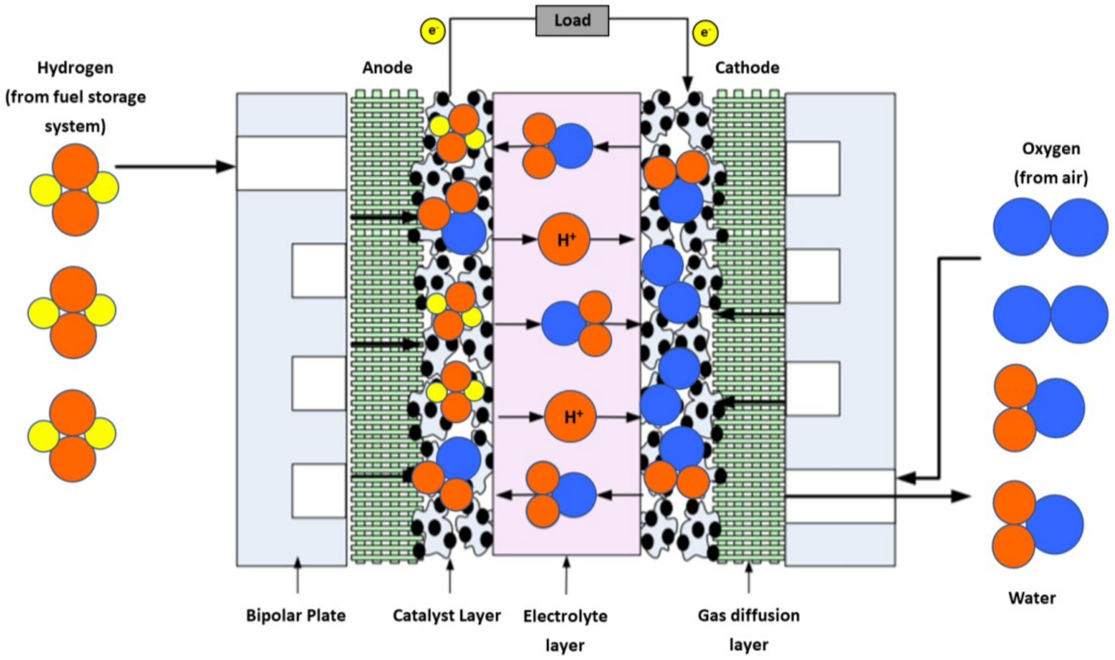

FIG. 1.1. SCHEMATIC DIAGRAM OF A PROTON EXCHANGE MEMBRANE FUEL CELL (PEMFC) [10]

The two electrochemical oxidation-reduction (redox) reactions of a PEMFC are:

- Oxidation at the anode: $2H_2 \rightarrow 4H^+ + 4e^-$ $E^0 = 0.00V$ vs. standard hydrogen electrode (SHE)
- Reduction at the cathode: $4H^+ + 4e^- + O_2 \rightarrow 2H_2O$ $E^0 = 1.23V$ vs. SHE
- The overall redox reaction: $2H_2 + O_2 \rightarrow 2H_2O$ $\Delta E^0 = 1.23V$

The fuel cell net operating process is exothermic, as not all enthalpy contained in the reactants can perform useful work [11]. Therefore, the PEMFC by-products are water and heat.

The main cell components are the membrane, catalyst layers (CLs), gas diffusion layers (GDLs) and bipolar plates (BPs). They are briefly presented below.

As its name suggests, the centre and key component of a PEMFC is the proton exchange membrane (or electrolyte layer). Its functions are to conduct the protons (H^+), but also to separate the reactants (H_2 and O_2) and block the electrons. Nafion (or another polymer electrolyte) is used, as it has the specific properties which fulfil all requirements. Water transport through the membrane is mainly driven by diffusion [12]. The catalyst layer (CL) is a multicomponent porous structure. Its different components are polymer, to transport hydrogen ions, carbon black to transport electrons, and platinum to catalyse the electrochemical (redox) reactions [13]. The pores allow free transport of reactants and water through the CL. The gas diffusion layer (GDL) is a hydrophobic porous medium, used to transport the reactants from the bipolar plates to the catalyst layers and to evacuate water. The non-uniform reactant flow from the BP channels is spread over the GDL surface. Therefore, the reactants arrive uniformly over the CL surface [24].

In a fuel cell, both sides of the membrane are coated with a catalyst layer, to form a catalyst coated membrane (CCM). This CCM is afterwards sandwiched between two gas diffusion layers, to form a Membrane Electrode Assembly (MEA). Individual fuel cells are typically combined in series into a fuel cell stack. In this stack, the MEA's are separated by bipolar plates, containing carved channels which are used to supply the reactants to the anode and cathode GDL surfaces and to circulate coolant. In a stack, the additional roles of the GDLs and BPs are to transport heat and electrons between cells. Few materials meet the conductivity requirements, whilst being resistant to corrosion. Carbon fibre paper or carbon cloth is used for the porous GDLs, whilst BPs are made out of graphite, metals, alloys, or carbon based composites [14].

1.2 Introduction to Proton Exchange Membrane Fuel Cells Break-in process

One essential step of the PEMFC manufacturing process, is its break-in procedure, also called conditioning, activation, commissioning, or incubation. This step is required for the produced cells to achieve high, stable and iso-performance. The process typically starts with placing the newly assembled fuel cell stack on an activation bench, where it is connected to an electric load, a cooling system, and supplied with reactants. Then, an activation protocol is applied, where the fuel cell produces power by following a predetermined current or voltage profile for multiple hours [15], [16]. During this period, fuel cell performance increases, until reaching a plateau. At this point, the fuel cell is broken-in and ready for operation. The terms "conditioning" and "incubation" can also be used to define a fuel cell performance recovery procedure. Similarly, "commissioning" can also refer to the post-activation factory acceptance test. Therefore, to prevent any confusion, only the terms "break-in" and "activation" are used in this manuscript.

Lowering fuel cell production cost, and therefore ensuring market access is one of the essential points that must be addressed to democratize fuel cell systems. The long duration (multiple hours) break-in step is currently the limiting factor to the fuel cell production line capacity. Having multiple activation benches for one production line is not a viable solution, due to their high costs. To achieve economic efficiency, the mechanisms behind fuel cell break-in and the associated methods must first be studied. With this knowledge, "smart" or "optimized" break-in protocols, which accelerate the activation process may be developed. During break-in, interconnections between the MEA components evolve, and morphological changes occur within each layer (membrane, CL, GDL). These mechanisms are detailed in the next section.

2 PEMFC break-in physical principles

In the literature, the mechanisms behind fuel cell break-in are often defined as the hydration of the membrane and the “activation” of the catalyst layers. This vague definition illustrates the lack of knowledge that currently exists in this area. Nor does it explain why it takes multiple hours for a fuel cell to reach high and stable performance (to be “broken-in”). Nevertheless, put together, the sparse research provides good theories to explain break-in mechanisms [17]–[19]. In this section, the different morphological changes undergone by a fuel cell during activation are presented one by one.

2.1 Membrane

To explain the polymer electrolyte break-in process, a quick introduction is given to its composition and structure. In the membrane, water is transported through hydrophilic chains containing SO_3^- sites, also called “active sites”, which can be in a protonated state. More active sites (more SO_3^- sites within the ionomer) results in a higher water content and thus a better proton conductivity. A hydrophobic backbone is required to “hold” the SO_3^- containing side chain and to ensure mechanical and chemical stability. To further increase mechanical stability, a chemical inert layer or “reinforcement” additives can be used to prevent multi-dimensional swelling. To further increase chemical stability, “radical scavengers” are added to neutralize radicals before they interact with the side chains. The ionomer structure is shown in FIG. 1.2, and a more detailed presentation of its composition is given in [17].

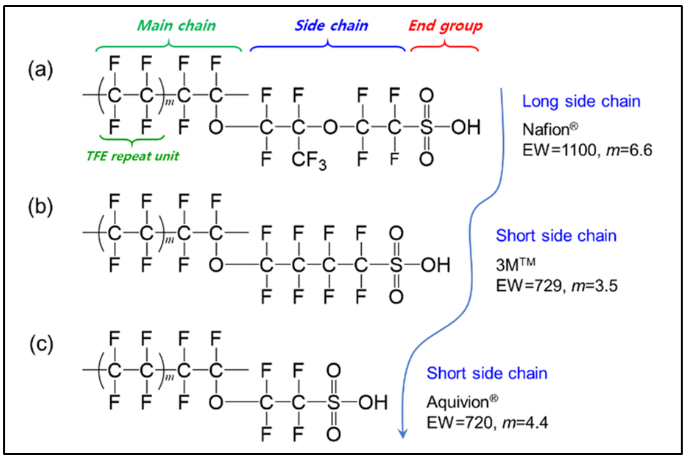

FIG. 1.2. MOLECULAR STRUCTURE OF THREE DIFFERENT POLYMER ELECTROLYTES [17]

The membrane water content (noted λ), corresponds to the number of water molecules per SO_3^- site [11]. It can be dissociated into three different regions, which are residual, bound and free water, where:

$$\lambda_{tot} = \lambda_0 + \lambda_B + \lambda_F \tag{1}$$

- Residual water (λ_0) forms the primary solvent shell. It possesses a strong bond, changes only at higher temperatures, and is often neglected as it does not depend on cell humidity conditions.
- Bound water (λ_B) regimes form around the primary shell, with a water content up to 6 water molecules per SO_3^- site.
- Free water (λ_F) regimes form with the increase in water domains and higher connectivity between the domains.

The fuel cell performance increase related to membrane activation is typically explained by its increase in water content (λ), and consequently its proton resistance reduction. The membrane activation process is actually much more complex, as it also involves swelling, polymer relaxation, decontamination, domain spacing, surface skin change, etc. [20]. These mechanisms are presented in the following subsections.

2.1.1 Membrane: Polymer hydration and structure change

The different "extreme" environmental conditions (humidity, pressure, temperature) that the membrane goes through during its production enforces a thermal and swelling memory. This memory imposes a certain membrane crystallinity level, which in turn defines its maximum water uptake in the free water regime region (λ_F). After production, the high crystallization degree results in low ionomer domain spacing, hindering water uptake, swelling and the mobility of the side chains and backbones [17].

When it is firstly hydrated during break-in, the ionomer structure undergoes multiple changes. The water domains in the membrane progressively grow and deform the polymer matrix, generating a swelling pressure. FIG. 1.3 is a schematic representation of the microstructure evolution undergone by the membrane water clusters during activation [21]. When two clusters coalesce: (i) the channels connecting the two clusters are diminished and (ii) the content of free water (λ_F) in the cluster increases (iii) distances between the sulfonate groups are reduced. These all contribute to minimize the energy barrier for proton transport.

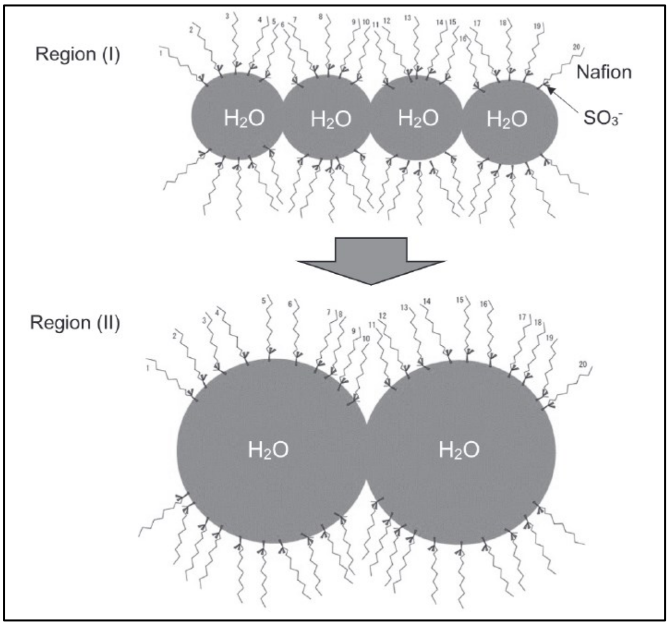

FIG. 1.3. SCHEMATIC DIAGRAM SHOWING THE COALESCENCE OF TWO WATER CLUSTERS DURING BREAK-IN WITH INCREASING CURRENT DENSITY [21]

Forming the continuous water network throughout the membrane is a sluggish process. It mainly depends on the time required for domain spacing (over 200 min) and polymer matrix relaxation (two to three orders of magnitude higher than the diffusion time constant). Kusoglu *et al.* have expressed the different processes (diffusion, polymer relaxation, domain spacing...) using an empirical fickian equation, where a different time constants is attributed to each process [20]. On FIG. 1.4, inter-domain spacing and consequently the size of the water domains increase with time is shown.

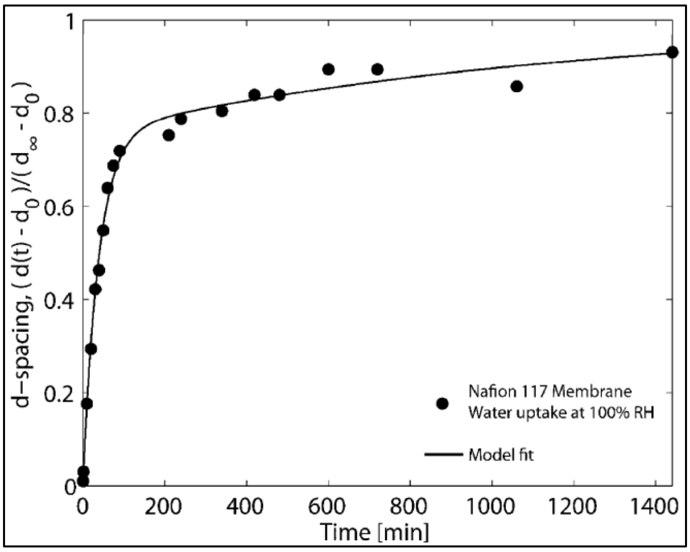

FIG. 1.4. SWELLING OF WATER DOMAINS WITH TIME FOR A MEMBRANE EXPOSED TO SATURATED WATER VAPOR AT AMBIENT TEMPERATURE [20]

2.1.2 Membrane: Surface skin rearrangement

The state of the membrane surface skin has a decisive impact on the diffusion rate within the polymer, and must be rearranged during activation. When firstly producing and introducing water, liquid water is formed at the ionomer surface. This transforms the membrane surface skin, by aligning the polymer bundles perpendicular towards the surface. The ionic conductive sites form a more hydrophilic skin layer, enhancing proton transport, reducing surface tension and therefore accelerating water uptake. The dependency of sorption kinetics on the water phase at the membrane surface, is known as the Schroeder paradox[1].

Apart from rearranging the polymer bundles, the formed liquid water film also ensures the connection between the membrane skin layer and the environment, therefore reducing proton transport resistance [17].

2.1.3 Membrane: Polymer decontamination

After its production, the fuel cell membrane is contaminated with a certain number of impurities, additives and other particles. These species reduce proton conductivity, affect electro-osmotic drag (water transported by the H^+ flow) and can moderately to severely affect cell performance. There is for example an excess of chemical additives (metal oxides and chemical complexes) which must be evacuated. Indeed, as previously stated, the membrane is doped with additives to mitigate chemical degradation, but they are often added to an excess to guarantee membrane chemical stability [22], [23]. Depending on the pre-break-in cell and/or membrane storage conditions, airborne species may also have contaminated the membrane [24]. The same goes for dust particles or other residues from the production step. Further in-situ contamination during the first start-up process must also be mitigated [17]. Indeed, as the cell voltage levels typically vary during break-in, it can generate metallic cations, which in turn can be introduced within the membrane.

---

[1] Schroeder's paradox: Nafion water uptake is different when exposed to vapor and liquid at the same activity

During activation, the generated water and proton flow both contribute to the mechanical migration and extraction of impurities [25]. Conveniently, in-situ metallic cations contamination during activation is also mitigated by a high water production and high relative humidity (RH) [17]. The removal of all contaminants from the membrane can however be a slow process (multiple hours).

As stated above, membrane decontamination increases proton conductivity to a certain extend. The most significant impact of membrane decontamination on cell performance is however related to the proton resistance and ORR (oxygen reduction reaction) kinetics at the cathode CL. This will be discussed in further detail in the following section, dedicated to the CL activation.

2.2 Catalyst layer

As previously stated, the catalyst layer is a multicomponent porous structure containing polymer, carbon black and Platinum. The regions where all elements connect are called active sites (not to be confused with the SO_3^- sites of the polymer) or three phase borders. Nafion is typically used in the CL, to transport the hydrogen ions to and from the active sites. FIG. 1.5 is a 2D representation of an active site in the CL.

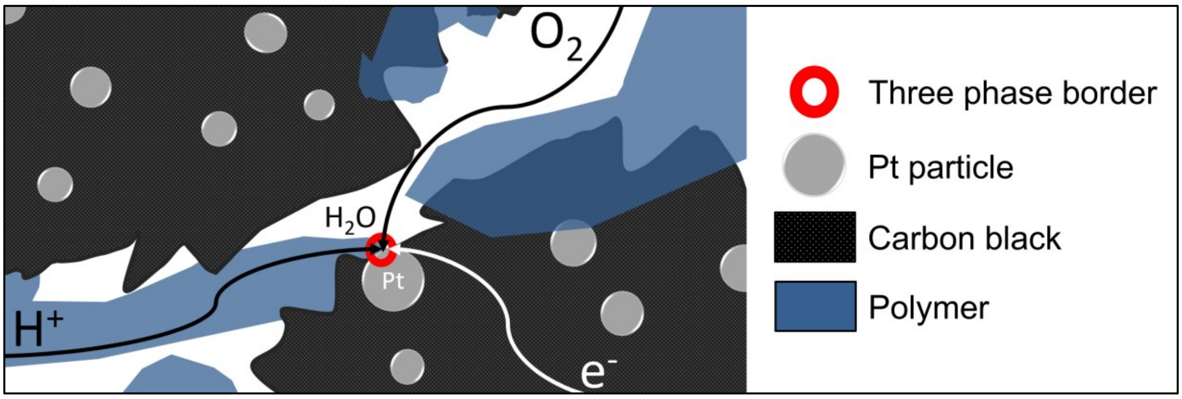

FIG. 1.5. 2D REPRESENTATION OF A THREE PHASE BORDER IN THE CL

The catalyst layer structure strongly affects overall cell performance, and is subjected to multiple structural changes during break-in. They concern all individual catalyst layer components (ionomer, carbon, catalyst and pores for gas diffusion) and are presented throughout the following subsections.

2.2.1 Catalyst layer: Pore structure change

The most common CL production method consists of directly dissolving Nafion with iso-propyl alcohol (IPA), to then be mixed with the carbon supported catalyst. This is to achieve a homogeneous distribution of the ionomer. This production method does not guarantee access to reactants, electrons, and protons in every region of the CL. Furthermore, particles, excess ionomer, and other impurities that are not anchored may also hinder the reactant diffusion and must be evacuated [17]. Nowadays, to increase the catalyst surface in the CL, the Pt nanoparticles are not only deposited on the outer surface of the carbon support, but also within the carbon cores via internal pores [26]. Unanchored particles may hinder the accessibility of the Pt located within these micropores.

During break-in, the reactants, heat and water transport evacuates the unanchored particles from the CL, but also directly affects the catalyst layer structure. The total number and volume of pores increase (porosity) as well as the number of twists and bends in those pore channels (tortuosity). Pore shape may also be affected [19]. This enhances the reactants mobility and therefore, reduces mass transfer resistance. This may be not limited to the CL, as it may also include the GDL and Micro Porous Layer (MPL). The pore opening, accompanied by the evacuation of unanchored particles also increases the number of active sites by opening new pores leading to formerly "dead regions" [18]. This enhances the cell mass activity (mA.mgPt^{-1}), and more specifically the total electrochemically active surface (ECSA) (m^2.gPt^{-1}).

2.2.2 Catalyst layer: Polymer hydration and structure change

Like the membrane, the polymer in the CL must be hydrated during break-in to enhance its proton conductivity. Increasing the CL polymer water content during activation is also essential for three other reasons, which are ionomer swelling, side chain reorientation and gas permeability increase.

The swelling pressure generated by the growth of water domains in the CL ionomer during break-in deforms and expands the polymer matrix. Maximizing the ionomer footprint increases the number of active sites as the electrolyte introduces into the CL. Ionomer swelling also increases the triple phase boundary (TPB) per active site, as it surrounds a larger surface of the Pt particle [27]. The joining between the different ionomer sections may also reduce the proton transport resistance between the CL and the membrane.

During break-in, as soon as water is produced, the polymer side chains orient themselves towards the Pt surface (FIG. 1.6). This reorientation occurs due to the catalyst hydrophilic character, and improves the proton conductivity inside the catalyst layer [17]. Simultaneously, the production of a thin water film between the ionomer and the catalyst supports proton conductivity near the active sites, as well as the ORR activity.

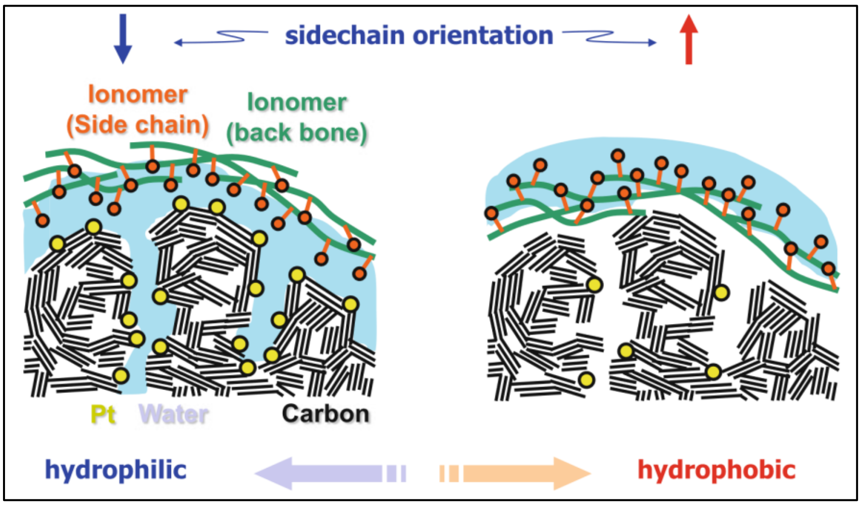

FIG. 1.6. SIMPLIFIED REPRESENTATION OF POLYMER SIDE CHAIN REORIENTATION NEAR THE CARBON SUPPORT [17]

Even though ionomer is an essential component in the CL, it negatively affects the mass transfer resistance. Indeed, it hinders the reactant accessibility to the active sites, as they must diffuse through the thin ionomer layer to reach the catalyst [28]. Oxygen diffusion resistance through the ionomer may even be the dominant loss compared to oxygen transport resistance through the GDL and CL pores (FIG. 1.7) [29]. The amount of ionomer in a CL is therefore limited, to obtain an acceptable compromise between proton conductivity and oxygen permeability.

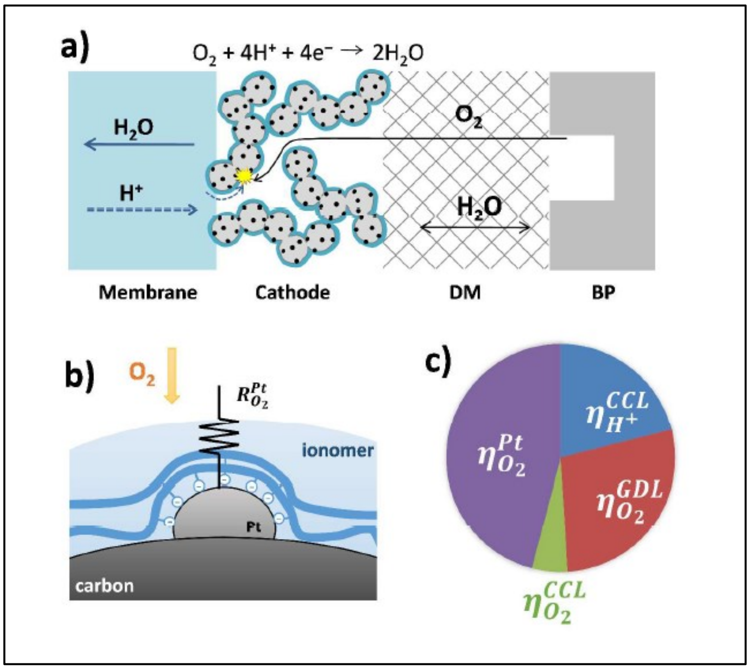

Fig. 1.7. Diagram of (a) species transport through MEA (b) local O_2 transport resistance (R_{O_2}) on Pt and (c) sum of mass transport losses (η_{O_2}) [29]

When the CL polymer hydrates during activation, its oxygen transport resistance reduces. Indeed, the ionomer phase-separates in aqueous and hydrophobic (polymer-backbone) rich domains. The gas permeability of the aqueous phase is an order of magnitude greater than that of the hydrophobic domain. The thin water film produced on the catalyst surface may also enhance the oxygen transport properties. Indeed, it mitigates direct sulfonate-Pt interaction, which is detrimental to oxygen transport near the Pt surface [28].

This said, some opposing views exist regarding the polymer hydration effects and performance increase. For example, a too thick water film may deteriorate the oxygen transport rate [17]. The water film may also hinder water uptake in the second layers (good proton conductivity is required over the whole catalyst structure and not only the catalyst sites). Side chain reorientation may also favour the sorption of end groups on the platinum surface and so further hinder oxygen diffusion. Catalyst layer polymer hydration mechanisms are still open for debate and must therefore be further studied.

2.2.3 Catalyst layer: Carbon support oxidation

On the CL carbon support, defect sites (C^+) which are prone to electrochemical oxidation may form C-OH groups. Consequently, carbon surface oxides may take shape on the catalyst surface (CO_{surf}) and then be oxidized to CO_2. This conversion process is defined as the carbon oxidation reaction (COR), and results in the loss of carbon support (Table 1.1). The COR typically occurs in a high potential environment (above 0.6V), which is achievable in a PEM fuel cell.

During activation, if the fuel cell is supplied with fuel (H_2/air) and no/little current is drawn from it, the high cathode potential initiates the carbon support oxidation reaction (COR). According to Kim *et al.* [27], the COR is partly responsible for the triple phase boundary (TPB) increase in the CL during break-in. The loss of carbon support increases the bond between the catalyst and the ionomer surrounding the Pt particles.

If the carbon supporting the Pt particle disappears, catalyst rearrangement may even occur, as it relocates to the ionomer. This increases the contact surface at the catalyst-ionomer-gas conversion point [30].

Expression
$C \rightarrow C^{+}_{(s)} + e^{-}$
$C^{+}_{(s)} + H_2O \rightarrow CO_{surf} + 2H^{+} + e^{-}$
$CO_{surf} + H_2O \rightarrow CO_2 + 2H^{+} + 2e^{-}$

TABLE 1.1. CO_2 FORMATION THROUGH THE CARBON OXIDATION REACTION (COR) [27]

When the carbon black is oxidized, its hydrophilic/hydrophobic properties are also affected. According to Kocha *et al.*, increasing the carbon support hydrophilic properties is required to obtain reproductible performance [24]. The increase of carbon hydrophobicity may also accelerate the CL ionomer hydration and surface skin rearrangement.

The enlargement of the TPB area by the COR is debatable. Indeed, the COR is typically considered as a severe fuel cell degradation mechanism for the following reasons: (i) Pt particle relocation results in the loss of the electron conductor phase, hindering electron transport. (ii) The loss of carbon support can also result in loss and/or agglomeration of catalyst particles and consequently ECSA reduction. (iii) The intermediate products of oxidation (CO_{surf}) may remain on the surface of metal catalyst particles and poison the catalytic sites with a subsequent loss of ORR activity [31]. (5) Reducing the hydrophobic properties of the carbon surface increases water transfer resistance resulting in less efficient reactant transport [24]. The necessity of carbon support oxidation to obtain reproductible performance, as well as its beneficial and detrimental effects during break-in must be further studied.

2.2.4 Catalyst layer: Catalyst decontamination

When a fuel cell is just assembled, many unwanted species are found on the catalyst surface. This “poison layer” or “impurity layer” adversely affects the ORR [28], [32] and limits the active surface [33]. These species, their nature and origins are presented below.

As previously stated, a certain number of chemical complexes are flushed out of the membrane during activation. As they are drawn toward the cathode CL, these impurities progressively adsorb on the Pt, which affects the ORR [28], [34] (FIG. 1.8). The amplitude of the catalyst contamination by the ionomer chemical additives depends on their nature (more severe with organic than inorganic additives) [22], [23]. With inorganic additives however (e.g. M-MnO_2), produced ions (e.g. Mn^{-}, Mn^{2+}) irreversibly interact with the sulfonic acid sites, resulting in lower final polymer proton conductivity [35]. Apart from chemical additives, other membrane compounds such as sulfonate groups and fluoride are drawn to the CL during break-in. A fraction of these species may be trapped in the MEA after production, and others may be formed during the break-in process as the membrane slightly degrades [28]. Carbonaceous species derived from alcohol, if the latter has been used to form the catalytic ink also contaminate the catalyst. A solution based on iso-propyl alcohol is typically used, for its quick and effective evaporation. When alcohol evaporates, it transforms into hydrocarbons and thus poisons the CL [36]. If solvents do not properly evaporate, the oxygen diffusion may also negatively be affected.

In addition to the contaminants derived from the MEA components, airborne species also contaminate the catalyst surface, and must be desorbed during break-in. A fuel cell manufacturing process typically includes extended storage periods of stacks or cell components, during which the catalyst is slowly being poisoned by the surrounding air [33]. Sulfur oxides (SOx), nitrogen oxides (NOx), carbon oxides (COx), propane, benzene and many other organic chemical species partly settle in the catalyst [34]. Poisoning occurs at extremely low concentration of impurity anions such as sulfate, chloride and nitrate (starting at 500 ppb for sulphur dioxide for example) [37]. Among air contaminants, S impurities (H_2S and SO_2) have been shown to cause the most important performance decay. Apart from airborne contaminants, a thick layer of surface oxides on the Pt surface also hiders the ORR. The amount of coverage and type of oxide species is mixed (PtOH, PtO, PtO_2 etc…). In addition to the surface oxides, there is a slow logarithmic growth of sub-surface oxide layers, via the "place exchange mechanism" [28], [34].

Catalyst decontamination corresponds to the desorption and removal of all previously mentioned surface-blocking species. This break-in mechanism is essential as it strongly increases the catalyst ORR and mass activity [28] and in turn severely affects cell performance. The oxide removal process is relatively quick and can take from a few seconds to 20 minutes [38]. The desorption rate of chemical additives is more sluggish, as can be seen on FIG. 1.8, which represents the performance recovery phase of a doped MEA.

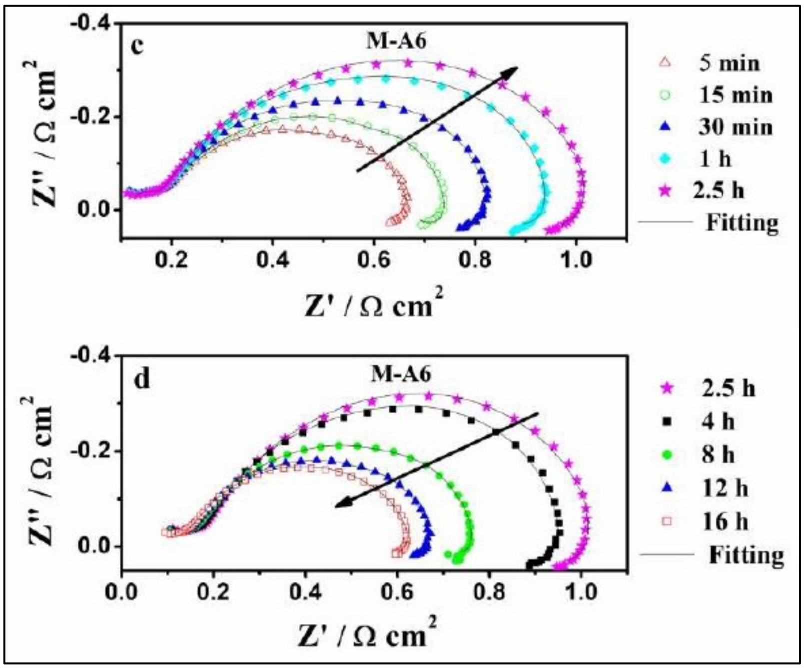

FIG. 1.8. EIS CURVES DURING BREAK-IN OF MEA DOPED WITH ORGANIC ADDITIVES [23]

2.2.5 Catalyst layer: Catalyst structure reorganization

To maximize the Pt surface to mass ratio ($m^2.gPt^{-1}$) and consequently the ECSA, Pt particles are machined into small spheres. The adsorption of oxygenated species in the catalyst surface however increases inversely proportional to Pt particle size. Thus, an optimal Pt particle size exists (2 to 4nm), where the ECSA is maximized, and the ORR is not hindered by the strong adsorption of oxygenated intermediate species [17].

Pt particle deposition on the carbon surface is not perfectly homogeneous. Consequently, Pt particles reorganize during activation, to reduce surface energy irregularities. During reorganization, Pt particles irreversibly increase in size through migration, agglomeration, and coalescence as well as Pt dissolution from the support and redeposition. The amplitude of each contribution depends on the size and location of the Pt on the carbon support, carbon support type, and the nature of the Pt-C interface [28].

Even though during break-in, the increase in Pt particle size reduces the ECSA ($m^2.gPt^{-1}$), an overall increase in mass activity ($mA.mgPt^{-1}$) is observed. This can partly be explained by the counterbalancing effect of other activation mechanisms such as catalyst decontamination (Fig. 1.9), which increase the “specific activity” or activity per site ($A.cmPt^{-2}$). This said, the catalyst structure reorganization is also partly responsible for the increase in mass activity.

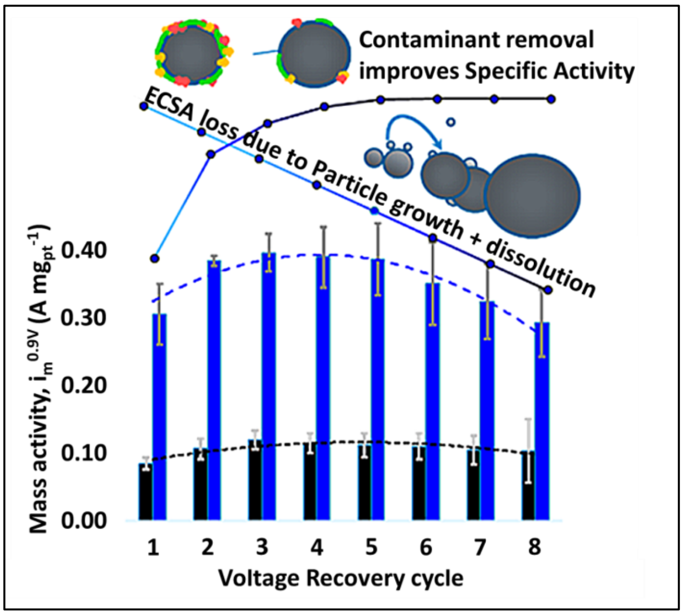

Fig. 1.9. Combined effects of catalyst decontamination and ECSA loss on fuel cell mass activity due to particle growth [28]

First, Pt dissolution may counter intuitively locally increase the ECSA, by dissolving Pt particles which block pores leading to formerly “dead regions” [17]. Second, by affecting the Pt structure sensitivity of the ORR, catalyst reorganization results in an increase in activity per site ($A.cmPt^{-2}$) [28]. Indeed, the increase of Pt particle size reduces the adsorption strength of oxygenated species (O, OH, OOH…), in favour of the ORR [17]. Furthermore, the rearrangement of catalyst particles also results in the rearrangement of the catalyst atomic structure (Pt-Pt and Pt-Cobalt coordination) [28], decreasing the Pt-O bond strength [38].

Third, as previously stated, before activation, a layer of subsurface Pt-oxides exists, which has been formed due to the place-exchange mechanism. At the start of break-in (first 20 minutes), as the platinum oxide dissolution is enhanced, sub-surface platinum is exposed, leading to a greater Pt surface roughness. During the following 200 minutes, the corners of the Pt particles are progressively rounded, and the rough faces are smoothed, therefore increasing the ORR mass activity [38].

2.3 Cell

The individual PEM fuel cell components are the CCMs (composed of the PEM and its catalyst layers), porous layers (GDLs with MPLs), Bipolar plates (BPs) and sealing gaskets [39]. To assemble the cell, all components are sandwiched and then clamped together at a certain predetermined pressure value. This seals and isolates the cell and maintains an adequate contact surface area between all components.

The cell ohmic resistance corresponds to the cumulated resistances of each component (of which the membrane has the highest value), but also the contact interface resistances between cell components [19]. During activation, the contact surface area between all components, and therefore the cell contact interface resistances evolve. This section may be referred to as the "mechanical" aspect of fuel cell break-in.

2.3.1 Cell: Interfacial contact resistance reduction

The interfacial contact resistances between cell components are significant contributors to the ohmic losses in PEMFCs. According to Netwall *et al.*, they may even be the main contributor to the total cell ohmic losses [39]. The contact resistance between the GDL and BP is considered as most significant, and therefore causes the highest potential loss [40]. This said, the surface contact resistances between the microporous, catalyst, and ionomer layers are also not negligible. Their values however rather depend on the MEA production methods and conditions (temperature, pressure, duration..), than stack compression [41], [42].

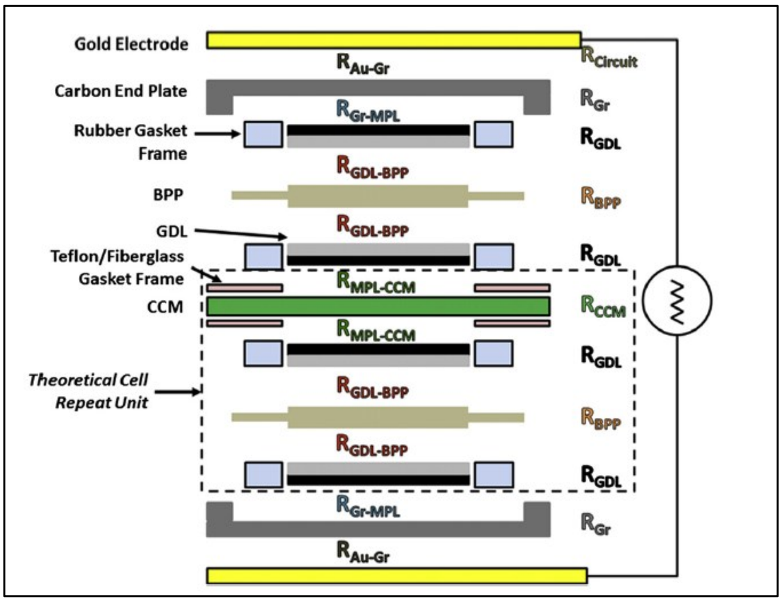

FIG. 1.10. CROSS SECTIONAL VIEW OF CELL COMPONENTS AND RESISTIVE COMPONENTS [39]

Before activation, the freshly assembled cell components have not had a chance to adapt and fit to each other's forms. Furthermore, as previously stated, during break-in, irreversible morphological and microstructural deformations/changes and variable water and heat production take place. Both points alter the cell contact interface resistances (FIG. 1.10). During activation, by adjusting the stack clamping pressure, the cell components can progressively be deformed until no more variations are observed, and the minimal area-specific resistance is reached [39].

2.4 Summary diagram and table

To conclude, multiple morphological changes occur during break-in and are mostly of an electrochemical nature and taking place in the MEA. The diagram shown in Fig. 1.11 is a simplified representation of the morphological changes endured by the MEA during activation.

For the membrane, there is the polymer hydration and structure change, surface skin rearrangement and decontamination. For the catalyst layer, there is the pore structure change, polymer hydration and carbon support oxidation, as well as catalyst decontamination and catalyst structure reorganization. These morphological changes directly affect cell properties such as the cell porosity, catalyst size, shape and activity, polymer chain orientation and spacing, etc. Cumulated, the break-in mechanisms contribute to reduce the entire spectrum of fuel cell resistances (reaction rate, ohmic and mass transfer).

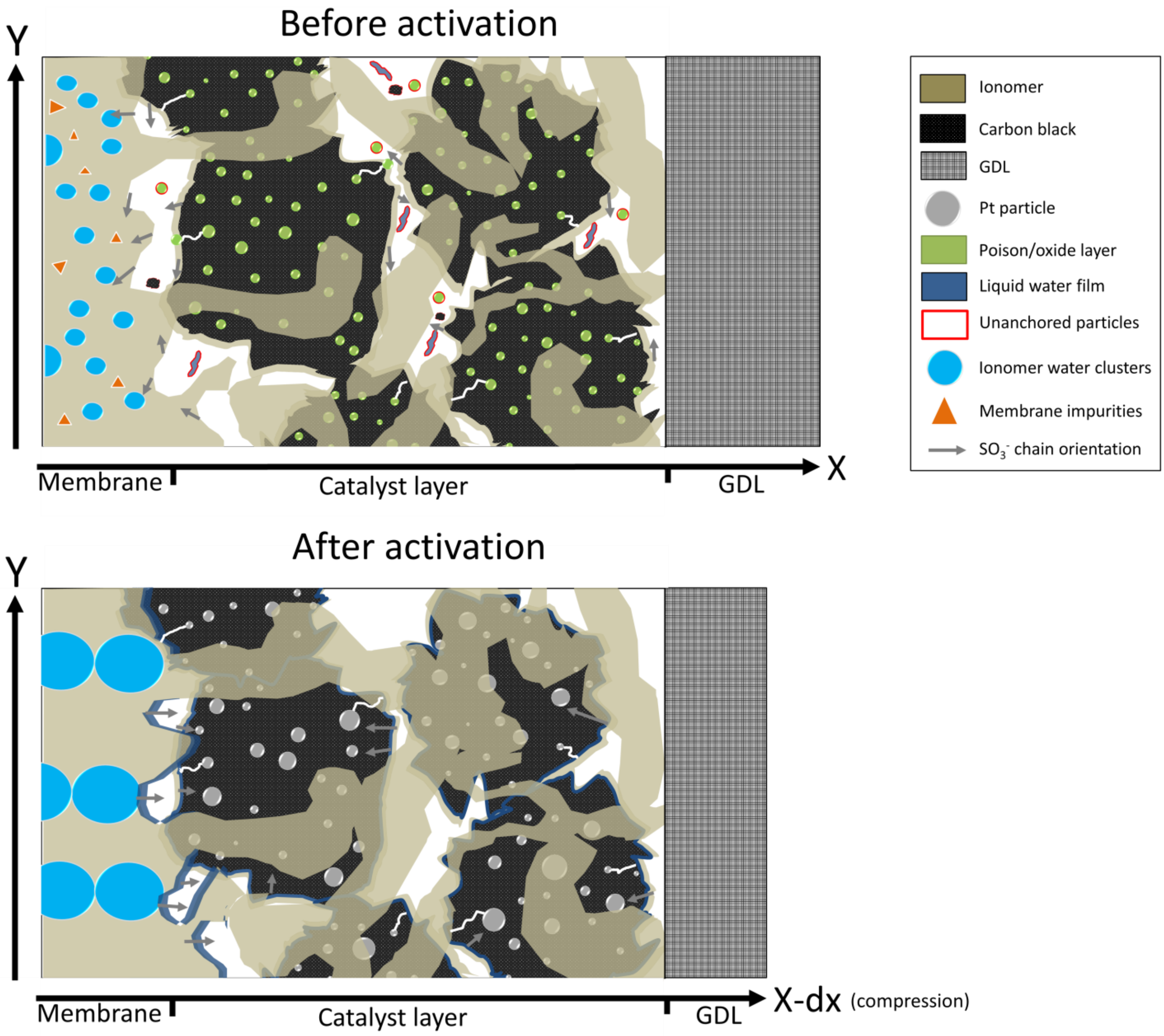

Fig. 1.11. Morphological changes endured by the MEA during break-in.

Mechanism	Time scale	Main Effect
Membrane		
Polymer hydration and structure change	> 200 min	Ohmic resistance reduction
Polymer surface skin rearrangement	Max 20 min	Ohmic resistance reduction
Polymer decontamination	Hours	Ohmic resistance reduction
Catalyst layer		
Pore structure change	Minutes – hours	Mass transport and reaction rate resistance reduction (ECSA increase)
Polymer hydration and structure change	/	Ohmic and mass transport resistance reduction
Carbon support oxidation	Minutes - hours	Reaction rate resistance reduction (ECSA increase)
Catalyst decontamination	Seconds - hours	Reaction rate resistance reduction (Specific activity increase)
Catalyst structure reorganization	Hours - days	Reaction rate resistance reduction (ECSA reduction, specific activity increase)
Cell		
Interfacial contact resistance reduction	Minutes	Ohmic resistance reduction

TABLE 1.2. BREAK-IN MECHANISMS, ASSOCIATED TIME SCALES AND MAIN EFFECTS

Using the knowledge behind break-in physics (TABLE 1.2), the fuel cell activation process and associated methods can be revisited. It is essential to understand these physical principles to investigate and correctly interpret the different existing break-in methods, presented in the following section.

3 PEMFC break-in experimental methods

As stated in the introduction of this manuscript, the break-in process typically consists of placing the fuel cell stack on an activation bench, where it produces power by following a predetermined current or voltage profile for multiple hours. The long duration break-in step is currently the limiting factor to the fuel cell production line capacity. In response to the new gathered knowledge regarding break-in mechanisms, a certain number of "smart" or "optimized" methods have been presented in the literature. These methods typically reduce the time required to break-in a fuel cell, or bring other improvements such as minimizing reactant consumption, simplifying the break-in process, reducing machinery cost, etc.

New activation methods are typically related with stress, by modifying the operating parameters or load profile. Some of these new methods are applied on a traditional activation bench whilst other are more exotic and use non-conventional machinery or processes. There are even methods which consist of partly integrating fuel cell break-in into the manufacturing process. In the literature, these new break-in procedures are often distinguished in two categories, which are "Online" and "Offline" activation. The definition between offline break-in (also called pre-treatment) and online break-in is however ambiguous. Some categorize pre-treatment as all protocols applied on fuel cell components before their full assembly. Others state offline methods as all protocols not requiring an electronic load and/or activation bench. In this manuscript, "offline" break-in, or "pre-treatment", or "ex-situ" methods are categorized as all methods applied pre-final fuel cell assembly. The second category of “online” or “in-situ” break-in is composed of all other methods, and are applied on fully assembled fuel cell stacks (whether they require a load and/or activation bench, or not).

Efforts have been made to summarize and categorize all methods throughout the following subsections. Methods that have similarities regarding their process / operating conditions are placed in the same category.

3.1 Break-in methods applied before final Fuel cell assembly (Offline break-in)

Even though it is not carried out on an activation bench, fuel cell pre-treatment can also be classified as a partial break-in procedure, as it affects the MEA morphology. If a fuel cell is pre-treated, it still needs to be broken-in on an activation bench, but for a shorter period. Fuel cells can be pre-treated instead of waiting for the activation bench to become available, consequently increasing the production line capacity. The fuel cell pre-treatment procedures found in the literature are presented in this subsection.

3.1.1 Electrode / MEA steaming / boiling

Electrode steaming/boiling involves treating the catalyst coated electrode in liquid water or steam, before MEA assembly. Using a simple household pressure cooker and 10 minutes of steaming, Kaufman *et al.* manage to increase an initial cell performance by over 50% (at 0.6V) [43]. The steam enhances CL porosity, washes out unanchored impurities and removes excess ionomer, which eases reactant transport and opens new active sites. It may also improve the CL ionomer crystallinity level and polymer arrangement, which in turn increases the free water content and total maximum water uptake [17]. The following MEA assembly process (called hot bonding) however fully dehydrates the polymer, and sets a thermal history, partly erasing the effects of the pre-treatment method. Some effects of electrode steaming on the polymer structure however remain, as the CL maintains an easier hydration characteristic after MEA assembly [43].

A method that consists of steaming an entire CCM and/or MEA has also been presented in the literature [44]. This more recent patent, (owned by the 3M corporation) suggests that the steam treatment should be applied at a super-atmospheric pressure for better performance. As this method is applied after the MEA hot bonding process, it is not followed by ionomer dehydration or crystallinity increase. Other issues related to CCM swelling and deformation however arise, which might make stacking impossible or cause reactant leaks. In [45], Zhiani *et al.* state that the method can be applied on a 7-layer MEA (composed with the sub-gasket). The sub-gasket material resistance to such levels of humidity and heat also remains questionable. It therefore might be preferable to steam treat the MEA when it is fully assembled in a stack. This process will be presented later on, in the “online” break-in section.

3.1.2 H_2SO_4 electrochemical treatment

This method consists of immersing a MEA in a diluted sulfuric acid solution, connecting it to a small load, and then carrying out potentiostatic and galvanostatic cycles. The potential is maintained between the limits of Platinum oxide (PtO) formation (>0.8V) and hydrogen evolution (<0V). The entire operation is carried out one time to treat the anode and one time for the cathode, by switching the polarities of the two sides of the MEA. According to Palanichamy *et al.*, this process may not only increase the CL porosity, but also desorbs surface-blocking species from the Pt surface [36]. Other studies suggest that when a polymer is treated with strong acids (such as H_2SO_4), it changes its elastic forces and swelling pressure, which in turn increases the membrane water uptake [46]. If the membrane is produced with basic ionomer material, it may also activate residual fluorinated side chain extremities (SO_3F to SO_3H), to build the proton conductive end group [17]. This pre-treatment method is however rather cumbersome/time-consuming due to membrane swelling, handling issues, dimensional variability and therefore not well-suited for mass production [24].

3.1.3 Membrane plasma sputter etching

Nguyen *et al.* tested the impact of different membrane pre-treatment methods on its surface ionic activity [47]. The ionic activity at the interface between the membrane and polymer phase in the CL has a significant impact on proton and water conductivity. Their tests included H_2O_2 wash (typically used to remove the membrane organic impurities [24], [43]), H_2SO_4 wash, as well as plasma sputter and reactive ion etching.

The first observation of Nguyen *et al.* was that the as-received Nafion membrane had lower surface activity than that calculated from its chemical formula. H_2O_2 wash and reactive ion etching further reduced the surface ionic activity, whilst H_2SO_4 wash had no negative impact. Sputter etching had the opposite effect, by increasing the surface ionic activity, close to what is expected from its calculated chemical formula.

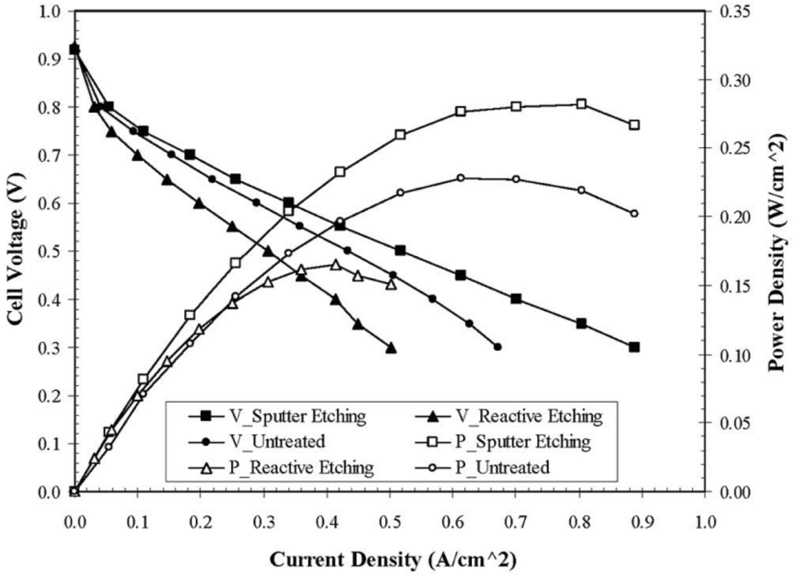

FIG. 1.12. EFFECT OF PLASMA ETCHING ON MEMBRANE SURFACE IONIC ACTIVITY AND FUEL CELL PERFORMANCE [47]

Indeed, the sputter etching method removes the hydrophobic Teflon-rich skin layer of extruded Nafion membrane [47]. It also increases the membrane roughness, improving its contact with the CL, resulting in a better performance [17] (FIG. 1.12). This skin structure change results in a membrane surface that may become hydrophobic quicker and remain so for a longer time after it has been in contact with liquid water.

3.1.4 GDL compression

As previously stated, break-in causes geometrical distortion of the stack, which can be mostly assimilated to GDL deformation [48]. To compensate the loss of compression and maintain optimal ohmic contact resistance, the stack clamping pressure can be adjusted [40]. This can however increase mass transfer resistance, by partly intruding the GDL into the flow-field channels, resulting in maldistribution of reactant gasses [39]. General Motors presented a GDL pre-treatment method that resolves this issue [48].

Their method consists of cyclically deforming the GDL using a press, until it converges to a certain thickness. The number of required cycles and applied pressure depend on the GDL material softness level, as soft material is more prone to adopting a compressive set. Consequently, the total GDL deformation and therefore interfacial contact resistance increase will be much less significant during break-in. Furthermore, if the stack clamping pressure is adjusted, less and more uniform GDL intrusion occurs (FIG. 1.13).

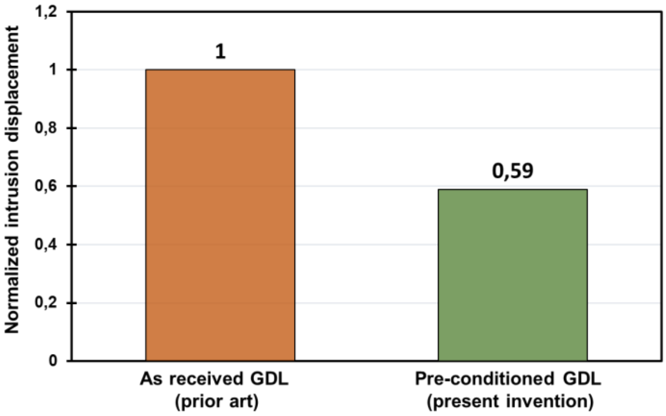

FIG. 1.13. NORMALIZED INTRUSION DISPLACEMENT OF AS RECEIVED GDLS COMPARED TO PRECONDITIONED GDLS [48]

3.2 Break-in methods applied after final Fuel cell assembly (Online break-in)

This subsection regroups all “online” break-in methods, that are carried out right after the fuel cell stack is fully assembled. They are more or less polyvalent and unconventional. The methods used to accelerate the activation process are presented one by one, from the least to the most distant from the traditional methods.

3.2.1 Optimized load profile activation

During the online break-in procedure, current is typically drawn from the stack using an electronic load, which can be configured for galvanostatic or potentiostatic operation. When producing current/water, the proton conductive channel is generated within the ionomer [24], impurities are washed out and the polymer surface reorganizes. Traditional CC/CV (constant current/constant voltage) break-in profiles, such as presented by the U.S. department of energy or E.U. joint research centre typically consist of maintaining the mean cell voltage within a reduced range (0.45 to 0.75V) [49], [50]. This is to ensure fuel cell durability, as the priority of standardized activation protocols is to prevent cell degradation, regardless of its specifications.

Many novel CC/CV profiles have been proposed in the literature, in the hope to accelerate the break-in process [15], [51], [16], [52], [53]. The current or voltage range, and dynamic variations of those profiles vary. The “current stepping” profile presented by Yang *et al.* [51] is for example based on the current profile typically used for polarization curves. Using a dynamic CV profile, Yuan *et al.* managed to activate a stack in only 2 hours, by cycling from 0.3 to 0.6V, for 20 seconds per cycle [18]. By increasing the CV/CC profile range and/or frequency, the catalyst surface becomes subjected to oxidation/reduction processes, combined with the cycling of the generated water, desorbing and evacuating surface-blocking species [24]. Variable voltage/water production also accelerates the CL pore structure change, evacuation of unanchored particles and carbon black oxidation. Furthermore, as different potential levels trigger different specific activation mechanisms, having a dynamic load profile covering an important potential range is preferable [27].

The different impacts galvanostatic and potentiostatic activation have on break-in have also been studied in the literature [27], [16], [54]. All authors confirm that CV operation is preferable. At CV, the proton flow is more uniform over the membrane surface, even if the membrane water content is not homogenous. At CC, the protons only go through the already hydrated Nafion sections (FIG. 1.14). Therefore, the activation mechanisms and water production rates are more uniform over the membrane surface with CV activation.

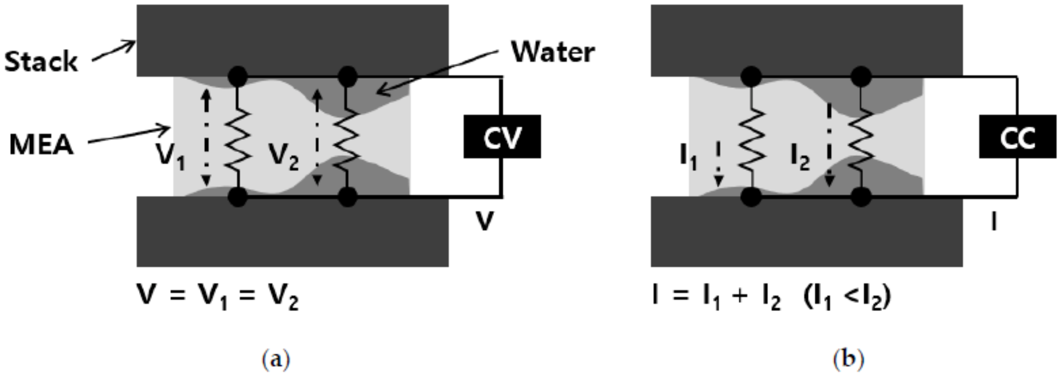

(a) (b)

FIG. 1.14. DIFFERENCE BETWEEN (A) CV OPERATION, AND (B) CC OPERATION [27]

To conclude, the optimal load profile may be dynamic, cover an important voltage range, and be carried out in CV mode. This said, CC control is much simpler to implement on a test station, and increasing the cell voltage cycling range and frequency generates thermal, fluidic and electrical imbalances. The impact of these stressors on stack durability is discussed in further detail in the next section of this chapter.

3.2.2 High temperature / pressure activation

According to PEM durability criteria, the cell and reactant temperatures must not exceed 75°C [55]. Almost all traditional break-in protocols (for cells using Nafion) respect these criteria, within a 5°C margin [16]. The cell pressure is also often limited to prevent mechanical failures or excessive reactant crossover.

The impact of the cell temperature and pressure conditions on activation time was first studied by Kaufman *et al.* on different types of MEAs [56], [57]. In each case, the elevated temperature and pressure resulted in shorter break-in times and better cell performance. Later studies confirmed the benefits of high cell temperature on activation time and performance, by testing cells up to 90°C [27] and 95°C [18]. FIG. 1.15 shows the decreasing trend of the membrane and polarization resistances with increasing temperature [18].

In the CL, the elevated pressure and temperature increases molecular agitation and therefore the pore opening rate and the ECSA. High temperatures also favour redox reactions (impurities/oxides desorption) and catalyst structure change kinetics (particle agglomeration, rounding...), resulting in an improved activity per site. This said, the maximum stack temperature should be limited (<100°C) to not affect the membrane crystallinity level (which could reduce ionomer water uptake [17]) and to avoid excessive water evaporation.

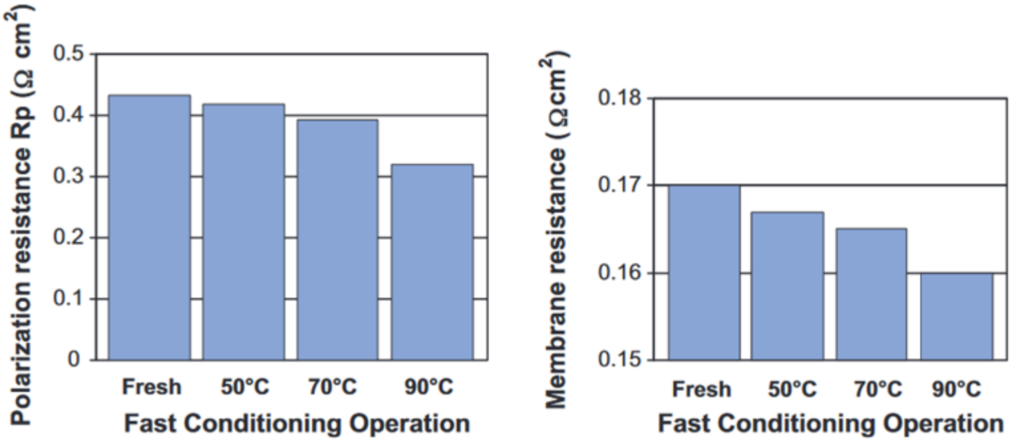

Fig. 1.15. EIS features of cells activated at 0.6V for 6 hours at different temperatures [18]

3.2.3 Supersaturated activation

Generating liquid water in the MEA during activation is essential to hydrate the polymer and change its structure, rearrange the surface skin, evacuate the Pt contaminants and non-bonded particles, etc. Therefore, the cell may be flooded in a “controlled” manner, to obtain liquid water without causing degradations.

Cho *et al.* propose the injection of water-saturated nitrogen for 2 hours to fully hydrate the ionomer [58]. An improved method, which guarantees liquid water formation within the stack, consists of injecting pure steam [45]. It can be categorized as the online variant of the MEA steaming method [44], without the CCM/sub-gasket deformation issues. As shown through Electrochemical Impedance Spectroscopy (EIS) and Cyclic Voltammetry (CyV), cell steaming significantly reduces ohmic and mass transfer resistances and increases the ECSA [45]. The low operation cost of this method is worth noting (no reactant consumption nor electric load), but it does require additional machinery (a vaporizer).

Temperature-controlled condensation methods have also been proposed in the literature, such as the "cooling after stop" technique [51]. This method simply consists of shutting down a stack and letting it passively cool down, without prior purging. An active rapid stack cooling variant of this method is presented in a Nissan patent [59]. The strategy applied in this patent slightly differs, as the stack is purged with dry reactants before cooling, and brought to an extremely low temperature (-1°C). With this strategy, water condensation is still significant during cooling, but there is no flooding risk upon restart. It however requires a temperature-controlled enclosure, or glycol cooling circuit, and presents risks of water freezing.

Temperature-controlled condensation techniques performed during stack operation also exist. Condensing during stack operation is hugely advantageous, as the current production-related mechanisms (presented in 3.2.1) occur simultaneously. Yang *et al.* propose to heat a stack to 60°C at the open circuit voltage (OCV), and then feed it with water-saturated reactants at 70°C while producing current, to force water condensation [51]. To avoid reactant depletion, the produced current must remain low. A variant of this method with more efficient heating is presented in a Toyota patent [60], where the calories are directly generated by the stack (called "heating power generation"). The phase where the water-saturated reactants are supplied is called "cleaning power generation" (Fig. 1.16). During this phase, the variable cathode potential also desorbs impurities from the catalyst surface.

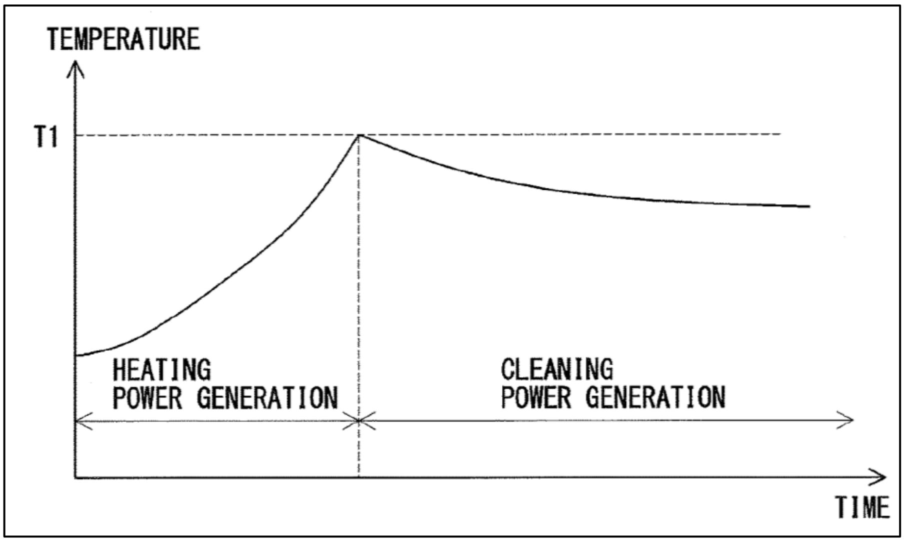

FIG. 1.16. STEPS OF THE SUPERSATURATED OPERATION PROTOCOL [60]

The Toyota patent variant of the supersaturated activation method is the best compromise between simplicity, efficiency, and versatility. This said, the “cooling after stop” technique may be suitable at the end of the break-in process, or when a shutdown phase is already foreseen during the protocol.

3.2.4 Short-circuit / pulsed activation

This method consists of accelerating the activation process by alternating between high power (e.g. short circuit) and low power (e.g. zero load) conditions. The high power phase is used to activate the stack, and the low power phase is required for the stack to "recover". In short circuit, the stack is at full capacity (water and heat production, gas flowrate…). The ionomer and catalyst restructuring break-in morphological changes are therefore accelerated. The cyclic fluctuation of the cathode voltage is favourable for the reduction and oxidation of different surface-blocking species, and the high gas flowrate ideal to evacuate them. Cyclic membrane swelling/shrinking may also be more efficient than constant high humidity conditions to accelerate the formation of a continuous water network [24].

To apply this method, Hyundai motor company [61] proposes to supply the fuel cell with reactants, connect it to a cooling circuit, and then connect a cable between the anode and cathode to generate a short circuit. The cell current is controlled by directly regulating the reactant supply (FIG. 1.17). According to the authors, cell degradations are avoided by switching to a low power mode each time the cell voltage is reversed for more than 30 seconds. Based on this reasoning, a complete 30-minute protocol is proposed (with a low flowrate for 1 minute and then a high flowrate for 3 minutes, for 7 repetitions).

This said, nothing ensures that short circuiting for less than 30 seconds, and the reactant regulation power control method do not degrade the stack. The associated heat dissipation and the inhomogeneity within the stack, amplified by reactant depletion may severely impact durability (carbon corrosion, membrane thinning...). A less "extreme" variant of this method is proposed by Galitskaya *et al.* [62]. It aims to greatly accelerate break-in, whilst conserving stack durability. In this version, a load is used to alternate the fuel cell voltage between 0.1V (quasi-short circuit) and OCV. In their research, optimal durations for these two steps were determined (high power and OCV for 40 and 20 seconds, respectively).

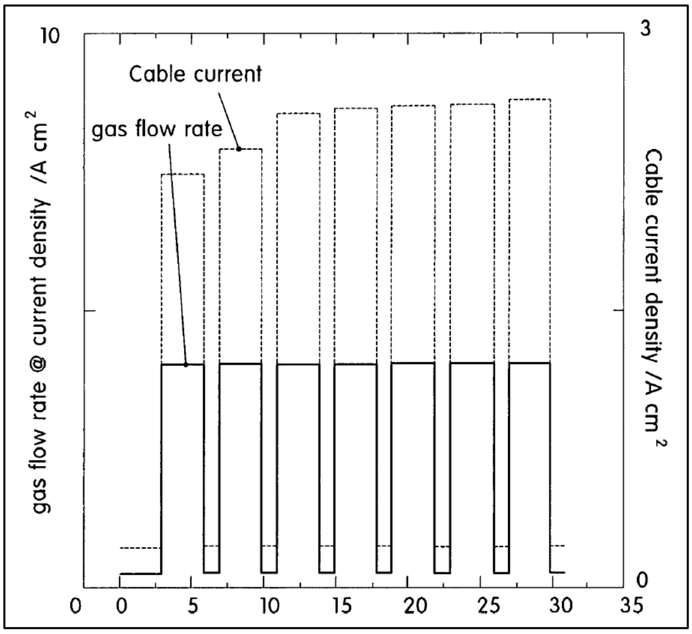

FIG. 1.17. SHORT-CIRCUIT BREAK-IN PROTOCOL [61]

3.2.5 Air braking / starvation activation

The "Air braking / starvation" method consists of briefly drawing power from a fuel cell in the absence of oxidant. When oxygen is depleted, hydrogen partially reforms at the cathode (FIG. 1.18), and the cell voltage progressively drops as the residual oxygen is consumed. Combined, low cell potential and hydrogen reforming create strong reducing conditions, therefore desorbing oxides and impurities from the catalyst surface. The absence of an air flow also increases the water molar fraction at the ionomer surface, as oxygen is consumed, and the produced water is not evacuated. Hydrogen reforming may also open pores leading to new active sites, or even enhance the TPB by irreversibly affecting the CL morphology (thickness) [30].

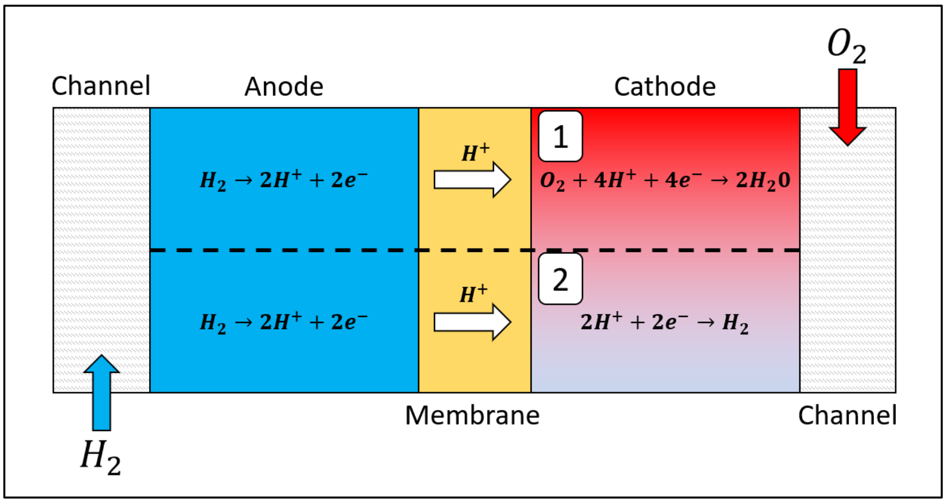

FIG. 1.18. ILLUSTRATION OF TWO ZONES AT THE CELL CATHODE DURING AIR STARVATION

Ballard first applied this method, by simply supplying a FC with reactants, requesting a current from a load, then cutting off the oxygen supply [63]. Balogun *et al.* propose a more compete version of this method, by also implementing high current and relaxation phases [64]. Additionally, a constant pressure gradient of 0.5 bar is imposed ($P_{anode} > P_{cathode}$), to force the passage of hydrogen to the cathode. The break-in mechanisms related to high current and relaxation phases have been presented in the previous section (e.g ionomer restructuring, catalyst structure change, impurity desorption and evacuation). The reducing conditions at high current of the Balogun method (0.3V) are however not as strong as for the pulsed activation method (0 to 0.1V), in favour of cell durability. Starving the cathode of air and forcing hydrogen crossover however make up for this shortcoming, by generating even stronger reducing conditions.

Balongun *et al.* fully activated a $5cm^2$ single cell in 40 minutes using their method (this said, more time may be necessary for large surface/number of cells stacks). Furthermore, if well controlled, contrary to the anode starvation method, cathode starvation can occur without degrading the cell [65]. Starving the cathode of air may also be applied on any test station, as it does not require additional machinery [66].

3.2.6 Reverse flow activation

Current production over the cell surface is typically not uniform, as a reactant concentration gradient exists between the gas inlet and outlet. This also induces a gradient in activation kinetics between the inlet and outlet regions, as observed by Park *et al.* on a segmented cell during activation [55]. The reverse flow method aims to reach balanced activation over the cell surface, by periodically changing the flow direction of reactants. This can be achieved by “port reversal”, which consists of reversing the stack upside down (FIG. 1.19), or “flow reversal” where the reactant inlet and outlet ports are permuted using quick connectors.

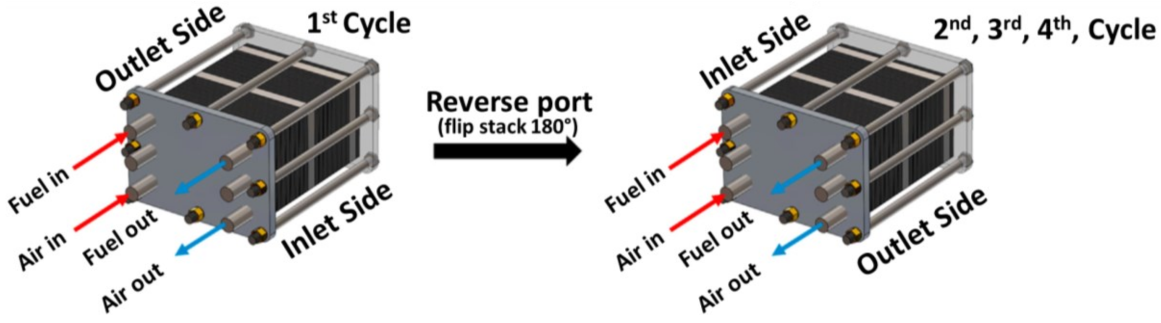

FIG. 1.19. PORT REVERSAL VARIANT OF THE REVERSE FLOW ACTIVATION METHOD [55]

To determine the efficiency of the reverse flow activation, Park *et al.* activated two identical 5 cell stacks using a conventional break-in protocol (0.6V constant voltage). Simultaneously, port reversal and then flow reversal was applied to one of the two stacks, resulting in a 43% activation time reduction, for similar final stack performance [55]. This said, reversing the stack upside down and/or permuting the reactants inlets/outlets is time consuming and might cause water management issues.

Another variant of this method named “air swing” uses a 4-way valve to periodically permute the cathode inlet and outlet during fuel cell operation (FIG. 1.20) [68]. Reversing the flow direction using a 4-way valve is less time consuming, and eliminates the need of an air humidifier, by reinjecting the produced water in the cathode. Furthermore, as the cathode flow is reversed during stack operation, it is temporarily starved of oxygen, triggering the cathode starvation-related break-in mechanisms presented in the previous section. The oxygen reduction and hydrogen reforming zones (see FIG. 1.18) also permute with the air swing method, resulting in a more uniform desorption of oxides and impurities.

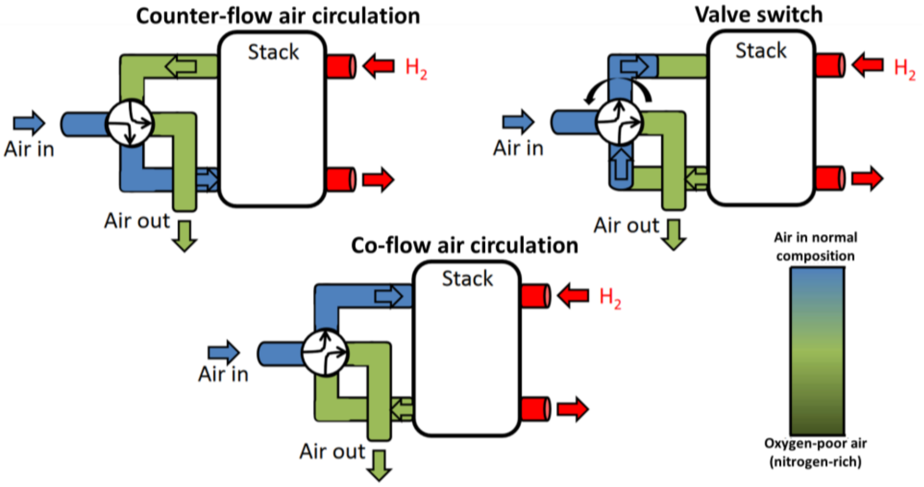

FIG. 1.20. AIR SWING PROTOCOL WORKING PRINCIPLE [68]

Contrary to the Park *et al.* method, changing the anode flow direction by using a 4-way valve should not be promoted, due to the severe anode starvation-related degradations [69]. Even if only the cathode is starved stack durability is not ensured with the air swing method. Indeed, with the 4 way valve, the starvation process is never total and might cause voltage fluctuations, thus degrading the CL components [69]. The impact of these stressors on stack durability is discussed in further detail in the next section of this manuscript.

3.2.7 Hydrogen pumping activation

The hydrogen pumping method, traditionally used for hydrogen purification or high efficiency compression, can be used to increase fuel cell performance [70], [71]. This method consists of firstly purging the cathode with an inert gas and then closing the cathode inlet whilst keeping the outlet open. Afterwards, using an external power source, hydrogen is pumped. This consists of oxidizing hydrogen at the anode, transporting protons through the membrane, and then reforming hydrogen at the cathode. This method has thus the potential to minimize hydrogen fuel loss, by recirculating it between the two compartments [24].

When pumping hydrogen, the hydrogen evolution reaction (HER) takes place at the cathode, whose activation mechanisms have been presented in the previous sections (FIG. 1.18). Using an external power source to pump hydrogen however results in more uniform activation over the cell surface, as the HER zone expands over the entire cathode area (zone 2 of FIG. 1.18). It however also implies that hydrogen pumping does not affect the ionomer structure, as no water is produced at the cathode (zone 1 of FIG. 1.18).

He *et al.* proved that the release of hydrogen does not only reduce the catalyst surface-blocking species, but also significantly increases the CL porosity and tortuosity. For this, they pumped hydrogen for 20 minutes (by supplying 200mA.cm^{-2}), on a cell whose catalyst surface-blocking species had already been desorbed [72]. Additionally, CyV and PolCurve measurements were taken before and after hydrogen pumping. These measurements confirmed that hydrogen pumping significantly increased cell performance whilst not desorbing additional catalyst surface species, as the ECSA variation was negligible (FIG. 1.21). The ECSA measured through CyV only accounts for the contact surface between the catalyst and the electrolyte, not the accessibility of oxygen molecules. Therefore, the forced passage of hydrogen to the active sites must have created new pores, improving oxygen transport accessibility and thus cell performance.

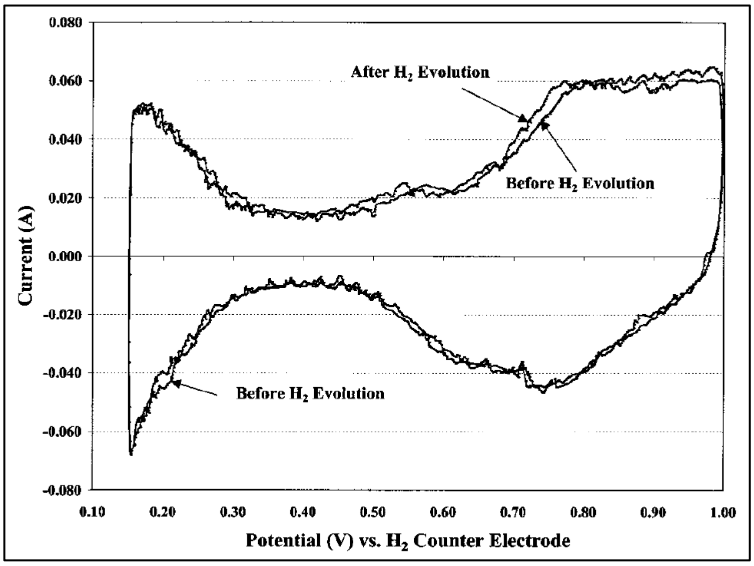

FIG. 1.21. CYV CYCLES BEFORE AND AFTER HYDROGEN PUMPING [70]

3.2.8 Reactant switch activation

The reactant switch activation consists of generating oxidizing or reducing conditions within the cell without producing current, by adjusting the anode and/or cathode gas compositions. Ballard and Hyundai motor company for example propose to fill and expose the cathode to hydrogen or another reducing gas, followed by stack sealing and storage [73], [74]. The reducing atmosphere desorbs oxides and other impurities from the catalyst. Pre-heating and humidifying the gas may accelerate the desorption process, and hydrate the ionomer to a certain extend. Another strategy to expose the cathode to a reducing atmosphere consists of purging it of air and imposing a vacuum, whilst supplying the anode with hydrogen [75]. The cathode fills with hydrogen, as the pressure difference forces H_2 crossover through the membrane (which may also affect CL porosity). With this setup, no direct hydrogen supply is required at the cathode input, but the pressure difference may tear the membrane.

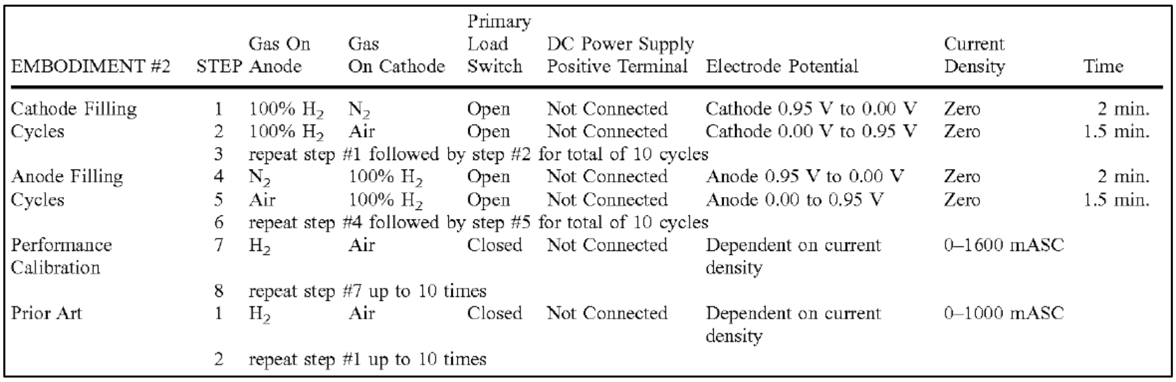

EMBODIMENT #2	STEP	Gas On Anode	Gas On Cathode	Primary Load Switch	DC Power Supply Positive Terminal	Electrode Potential	Current Density	Time
Cathode Filling Cycles	1	100% H_2	N_2	Open	Not Connected	Cathode 0.95 V to 0.00 V	Zero	2 min.
	2	100% H_2	Air	Open	Not Connected	Cathode 0.00 V to 0.95 V	Zero	1.5 min.
	3	repeat step #1 followed by step #2 for total of 10 cycles						
Anode Filling Cycles	4	N_2	100% H_2	Open	Not Connected	Anode 0.95 V to 0.00 V	Zero	2 min.
	5	Air	100% H_2	Open	Not Connected	Anode 0.00 to 0.95 V	Zero	1.5 min.
	6	repeat step #4 followed by step #5 for total of 10 cycles						
Performance Calibration	7	H_2	Air	Closed	Not Connected	Dependent on current density	0–1600 mASC	
	8	repeat step #7 up to 10 times						
Prior Art	1	H_2	Air	Closed	Not Connected	Dependent on current density	0–1000 mASC	
	2	repeat step #1 up to 10 times						

FIG. 1.22. REACTANT SWITCH ACTIVATION STEPS [76]

A more complete method presented by Schrooten *et al.* consists of cycling the electrodes potentials between 0 and 0.95V, through permutation between N_2, air and H_2 at the anode and cathode sides (FIG. 1.22) [76]. Complete oxidation and reduction cycles occur, to fully desorb the electrodes catalyst surface-blocking species. Exposing the cell to different gasses is a very cost-effective way to desorb those species and does not require a load. Consequently however, the previously presented current production-related activation mechanisms (membrane water network generation, impurity migration, side chain reorientation...) do not occur. This method also presents risks, in the case of an incomplete purge prior to a reactant switch step. The simultaneous presence of air and H_2 within the same volume, can severely degrade the cell (along the same mechanisms as those caused by H_2/O_2 crossover). Finally, the oxide/impurity desorption rates with these methods have slow kinetics. Therefore, methods such as hydrogen exposure may only be of interest to apply on assembled fuel cells during their storage period before they are put on an activation bench.

3.2.9 Cyclic Voltammetry activation

As previously stated, the amount and type of oxides/impurities coverage on the platinum surface is mixed [34] (PtOH, PtO, PtO_2, sub-surface oxides, airborne species [33], manufacturing residues [34], [36], etc.). Adsorption/desorption mechanisms strongly depend on the potential of the medium, and the ideal potential varies for each specie, depending on its nature and the desired reaction (oxidation/reduction). To efficiently reach each desorption potential, the CyV electrochemical characterization method may be used. Multiple oxides and impurities can be desorbed or transformed into less harmful molecular species with each potential sweep [63]. As the cell voltage is imposed by an external source, low cathode potentials can be reached without forcing short circuits or reactant starvations, and the maximum potential is not limited to OCV. In addition to catalyst impurity desorption, the consecutive oxidation/reduction cycles may also accelerate Pt particle rounding and agglomeration, increasing the ORR mass activity [38]. During the backwards potential sweep, the HER reaction occurs, which (as seen in the previous sections) affects the cathode CL porosity.

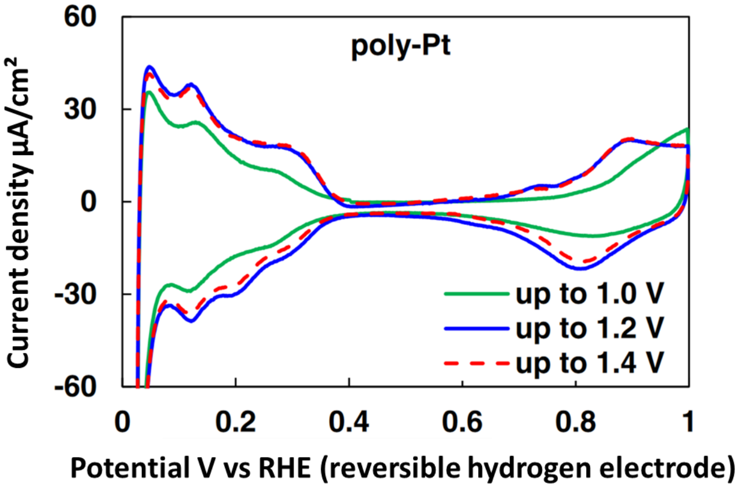

FIG. 1.23. EFFECTS OF MAXIMUM POTENTIAL ON VOLTAMMOGRAM AFTER THE BREAK-IN PROCESS [34]

He *et al.* applied the hydrogen adsorption/desorption CyV method on pre-humidified cells (using water saturated N_2) [58], [77]. Only 23.2 minutes (30 cycles at 50mV.s^{-1} steps for a voltage range from 0.04 to 1.2V) were required to fully desorb the catalyst surface impurities. The CyV method efficiency may even further be improved by optimizing the potential scan rate, scan direction and amplitude. According to Shinozaki *et al.*, increasing the scan rate (here 500mV.s^{-1}) is favourable, as the number of cycles is a stronger accelerant for activation rather than the total duration [34]. Cycling up to 1.2V is also preferable, as at 1V (~OCV) some contaminants are not oxidized/removed, and at 1.4V the desorption rate is not improved and the cell degradation rate increases (FIG. 1.23).

Another cyclic voltammetry characterization method, named CO stripping, can also be applied to activate a fuel cell [78]. It consists of firstly poisoning the cathode catalyst using a diluted nitrogen/CO mixture, and then cleaning it by oxidizing the absorbed CO [79]. By applying this method on an activated cell, Xu *et al.* managed to further increase its performance, by 29% [80], [72]. During CO contamination, a potentiostat imposes the cathode potential at 0.5V to favour CO absorption whilst preventing the HER (which would interfere with the results). After 30 minutes of cathode contamination, it is purged with pure nitrogen, and the adsorbed CO on the platinum is oxidized by CyV (between 0.5 and 1V to impede the HER). The first 3 potential cycles showed current peaks around 0.76V corresponding to the oxidation of CO into CO_2 (FIG. 1.24). During the 4th cycle, the absence of current peaks confirmed total CO desorption. In addition to the cathode potential sweep, it is thought that when the CO oxidizes, it directly carries away a certain number of other species, accelerating the catalyst impurity desorption process.

There are durability concerns related to potential sweeping, as it can generate metallic cations, which in turn can decrease ionomer proton conductivity, and change electroosmotic drag. In-situ mitigation against contamination typically consists of increasing the cell water production rate [17]. However, drawing current is not possible during CyV. Consequently, the current production-related activation mechanisms do not occur. Similarly, potential levels up to and beyond OCV may also degrade the stack [81].

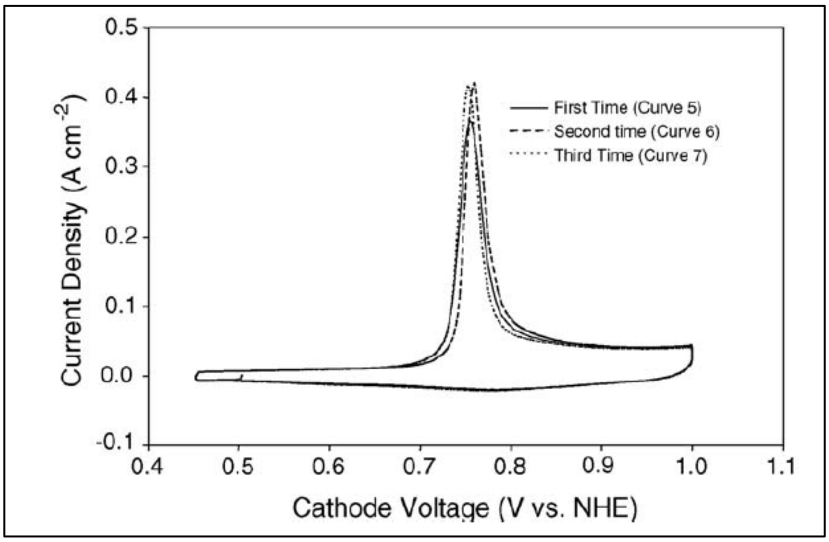

FIG. 1.24. CV CYCLES USED TO OXIDIZE THE CO [80]

3.2.10 Compression cycles activation

The compression cycles activation is the only online method related to the mechanical break-in mechanisms. As previously stated, after assembly, the different cell elements have not had a chance to adapt and fit to each other's forms. Furthermore, during activation, irreversible microstructural deformations and variable water and heat production take place, altering the cell contact interface resistances.

Netwall *et al.* propose a mechanical break-in method, to apply after electrochemical activation [39]. It consist of firstly letting the cell undergo a compression and relaxation cycle using a mechanical press. This decreases the area-specific resistance, as the GDL is being formed into compression with the BP. FIG. 1.25 is an example of three compressive load cycles, applied up to 1.4MPa. The first compression cycle exhibits the area resistance hysteresis as a function of compression stress, indicative of a mechanical break-in response. Subsequent compression/decompression cycles all follow the same path.

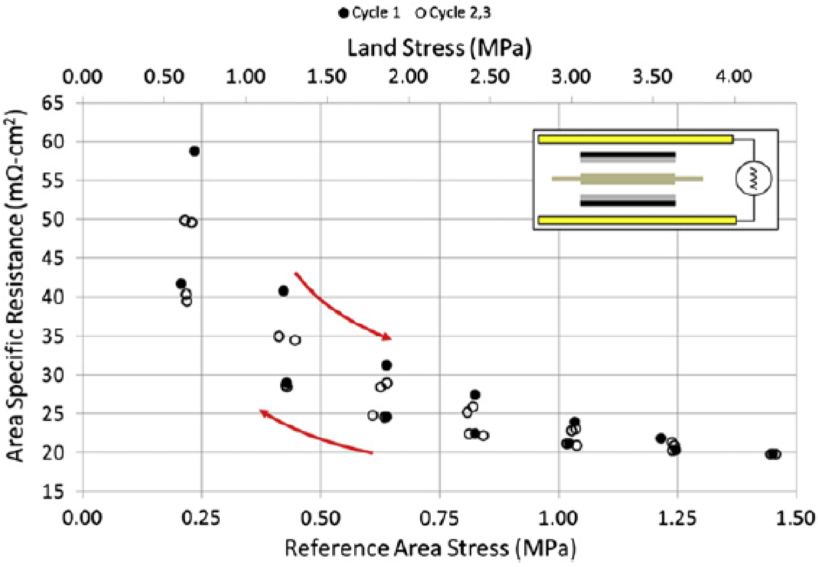

FIG. 1.25. MECHANICAL BREAK-IN COMPRESSION CYCLES [39]

After the compression/decompression cycle, the cell is once again compressed and maintained at a fixed optimal compressive load. The optimal compressive stress must ensure low area-specific resistance and maintain of compression during fuel cell operation whilst preventing mechanical degradation of cell components. As seen on FIG. 1.25, the area-specific resistance greatly decreases until 1MPa, and then slowly converges to a minimum value. Netwall *et al.* determined that compressive stress of at least 1MPa is required to remove the temperature dependency on the compression level. This said, stresses greater than 1.38MPa showed significant material damage, and negligible improvement in area-specific resistance. Therefore, the ideal compressive stress post break-in in their example is within the 1 to 1.38MPa range.

Some additional considerations should be taken when determining the optimal clamping pressure. Increasing compression inhibits mass transfer by reducing the GDL porosity [40], and by partly pushing the GDL material in the reactant flow channels [48]. Furthermore, compression also affects the membrane crystallization and ionic domain spacing, influencing water uptake [17]. This topic must be further studied.

4 PEMFC break-in characterization

Break-in characterization, also named break-in monitoring or diagnosis consists of quantifying fuel cell activation evolution, completion, and cell component state of health.

There are two purposes related to fuel cell break-in characterization:

- **Standardization**: Obtaining accurately repeatable break-in protocols, by ensuring that no unexpected event has occurred during activation and guaranteeing iso-performance and durability. In addition to the post activation factory acceptance tests, it certifies that all delivered fuel cells to the customer meet specification requirements. It also guarantees that stacks dedicating to testing are fully conditioned, preventing inaccurate baseline metrics and misidentification of phenomena [13].

- **Benchmarking**: Comparing novel break-in protocols with the existing ones with respect to performance and impact on durability.

In this section, the traditional and novel PEMFC activation characterization methods are first presented. Afterwards, the limits related to break-in protocol benchmarking are discussed.

4.1 PEMFC break-in characterization methods

4.1.1 Traditional break-in characterization methods and limits

Traditionally, the metric used to quantify break-in evolution and completion is the cell voltage, tracked at a certain iso-current value, or vice versa. Several break-in completion criteria exist in the literature.

The most common criterion in the literature is based on performance convergence. For example, the US Fuel Cell Council defines it by a cell voltage deviation below 5mV between two measurements at $800mA.cm^{-2}$ [15]. In other cases, the criterion is poorly defined as “no further observable increase in performance” [16]. There is a lack of standardization in the literature with this criterion, as different threshold voltage/current deviation ($\Delta U/\Delta I$), and convergence time (Δt) values are used. Variable metrics (current/voltage/power) are also used to quantify break-in evolution, at different values, and scales (cell/stack). In the industry, another end-of-break-in criterion is often used and defined as reaching a certain performance threshold value. Both criteria are of little scientific rigor, as reaching a cell performance threshold value or convergence does not guarantee that it has completed its morphological transformations. This has for example been proven with the CO-stripping method, which further activated a cell which had already reached stable performance [80].

A third criterion consists of waiting until the first decay in performance is observable, meaning that the stack is fully activated, as fuel cell ageing has started [24]. This criterion may be viable for traditional activation protocols, which are carried out using “safe” and stable operating conditions. Novel accelerated break-in methods however go against the durability guidelines, by causing flooding, starvations, applying high temperatures/pressures, high amplitude current/voltage fluctuations, etc. [82]. Even though activation increases cell performance, it does not mean that it is impervious to degradations.

Simultaneous fuel cell break-in and ageing has been observed in the literature (FIG. 1.26) and is typically called over-conditioning [24]. Therefore, not only break-in but also ageing morphological changes should be monitored during activation. This is essential, as cell durability is one of the other hurdles that limits fuel cell mass production. It is however not easy to decorrelate break-in from ageing by tracking performance evolution, as the performance increase caused by fuel cell break-in hides the performance decrease caused by ageing. When testing novel break-in protocols, they can and should systematically be followed by an ageing protocol at least once. This is essential to precisely identify the long-term effects of the irreversible MEA microstructural changes caused by fuel cell break-in [83]. Post activation ageing protocols have been applied several times in the literature [54], [64] but not systematically, as they are costly and time consuming.

Using advanced (mostly electrochemical) characterization methods, break-in evolution, completion and impact on ageing can be quantified more precisely, and correlated with the activation and ageing mechanisms. These characterization methods, as well as the different morphological changes they can monitor are presented separately throughout the following subsections.

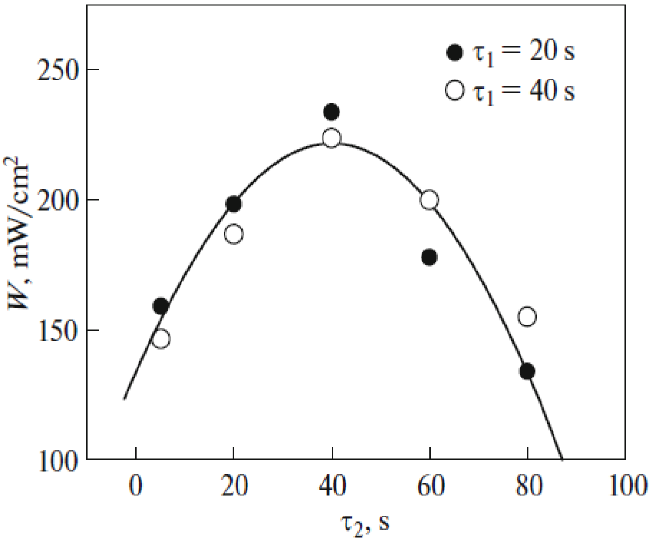

FIG. 1.26. EXAMPLE OF OVER-CONDITIONING WHEN INCREASING LOADING TIME (τ_2) ON PULSED ACTIVATION METHOD [62]

4.1.2 Polarization curve (PolCurve)

Polarization curves represent the fuel cell performance cartography over its entire operating range, by displaying the average steady-state cell voltage as a function of current density. The S-shaped PolCurve can be divided in three different regions, to evaluate the reaction rate, ohmic and mass transport losses evolution.

Reaction rate losses represent the energy required for the electrochemical reactions to take place on the catalyst surface and are therefore related to the ECSA and activity per site. By monitoring these losses, catalyst impurity desorption and structural changes (which affect the ORR reactions) can be quantified. The catalyst activity evolution can be further analysed by extracting specific parameters from the reaction rate losses expression [84]. Changes in Tafel slope are for example related to changes in Pt oxide coverage [28].

The ohmic resistance corresponds to the cumulative resistances of all cell components, but also the contact resistance between each component. Its evolution during activation can be related to the cell interfacial contact (mechanical activation), and the ionomer (water sorption and impurity evacuation).

Mass transfer losses are related to reactant and ion mobility to and from the active sites, and the available catalyst area and activity [84]. These losses evolve with GDL/CL porosity, removal of unanchored particles, the production of a water film on the catalyst surface and hydration of the ionomer surrounding the platinum.

4.1.3 Electrochemical Impedance spectroscopy (EIS)

The electrochemical impedance spectroscopy (EIS) is a powerful in-situ diagnostic method, typically carried out at 0.5, 1 or 1.5A.cm^{-2}. It consists of adding a sinusoidal current perturbation to the base signal, which is swept over a large frequency range. On a Nyquist plot, the fuel cell losses can be dissociated from the frequential impedance response using an equivalent resistance/capacity model. Like PolCurves, it displays the ohmic (high frequency), kinetic (mid-frequency), and mass transfer (low frequency) losses in the fuel cell [67]. With the EIS method however, the different losses are better dissociated, and provide more precise measurements for one fixed current density. Additionally, the slope of the high frequency arc provides information regarding the CL and GDL pore shape and size [19]. Indeed, if the slope of high frequency arc of the Nyquist plot is steeper, the entrance of pores is larger (FIG. 1.27).

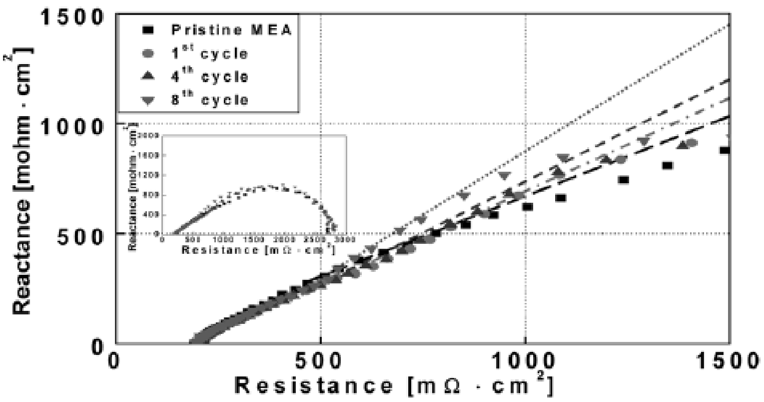

FIG. 1.27. NYQUIST HIGH FREQUENCY SLOPE EVOLUTION DURING BREAK-IN [19]

The capacitance characteristics of an EIS curve are also indicators of the triple phase boundary area available for promoting catalytic reactions. They can be related to all morphological changes that increase the ECSA (such as PEM swelling, which generates a better connection between the three phases [83]).

4.1.4 Cyclic Voltammetry (CyV)

As previously stated, the CyV method can be used to activate and/or characterize a fuel cell. The area specific activity measured through CyV is an indicator of impurity levels that do not impede the accurate measurement of the ORR activity of Pt based catalysts [34]. Monitoring the evolution and stabilization of the kinetic, mixed and limiting current areas can therefore indicate the impurity desorption level (FIG. 1.28).

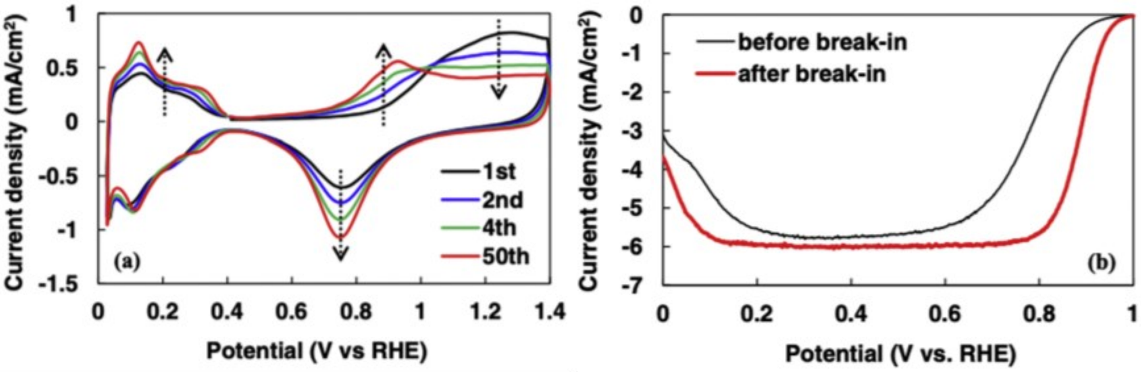

FIG. 1.28. CHARACTERIZING DEGREE OF IMPURITY DESORPTION DURING BREAK-IN USING CYV [24]

Like EIS curves, voltammograms provide the value of the double layer capacitance [17]. Through the hydrogen adsorption and desorption areas, the ECSA value can also be specified, and the mean Pt particle size can be estimated [85]. With CyV, the permeation current (O_2 and H_2 crossover) can also be determined [86]. As reactant permeability through the membrane increases with water content [28] it is an image of its degree of activation. Additionally, H_2 crossover can be quantified using the linear sweep voltammetry (LSV) method, which consists of sweeping the voltage in a single direction, at a slower scan rate [84]. Combined with the Nernst equation and OCV measurements, the LSV method provides a precise estimation of the H_2 crossover rate.

4.1.5 Output gas / water composition analysis

Information regarding the stack degree of activation and state of health during break-in can be extracted from the cell anode/cathode output gas and water compositions.

Gas crossover rates and therefore membrane water content can be estimated by measuring the O_2 and H_2 flowrates at the anode and cathode outputs, respectively. Additionally, the concentration of different emissions (e.g. sulfate and other impurities) can be used to quantify ionomer and catalyst surface decontamination [67]. Similarly, fluor and hydrogen peroxide emissions can be related to ionomer and catalyst binder degradations [28], [67], and CO_2 concentration to the degradation of the carbon support. With specific filters at the gas channel outputs, Pt particle loss related degradations may also be quantifiable.

4.1.6 Post-mortem

When carrying out a first full analysis of a novel break-in procedure, intrusive and destructive methods can be applied to observe cell materials evolution during activation and ageing.

The main component from which information can be drawn through microscope observations is the CL. More specifically catalyst characteristics such as Pt particle size, which evolve during break-in and ageing, can be quantified [54]. To determine the optimal clamping pressure for one stack configuration, post-mortem must also be used to quantify GDL material deformation / inclusion into the BP [39], [40].

4.2 PEMFC break-in protocols benchmarking and limits

As previously stated, fuel cell break-in characterization is essential for standardization, but also benchmarking purposes, to determine the optimal reproductible break-in protocol. When a novel break-in protocol is defined, it can be ranked to determine its performance relative to the other existing protocols.

4.2.1 Traditional PEMFC break-in protocols benchmarking and limits

To maximize break-in economic efficiency on a mass manufacturing scale, multiple metrics such as activation time, material and fuel cost, and impact on durability must be considered [27]. This said, industrial actors mostly focus on reducing break-in time and obtaining the best final cell performance (considered as the most important factors to reduce the fuel cell production cost per kW). Therefore, benchmarking as presented in the literature is often only based on those metrics [16], [17], [87] (FIG. 1.29).

The process used in the literature to benchmark break-in methods is straightforward. Indeed, benchmarking tables are directly based on the experimental results provided by the different authors of the break-in methods in their papers. However, these authors did not apply the same end-of-break-in criteria for their experiments. Therefore, it is not wise to draw conclusions based on these results. For improved benchmarking, the efficiency of each method must be revaluated experimentally, this time by using identical standardized advanced characterization methods as presented previously.

Apart from standardizing break-in characterization using advanced methods, there are several other "provisions" or "precautions" to be taken when comparing break-in methods. Indeed, the measured efficiency of a break-in protocol strongly depends on the characteristics of the used PEMFC. The main

PEMFC characteristics which influence the benchmarking results are its materials, size, and manufacturing methods. These points are discussed one by one in the following subsection.

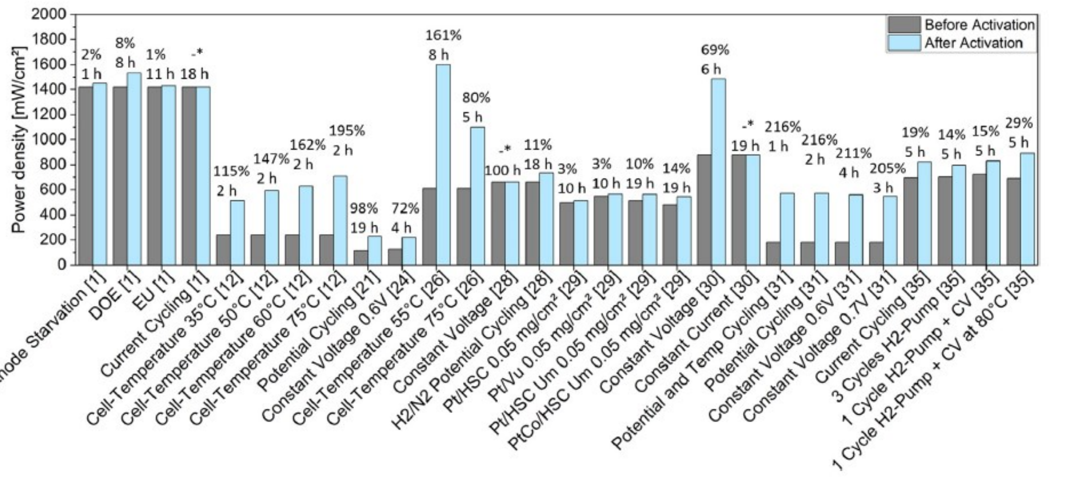

FIG. 1.29. EXAMPLE OF BREAK-IN METHODS BENCHMARKING (FROM VARIOUS SOURCES FROM LITERATURE) [17]

4.2.2 Impact of PEMFC characteristics on benchmarking

The PEMFC stack dimensions (cell area / number of cells) greatly influence the efficiency of a break-in protocol [82]. On large stacks, reactant, water and heat distribution is less uniform over the cell surface, resulting in longer activation times. Furthermore, the efficiency order in which activation methods are ranked may also depend on the stack size. Indeed, break-in methods such as reverse activation (that focus on homogenizing activation over the cell surface) may be ranked higher if applied on large area cells. Similarly, the effect of compression cycles activation may be more noticeable on stacks with a large number of cells.

The measured performance of a break-in method is also closely related to the PEMFC manufacturing method and used materials [8]. The time to condition a cell to its peak performance is unique for an electrode system and will depend to a great extent upon the CL. Variables and processes such as the used solvent ink formulation [88], drying and deposition technique, ionomer and carbon type and ionomer loading significantly impact the electrode morphology [24], [28]. This will in turn affects the evolution of proton conductivity, but also ECSA and mass transport losses during activation [17]. Impurity desorption disparities also exist between high loaded and low loaded electrodes, and the type of Pt-alloy [24], [28]. Therefore, different numbers of oxidation/reduction cycles are required to yield the peak performance.

Silva *et al.* observed variable break-in kinetics depending on membrane type and thickness [89]. More specifically, material characteristics like equivalent weight, side chain length, crystallinity, scavengers and reinforcements all affect the membrane morphological changes during activation [17]. The membrane water uptake characteristics in the free water regime (λ_F) during activation also depends on its manufacturing process (as it imprints a certain mechanical and thermal history). The proton conductivity increase rate also depends on the membrane additive dosage and formulation [22], [23]. Furthermore, if MEAs are directly bought from a manufacturer (not produced in-house) pre-treatment methods may already have been carried out by them. This information is typically not divulged. FIG. 1.30 displays variable membrane pre-treatment method (boiling) efficiency, dependent on the type of membrane [89].

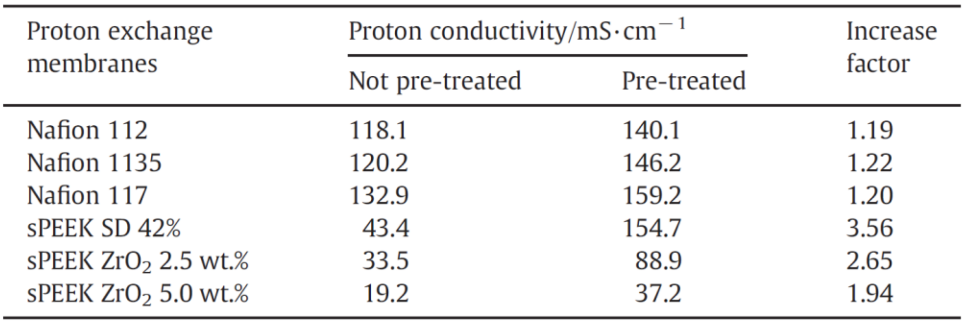

Proton exchange membranes	Proton conductivity/$mS \cdot cm^{-1}$		Increase factor
	Not pre-treated	Pre-treated	
Nafion 112	118.1	140.1	1.19
Nafion 1135	120.2	146.2	1.22
Nafion 117	132.9	159.2	1.20
sPEEK SD 42%	43.4	154.7	3.56
sPEEK ZrO_2 2.5 wt.%	33.5	88.9	2.65
sPEEK ZrO_2 5.0 wt.%	19.2	37.2	1.94

FIG. 1.30. MEMBRANE BOILING PRE-TREATMENT PERFORMANCE INCREASE, FOR DIFFERENT TYPES OF MEMBRANES [89]

Bipolar plate surface roughness affects the resistive contact with the GDLs [39], and therefore the compression break-in cycle efficiency. The flow field layout (serpentine, parallel..) has also proven to influence break-in performance [90]. Finally, pre break-in cell storage conditions affect Pt [58] and ionomer [24] contamination and consequently activation time.

5 Conclusion

To conclude, multiple morphological changes occur within the PEMFC during activation, and are mostly related to the MEA electrochemistry. For the membrane, there is the polymer hydration and structure change, surface skin rearrangement and decontamination. In the catalyst layer, there is the pore structure change, polymer hydration and carbon support oxidation, as well as catalyst decontamination and Pt structure reorganization. These morphological changes directly affect cell properties such as porosity, catalyst size, shape and activity, polymer chain orientation and spacing, etc. The cumulated contributions of the activation mechanisms reduce the entire spectrum of fuel cell resistances (reaction rate, mass transfer and ohmic).

It is possible to pre-treat fuel cell components to reduce the time spent on an activation bench by using steam, sulfuric acid, plasma or through compression. Dynamic, potentiostatic, high temperature/pressure and supersaturated operation promote the break-in kinetics. Generating oxidizing and reducing conditions during activation is essential, and can be achieved by short circuit, CyV cycling, cathode starvation or reactant switch. Uniform activation over the cell surface can be achieved with methods such as reverse flow activation or hydrogen pumping. At the end of break-in, a mechanical compression cycle can be used to minimize the cell interfacial contact resistance. Cost-reduction optimization processes that don’t require a load such as steam injection, or hydrogen exposure exists. They are however generally time consuming and less efficient.

Developing the optimal reproductible activation protocol, based on the methods above is not a simple task. In the literature, no standardized nor efficient processes are applied to characterize break-in evolution, completion, and impact on ageing. Better reproducibility can be achieved using advanced electrochemical characterization, combined with post-mortem and cell output species analysis. Using these same characterization methods, more precise benchmarking can also be achieved. This said, benchmarking results are only valid for the fuel cell on which the activation protocols have been tested. Indeed, the efficiency of an activation method strongly depends on fuel cell characteristics (dimensions, production methods and materials).

Chapter 2: Ionomer break-in analytical model: model development, validation, and adaptation to the activation process

1 Ambitions/purpose

Being able to simulate the behavior of a fuel cell going through an activation process is beneficial in several respects. In many cases, it can replace excessive costly trial-and-error experimental applications, and be used to obtain a better general understanding of the break-in procedure. However, to our knowledge, no model capable of simulating one or multiple break-in mechanisms (presented in chapter 1), currently exists. This chapter is dedicated to the development of such a model.

There are many complexities involved with the development of a model, specific to fuel cell activation. Its equations must mostly rely on physical parameters, as the activation process greatly depends on fuel cell characteristics (e.g. used materials and properties, dimensions, etc.). However, most break-in morphological changes (e.g. catalyst structural changes) are not fully understood and therefore currently impossible to describe using physical equations. This said, many physical equations to simulate polymer hydration (post-activation) have been presented in the literature [91], [92]. Fundamentally, these equations are also valid to describe the membrane hydration mechanisms during break-in, and can therefore serve as base for an ionomer activation model. In these equations, only the absolute values of the water transport, sorption, conductivity, etc. coefficients must be adapted to fit the time constants during fuel cell break-in.

For the reasons stated above, the analytical model developed in this manuscript focusses solely on the ionomer activation mechanisms and more specifically on its ohmic losses evolution. The strategy used to develop this model (Fig. 2.) are (i) creating a functional water transport model for a PEMFC MEA in normal operation (post-activation), based on the equations from the literature, (ii) validating this model using experimental data of an activated stack, (iii) adapting the water transport model equations, by implementing specific variables related to the break-in process, based on the gathered knowledge of chapter 1.

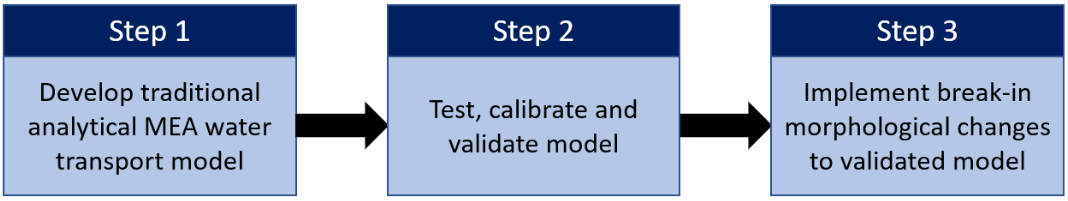

Fig. 2.1. Ionomer break-in model development process

Many models have been developed to improve water management in the MEA (post activation), as maintaining a water equilibrium is essential for optimal fuel cell performance and durability [93]–[95]. Most of them are based on the same long-established and well-known water transport equations. Steady state models use the water balance principle to determine water concentration conditions in the MEA, for constant operating conditions [11], [96]–[99]. In these models, all water transport equations are set up, which are then cancelled out (using the flow conservation laws in equilibrium). With these numerical representations, the water concentration profile can be determined for one set of constant operating conditions. In this water balance equation, multiple aspects must be taken into account, such as the cell operating conditions (reactant flow rate, temperature, pressure). Parameters proper to fuel cell current production must also be considered (electrochemical water production, heat production/cooling and reactant depletion) [100]. Apart from the operating conditions, the water flow rates through each cell element must be quantified. This implies precisely knowing cell elements properties and defining the phenomena responsible for water transport.

A steady state model is however not adapted to our application, as the model must simultaneously integrate multiple dynamic processes occurring at different time constants. Indeed, it must both simulate the sluggish membrane activation structural changes and the rapid water transport kinetics throughout the MEA, as their variations are co-dependent. Thankfully, many models presented in the literature are dynamic [101]–[103]. When integrating the time variable, the fuel cell water management equation complexifies. In non-equilibrium conditions, the heat and mass flows cannot be cancelled out (as the flow conservation laws cannot be applied). Furthermore, as a membrane can hold a significant amount of water, its “reservoir”-like behavior must be considered [104]. Dynamic models are thus often based on equation resolution approximations, with a compromise between precision and computation time [105].

This chapter is dedicated to the presentation of the ionomer activation model, based on the Finite Volume Method (FVM), and more specifically on its structure and development process. The tool used to develop and execute the model is Matlab™. In a first section, the model base structure and equations are presented. Afterwards, a focus is set on the water flow equations inside of the domain, followed by their resolution process, and the presentation of the model output. The fifth section is dedicated to model calibration and validation. In the last section, the model is adapted to simulate the ionomer activation process.

2 Model base structure and equations

2.1 Finite volume method

The finite volume method is used to numerically resolve partial differential equations, by transforming the function from a continuous state to a discrete approximation [106]. For this, the studied domain is divided into a finite number of elements, to obtain a time and space mesh. Inside of each mesh element, also called “control volume”, all conditions are considered as homogenous. All mesh element boundaries all linked through linear equations. These equations are based on conservation laws, as will be presented in this section.

The FVM has become especially effective with the arrival of computer software, capable of resolving large numbers of simple equations. It has now become a well-known method, mainly applied in the thermodynamics and fluid mechanics fields, to simulate heat and mass transfer [107]. It can however also be used in other domains such as solid mechanics applications, to resolve stress analysis problems for example.

The four characteristic features of a FVM model are:

- The mesh domain (modeled elements, number of dimensions, mesh size, mesh shape…).
- The physical parameter, quantified for every mesh element (temperature, concentration...).
- The conservation law on which the transport equations between control volumes is based.
- The boundary conditions (equations at the domain borders).

In this model, the physical parameter quantified for each control volume is the molar water concentration, written c_{H2O}. The simulated domain, boundary conditions, and equations between mesh elements are presented in the next sections of this chapter.

2.2 Simulated Domain

As stated in the introduction of this manuscript, both sides of a fuel cell membrane are coated with a catalyst layer, to form a catalyst coated membrane (CCM). This CCM is afterwards sandwiched between two gas diffusion layers, to form a MEA. In a fuel cell stack, the MEAs are separated by bipolar plates, containing carved channels. These channels supply the reactants to the anode and cathode GDL surfaces.

Reactant/water transport through the bipolar plates channels is generated by convection, which is difficult to put into equation. The channel structure must be considered, as well as the fluid velocity, viscosity, etc. Due to frictional effects, the gas velocity tends towards zero at the GDL/ bipolar plate (BP) boundary [11]. In the GDL, water transport is thus only generated by diffusion and capillarity. In other words, the flow only depends on a water concentration gradient (not velocity).

The membrane is the focus and centre of this model. Its hydration depends strongly on the water concentration at the membrane/catalyst layer (CL) interfaces. For the best compromise between model accuracy and computation time, only the GDL, CL and membrane are included in the domain. An estimation of the mean water concentration at the domain limits (GDL/BP interface) is made. This estimation depends on reactant RH, stoichiometry, cell current, and will be discussed further in following subsections.

All flows responsible for water transport in an MEA are one-dimensional (from anode to cathode), except for diffusion. For further simplification, all conditions (water supply and production, cell temperature…) are considered as uniform over the cell surface. This results in symmetry conditions along two axes of the domain (zero net water concentration gradient). The final one-dimensional domain is represented in FIG. 2.2 (number of mesh elements not to scale). This dimension is essential to simulate ionomer activation, as many mechanisms (such as ionomer surface skin reorientation) highly depend on the specific water concentration conditions at the membrane surfaces. Even though very computation time effective, the drawbacks related to domain simplification are worth mentioning. The activation gradient over the membrane surface is not identifiable, as it occurs over the two dimensions which are not simulated. Furthermore, not including the BP to the simulated domain results in imposing less precise boundary conditions at the BP/GDL interfaces.

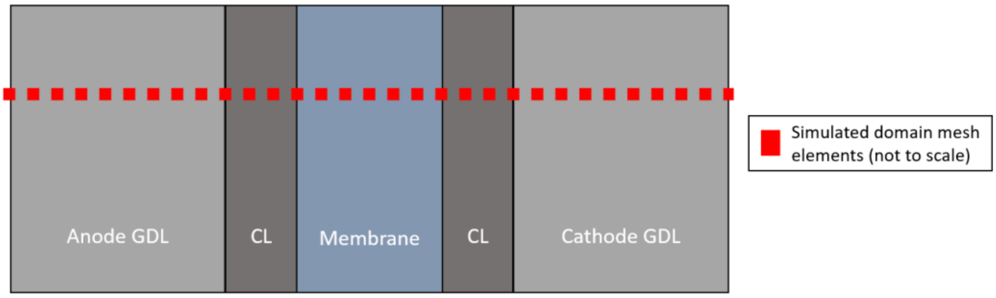

FIG. 2.2: SIMULATED DOMAIN

2.3 Time and space discretization

The simulated domain represented in FIG. 2.2 is spatially and temporally discretized, to obtain a time and space mesh. The total number of mesh elements corresponds to the domain size and simulation time, multiplied by the time and space intervals (Δt and Δz), respectively. The number of equations to solve is proportional to the number of mesh elements.

To create the discretized domain, the molar water concentration variations must be expressed as a function of time and space intervals. The relation between molar water concentration and time is expressed by using the mass conservation equation:

$$\mathrm{c}_{H2O}{}_i^{t+\Delta t} = \mathrm{c}_{H2O}{}_i^{t} + \frac{\partial \mathrm{c}_{H2O_i}}{\partial t}\Delta t \tag{2}$$

Space is integrated in this equation, by expressing the flows that each control volume shares with its neighbours (total incoming and outgoing water flows):

$$\frac{\partial \mathrm{c}_{H2O_i}}{\partial t} = \frac{\sum J_{H20\,(i-1,\,i\,)} - \sum J_{H20\,(i,\,i+1)}}{\Delta z} \tag{3}$$

With J_{H20} the water flow (mol.m^{-2}.s^{-1}) and Δz the space interval, equal to the control volume length (m). The different water flow equations within the MEA are determined in the third section of this chapter.

2.4 Domain boundaries

At the limits of the simulated domain, boundary conditions must be applied. As the domain represented in FIG. 2.2 is one-dimensional, two dimensions must be eliminated. For this, symmetry boundary conditions are imposed (no flow). The boundaries of the third dimension are located at the anode and cathode GDL/bipolar plates interfaces. As previously stated, the physical parameter quantified for each mesh element is the molar water concentration. Thus, the domain boundaries must be expressed in mol.m^{-3}.

The water vapor concentrations at the anode and cathode channel inputs are known:

$$\mathrm{c}_{H2O}{}_{in}^{t} = \frac{RH}{100}\frac{P_{sat}^{H2O}}{R.T} \tag{4}$$

With RH and T the reactant input relative humidity and temperature [K], P_{sat}^{H2O} the saturation pressure [Pa], and R the perfect gas constant.

At infinite stoichiometry and constant cell temperature one could consider the water concentration at the domain boundaries to be equal to (4). This is however not the case, especially at the anode, where the stoichiometry is typically set at $\nu_a \approx 1.5$, to limit hydrogen and/or recirculation pump energy consumption. At the cathode, the air stoichiometry is also limited at $\nu_c \approx 2$, for compressor sizing and energy consumption reasons. Estimating correct water concentration values at the GDL/BP boundaries is tricky. This is especially true in a dynamic model, where the boundary condition (BC) values vary over time. FIG. 2.3 illustrates this issue, by representing the reactant and water flows through a PEM fuel cell. In this figure, Q_a and Q_c

correspond to the theoretical minimum hydrogen and air flows required by the cell, respectively (for $\nu_a = \nu_c = 1$). As can be seen on this figure, the BC must account for reactant depletion, and water produced by the stack. To estimate their values, multiple assumptions are made.

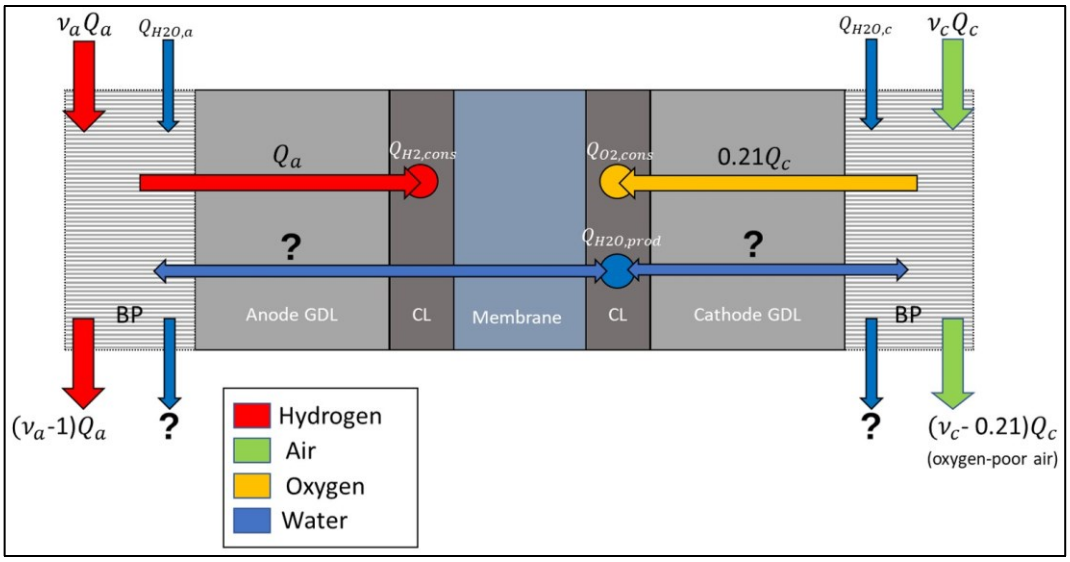

FIG. 2.3: WATER/REACTANT FLOWS IN A FUEL CELL

2.4.1 Reactant depletion

In a fuel cell, the reactant gasses are typically maintained at super-atmospheric pressures to increase performances [108]. For this initial "buffer volumes" of humid reactants are injected into the anode and cathode channels, to reach the pressure setpoints. The channels are afterwards continuously supplied with reactants at chosen stoichiometries (ν) and consumed by the cell at a rate of ν_{cons}. In a PEMFC, ν_{cons} is equal to 1 at the anode and 0.21 at the cathode due to the presence of nitrogen (FIG. 2.3). To maintain the pressure setpoint, gasses exit the anode at a rate of $\nu - \nu_{cons}$ (assuming negligible fuel crossover).

As reactants get depleted throughout the BP channels, the water mole fraction increases. If only reactant depletion is considered, the average BP channel water concentration equals the input water concentration times the average stoichiometry (ν_{av}). In this case $\nu_{av} = \nu_{in} - 0.5\nu_{cons}$. This average water concentration is part of the boundary condition equation system, to which the effect of water production must be added.

2.4.2 Water production

In a cell, when drawing current, water is produced electrochemically at the cathode catalyst layer (FIG. 2.3). Water concentration in the CL can thus exceed the concentrations in the BP channels, reversing the diffusion flow [11]. As this flow supplies water to the BP channels, it must be considered in the BC equations. For this, two assumptions are made.

- The fraction of produced water that crosses the membrane (from the cathode to the anode) is considered as constant for one set of operating conditions. The value of this fraction noted f_c, must be considered in the BC. Its value (between 0 and 1) must be determined experimentally, as is detailed in section 5.2 of this chapter.

- All liquid water at the domain boundaries gets expelled by the BP gas flow. This makes most physical sense, as the small droplets that form at the GDL/BP boundary typically get expelled by the convective flow in the bipolar plate [11]. Mathematically, this results in imposing a limitation to the maximum boundary water concentration value ($c_{H2O_{\mathrm{sat}}}$), corresponding to (4) at saturation.

A second by-production during fuel cell operation is heat. The calories produced by a fuel cell stack are typically evacuated by circulating a heat transfer fluid between each set of 2 cells. As the cooling gradually accumulates calories, a temperature gradient is generated within each cell. To avoid condensation at the cathode (which is most prone to cell flooding), it is typically set in co-flow with the cooling, whilst the anode is in a counter flow configuration. These cell temperature gradients must be included in the maximum anode and cathode boundary water concentration expressions ($c_{H2O_{\mathrm{sat}}}$). These concentrations are calculated using (4) for 100% RH, where T corresponds to the mean temperature between the gas inlet and outlet.

2.4.3 Boundary condition expression

The final expression of the boundary conditions equation, integrating all previous assumptions, equals:

$$c_{H2O_{BC}} = \begin{cases} \nu_{av} c_{H2O_{in}}^{t} + \alpha_c c_{H2O_{prod}}^{t} & , c_{H2O_{\mathrm{BC}}} < c_{H2O_{\mathrm{sat}}} \\ c_{H2O_{\mathrm{sat}}} & , c_{H2O_{\mathrm{BC}}} \geq c_{H2O_{\mathrm{sat}}} \end{cases} \tag{5}$$

Where $c_{H2O_{\mathrm{sat}}}$ is calculated for the mean temperature in the BP channel, with co-flow and counter-flow configurations for the cathode and anode sides, respectively. The α_c coefficient equals f_c for the anode and $1 - f_c$ for the cathode.

3 Water flow expressions

Within the MEA components (GDL, CL and membrane), water transport is generated by different flows. Determining the detailed expressions of those flows is the subject of this section.

3.1 Gas diffusion layers

The GDL is a porous medium, used to transport the humid reactants from the bipolar plates to the catalyst layers. During this transport, the non-uniform reactant flow from the bipolar plate channels is spread over the GDL surface. This allows the reactants to arrive uniformly over the catalyst layer surface [109]. As previously stated, due to frictional effects at its border with the BP, water vapor transport through the GDL is only generated by diffusion. To describe transport of one specie through diffusion, Fick's law is typically used [107]. This law states that the diffusion rate is directly proportional to a water concentration gradient.

The general form of Fick's diffusion equation is given below:

$$J_{diff} = -D \frac{dc}{dz} \tag{6}$$

With D, the diffusion coefficient, dc and dz the concentration and position variations for the studied specie, respectively.

In this model however, the presence of multiple gaseous species, and the porous nature of the GDL must be considered. Furthermore, liquid water transport through capillarity must also be integrated and coupled to the diffusion equations [110].

3.1.1 Multicomponent diffusion

In a GDL, two or three different gas species typically coexist. At the anode, H_2 and (in most cases) H_2O are fed during nominal fuel cell operation. In addition to those species, N_2 can also be found (during stack purge phases for example). At the cathode, air is typically injected. Even if only the main components of humidified air are considered, three species are present (O_2, N_2 and H_2O).

To describe the diffusion of three or more species, multicomponent diffusion models such as the Maxwell–Stefan equation are typically used [11]. As no nitrogen is generated or consumed in a fuel cell, no significant N_2 concentration gradient exists. Thus, for simplicity, the presence of nitrogen is ignored for the determination of the diffusion coefficient.

To describe the transport of water through another gaseous specie, Fick's binary diffusion equation can be used [11]. This simply consists of applying a binary diffusion coefficient to Fick's diffusion equation (6). This coefficient, written $D_{i,j}^{bi}$, can be applied for the diffusion of specie "i" in "j", and simultaneously the diffusion of specie "j" in "i". At the anode and cathode GDLs, the two species are H_2 and H_2O, and O_2 and H_2O, respectively.

The binary diffusion coefficient value is determined using the Stattery-Bird equation [111]:

$$D_{i,j}^{bi} = \frac{10.1325}{P_{tot}} a \left(\frac{T}{\sqrt{T_{crit,i}\, T_{crit,j}}}\right)^{b} \left(\frac{P_{crit,i}\, P_{crit,j}}{101\,325^{2}}\right)^{\frac{1}{3}} \left(T_{crit,i}\, T_{crit,j}\right)^{\frac{5}{12}} \left(\frac{10^{-3}}{M_i} + \frac{10^{-3}}{M_j}\right)^{\frac{1}{2}} \qquad (7)$$

With T_{crit} , P_{crit} the critical temperature and pressure of the specie, and M its molar mass. Their values, as well as the values of the a and b constants can be found in [11]. With this equation, the binary diffusion coefficients $D_{H2,H2O}^{bi}$ and $D_{O2,H2O}^{bi}$ are determined for the anode and cathode GDLs, respectively.

3.1.2 Porous medium diffusion

A porous material is defined by two main properties, which are its porosity and tortuosity [112]. Porosity, also called "void fraction", is the ratio of the volume of pores in a material, to the total volume of mass. Tortuosity relates to the number of twists and bends in those pore channels (dimensionless quantity). The porous nature of the GDL must be considered in the diffusion flow expression.

To integrate porosity and tortuosity, the Bruggeman's correction can be applied to the diffusion coefficient, using the following equation:

$$D_{i,j}^{eff} = \varepsilon^{\tau} D_{i,j}^{bi} \qquad (8)$$

With ε and τ being the mean GDL porosity and tortuosity, respectively.

In a GDL, porosity and tortuosity levels evolve. As reactants diffuse through the GDL (from the BP to the CL), the pores progressively increase in number and decrease in size. One section close to the CL is even often differentiated in the literature, as the micro porous layer (MPL) [109]. Porosity and tortuosity levels are however complicated to quantify [112]. Mean values across the entire diffusion layer are often measured. Thus, in this model, the GDL is considered as being one single element, with identical physical properties (mean porosity and tortuosity). The usual mean GDL porosity is ~0.4, but the tortuosity can greatly vary from 1.5 to 10, depending on pore structure configuration [11].

3.1.3 Capillarity

In this model, liquid water transport is expressed through capillarity. Fortunately, its expression can be adapted to be proportional to a liquid water concentration gradient. This is very convenient as it simplifies the mathematical combination between liquid and vapor water transport. To quantify the capillarity flow, using a Fick-like expression, a capillary diffusion coefficient is established [110], [113]:

$$D_{\mathrm{cap}} = \frac{K_0 s^e}{\nu_l} \frac{\partial P_c}{\partial s} \frac{v_{H2O\ liq}}{V_{pore}} \tag{9}$$

Where K_0 is the intrinsic permeability [m^2], s the liquid water volume fraction per unit of volume, e the exponential coefficient for phase permeability, ν_l the liquid water kinematic viscosity [m^2.s^{-1}], P_c the capillary pressure [N.m^{-2}] and $v_{H2O\ liq}$ the liquid water specific volume [m^3.kg^{-1}].

The derivative of the capillary pressure is equal to:

$$\frac{\partial P_c}{\partial s} = -\sigma\, cos(\theta_c) \sqrt{\frac{\varepsilon}{K_0}} (1.417 - 4.24s + 3789s^2) \tag{10}$$

Where σ is the surface tension [N.m^{-1}] and θ_c the liquid water contact angle [rad].

The liquid water volume fraction is calculated using:

$$s = \frac{V_{H2O\ liq}}{V_{pore}} \tag{11}$$

Where V_{pore} and $V_{H2O\ liq}$ are the pore and liquid water volume fractions, respectively. To simplify the resolution process, the liquid water volume fraction of each mesh element (s) is considered as constant during one timestep.

Between each timestep, the phase change between liquid and vapor is considered using the following expression [114]:

$$S_{vl} = \begin{cases} k_c \varepsilon (1-s) x_v (c_{H2O_{tot}} - c_{H2O_{sat}}) & , c_{H2O_{tot}} > c_{H2O_{sat}} \\ k_e \varepsilon s \dfrac{\rho_{H2O}}{M_{H2O}} RT_{cell} (c_{H2O_{tot}} - c_{H2O_{sat}}), & c_{H2O_{tot}} \leq c_{H2O_{sat}} \end{cases} \tag{12}$$

Where S_{vl} is the volumetric phase change rate [mol.m^{-3}.s^{-1}], x_v the vapor mole fraction and k_e/k_c the evaporation/condensation coefficients, respectively. Their units and values are provided by Meng [114].

3.2 Catalyst layer

The catalyst layer is a multicomponent porous structure. There is Nafion, to transport hydrogen ions, carbon black to transport electrons, and platinum to catalyse the electrochemical reactions. The pores allow free transport of the humid reactants. Many similarities exist between the CL and the GDL. Both are porous, and contains up to three different gaseous species (H_2/O_2, N_2 and H_2O). In both cases, water transport is driven by diffusion and capillarity. A few dissimilarities however exist, and are specified in this subsection.

3.2.1 Porous medium diffusion

In the CL the scale length of the system is comparable to the free mean path of the molecules that diffuse through it. In other words, the gas molecules collide with the pore walls more frequently than with each other. In this case, the Bruggeman's correction cannot be applied. To describe the diffusion of gas molecules that frequently collide with pore walls, the Knudsen coefficient is used.

The expression of the Knudsen coefficient is given below [115].

$$D_i^K = \frac{d}{3}\left(\frac{8R.T}{\pi M_i}\right)^{1/2} \tag{13}$$

Where R is the ideal gas constant, T is the gas temperature, and M the molar mass of the specie (water in this case). The constant d is the mean pore size in the catalyst layer.

The Knudsen diffusion coefficient (13) is assembled with the binary diffusion coefficient (7), to form the final effective diffusion coefficient (14).

$$D_{i,j}^{eff} = \left(\frac{1}{D_{i,j}^{bi}} + \frac{1}{D_i^K}\right)^{-1} \tag{14}$$

3.2.2 Water production

Water is produced in the cathode CL as a by-product of the PEMFC reduction reaction. This source term must be integrated into the equation system. The amount of water produced by a PEM fuel cell is directly proportional to the current that is drawn from it. In this model, the PEMFC current is an input variable and is independent of reactant transport. Reactant starvation effects are thus not taken into account in this model.

The water flow related to current production is determined using the Faraday law (in [mol.m^{-2}.s^{-1}]):

$$J_{prod}^{CL\,cat} = \frac{i}{2F} \tag{15}$$

Even though this water is produced at the cathode CL, it can be considered as instantaneously dissolved within the membrane [116]. This also makes most physical sense, as the catalyst particles on which the water is produced are directly surrounded by the hydrophilic Nafion binder [29]. Since (15) is not subjected to a sorption flow, it is directly integrated into the membrane mesh element located at the cathode CL border.

3.3 Membrane

Located at the centre of the fuel cell, the membrane can be assimilated to a water reservoir inside of the MEA, which swells and shrinks during hydration and dehydration, respectively. Its water sorption capacity depends on the water concentrations found at the membrane/CL interfaces [117]. The relation between membrane water uptake capacity, and the water concentration at its borders, must first be quantified.

Water transport through the membrane must also be determined. In the polymer, three flows responsible for water transport coexist. They are diffusion, electro-osmosis, and pressure gradient flows (FIG. 2.4) [12]. All those flows are typically expressed as function of water content, not concentration. Water content, as well as its relation to water concentration is presented in the next subsection.

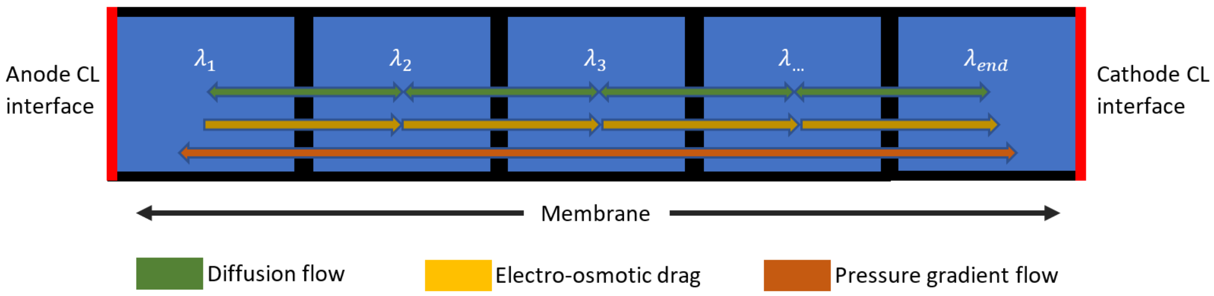

FIG. 2.4: MEMBRANE WATER TRANSPORT FLOWS THROUGH 5 MESH ELEMENTS

3.3.1 Water content and concentration

The membrane water content (λ) corresponds to the number of water molecules per sulfonic acid (SO_3^-) group (see section 2.1 chapter 1). The FVM model presented in this chapter relies on water concentration variations to determine water transport. As water transport expressions in the membrane are proportional to water content, and not water concentration, the equation between the two parameters must be defined.

The relation between water content (λ) and water concentration (c_{H2O}) is often misunderstood. Indeed, two different equations in the literature express water content as function of water concentration:

- One equation is used to relate water content to water concentration inside of the membrane. This equation truly relates the two parameters, based on physics.
- The other equation is used to express the mean membrane water content at equilibrium (at steady state), relative to the water concentration conditions at the CL/membrane interfaces.

Both these equations must be integrated into the model to quantify the membrane water sorption flow.

a) Through the membrane

In the membrane, water content equals the number of H_2O molecules per SO_3^- group. Per unit of volume, this corresponds to the water concentration divided by the sulfonic charge concentration of Nafion ($c_{SO_3^-}$). To account for membrane swelling during hydration, whilst maintaining the dry membrane coordinates, a correction is applied to this equation. This is known as the Siegel formula, such as presented by [12], [118], [119]. The relation between c_{H2O} and λ in the membrane is thus equal to:

$$\lambda_{mem} = \frac{c_{H2O}}{c_{SO_3^-} - s^*.\,c_{H2O}} \tag{16}$$

Where s^* is the expansion factor coefficient related to ionomer swelling. Derived from the measured thickness of a dry and fully hydrated Nafion117 membrane, it is equal to 0.0126 [97].

The value of the sulfonic charge concentration in Nafion is determined using its equivalent weight formula [11]. Equivalent weight corresponds to the atomic weight of a specie, divided by its valence. As the sulfonic group of Nafion ($SO_3^-H^+$) has a valence of 1 (can only accept one electron), its equivalent weight equals its average weight. The sulfonic charge concentration in Nafion is thus equal to:

$$c_{SO_3^-} = \frac{\rho_{dry}}{M_n} \tag{17}$$

With ρ_{dry} and M_n the dry density and equivalent weight of Nafion, respectively.

b) CL/membrane interface

Membrane water content, relative to water concentration conditions at the CL/membrane interfaces has first been determined experimentally by Zawodzinski [120]. For this, membranes were equilibrated above aqueous solutions of various lithium chloride concentrations and then weighed. From this weight, the mean membrane water content was determined. They determined a nonlinear relation between membrane water uptake capacity and water concentration (FIG. 2.5). This relation can be expressed using the gas water activity (aw). The empirical relations of [120] were determined at 30°C, and for a Nafion 117 membrane. Springer *et al.* [97] completed this relation with their data, to account for the presence of liquid water. In their experiment, water content could reach up to 16.8 (at 80°C). They considered a corresponding "artificial" maximum water activity of 3. For the continuity of the equations, the increase between the maximum water content measured by [120], and their value (16.8) is considered to be linear relative to water activity.

Three years after Springer *et al.*, Hinatsu *et al.* carried out similar experiments [121], but this time at 80°C and with multiple types of membranes (FIG. 2.5). For water activities greater than 1, they however only provide the water content value of a Nafion 117 membrane fully immersed in liquid water at 80°C (equal to 17.808). It is worth noting that the measured saturation water content (for $aw = 1$) is much lower for Hinatsu's expression relative to the one presented by Zawodzinski (9.2 versus 14). To apply the more precise data provided by Hinatsu for $aw \leq 1$, whilst avoiding discontinuity at $aw > 1$, the same linear water content increase assumption as presented by Springer is applied to the Hinatsu equation:

$$\lambda_{eq} = \begin{cases} 0.3 + 10.8aw - 16aw^2 + 14.1aw^3, aw < 1 \\ 9.2 + 4.304(aw - 1) \qquad ,1 \leq aw \leq 3 \end{cases} \tag{18}$$

The water activity value, relative to the assumptions made by Springer ($aw = 3$ for only liquid water) can be expressed in the following form [116]:

$$aw = \frac{c_{H2Ov}RT}{P_{sat}^{H2O}} + 2s \tag{19}$$

With T, aw, P_{sat}^{H2O} and s the temperature, water activity, saturation pressure and liquid water volume fraction at the membrane surface, respectively.

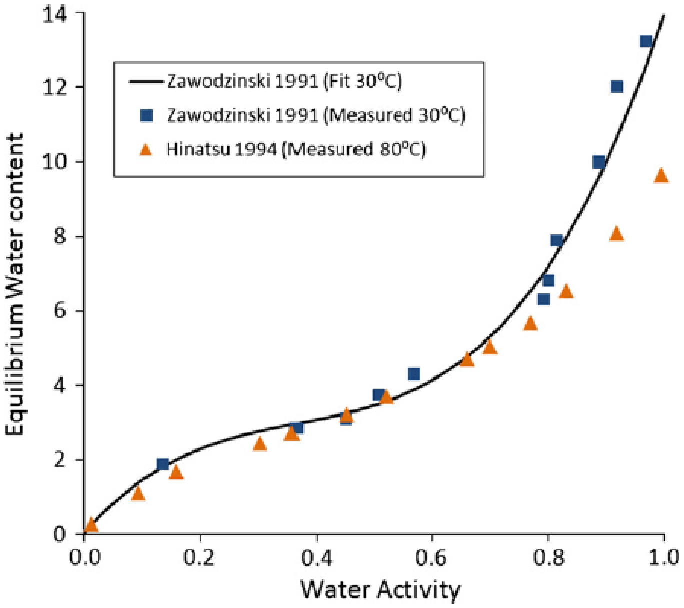

FIG. 2.5. EQUILIBRIUM MEMBRANE WATER CONTENT MEASUREMENTS AT DIFFERENT WATER ACTIVITIES [122]

c) Water sorption / desorption rate

The water sorption expression is defined using both the water content through the membrane (16) and the equivalent water content at the borders between the membrane and CLs (18). To express the transient behavior of water sorption/desorption, Berning *et al.* [99] propose the following equation (in [mol.m^{-2}.s^{-1}]):

$$J_{sorp} = k_{sorp}.\frac{\rho_{dry}}{M_n}(\lambda_{mem} - \lambda_{eq}) \tag{20}$$

With the sorption coefficient k_{sorp} equals to:

$$k_{sorp} = \begin{cases} k_a = 1{,}14.10^{-5}.f_v.e^{2416\left(\frac{1}{303}-\frac{1}{T_{cell}}\right)}, & \lambda_{mem} < \lambda_{eq} \\ k_d = 4{,}59.10^{-5}.f_v.e^{2416\left(\frac{1}{303}-\frac{1}{T_{cell}}\right)}, & \lambda_{mem} > \lambda_{eq} \end{cases} \tag{21}$$

Where T_{cell} is the mean fuel cell temperature [K], and f_v the membrane water volume fraction equal to:

$$f_v = \frac{\lambda_{mem}\, V_{mol\,H2O}}{V_{mol\,mem} + \lambda_{mem}\, V_{mol\,H2O}} \tag{22}$$

To simplify the resolution process, the membrane water volume fraction (f_v) is considered as constant during one timestep. Now that the equations used at the boundaries between the membrane and catalyst layers have been defined, water transport through the membrane must be expressed.

3.3.2 Diffusion flow

Zawodski *et al.* [123] have measured the diffusion of water in Nafion 117 membranes using nuclear magnetic resonance (NRM). This research has proven that water diffusion through the membrane takes place down a “chemical potential gradient”, which is function of water activity in the membrane. This gradient has been injected into the traditional Fick’s law expression (6), using a chemical diffusion coefficient:

$$D_{chem} = \left(\frac{dln(aw)}{dln\ c_{H2O}}\right) D^* \tag{23}$$

With D^* , the intra-diffusion coefficient, determined by NRM at 30°C, as function of water content λ.

Based on Zawodski *et al*'s findings, Springer *et al.* [97], adjusted the diffusion flow expression. For this, they assumed that the intra-diffusion coefficient directly relates water diffusion in the gradient in the logarithm of water activity. Membrane swelling is also taken into account within the diffusion coefficient:

$$D_{\mathrm{w,30°C}} = D^* \left(\frac{1}{1 + s^* \lambda^2} \frac{\lambda}{aw(17.81 - 79.70aw + 108aw^2)}\right) \tag{24}$$

With s^* the expansion factor coefficient related to membrane swelling (measured at 0.0126).

Springer *et al.* then adjusted (24), to fit a range of temperatures. For this, they used the measurements of Yeo *et al.*, who studied changes in Nafion proprieties with temperature [124]. By solving (24) for different water contents and temperatures (T_{cell}), the diffusion coefficient expression becomes:

$$D_{\mathrm{w}} = D_\lambda e^{\left[2416\left(\frac{1}{303} - \frac{1}{273 + T_{cell}}\right)\right]} \tag{25}$$

The D_λ coefficient, presented by Springer *et al.* [97], is a third-degree polynomial function and is only valid for $\lambda > 4$. This expression has been simplified and adjusted to fit all water content values [125], [126]:

$$D_\lambda = \begin{cases} 10^{-6} & ,\lambda < 2 \\ 10^{-6}\left(1 + 2(\lambda - 2)\right) & ,2 \leq \lambda \leq 3 \\ 10^{-6}\left(3 - 1.67(\lambda - 3)\right) & ,3 \leq \lambda \leq 4.5 \\ 1.25 \times 10^{-6} & ,\lambda \geq 4.5 \end{cases} \tag{26}$$

The water diffusion flow in the membrane is expressed relative to a water content gradient, and equals:

$$J^M_{H2O\ dif\ (i-1,i)} = D_{\mathrm{w}} c_{SO_3^-} \frac{(\lambda_{i-1} - \lambda_i)}{\Delta z} \tag{27}$$

3.3.3 Electro-osmosis flow

One of the main membrane functions is to conduct H^+ protons from the anode to the cathode. As they move, they carry water with them through momentum (Newton’s law of action and reaction) [127]. This flow is thus one dimensional and unidirectional (from anode to cathode).

Water transport through electro-osmosis is quantified using the electro-osmotic drag coefficient (n_d). This corresponds to the number of water molecules transported per proton. Based on the measurements presented in [128], for a fully hydrated membrane, $n_d^{sat} = 2.5 \pm 0.2$ (measured between 30 and 50°C). The maximum n_d value is assumed to be valid at higher cell temperatures, and to vary linearly with membrane water content. With their measurements, a maximum water content of 22 was reached. Relative to water content, the drag coefficient expression becomes:

$$n_d = n_d^{sat} \frac{\lambda}{22} \tag{28}$$

The flow of protons crossing the membrane is determined using Faraday's law. This flow multiplied by the electro-osmotic drag coefficient provides the electro-osmosis water flow expression.

$$J_{osm\,(i-1,i)}^{M} = 2n_d^{sat} \frac{\lambda_{i-1}}{22} \frac{j}{2F} \tag{29}$$

In (29), the first membrane mesh element is located at the anode CL/membrane interface. The model input parameter j, corresponds to the fuel cell operating current density. The Faraday constant F, is multiplied by 2, to convert the hydrogen flow to a proton flow.

3.3.4 Pressure gradient flow

A significant pressure gradient can exist between both sides of the membrane. In this case water is transported through the membrane by convection. This flow is often neglected, as for most PEM fuel cells, no significant pressure gradient exists during nominal operation. However, as the purpose of this model is to study the behavior of a membrane during break-in, this flow is taken into account.

In the membrane, the pressure gradient flow is one dimensional (from anode to cathode). It can also be considered as one-directional (from anode to cathode or cathode to anode). Based on a form of Schögl's equation of motion, the water flow rate relative to the pressure gradient has been defined [129], [130]. Assuming the pressure gradient to vary linearly through the membrane, we have for every mesh element:

$$J_{\Delta P\,(i-1,i)}^{M} = \frac{\varphi_{H2O_x}\, k_{hydro} c_{SO_3^-} \lambda_x}{\mu_{H2O}} \frac{\Delta P}{\Delta z} \tag{30}$$

Where φ_{H2O} is the water volume ratio in the membrane, k_{hydro} is the membrane's hydraulic permeability [m²], μ_{H2O} is the water viscosity [Pa.s] and P the membrane pressure [Pa]. The mesh element x, corresponds to "i-1" if $P_{an} > P_{cat}$, and to "i" if $P_{cat} > P_{an}$.

The water volume ratio in the membrane is proportional to water content, and is expressed as:

$$\varphi_{H2O_x} = \frac{0.35}{16.8} \lambda_x \tag{31}$$

4 System resolution and visual representation on Matlab™

4.1 System resolution

4.1.1 Form of the equations

For every mesh element in the domain, equations are set up in an implicit form. The comprehension and resolution of a system composed of implicit equations is trickier than an explicit system. An implicit system has however one major advantage over the explicit one. Indeed, it prevents the calculated solutions at "$t + 1$" from diverging. This implies that the water concentration of the mesh "i" at the timestep "t" is put into equation as a function of the "$i - 1$", "i" and "$i + 1$" mesh elements, at the timestep "$t + 1$":

$$c_{H2O}{}_i^t + C_4 = C_1 c_{H2O}{}_{i-1}^{t+1} + C_2 c_{H2O}{}_i^{t+1} + C_3 c_{H2O}{}_{i+1}^{t+1} \qquad (32)$$

With "C_1" to "C_4" in (32), being coefficients calculated using the water flow equations presented in section 3.

4.1.2 LU Matrix resolution

Between timesteps, the following matrix system must be resolved:

$$A.X^{t+1} = X^t + Res \qquad (33)$$

- The vectors "X^t" and "X^{t+1}" are composed of the water concentration values of each mesh at the timesteps "t" and "$t + 1$" respectively.
- The tridiagonal matrix "A" is composed of the "C_1", "C_2" and "C_3" coefficients of each mesh, as presented in (32).
- The vector "Res" is composed of the "C_4" coefficients of each mesh, as presented in (32). Their values do not depend on water concentration.

This matrix system is resolved through LU decomposition (no Matlab™ toolbox required). It consists of decomposing the equation into a product of two triangular matrixes resulting in reduced computation time.

4.2 Visual representation of model output (post-activation)

In this subsection, the visual representation of the model output, for nominal fuel cell operating conditions (post-activation) is presented and commented. Its aim is to highlight the information that can be drawn from the figures provided by the model, and to confirm nominal model behaviour in its current state.

4.2.1 Model inputs and initial conditions

The model output example displayed in this section is for traditional fuel cell properties and operating conditions (typical of what can currently be found on the market). The specific model inputs (operating conditions and MEA properties) are specified in TABLE 2..

Dimensions	**Values**
Membrane [µm]	20
CL [µm]	10
GDL [µm]	350
Operating conditions	
Cooling input/output temperature [°C]	70/80
Pressure an/cat [bara]	2/2.1
Current density [A.cm^{-2}]	1
RH an/cat inputs [%]	50/30
Stoichiometry an/cat	1.5/1.8
Discretization	
Space interval $dz_{GDL}/dz_{CL}/dz_{Mem}$ [µm]	11.66/0.2/0.2
Time interval dt [s]	5.10^{-3}
Total time	
Simulation [s]	80
Computation [s] core i5 V9 2.5gHz, 32gbRAM	35

Table 2.1: Model input fuel cell properties and operating conditions

For this example:

- The MEA is fully broken-in and dry (c_{H2O} set at 1mol.m^{-3} for all mesh elements).
- All operating conditions remain constant over time.

4.2.2 Model output figures and analysis

The model results are represented on a three-dimensional figure. With this configuration, the water concentration evolution is displayed through space and time. Water content evolution through the membrane is also given by the model, which has been recalculated using (16). These are the type of dynamic displays that can be implemented on a fuel cell test station interface to simulate and visualize the membrane hydration level (and consequently state of activation) in real time. This would provide additional real time information regarding the ionomer activation process, and possibly prevent premature ageing by identifying punctual faulty conditions (drying or flooding) to [131]–[133]. On the example below, membrane water content (z axis) evolution through the membrane is displayed. Fig. 2.6 represents membrane hydration during the first 2 seconds of fuel cell operation. During this time, the membrane hydration profile reaches about 35% of its final value. Fig. 2.7 confirms numerical system convergence after 20 seconds. With standard fuel cell dimensions and operating conditions, membrane hydration can be divided in multiple steps.

During the first 0.5 seconds, all the water produced by the cell is dissolved within the membrane at the cathode side. During this time, the “reservoir” effect of the ionomer is visible, as the accumulated water is slowly filling its centre. After 0.5 seconds the water sorption/desorption coefficients become significant, resulting in a progressive increase of water sorption at the anode, and a desorption of a fraction of the produced water to the cathode CL/GDL. One second later (t=1.5s), the water concentration at the cathode has increased enough for the membrane to start hydrating through sorption once again. Between 2 and 8 seconds, the membrane water content quickly increases. After 8 seconds, liquid water starts to form at the cathode ($\lambda = 9.2$, see FIG. 2.5) which drastically reduces the rate at which the water content increases (see (17-18)). At 10 seconds, a flow equilibrium is starting to take shape. To let the solution reach 99.95% of the final equilibrium, 20 seconds are required.

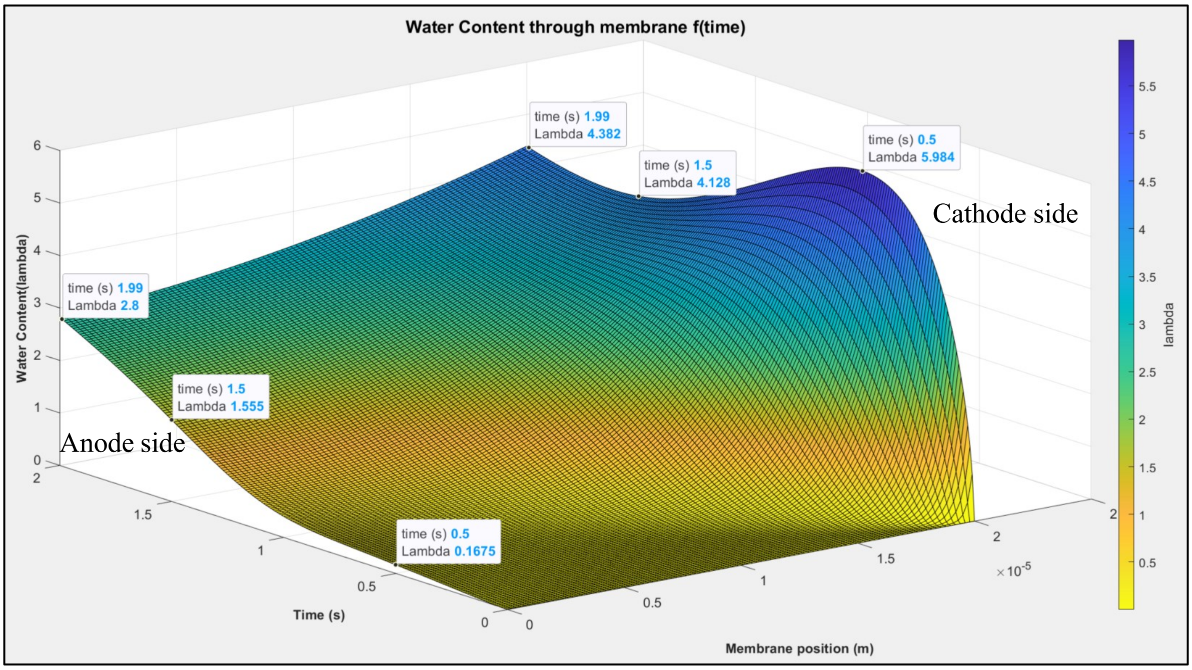

FIG. 2.6: WATER CONTENT IN MEMBRANE F(TIME), FIRST 2 SECONDS

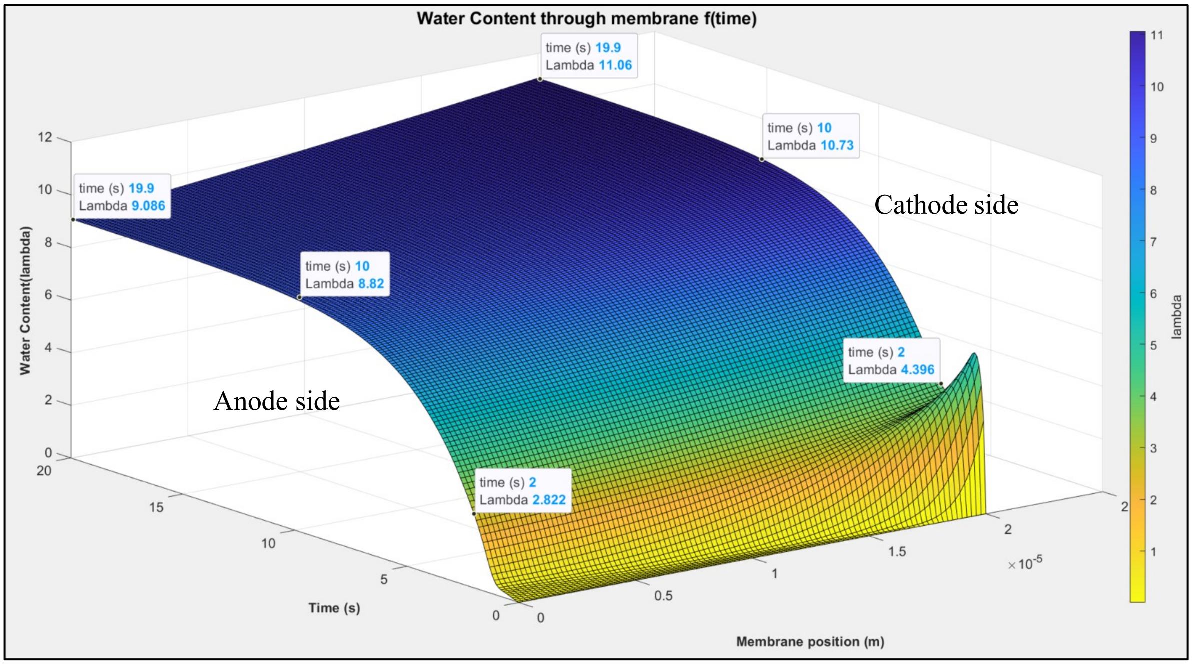

FIG. 2.7: WATER CONTENT IN MEMBRANE F(TIME), 20 SECONDS

Other characteristics of the model behaviour have been verified by studying its output for a variety of operating conditions. Yan *et al.*, who investigated the transient behaviour of MEA water transport, found a strong correlation between the membrane water content profile gradient, convergence time, and the current density [134]. The same conclusions are made with this model. When increasing the current density (of TABLE 2.) from 1 to 2 A.cm^{-2}, the water content gradient grew from 18 to 34%, and the convergence time (to 95% of the final value) reduced from 9 to 4.6 seconds. Simulations at idle conditions (no current or heat production) and saturation for the gas inputs, confirm the convergence to a null-gradient profile at $\lambda = 9.2$ (corresponding to equilibrium sorption at 100% RH (18)). The drying threshold (considered at $\lambda = 8$) is obtained by the reducing the pressures (of TABLE 2.) by 750mbar or increasing the cell temperature by 10°C, which concurs with PEMFC durability standards [55].

As previously stated, the membrane sorption isotherm profile trend is known, but its absolute value varies in the literature [135]. This decisive parameter to the ionomer water profile depends on many ionomer properties (mechanical, thermal history, type of ionomer, pre-treatment..) [136]. Due to this lack of definitive reference data [91], [135], many models assume the most commonly used equation (*Springer*, measured at 30°C [97]) to be valid for all use cases [137]–[139]. This can however lead to numerical results that show lower losses than observed in the experiments [140]. Consequently, before implementing the break-in structural changes to the model, it must first be validated using experimental data (post-activation).

5 Model calibration and validation

To determine the model's ability to correctly simulate membrane hydration for a specific cell (post-activation), it must be calibrated and validated. These two processes are presented throughout this section.

5.1 Calibration

This model is mainly based on water transport equations, whose coefficients values are known. The f_c coefficient used for the model boundary conditions (5) is however not provided by the literature. For this model, cartographies of data provided by SYMBIO have been used to determine f_c. These cartographies are not provided in this section, but the experimental protocol on which they are based is briefly presented.

The aim of the experiment to set up on a fuel cell test station is to precisely quantify the mass of water exiting the fuel cell anode. For this, a condenser and a scale or a flowmeter can be used at the anode output for example. The mass flowrates entering the anode and cathode are known, as well as the amount of water produced by the fuel cell. Thus, based on the water balance equation principle (FIG. 2.3), the total mass of water which crosses the membrane from the cathode to the anode can be determined. By applying this method for different operating conditions, the cartography of f_c can be determined.

5.2 Validation

Model validation typically consists of setting up a test protocol, where identical input parameters are chosen for the experiment and for the simulation. The model accuracy is afterwards determined by residual analysis between the two output results. Measuring the water concentration profile throughout the MEA typically requires very specific and expensive equipment (using optical methods such as "Small Angle Neutron Scattering", or SANS) [141]. Other methods however exist to validate the model, at least to a certain extend. In this section, a model validation method is used, based on the relation between membrane resistance and water content.

5.2.1 Model

The model provides the membrane water content profile evolution over time. Using two simple equations, the total membrane resistance can be determined from the water content values [97] [142]. The electric conductivity [S.m^{-1}] of all mesh elements in the membrane is determined using:

$$\sigma = (0.5139\,\lambda - 0.326)e^{1268\left(\frac{1}{303}-\frac{1}{T_{cell}}\right)} \tag{34}$$

Its inverse corresponds to electrical resistance. The total ionomer resistance is determined by integrating all local resistance values over the membrane thickness (z_m).

$$R_m = \int_0^{z_m} \frac{dz}{\sigma(\lambda)} \tag{35}$$

5.2.2 Experiment

As this model aims to be implementable on a test station interface for real time simulation, it has been validated using a fuel cell stack. More specifically, the experiment has been applied on a 263cm^2 10-cell PEMFC stack, using a 5kW test station. As they are only briefly used here but extensively used in the last chapter of this manuscript, the test station and fuel cell stack are presented in further detail in chapter 4.

The experimental validation protocol consists of firstly completely cooling down and purging a fuel cell stack with dry nitrogen. Afterwards, the reactant pressure, stoichiometry and stack temperature conditions of TABLE 2. are imposed. Finally, the RH and current setpoints of TABLE 2. are instantaneously applied to the stack and held for 80 seconds. This process has been repeated 3 times, from which the mean cell ohmic resistance evolution curve has been determined (based on electrolyte resistance domination over other components [11]). The resulting experimental and simulated membrane resistance data is shown in FIG. 2.8.

FIG. 2.8 displays a slight dynamic offset between the experimental data and the model, during the 13 first seconds. Indeed, the model converges more quickly than the experimental data. This was to be expected, as the MEA model does not account for the test station response time, related to the humidifiers, pressure, and flowrate regulators PID controllers. At 13 seconds, the model resistance has converged to >95% of its final value, and the experimental curve fluctuates slightly above the model data with a mean relative error of 6%. After 40 seconds the experimental membrane resistance evolves once again, leading to a maximum relative error of 20% between the experimental data and the model.

This precision rate is not perfect, given the reduced simulated domain (1D, limited to the MEA) and the chosen model validation method. This said, as previously stated, developing a model that is dynamic and suited for real time applications, comes with sacrifices in precision. For this application, the results are sufficiently accurate as they can correctly simulate the general membrane hydration evolution and identify events such as fuel cell drying or flooding. Now that the ionomer water transport model has fully been developed, and confirmed to be sufficiently precise (and not diverge), the break-in structural changes may be implemented.

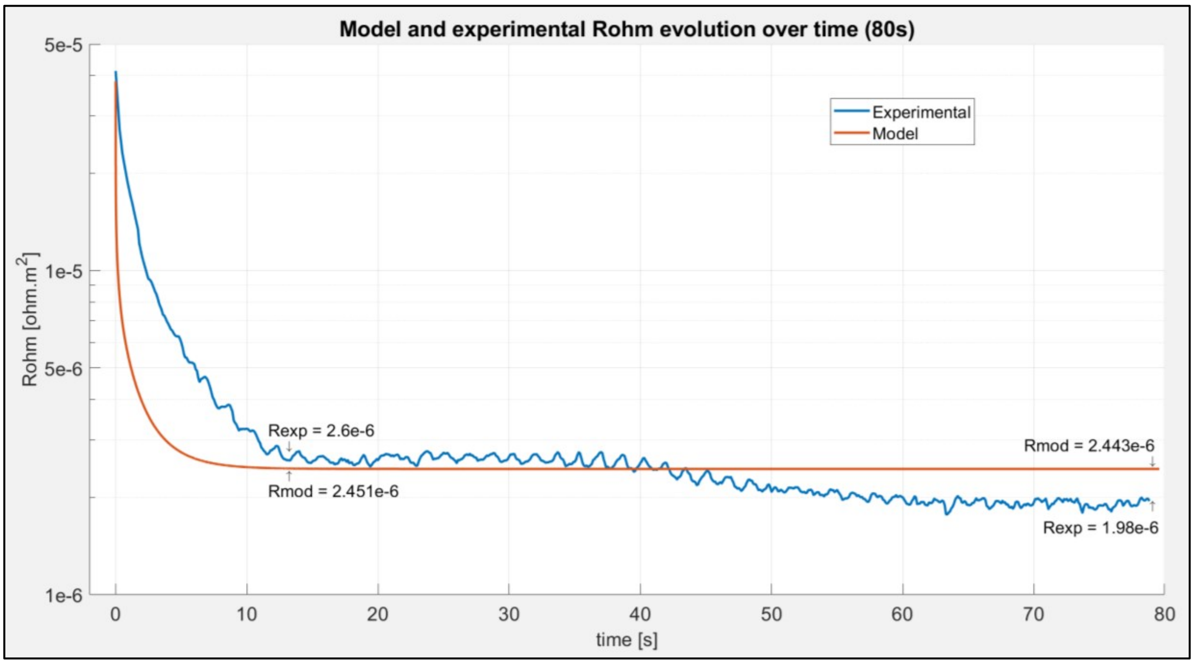

FIG. 2.8. MEMBRANE OHMIC RESISTANCE EVOLUTION FOR MODEL AND EXPERIMENTAL DATA

6 Integration of fuel cell break-in structural changes into model

This section is dedicated to the integration of all fuel cell break-in structural changes that affect the ionomer proton resistance, into the water transport model. A few cases exist in the literature, where mechanisms such as domain spacing, polymer relaxation, etc. are considered and/or implemented to water transport models. In these models however, all processes which affect the membrane water content evolution are dissociated (considered to not affect each other), as coupling all mechanisms would increase the complexity of the equation system. For this, empirical approaches are used, by affecting one time constant to each phenomenon, and consider the membrane water mass evolution as being the sum of all processes ($\Delta M_{tot} = \Delta M_{\text{diffusion}} + \Delta M_{\text{domain spacing}} + \ldots$) [20].

During fuel cell activation, the membrane morphology is irreversibly affected. The time constants related to mechanisms such as domain spacing or surface skin change may vary, and their evolution may strongly affect / be affected by the water transport flows (diffusion, sorption...). Therefore, the approach used in this model is to directly integrate the membrane activation mechanisms into the previously presented water transport equations, so that a correlation exists between the different processes.

The activation mechanisms which alter water sorption and transport through the membrane are implemented in the form of resistances, where each resistance represents a separate physical phenomenon. The value and evolution of these resistances during activation vary relative to the MEA humidity conditions and operating parameters (e.g. λ_{mem}, aw, I). Implementing these resistances, quantifying their initial values and estimating their evolution laws and rates is the subject of this section. In a first subsection, the resistances that are directly related to the ionomer (in-situ) are studied, quantified, and integrated into the model. Afterwards the activation mechanisms related to other cell components (ex-situ), which can also affect water transport, are mentioned. Finally, the impact of the break-in coefficients on the model output is studied.

6.1 Ionomer structural changes (in-situ)

As seen in chapter 1, the membrane's nanostructure has to accommodate for the growth of water domains while providing a pathway for the mobility of water molecules [20]. The surface skin must also become more hydrophilic, and the membrane additives/impurities must be evacuated. The activation mechanisms that are directly related to the ionomer can therefore be dissociated into three resistances: R_{dspac} (domain spacing), R_{skin} (surface skin), and R_{cont} (contamination).

Little knowledge specific to membrane hydration mechanisms during activation exist. Furthermore, it is unclear how much each ionomer morphological change contributes to the ohmic resistance reduction. Nevertheless, using the available knowledge and experimental data provided by the literature, their values, evolution laws and kinetics relevant to cell operating conditions, can be estimated. A few first comments can be given by analysing the typical evolution of the cell resistance during activation by mere hydration of the membrane (FIG. 2.9). As the non-activated MEA is treated by steam, the presence of liquid water is ensured, but no proton flow exists [17]. The cell resistance decrease is therefore only linked to the polymer surface structure change and domain spacing, as no proton flow initiates the ionomer additives/impurities migration.

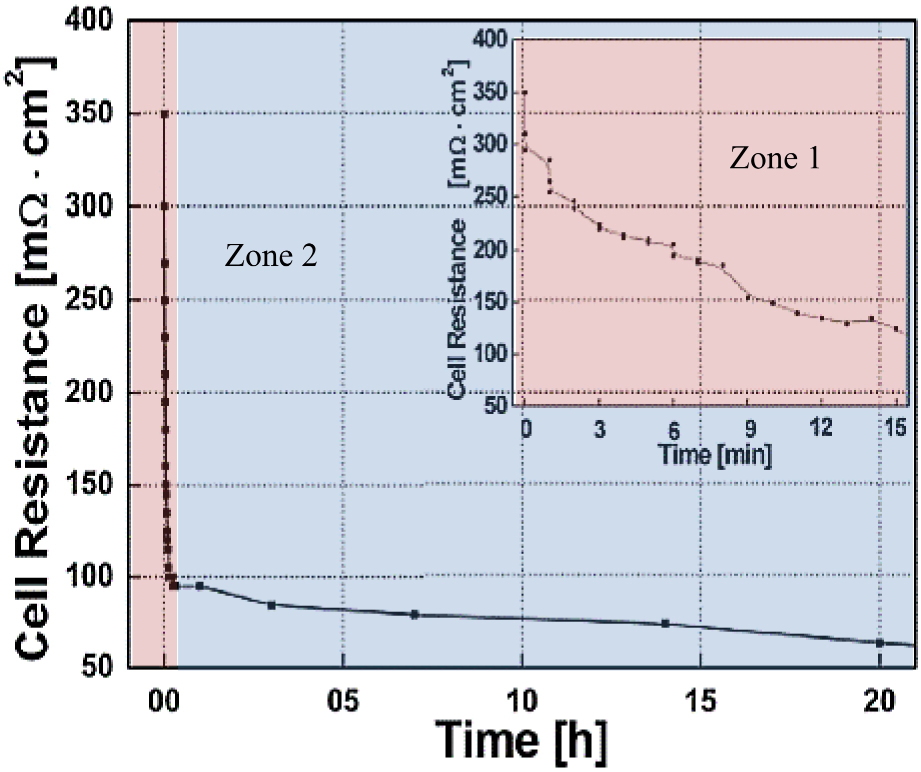

FIG. 2.9. CELL RESISTANCE EVOLUTION DURING MERE HYDRATION TREATMENT OF A NON-ACTIVATED IONOMER [19]

The membrane resistance curve can be divided into two zones. The initial 16 min (zone 1) corresponds to a quick and important drop, followed by a sluggish progressive resistance reduction over the following hours (zone 2). This trend correlates well with the typically measured cell voltage evolution during break-in [18], [64], [143]. According to the literature, water uptake is suggested to be limited by the interfacial transport during the earlier times of the sorption whereas relaxation of polymer matrix with time allows more water to be absorbed [20]. This is also makes most physical sense, as the membrane surface is the first to be in contact with liquid water, and the membrane water clusters will push against the polymer matrix only when they have reached a certain size.

The R_{skin} and R_{dspac} coefficients must thus be inserted into the model in a way that sorption at the membrane surface is the limiting mechanism to water uptake at the beginning of the activation process. A transition of the limiting mechanism must afterwards occur, so that it progressively becomes the domain spacing process within the membrane. The R_{cont} may be simpler to implement, because mostly dependent on the current, and not directly affecting water transport. The specific equations and evolution laws used for each morphological change, are detailed below.

6.1.1 Membrane surface skin transformation

The transformation of the membrane surface skin is known to affect its hydrophobicity proprieties (hydrophobic to hydrophilic) and accelerate water uptake [144]. It is therefore directly related to the sorption kinetics at the membrane/CL interface. This mathematically translates into penalizing the sorption coefficient (21), by imposing a surface skin resistance whose value evolves during activation.

$$k_{sorp\_act} = k_{sorp}(1 - R_{skin}(f(aw, I_{cell}, t))) \tag{36}$$

As previously stated, this mechanism severely affects the MEA performance [17] and is the limiting factor to water uptake during the initial duration of the activation process [20]. The surface skin is thus considered to initially be fully hydrophobic ($R_{skin} = 1$), for it to be a a full initial "barrier" to membrane hydration during break-in (zone 1 of FIG. 2.9). The produced water (15) is also concerned by this surface skin resistance. Its effect is known to eventually converge to zero for a fully activated ionomer ($R_{skin} = 0$).

Finding data to quantify the evolution law and kinetics of R_{skin} is not a simple task. According to the literature, rearrangement of the side chains is promoted when liquid water is in contact with the membrane surface [145]. FIG. 2.10 illustrates this process, as the contact with liquid water causes the hydrophilic domains to move to the surface of the hydrophobic backbone matrix [144]. This said, experimental studies have shown a progressive increase in the conductive surface area with humidity, instead of an abrupt discontinuity when reaching saturation [20]. This can be explained by the fact that as the (sub-saturation) mean humidity conditions increase, the likelihood of local condensation points also grows, locally aligning the polymer bundles. Therefore, in this 1D model, the surface skin is considered to start its transformation for mean sub-saturation conditions, and progress with the increase in vapor humidity. A gradual increase approach is more suitable for the continuity of the equations, and is more relevant than an instantaneous transformation of the surface skin when reaching saturation. Based on these remarks, the chosen criterion that must be respected for the surface skins (anode and cathode) to reduce over time is $aw > 1 - R_{skin}$.

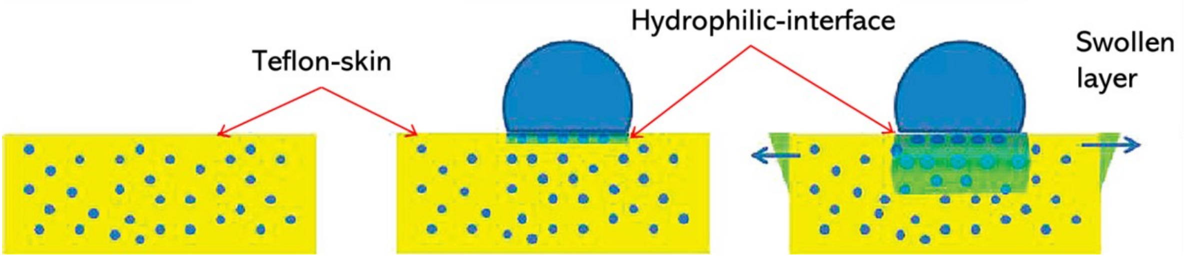

FIG. 2.10. RESTRUCTURING OF NAFION SURFACE BY EXPOSURE TO LIQUID WATER [144]

If the water activity condition is respected, the skin resistance will evolve with time according to a certain law. The different phenomena related to membrane water mass increase over time have been expressed by Kusoglu *et al.* as a series of exponential functions (which had the best fit with experimental sorption data) [20]. From these two conditions, the final form of the skin resistance evolution with time is displayed below.

$$R_{skin\ i+1} = \begin{cases} A.exp\left(\dfrac{-t}{\tau_{mean\ f(I_{cell},t)}}\right) & ,aw_i > 1 - R_{skin_i} \\ R_{skin_i} & ,aw_i \leq 1 - R_{skin_i} \end{cases} \tag{37}$$

In this equation, A is constant and equals 1 (to initially be fully hydrophobic). The τ_{mean} value is re-evaluated at each iteration of the program. It corresponds to the mean time constant to which R_{skin} evolves.

In the literature, immersion of Nafion membranes in liquid water reportedly causes the surface skin to rearrange within minutes, or even seconds. With pure vapor, this equilibrium is not reached after multiple hours [17]. Relating these durations to an ionomer in a fuel cell is not simple, as its surface is typically not in contact with purely liquid nor vapor phase water (local condensation/evaporation). Furthermore, the produced current is considered as an accelerant of surface skin transformation, as it directly generates a liquid water film on the catalyst, next to the membrane surface [17]. In this model, a baseline time constant (τ) of 10^4 seconds is considered for the surface skin change when the minimum humidity (aw) criterion of (37) is respected, but no current is produced. This constant is considered to linearly reduce with the current density, to 10^3 seconds at 1A.cm^{-2}, as liquid water is produced on more and more active sites. Above this value, the liquid water production is considered as global (no further increase in participating Pt surface), and the time constant reduces inversely proportionally to the produced water (e.g. 5.10^2 sec at 2A.cm^{-2}).

6.1.2 Membrane domain spacing and polymer relaxation

Domain spacing impacts the total theoretical maximum water uptake capacity of the membrane, as the relaxation of the polymer matrix with time allows more water to be absorbed [20]. Therefore, it directly impacts the membrane water sorption equilibrium. This equilibrium depends on the membrane water content, and the equivalent water content at its borders. Thus, imposing a penalty coefficient in the equivalent water content equations at membrane/CL interfaces (18) makes most physical sense.

$$\lambda_{eq\_act} = \lambda_{eq}(1 - R_{dspac}(f(I_{cell}, \lambda_{mem}, \lambda_{eq}, t))) \tag{38}$$

Initially, this resistance will increase with the growth of water clusters, as they slowly combine and put more stress against the polymer chains. Afterwards, it will progressively decrease with time as the membrane morphology slowly adapts itself to the presence of the water. In other words, the domain spacing resistance and membrane water content evolutions are co-dependent, as R_{dspac} affects λ_{mem} through (38), but λ_{mem} simultaneously affects the value and evolution of R_{dspac}. It this model, the resistance to the growth of water clusters is considered to vary linearly with the ionomer water content (no distinction is made between the residual, bound, and free water regimes to avoid discontinuities). The following equation can thus be setup:

$$R_{dspac} = C_{dspac} . \lambda_{mem} \tag{39}$$

With this configuration the fundamental dependence of the water content and the stress put against the polymer chains is expressed. Indeed, (39) results in a low initial R_{dspac} value which becomes more significant as the water clusters increase by size. The sluggish domain spacing resistance reduction for a fixed water content, is described through the C_{dspac} coefficient.

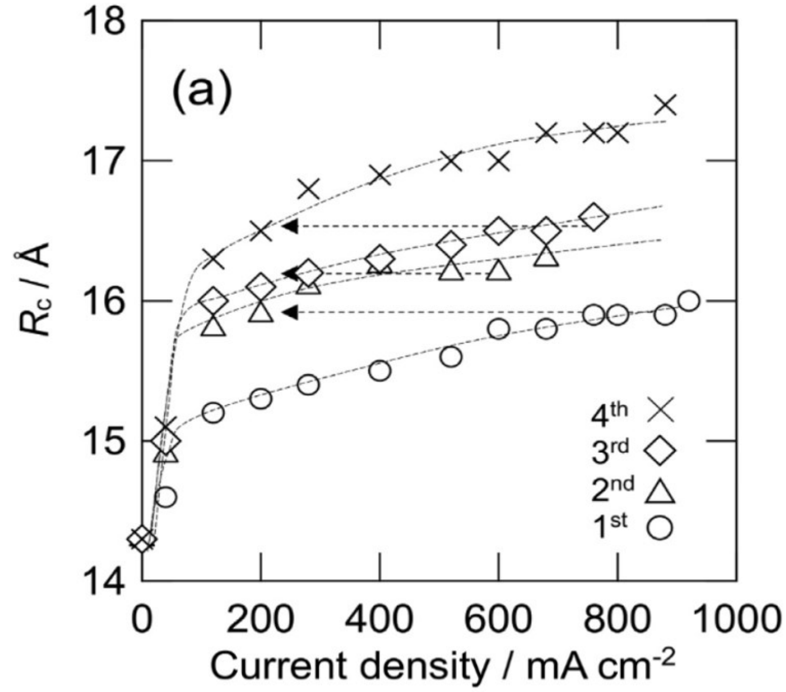

FIG. 2.11. PROGRESSIVE AND IRREVERSIBLE WATER CLUSTER RADIUS INCREASE (Y-AXIS) WITH CURRENT DENSITY CYCLES (X-AXIS) [21]

Quantifying the absolute value and evolution law of C_{dspac} is complex and may greatly depend on the membrane proprieties. What is certain, is that its value will only evolve between timesteps, if the equivalent water content at the membrane interface is higher than within the membrane. Indeed, if this condition is not met, the water surplus will be expelled from the membrane (desorbed), instead of pushing against the polymer chains. Secondly, the value of C_{dspac} is known to only decrease over time, as Ueda *et al.* [21] have proven that the increase in mean water cluster radius during activation is a permanent process (FIG. 2.11).

The effect domain spacing has on the membrane water sorption process during activation is estimated using experimental data from the literature. In Fig. 2.9, the total relative membrane resistance reduction attributed to domain spacing (zone 2) is of around 20%. Ueda *et al.* obtained a similar total ohmic resistance reduction of approximatively 16% during break-in, as the water cluster size progressively increased during the ~10 hour long activation process [21]. Based on these figures, the resistance is estimated to initially be equal to 15% for the water content of a membrane equilibrated above saturated water vapor ($\lambda = 9.2$). According to (18) and (39), this corresponds to an initial C_{dspac} value of $1.09.10^{-2}$, which is known to eventually converge to null for a fully activated ionomer.

As with the surface skin change, the exponential law proposed by Kusoglu *et al.* is applied to describe the domain spacing resistance evolution over time (for a fixed membrane water content) [20]. When considering all conditions, the expression of the C_{dspac} coefficient can be summed-up below.

$$C_{dspac\ i+1} = \begin{cases} B.exp\left(\dfrac{-t}{\tau_{mean\ f(I_{cell},t)}}\right) & ,\lambda_{eq_i} > \lambda_{mem_i} \\ C_{dspac_i} & ,\lambda_{eq_i} \leq \lambda_{mem_i} \end{cases} \tag{40}$$

In this equation, B is constant and equal to $1.09.10^{-2}$ (to obtain the correct initial C_{dspac} value at t = 0). The τ_{mean} value is reevaluated at each iteration of the program, and corresponds to the mean time constant to which R_{dspac} evolves.

According to Kusoglu *et al.* , the time constants (τ) related to domain spacing are located within a 1.10^{3} to 1.10^{5} seconds range [20]. These values are also used for the fitted curve of Fig. 1.4 in the first chapter of this manuscript. As with the surface skin, the cell current is once again considered as the main accelerant to reduce the overall domain spacing resistance. Indeed, Ueda *et al.* demonstrated that the coalescence and consequently growth of water clusters accelerates with current [21]. Therefore, τ is considered equal to 1.10^{3} at $1A.cm^{-2}$, and 1.10^{5} at $0A.cm^{-2}$. An additional dissociation is made at $0.2A.cm^{-2}$, where the τ value is set at 1.10^{4}. Indeed, Ueda *et al.* clearly identified it as a triggering point after which the current starts influencing water cluster size growth [21]. Between each current density point, τ is considered to vary linearely, and further decrease proportionally to the current density at values above $1A.cm^{-2}$. With these time constants, the domain spacing reduction can be quasi-completed within 30 minutes at $3A.cm^{-2}$ and be very sluggish at $0A.cm^{-2}$ (>100 hours). At $0.2A.cm^{-2}$, around 15 hours are required to almost fully remove the domain spacing resistance, which corresponds to the duration of break-in processes around this current density value [16].

It is worth noting that water uptake kinetics may also accelerate with temperature, as shown by the measurements (using saturated vapor) of Majsztrik *et al.* [145]. However, for the sake of model simplicity, the cell temperature effects are considered as negligible, compared to the dominant effect of the current.

6.1.3 Membrane decontamination

Unlike the other ionomer activation processes, membrane impurities do not affect its ohmic resistance by altering its water uptake kinetics. Indeed, the presence and migration of membrane impurities is known to lower its capacity to conduct protons, mainly by direct interaction with the sulfonic acid sites [22]. Thus, it directly affects the relation between the ionomer water content (number of water molecules per SO_3^- site), and its proton conductivity. What makes most physical sense, is to keep the linear relation (for a fixed temperature) between conductivity and water content (34) as well as its y-intercept, but to reduce the slope of the curve. Thus, a penalty coefficient is added to the membrane conductivity term, in the following form.

$$\sigma_{act} = \sigma\left(1 - R_{cont}\left(f\left(I_{cell}, aw_{ca}, t\right)\right)\right) \quad (41)$$

During break-in, the migration and evacuation of impurities from the membrane slightly increases its proton conductivity. This said, it can cause the opposite effect on the ionomer within the cathode CL, as the migrated species can interact with the Pt surface, and generate ions that severely contaminate the surrounding polymer [23]. The R_{cont} coefficient can therefore decrease or increase during activation. Its evolution will depend on the humidity conditions, as in-situ mitigation against contamination is known to be possible with a high RH [17]. In this model, the severity of polymer contamination at the cathode is considered to vary linearly with gas humidity. Contamination is maximized for fully dry conditions at the CL ($aw = 0$), and is null at the saturation point ($aw \geq 1$).

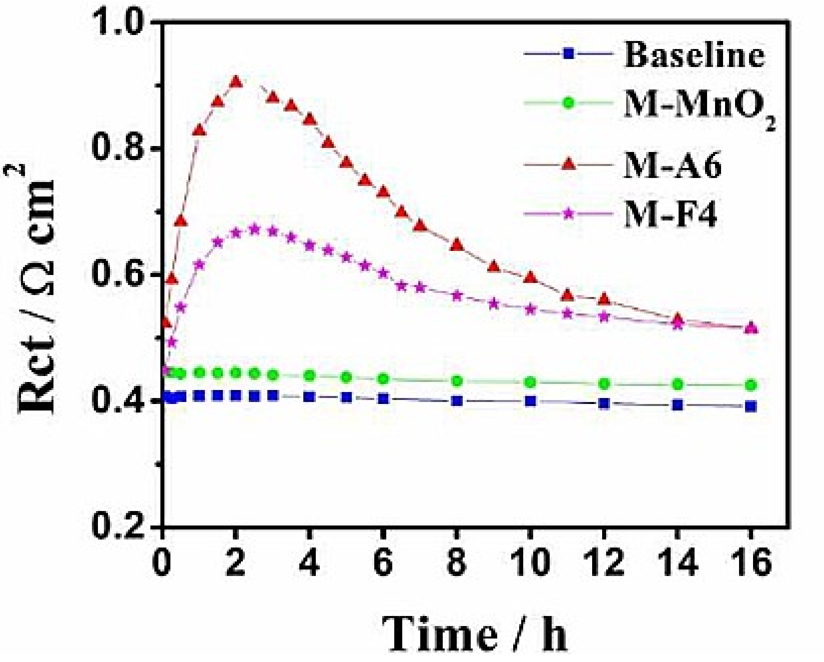

FIG. 2.12. CHARGE TRANSFER RESISTANCE EVOLUTION DURING BREAK-IN (AT 0.2A.CM^{-2}) OF CELLS CONTAINING MEMBRANES DOPED WITH DIFFERENT ADDITIVES [23]

By testing the activation of cells containing ionomers with different additives, Yuan *et al.* measured a maximum proton conductivity reduction (by CL polymer contamination) of 10% [23]. This value is considered as being the maximum proton conductivity reduction that can be caused by the ionomer activation process (for $aw = 0$). In contrast, there is no data regarding the beneficial impact of additive removal on membrane proton conductivity, but it is thought to be less significant than the CL polymer contamination (see section 2.1.3 of chapter 1). In this model, the maximum proton conductivity gain with membrane decontamination is considered to be one order of magnitude lower than the maximum loss (+1% versus -10%). One must keep in mind that these figures are generalized, rough estimations. In reality the severity of ionomer contamination greatly depends on the types of membrane additives and their dosage [22], [23].

As previously stated, during membrane decontamination, the additives and other impurities migrate to the cathode CL, which is considered to be generated by the unidirectional proton flow. As for water transport through the electro-osmotic drag coefficient (28), one can state that a fixed amount of impurities are dragged per proton that crosses the membrane. In other words, the impurity desorption rate is directly proportional to the flowrate of protons that cross the membrane, and consequently also proportional to the cell current, as stated by the Faraday law (15).

To express the membrane impurity migration kinetics, the total amount of charge required to fully migrate all impurities, must be determined. This can be estimated through the evolution of charge transport resistance during activation. The charge transfer resistance provides information regarding the ORR kinetics, and consequently the adsorption of membrane additives on the catalyst surface. It is thus an indicator of the impurity migration time. Using this method, Yuan *et al.* measured a progressive migration during the initial 16 hours of conditioning at $0.2A.cm^{-2}$ for membranes doped with different types of additives (FIG. 2.12) [23]. Further impurity migration has been measured after the initial 16 hours, but in smaller quantities. By assuming full impurity/additive migration after 16 hours at $0.2A.cm^{-2}$, the total charge density required for complete membrane decontamination is equal to Q_{ref} $=1.2.10^4C.cm^{-2}$.

Using all previously stated conditions, the final form of the contamination resistance evolution equation is displayed below

$$R_{cont_{i+1}} = \begin{cases} R_{cont_i} - C\dfrac{dt.I_i}{Q_{ref}} & ,Q_{tot} < Q_{ref} \\ R_{cont_i} & ,Q_{tot} \geq Q_{ref} \end{cases} \tag{42}$$

Where the initial value of R_{cont} is 1%, and C equals $0.01 - 0.1.(1 - aw_{ca,vap_i})$, for the resistance to remain between the 0 and 10% boundaries, and depend on the cathode vapor water activity conditions.

6.2 Structural changes of other cell components (ex-situ)

In addition to the activation mechanisms that directly take place within the ionomer, ex-situ morphological changes (occurring at the CL, GDL or cell level) also influence its proton resistance evolution. Indeed, these structural changes alter water transport and/or generation, consequently also affecting the membrane water uptake kinetics. As seen in chapter 1, multiple activation mechanisms limit the cell achievable current / water production rate, by altering the reaction-rate and mass transfer losses. The reaction rate kinetics are for example initially limited by the Pt structure change and its surface decontamination (by affecting the ECSA and ORR). Mass transfer losses evolve during the initial minutes / hours of activation [17], through the change in properties of the porous media, used to transfer water and reactants. The pore opening effect within the CLs for example changes its porosity (ε) and tortuosity (τ) values, and can consequently affect its diffusion rate (8). The flow of the supplied humid reactants may thus take longer to reach the active sites, limiting the current. This said, reduced initial porosity and tortuosity may be beneficial to ionomer hydration kinetics, as less produced water is evacuated from the cell. The GDL hydrophobicity proprieties are also known to evolve during break-in. As it becomes more hydrophilic, the overall water content at the membrane surface increases, but once again reactant diffusion and thus the produced current is hindered.

Consequently, estimating the maximum achievable current would require implementing all fuel cell activation mechanisms in the model. However, as stated in the introduction of this chapter, the effects and evolutions of those mechanisms are currently not sufficiently understood nor correctly quantifiable, for implementation in an analytical model. There are for example clear complexities involved with the estimation of pore opening kinetics. They depend on many operating conditions and their associated coefficients (porosity and especially tortuosity) are hard to quantify experimentally. Similar statements can be given in regards of the GDL hydrophobic properties, and the numerous mechanisms occurring on the Pt surface. Furthermore, as seen in the previous subsection, multiple hypothesises were already required to integrate the in-situ activation processes. Therefore, to avoid aggravating the uncertainty factor and overall complexity of the ionomer activation model, all current-limiting break-in mechanisms are not considered.

6.3 Impact of activation mechanisms on model output

In this subsection, the impact of the addition of the break-in coefficients on the model output (membrane water content and conductivity evolution) is firstly studied. Secondly, the membrane activation kinetics for different model inputs (cell operating conditions) are displayed and discussed.

6.3.1 Model output for ionomer during activation versus post-activation

During activation, the ionomer water content profile evolution over time (for the conditions shown in TABLE 2.) has the same general trend as the one displayed for an ionomer post-break-in (FIG. 2.7). This evolution however occurs over different time scales, as the break-in mechanisms cause a shift in the duration required for water uptake to gain momentum. This is followed by a progressive water content increase and convergence, instead of quasi-instantaneously reaching an equilibrium. FIG. 2.13 displays the conductivity and water content evolution (during 5 hours) of one membrane during activation and one post-activation.

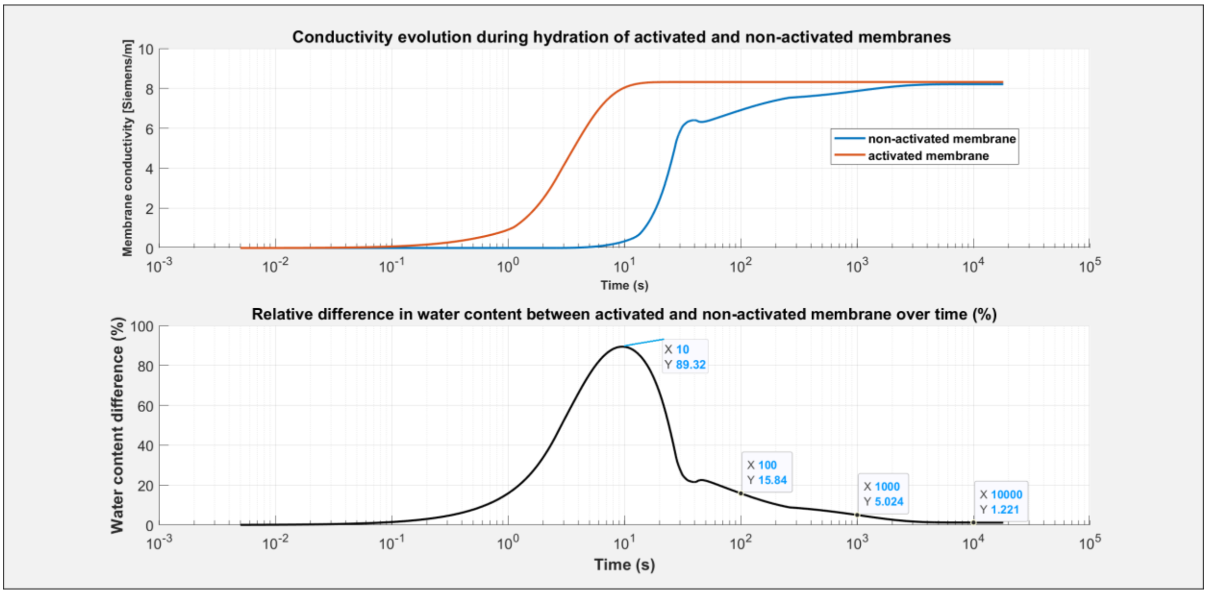

FIG. 2.13. PROTON CONDUCTIVITY EVOLUTION FOR ONE ACTIVATED AND ONE NON-ACTIVATED MEMBRANE DURING HYDRATION

The effects of the initial barrier to water sorption, followed by a sluggish increase in water cluster size are clearly visible on FIG. 2.13. After 5 hours, the water content of the non-activated membrane starts converging to ~99% of the post-activation value, for the operating conditions presented in TABLE 2.. The non-activated ionomer conductivity curve (blue) follows a slightly more complex evolution law than the three pseudo-linear segments curve of the activated ionomer (red). This illustrates the impact and co-dependence between the break-in mechanisms and the other water transport processes within the membrane.

The initial conductivity value is null, because according to (34), ionomer conductivity becomes positive (no full barrier to proton transport) only when λ reaches 1.58. One must however keep in mind that there may be residual water in the polymer (see section 2.1 of chapter 1), which is not considered in this simulation. Similarly, as previously stated, the limitation of the initial achievable current is not simulated, and instead directly set at $1A.cm^{-2}$. As will be seen in chapter 4, when activating a fuel cell, the first current increase process is incremental. This said, $1A.cm^{-2}$ can typically be reached within the first minute(s) of activation.

6.3.2 Model output for ionomer during activation for different operating conditions

To evaluate the impact of other operating conditions on the ionomer activation kinetics, results for multiple scenarios are displayed in TABLE 2.2. They are based on the operating conditions of TABLE 2., where one variable is modified for each simulation.

	λ_{mem} f(t)				Percentage activated (after 5 hours)			
	10^1 s	10^2 s	10^3 s	10^4 s	σ_{mem}	R_{skin} (an/ca)	R_{dspac}	R_{cont}
Nominal conditions (Table 2.)	0.76	8.45	9.54	9.92	98%	100% / 93%	100%	99.7%
No current ($0A.cm^{-2}$)	0	0	4.93	5.28	90.7%	99.2% / 69.5%	93.2%	99%
Low current ($0.2A.cm^{-2}$)	0.02	3.07	5.81	6.31	94.5%	99.2% /74.8%	98.4%	98.6%
High current ($2A.cm^{-2}$)	3.1	10.58	11.77	11.95	100%	100% / 100%	100%	100%
No humidity (0% RH)	0.74	6.12	6.21	6.21	83.7%	78.6%/68%	91.6%	96.8%
High humidity (100% RH)	0.76	9.11	10.23	10.69	100%	100% / 100%	100%	100%
High stoichiometry (3/3 fsa/fsc)	0.75	7.11	7.87	8.12	92.5%	95.9% / 79.1%	100%	97.9%
High temperature (80/90°C in/out)	0.75	6.7	7.34	7.55	89.1%	99.6 / 71.5%	100%	97.1%
High pressure (3/3 barabs an/ca)	0.76	9.11	10.23	10.69	100%	100% / 100%	100%	100%

TABLE 2.2. IONOMER ACTIVATION KINETICS, FOR VARIABLE MODEL INPUTS, DURING 5H OF BREAK-IN

As shown in TABLE 2.2, the current is a decisive parameter in regards of the break-in kinetics. This was to be expected, as the activation mechanisms (36,38,41) directly and strongly depend on this metric. The absence of current results in a very sluggish water content evolution, as no liquid water is produced at the membrane interface. Drawing current during activation, even for a short period of time, is therefore essential to drive the ionomer transport mechanisms (sorption, diffusion...), which are initially minimized for a fully dry membrane. However, as previously stated, there may already be residual water within the membrane before activation (see section 2.1 of chapter 1). In this case the initial barrier to water sorption and transport, and the associated effect of current is slightly overestimated in this model.

Contrary to the current, the other cell operating conditions (RH, FS, T, P etc.) are not directly integrated into the R_{dspac}, R_{skin}, and R_{cont} coefficients. These operating conditions indirectly affect the break-in kinetics by altering water activity at the ionomer surface. The input gas humidity has a clear influence on the ionomer activation process. Increasing the gas humidity (for the conditions of TABLE 2.) to saturation results in a complete (100%) membrane break-in. Interestingly, for dry gasses, the water content evolves at the same rate during the initial 10 seconds of hydration, but rapidly converges to a threshold value (after ~100 seconds). As the water activity at the membrane surface remains low, most activation mechanisms stop evolving. This results in incomplete polymer break-in, regardless of activation time, as well as irreversible membrane contamination. Thus, to fully activate a ionomer, humidifying the input gasses is mandatory (in addition to the water produced by the cell).

As seen in the previous chapter, high temperatures, pressures, and flow rates are known to accelerate the fuel cell activation process. In TABLE 2.2, the benefits of a high pressure on ionomer break-in are clearly visible, but the increasing the cell temperature or stoichiometry show the opposite effect. One must however keep in mind that the activation mechanisms that are accelerated by these metrics (CL pore structure, catalyst impurities desorption…) do not directly concern the ionomer. In this model, a higher temperature or flowrate results in incomplete ionomer activation, as the gas holds or transports more of the produced water, resulting in a reduced RH within the cell. Additionally, as previously stated, possible beneficial aspects of cell temperature on membrane water sorption kinetics [145] have not been considered in this model. What is certain, is that if a cell is activated at a high temperature or flowrate, it must be combined with an elevated input gas humidity, to fully break-in the ionomer.

The simulations put forward in this subsection highlight the strong dependence of ionomer break-in kinetics on cell operating conditions. This also supports the idea that an activation gradient exists within the MEA surface, caused by $I, RH, FS, T, P,$ etc. gradients (see section 3.2.6 of chapter 1).

7 Conclusion

In this chapter, an analytical dynamic ionomer activation model has been developed, through three main steps. First, a functional one-dimensional water transport model for a PEMFC MEA in normal operation (post- activation) was developed. Based on the mass conservation principle, the domain is divided in a finite number of elements using the FVM method. Water vapor transport through the multi-gaseous porous media (electrodes) is simulated using Fick, Stattery-Bird, Bruggeman and Knudsen equations. Liquid water transport is considered through capillarity. Membrane water sorption is quantified using a transport flow depending on the equilibrium water content at both sides of the membrane/catalyst layer interfaces. Through the membrane, a mix of diffusion, convection, and electro-osmosis equations is set up. The equations relating all mesh elements are set up in an implicit form and resolved by LU decomposition. This computationally effective resolution method allows for real time simulation (and thus the possibility to implement the model on an activation bench interface).

Second, at this stage of the model development, an ohmic resistance model validation technique has been applied. This confirmed its ability to correctly simulate water transport for a fuel cell stack (post-activation). Third, the functional validated water transport model has been adapted to the activation process.

For this, specific variables related to the break-in mechanisms have been implemented into the water transport equations, based on the gathered knowledge of chapter 1. Only the “in-situ” (directly occurring within the ionomer) activation mechanisms were considered in this model. They are divided into three resistances, representing membrane domain spacing, surface skin change, and decontamination.

The model output displays the membrane water content profile evolution over time, which is used to study its hydration behaviour and to obtain a better understanding of its activation process. For nominal cell properties and operating conditions (post-activation) and a dry membrane, a flow equilibrium starts to take shape after 10 seconds. During activation, the membrane water content profile evolution has the same general trend as the one of a membrane post-activation. This evolution however occurs over different time scales, as the break-in mechanisms cause a shift in the duration required for the conductivity increase to gain momentum. The model output clearly indicates that drawing current during activation is mandatory for the ionomer to reach the post-activation performance, and accelerate break-in. Additionally, the significant influence of the other operating conditions (RH, FS, T, P...) on the activation kinetics is studied. Badly chosen operating conditions can lead to a relatively quick performance stabilization, from which it could be wrongly assumed that the cell has fully been activated (see section 4.1.1 of chapter 1).

The absence of clear knowledge regarding ionomer break-in durations and evolution laws, as well as uncertainties of the ionomer sorption equilibrium [135], [136] or diffusivity [20] values are pointed out. Consequently, multiple assumptions were used to set up the polymer water transport equations and integrate the activation mechanisms. Additionally, the activation of the polymer pathways in the catalyst layer has not been considered separately, even though it may differ from the membrane break-in kinetics. Regardless, the model provides clear indications on the sensibility of different operating conditions on ionomer activation kinetics. In chapter 4, this model will be used to aid in the definition of fuel cell activation protocols. Comparing the simulations with the experimental data will also provide feedback for future model improvements (additional features, increasing precision, etc.).

Chapter 3: Fuel cell break-in Diagnosis: creation of experimental database for useful information extraction and development of diagnosis tool

1 Ambitions/purpose

In the quest to optimize the fuel cell activation process, the analytical model established in the previous chapter can be used to replace excessive costly trial-and-error experimental applications. However, as previously stated, the current lack of knowledge regarding fuel cell break-in implies that simulations of the activation process remain relatively uncertain and incomplete. One can thus not solely rely on an analytical fuel cell model to fully optimize an activation protocol and ensure that it does not degrade the cell. Therefore, additional qualitative monitoring and characterization of experimental break-in data is needed [66].

In the first chapter of this manuscript, a certain number of advanced fuel cell characterization methods have been put forward, to better monitor, understand and optimize activation protocols. There are however a number of complexities involved when using these methods during break-in. Apart from their time consuming character, characterization by EIS, CyV and PolCurves also break-in the cell (thus affecting its performance). Consequently, they cannot be used in a straightforward way to determine the “state of activation” of the cell during break-in [24]. To a certain extent, characterization can be accelerated for some parameters (EIS at fixed frequency, current intercept method, etc.), but it still disturbs the activation process. Furthermore, in the literature, electrochemical analysis has previously provided contradictory results (e.g. ECSA evolution [28], [85]). Therefore, to characterize fuel cell break-in, a combination of methods must be applied to provide complementary information, and redundance. As an example, Silva *et al.* carried out a thorough analysis of the MEA activation procedure, using multiple electrochemical characterization methods [85]. In their tests, it is actually the electrochemical characterization of the MEA that activates it.

Other “non-intrusive” solutions exist to monitor the impact of the activation process on fuel cell degradation. Indeed, many efforts have been taken in the literature to develop such a tool, capable of determining if a fuel cell is in “faulty” operation (possibly leading to degradations). This is commonly called fuel cell “diagnosis”, which uses characteristic features in the experimental data to detect and identify faulty conditions [146]. It is especially relevant to implement a tool of the sort on an activation bench, as many metrics (e.g. temperature, pressure, relative humidity) are typically measured and available (unlike a fuel cell vehicle, to limit the cost/weight [147]). By implementing this data monitoring tool, fuel cell ageing may be prevented during break-in. The same methodology may also be applied to monitor the evolution of the activation process itself. This could be achieved by associating characteristic features to the morphological changes occurring during break-in (see section 2 of chapter 1). Indeed, even though break-in kinetics greatly depend on cell materials, design, etc. the characteristic signatures in its experimental data may be universal (similar to traditional diagnosis, to detect and identify faults). The development of a diagnosis tool that can quantify the “state of activation” during break-in, is the main subject of this chapter.

2 Diagnosis tool principle, structure, and adaptation to the break-in process

In this section, the general functional principle of a fuel cell diagnosis tool, and the range of methodologies provided by the literature are firstly presented. Secondly, a novel diagnosis tool adapted to the break-in process is proposed, and its structure and objectives are introduced.

2.1 Presentation of fuel cell diagnosis principle and selection of diagnosis method

The objective of a fuel cell diagnosis tool is to investigate the PEMFC state of operation in a non-intrusive manner. This type of methodology is commonly applied to detect and identify faulty cell operation (faulty being conditions that could lead to degradations). For this, useful information is extracted from the experimental fuel cell data measurements (e.g. voltage, pressure, temperature) and analysed to identify specific patterns. Using these patterns, which can for example be images of faulty cell conditions (e.g. drying, flooding), a diagnosis tool can translate the raw experimental data into a fuel cell state of health. With this information, corrective actions may be taken to mitigate premature fuel cell degradation (if necessary) [148].

Many fuel cell diagnosis processes exist. They are dissociated into two categories, which are the model based [149] and non-model based [146] methods (see FIG. 3.). As their name suggests, model based approaches consist of applying a residual analysis between a healthy fuel cell model output and the measured experimental data [150]. With non-model-based methods, signature characteristics within the fuel cell output data are directly analysed to determine the PEMFC state of health. The non-model-based signal processing methods are the focus of this chapter. Indeed, no viable solutions currently exist among the model-based methods for our application. Black box models for example require a vast amount of experimental data, whilst equivalent circuit models rely on EIS curves (which would alter the stack performance during break-in). Other grey box models that simulate fuel cell activation currently remain too uncertain (see chapter 2).

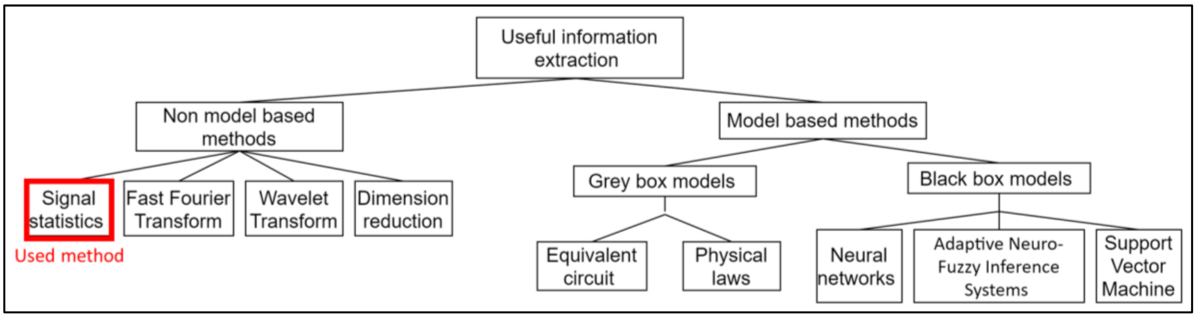

FIG. 3.1. SCHEMATIC SUMMARY OF THE DIFFERENT USEFUL INFORMATION EXTRACTION METHODS [151]

Among the non-model based diagnosis methods (see FIG. 3.), the statistical analysis variant [152] will mostly be used in this chapter. Indeed, Fast Fourier Transform [153] or Wavelet Transform [154] approaches require a high resolution signal, but the data acquisition frequency of an activation bench is often limited. The dimension reduction method is most often dedicated to cases where the data feature storage capacity is limited (e.g. for embedded applications). This is not the case on an activation bench, as there are no specific limitations regarding the number of available sensors or the computing power of an embedded calculator. Now that the functional principle of fuel cell diagnosis has been presented, and an associated methodology has been selected, the structure of the diagnosis tool applied to fuel cell break-in may be presented.

2.2 Presentation of fuel cell break-in diagnosis tool structure

As previously stated, fuel cell diagnosis tools are typically applied to detect/identify faulty conditions. During break-in, it is essential to do so (presented in further detail in subsection 2.3). More importantly however, as stated in section 1, the main objective of this chapter is to quantify the evolution of the break-in process itself using the signal-based diagnosis methodology. As seen throughout the literature being in faulty conditions greatly affects the stack behaviour [155]. Thus, before attempting to measure the fuel cell activation state using the raw experimental data, one must ensure that the stack does not operate in faulty conditions (in this order). If faulty conditions exist, corrective actions must be taken (actions whom are also vastly studied in the literature [156], and thus not treated further in this chapter) to bring the stack back to nominal operation. Afterwards, the "state of break-in" may be evaluated. The two layers of a complete fuel cell activation diagnosis tool (to detect/identify faults and quantify break-in evolution) are shown in Fig. 3.2.

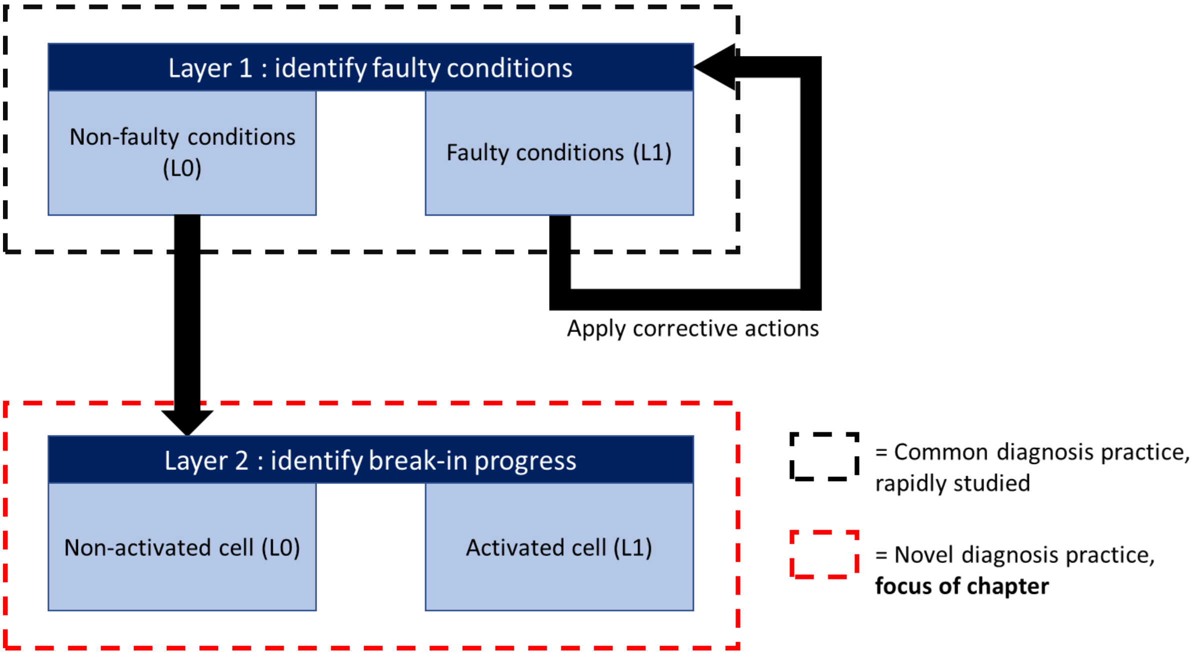

Fig. 3.2. Complete two-layer fuel cell break-in diagnosis tool

The first layer of the 2-layer diagnosis tool presented in Fig. 3.2 (diagnosis to detect and identify faults), is widely studied the literature, and therefore not developed in this chapter. This said, as (to our knowledge) no fault identification diagnosis methods have ever been applied during fuel cell activation, its correct operation during this process is rapidly verified (section 2.3). The second layer, which has the novel purpose of identifying the fuel cell break-in process progress, has fully been developed. It is introduced in section 2.3 and its detailed development process is described throughout the following sections.

2.3 Diagnosis to detect and identify faulty conditions during break-in (layer 1 of Fig. 3.2)

During fuel cell operation, faulty conditions may occur and result in one or multiple degradations. This is especially true during fuel cell activation, as more and more protocols use "exotic" and variable operating profiles (current, pressure…) in the aim to accelerate break-in [18], [24], [87]. Detailed studies and exhaustive lists of all the faulty conditions, as well as associated reversible and irreversible degradation mechanisms within a PEM fuel cell are provided in the literature [157]. The main faulty conditions within a PEMFC are cell drying, cell flooding, starvation, and poisoning [157]. Many fuel cell degradation mechanisms exist, and concern all cell components (membrane, CLs, GDLs, BPs and sealing gaskets) [158].

This said, not all conditions which are traditionally considered as faulty and leading to degradation mechanisms are considered as unfavourable or harmful during break-in. Indeed, as seen in the first chapter of this manuscript, some “degradation” mechanisms (e.g. carbon support corrosion [27], CO poisoning [80]), are promoted to accelerate the break-in process. Similarly, operating conditions that are typically avoided to prevent any possible degradation (e.g. potential variation [18], condensation [143]) are also applied during activation. Two degradation mechanisms must however always be prevented during break-in, and are also the most likely ones to occur. They are excessive stack flooding (leading to starvations, which can be especially harmful at the anode), and stack dehydration. On one hand, monitoring stack dehydration is essential to prevent membrane drying (pinholes/cracks formation, ohmic resistance and permeability increase, etc.) [159]. On the other hand, excessive GDL/CL flooding may result in anode and cathode starvations (Pt dissolution and carbon corrosion) [160].

The literature provides a number of statistical features associated to these two faults [146], [161]. However, during break-in, the fuel cell voltage (of individual cells and on a stack level) increases and varies in a “non-nominal” manner (nominal being post-activation operation). The morphological changes occurring during activation may further induce the behaviour of the stack, and affect the statistical data features related to faulty conditions. Therefore, the ability of the statistical features from the literature to correctly represent flooding/drying during the break-in process (feature “compatibility” with the fuel cell activation phase) must be verified. In the following subsections, the statistical features related to flooding/drying are presented, and the similar stack response to these faults during break-in is verified experimentally.

2.3.1 Fuel cell dehydration

Fuel cell dehydration is a faulty condition that may be caused by a number of malfunctioning components during the PEMFC’s lifetime (humidifier, compressor, cooling system, etc.). During break-in, the single most likely cause of cell dehydration on which all the attention must be focused, is stack overheating. Indeed, high temperature [57] and variable load [62] (and thus variable heat production) fuel cell operation is promoted during activation. Stack-overheating-related fuel cell dehydration can be identified through a drop of the center cell voltages, as they are the furthest away from the thick end plates, which are cooled by convection [162]. Consequently, the statistical features related to this fault are the ones that quantify the cell voltage distribution characteristic (such as the standard deviation or skewness equations) [163]. The specifications of the main existing statistical features are detailed later on in this chapter (section 4.2).

FIG. 3.3 illustrates the impact of this faulty condition on the PEMFC operation, by displaying an overheated (and thus dehydrated) fuel cell voltage profile (during activation). This test has been carried out on a GEN1 fuel cell stack (10 cells), and on the TB07 test station (FIG. 3.10). All specifications of this stack and testbench are provided in the fourth chapter of this manuscript (dedicated to the experimental break-in applications). For this example, the stack is overheated at over 10°C above its nominal temperature of 82°C (at the cooling output), and elucidates the clearly identifiable pattern within the cell voltage data. This figure confirms that the stack has the same response to drying during break-in, and that the traditional statistical features may thus undoubtedly be used to detect this fault.

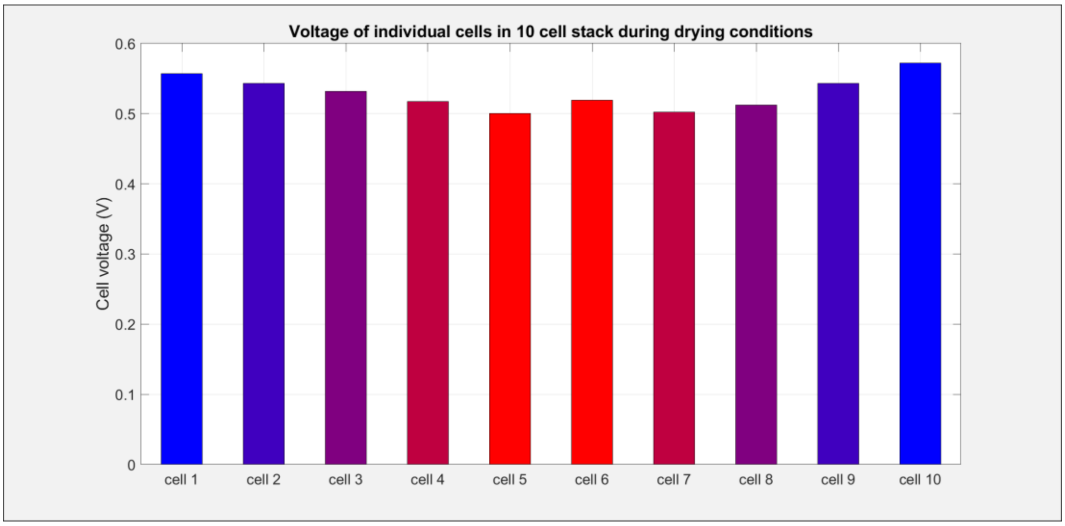

FIG. 3.3. EXAMPLE OF FUEL CELL DRYING IMPACT ON CELL VOLTAGE GRADIENT WITHIN THE STACK (APPLIED ON GEN1 FUEL CELL STACK, DURING BREAK-IN AT 1.5A.CM^{-2})

2.3.2 Fuel cell flooding

As for fuel cell dehydration, cell flooding may (among other reasons) traditionally be caused by humidifier, compressor, or cooling system malfunctions during its lifetime. When activating a fuel cell, the presence of liquid water within the cell is not prevented, but promoted (to accelerate the break-in process [60]). This said, the transition point at which the abundant presence of liquid water hinders reactant diffusion and consequently starves the cell must not be reached.

Regardless of the event responsible for cell flooding, this fault can be identified (at the anode and/or cathode) through the pressure gradient between the fuel cell gas channel input and output. On one hand, the pressure losses within the stack increase [164], and on the other hand, the “noise” of the signal increases. The amplitude of the pressure losses and fluctuations, depend on the severity of the flooding process. If cell flooding results in H_2 and/or air starvation(s), a similar fluctuating pattern will appear within the cell voltage data, accompanied by an overall stack voltage drop [165]. Once again, the voltage fluctuations and drop increase with the severity of the starvation process. Therefore, statistical features which represent this fault are for example the mean amplitude of the total pressure losses, and the amplitude of the pressure fluctuations. In case of severe flooding (leading to starvations), the same features may be applied to the stack voltage data. As the absolute values of these features increase with the severity of cell flooding, different intermediate degrees of flooding are typically identified [15].

FIG. 3.4 displays the pressure gradient between the input and output of a flooded anode, during the activation of a GEN1 stack (11 cells) on the B057 testbench (see chapter 4). Here, anode flooding is provoked by insufficient stack heating (over 10°C below its nominal temperature of 82°C), combined with the injection of water-saturated reactants (100% RH). This figure confirms that the stack has the same response to flooding during break-in, and that the traditional statistical features may thus also be used to detect this fault.

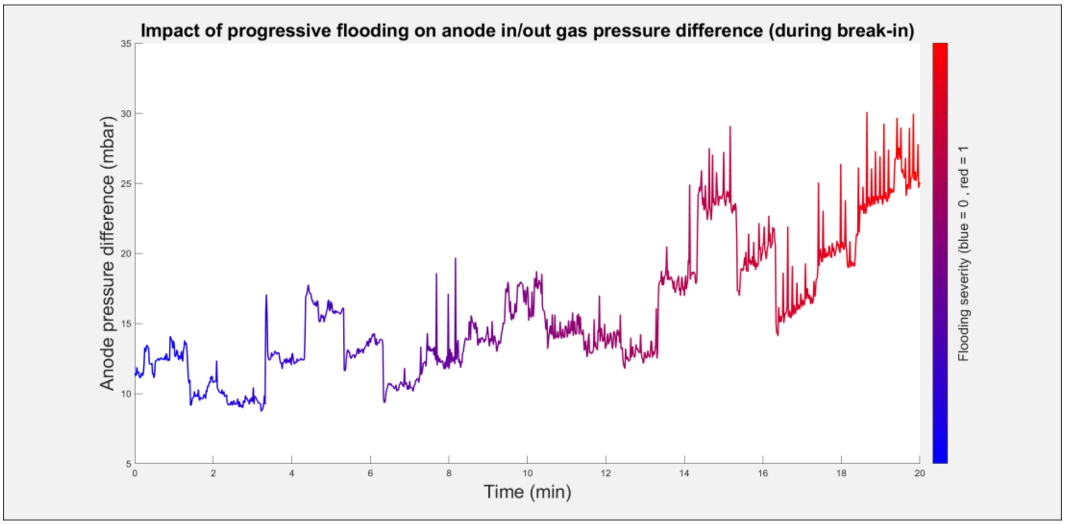

Fig. 3.4. Example of progressive fuel cell flooding impact on pressure difference between anode input and output (applied on GEN1 fuel cell stack, during break-in)

To sum up, the stack behaviour and response to drying and excessive flooding has proven to be the same during break-in as for normal operation (post-activation). Traditional statistical diagnosis methods and features are thus adapted to determine the main faulty conditions that may occur during break-in. In other words, diagnosis tools provided by the literature can directly be implemented on an activation bench to successfully prevent degradations (layer 1 of Fig. 3.2). As many diagnosis tools (to find faults) exist in the literature, [146], [6], [149], this subject is not treated further in this chapter. Instead, as stated in the abstract of this manuscript, the main focus of this chapter is to develop a diagnosis tool that is capable of monitoring the “state of activation” of the fuel cell (layer 2 of Fig. 3.2). This concept is introduced in the next subsection.

2.4 Diagnosis to determine the evolution of the break-in process (layer 2 of Fig. 3.2)

As stated in section 2.1, the non-model-based statistic diagnosis approach has been selected to develop the break-in diagnosis tool that is presented throughout this chapter. Consequently, similar to the process used to detect and identify faults, the evolution of the break-in process is determined, using characteristic features within the fuel cell data. More specifically, the morphological changes occurring in the fuel cell during its activation process must be linked to specific patterns within the experimental data. Contrary to the data features related to faulty conditions, signature characteristics related to break-in morphological changes are not available in the literature. Thus, to be able to monitor the “state of activation”, one main challenge and objective of this chapter is to determine and quantify statistic features related to the break-in process.

Ideally, the diagnosis tool should be capable of tracking the evolution of each dissociated morphological change related to fuel cell break-in. With this, an end-of-break-in criterion could be specified for each dissociated mechanism. This would result in a much more precise criterion than the ones who are currently used (see section 4.1.1 of chapter 1). Identifying each specific morphological change related to break-in is however complex, as there are a large number of them (see Table 1.2 of chapter 1), and they remain more or less theoretical. Therefore, the activation mechanisms have been regrouped into three main categories (according to a similarity criterion). Additionally, only the “electrochemical” break-in mechanisms are considered, as no compression/decompression cycles are applied to the stack. Thus, “mechanical” break-in does not take place (see section 2.3.1 of chapter 1). The three fuel cell break-in categories (englobing all morphological changes) to identify are detailed in the following subsections.

2.4.1 Ionomer activation

The first break-in category, entitled “ionomer activation” is centred around the polymer and englobes all structural changes related to its break-in process. This corresponds to the membrane hydration, structure change, surface skin rearrangement, and decontamination (see TABLE 1.2 of chapter 1). It also takes account for the polymer hydration within the CL. This category is thus mostly related to the processes induced by the introduction of water within the cell. As seen in section 2 of chapter 1, the polymer hydration is the mechanism which has the most profound effect on the FC performance (and most likely on its behaviour).

2.4.2 Catalyst layer pore structure activation

This second category is dedicated to one morphological change, which is the CL pore opening effect (and the associated evacuation of residues and non-anchored impurities from the cell). No other structural changes are associated to this mechanism as it is the only one induced by high cell pressure and flowrate.

2.4.3 Catalyst activation

The last category is mainly dedicated to the catalyst. It englobes the decontamination of the catalyst surface (desorption and evacuation of oxides/impurities) and the reorganization of the catalyst structure. In addition, the carbon support oxidation mechanism is also placed in this category, for its similarities with the oxidation of the catalyst surface species. The COR is however considered as having a negligible effect on cell performance (and thus its behaviour), relative to the catalyst structural changes (section 2 of chapter 1).

Now that the parameters to monitor by the break-in diagnosis tool have been selected, characteristic features related to each set of activation mechanisms (subsections 2.4.1 to 2.4.3) must be determined. The process that is used to detect and identify characteristic features within experimental data starts with the creation of a specific database, that contains the discernible useful information. Generating this “useful information database”, is the subject of the following section.

3 Experimental campaign to generate database for break-in diagnosis

This section is dedicated to the presentation of the experimental campaign, used to generate the “useful information database”. Firstly, the utility and purpose of this database is rapidly elucidated, followed by the presentation of the protocol used to generate this specific data. Secondly, the test plan, used equipment and experimental applications of this protocol are put forward.

3.1 Preparation of protocol, used to extract useful information

As previously stated, in order to determine characteristic features, the “useful information database” must first be generated. The specificity of this database is that the condition in which the stack operates is known (in other words, the data is "labelled"). For traditional diagnosis (to detect/identify faults), this consists of running the stack in nominal conditions during a certain period of time, followed by the deliberate generation of one specific faulty condition (FIG. 3.5). The comparison of the data where the fault is known, to data in normal conditions is used to determine the characteristic features of that fault. This process is applied once for each faulty condition within the stack, in order for them to be dissociable. A similar approach may be used to generate a learning database, whose purpose is to determine characteristic data features, representative of each set of activation mechanisms (2.4.1 to 2.4.3)

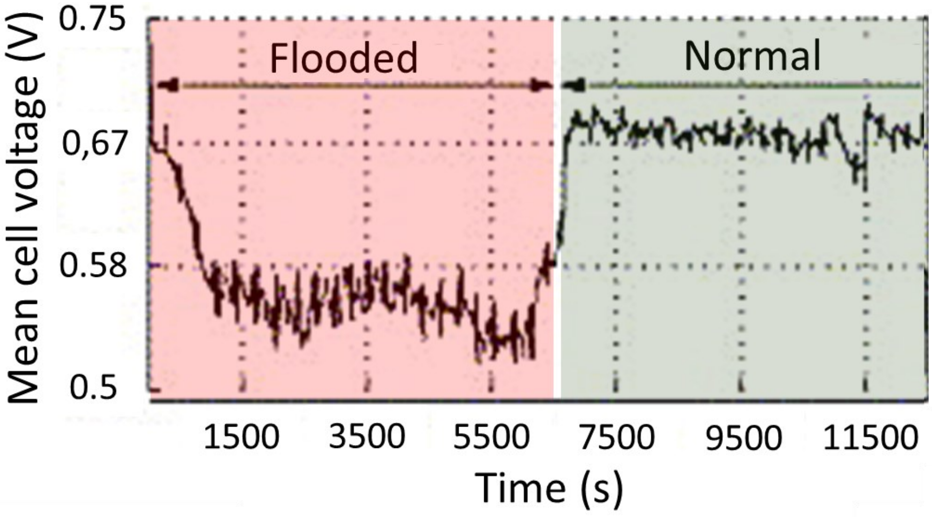

FIG. 3.5. TYPICAL USEFUL INFORMATION DATABASE FOR (SIGNAL BASED) DIAGNOSIS TO DETERMINE CHARACTERISTIC FEATURES OF FAULTY OPERATION [166]

As for typical useful information databases (to detect and identify faulty conditions), there must be one database per set of fuel cell activation mechanisms (subsections 2.4.1 to 2.4.3). In other words, each set of activation mechanisms (ionomer/CL pore structure/catalyst) must occur separately. Additionally, each database must be divided in two portions, one being the "activated" portion and another being the "non-activated" portion (similar to "faulty"/"non-faulty" conditions). The protocol, for which each set of break-in mechanisms occurs separately, and fully goes from "non-activated" to "activated", is presented in FIG. 3.6.

In the test plan of FIG. 3.6, the ionomer is progressively activated in a first step (~80 to 250min), followed by the CL pore structure (~315 to 345min), and the catalyst (~380 to 590min). The duration of each step corresponds to the time required for the cell performance to converge during that step (after which the fuel cell activation mechanisms is considered to be completed). The main data of interest for the diagnosis tool is however not the one during each step, but more so the portions of data before and after each step. Indeed, the data measured before and after each step correspond to the "non-activated" and "activated" sections, respectively (e.g. non-activated ionomer/activated ionomer for step 1).

The learning database for the diagnosis tool (non-activated/activated data), should ideally be measured for a vast range of operating conditions, and for a long stabilization time per set of operating conditions. Similarly, one should also ideally have intermediate labels (e.g. partly activated ionomer). With a vast range of available data, more precise features can be determined, to thus better monitor the break-in process. However, in the case of fuel cell activation, this would result in distorting the measured data, as the measurements themselves simultaneously break-in the cell [24]. The chosen compromise for this test plan is to put the cell through a reduced range of stabilized current points, only once before and after each activation mechanism. As shown on FIG. 3.6, its profile is similar to an upwards PolCurve, but with less steps, a shorter stabilization time per step, and a lower peak current (as cell performance remains limited during break-in).

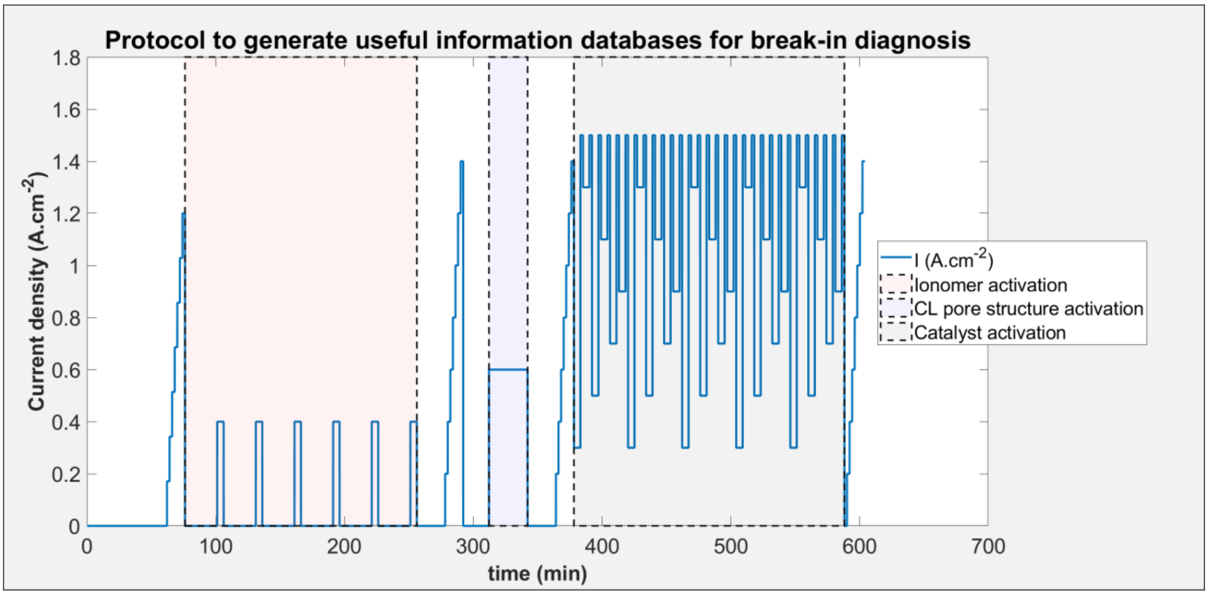

FIG. 3.6. CURRENT PROFILE OF BREAK-IN PROTOCOL TO GENERATE USEFUL INFORMATION DATABASES FOR IONOMER ACTIVATION, CL PORE STRUCTURE ACTIVATION AND CATALYST ACTIVATION

Ideally, there should also be one database per situation (non-activated/activated), for the 3 different categories of morphological changes. This would result in $2^3 = 8$ total possibilities, and 8 total databases (8 variants of the protocol shown in FIG. 3.6, where for each variant, two or more steps are permuted). It is however impossible to obtain the database for most "hybrid labels" (e.g. non-activated ionomer/non-activated pore structure/activated catalyst). Indeed, the catalyst activation protocol also acts on the pore opening effect, as well as the hydration of the ionomer. The pore opening and ionomer hydration steps can be inverted to a certain extent, as the pore opening step is of short duration and carried out at low RH (see section 3.1.2). Therefore, as will be specified in section 3.2, a protocol where the pore opening and ionomer activation steps are permuted has been applied (to obtain 5 total databases). The 5 dissociated 'labels' are thus, for the ionomer, CL pore structure and catalyst activation: label 1 = 0/0/0, label 2 = 1/0/0, label 3 = 0/1/0, label 4 = 1/1/0, label 5 = 1/1/1, respectively. The numbers 0 and 1 correspond to "non-activated" and "fully activated", respectively. The specific precautions taken and operating conditions used to dissociate each step of the fuel cell break-in process are detailed throughout subsections 3.1.1 to 3.1.3.

3.1.1 Ionomer activation

This step has been inspired by the break-in process of Cho *et al.*, who dissociated the hydration of the ionomer from the rest of the activation procedure [58]. The polymer is mainly activated (zone 1 of FIG. 3.6) by circulating humidified nitrogen through the anode and cathode channels. During most of this step, no current is drawn from the cell, as it is known to affect the CL pore structure and the catalyst itself (impurity desorption and other structural changes). Every 25minutes, the stack is supplied with H_2 and O_2 and the current is adjusted in order to obtain a mean cell voltage of 0.65V, and held at this current value for 5 minutes. This step has multiple functions. First, it provides information regarding the stack performance, and thus the duration required for the ionomer to be fully activated (considered as fully activated when no more performance increase is observable). Periodically drawing current also aids to overcome possible sorption and domain spacing barriers (a proton flow may be required to beat these limitations [17], [21]). The value of the current density is chosen to remain in a voltage range between 0.65 and 0.75V, to prevent reaching reducing (or oxidizing) conditions which would desorb impurities from the catalyst. Consequently, the stack performance is evaluated whilst having minimal impact on the catalyst activation structural changes.

To further avoid affecting the CL porosity, the ionomer activation step is carried out at the lowest admissible gas pressure (1barabs + pressure losses). The gas flowrate is also limited (equivalent to the nominal mass flowrate of reactants at 0.5A.cm^{-2}). Once again, to prevent opening the CL pores and affecting the catalyst structural changes by increased molecular activity, the stack temperature is limited to 70°C. Low temperature operation also aids in the hydration of the polymer when drawing current, as more of the produced water condenses. The (anode and cathode) gas input relative humidity is set to 75%. This value has been chosen as a compromise to promote the hydration of the ionomer whilst preventing cell flooding (faulty conditions result in unusable data, see section 2.3). FIG. 3.7 summarizes the ionomer activation step.

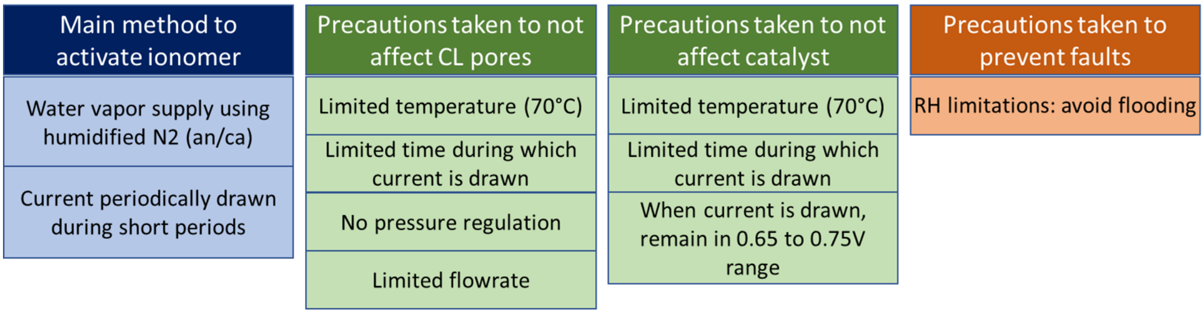

Main method to activate ionomer	Precautions taken to not affect CL pores	Precautions taken to not affect catalyst	Precautions taken to prevent faults
Water vapor supply using humidified N2 (an/ca)	Limited temperature (70°C)	Limited temperature (70°C)	RH limitations: avoid flooding
Current periodically drawn during short periods	Limited time during which current is drawn	Limited time during which current is drawn	
	No pressure regulation	When current is drawn, remain in 0.65 to 0.75V range	
	Limited flowrate		

FIG. 3.7. SUMMARY OF METHOD AND OPERATING CONDITIONS USED DURING IONOMER ACTIVATION STEP

3.1.2 Catalyst layer pore structure activation

Catalyst layer pore structure opening is induced (zone 2 of FIG. 3.6) mainly by operating the stack at an elevated pressure and cathode gas flowrate. The (anode and cathode) gas pressure, set at the maximum admissible value of 2.5barabs increases the force applied by the gaseous species in the CL channels, to accelerate the pore opening rate. Simultaneously, the cathode stoichiometry is set at 4. The elevated cathode stoichiometry/flowrate has two functions. Firstly, it counterbalances the operating conditions which induce cell flooding, which are the elevated reactant pressure and reduced temperature (set at 70°C, to prevent affecting the catalyst structural changes). Secondly, it favours the evacuation of unanchored particles from the porous structure. The anode CL pore opening effect during break-in is considered as negligible relative to the cathode side (as the anode CL is thinner, contains less Pt, and has fewer reaction rate and mass transport losses). Additionally, the anode is much less prone to flooding. Consequently, the anode stoichiometry is maintained at its nominal value (of 1.5) to avoid unjustified excessive hydrogen consumption.

As for the previous step, the mean cell voltage is maintained in a specific range (0.65 to 0.75V) which prevents catalyst decontamination and other structural changes (reaching oxidizing and reducing conditions).

During this step, input RHs at the cathode and anode gas channels have been set to 50%. With these setpoint, according to the mass conservation principle, there are no cell drying or flooding risks near the reactant input and output zones, respectively. The CL pore opening step is summarized in FIG. 3.8.

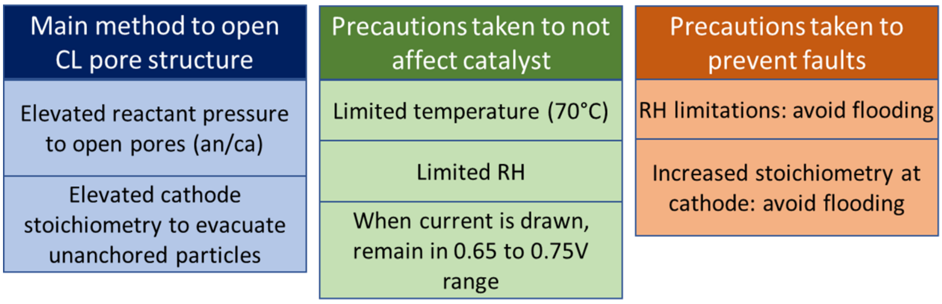

Main method to open CL pore structure	Precautions taken to not affect catalyst	Precautions taken to prevent faults
Elevated reactant pressure to open pores (an/ca)	Limited temperature (70°C)	RH limitations: avoid flooding
Elevated cathode stoichiometry to evacuate unanchored particles	Limited RH	Increased stoichiometry at cathode: avoid flooding
	When current is drawn, remain in 0.65 to 0.75V range	

FIG. 3.8. SUMMARY OF METHOD AND OPERATING CONDITIONS USED DURING CL PORE OPENING STEP

3.1.3 Catalyst activation

The catalyst is activated by operating the cell under a large voltage range, and at an elevated gas flowrate, RH, and cell temperature. As previously stated, this activation step must remain in last position (zone 3 on FIG. 3.6), as its operating conditions would inevitably open the CL pore structure and hydrate the ionomer. The catalyst is decontaminated, and its structure is reorganized by reaching different current levels, to oxidize/reduce all impurities (per 0.2A.cm^{-2} iso-current increments, each lasting 5 minutes). All 5-minute iso-current steps are separated by a 2-minute high current step (1.5A.cm^{-2}, limited by cell performance during break-in). The high current step evacuates the desorbed impurities, induced by the elevated water production rate and gas flowrate. This cycle is repeated until the performance is stable between two steps at 1.5A.cm^{-2}.

Additionally, the evacuation rate of the desorbed impurities with the reactants flow is enhanced by increasing the reactants flowrate/stoichiometry to 1.9 and 2.5 at the anode and cathode, respectively. This high flowrate, coupled to elevated reactant pressures (2barabs anode/cathode) also prevents reactants starvations on both sides. Once again, this faulty condition (caused by the dynamic current variation and elevated humidity conditions) would result in non-usable data. Similarly, the temperature is set at its nominal value (80°C), to promote the impurity desorption rate, whilst avoiding reaching drying conditions. As for the previous step, the input RH at the cathode and anode gas channels is set to 50%. With this value, the flow of humid reactants promotes the evacuation of desorbed catalyst impurities, whilst preventing cell flooding (equivalent cathode output RH equal to ~100%.). FIG. 3.9 summarizes the catalyst activation step.

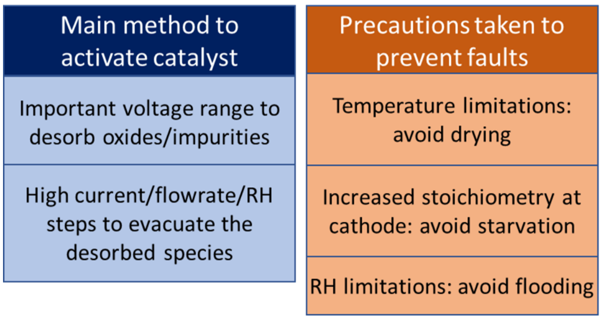

Main method to activate catalyst	Precautions taken to prevent faults
Important voltage range to desorb oxides/impurities	Temperature limitations: avoid drying
High current/flowrate/RH steps to evacuate the desorbed species	Increased stoichiometry at cathode: avoid starvation
	RH limitations: avoid flooding

FIG. 3.9. SUMMARY OF METHOD AND OPERATING CONDITIONS USED DURING CATALYST ACTIVATION STEP

Now that the specific protocol, adapted to the extraction of useful information (related to the fuel cell activation mechanisms) has been defined, it must be tested. The test plan and experimental applications of this protocol are specified throughout the following subsection.

3.2 Test plan and experimental applications of protocol

To generate the experimental data of the "useful information database", the protocol presented in FIG. 3.6 has been applied on a test station (typically dedicated to fuel cell characterization), provided by the FClab. This testbench is suitable, as it has the ability to reach an important range of operating conditions, whilst monitoring all main fuel cell operating parameters (cell/stack voltage, temperature, pressure, etc.). FIG. 3.10 provides the P&ID of the test station. This testbench (interface, control, etc.) is presented in further detail in the fourth chapter of this manuscript, which is fully dedicated to the experimental break-in applications.

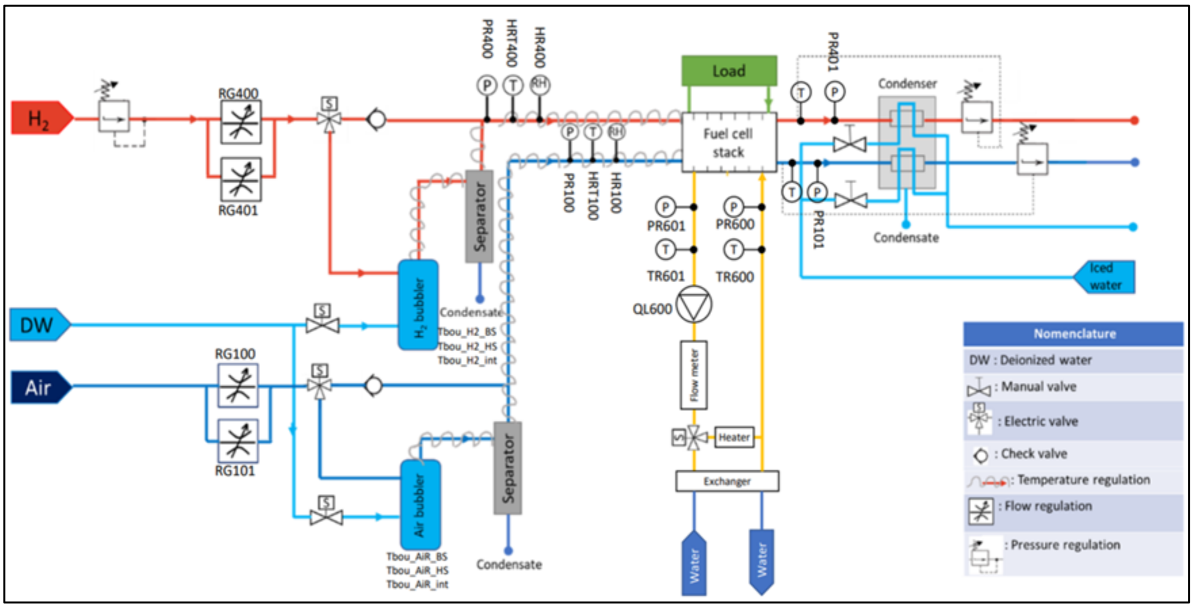

FIG. 3.10. FCLAB TEST STATION (REFERENCE: TB07) PIPING AND INSTRUMENTATION DIAGRAM (P&ID)

The protocol presented in FIG. 3.6 has not been applied only once on a single fuel cell, but multiple times on a variety of fuel cell stacks. This increases the amount of available data from which to subsequently extract useful information (features). Additionally, for each new experimental application, one or multiple parameters of the protocol and/or used fuel cell were varied (see TABLE 3.). The gathered data for each additional test further feeds the useful information database, in the aim to generalise the diagnosis tool to a broader range of fuel cells and conditions. To obtain data, representative of fuel cells dedicated to automotive applications, large surface (1:1 scale) stacks are used. Only the number of cells per stack is not representative of the ones that will be mass produced, for cost related reasons (fuel consumption, production cost per cell etc.). As for the TB07 test station, the stack specifications are presented in further detail in the fourth chapter of this manuscript. The applied test plan (used stack, protocol reference etc.) is summarized in TABLE 3..

Firstly, a "base" 10-cell Symbio GEN1 stack technology has been activated using the protocol presented in section 3.1. Thereafter, an identical stack technology, containing less cells (4 cells) has been activated using the same protocol, to elucidate the impact of this characteristic on the stack response. As previously stated, all activation mechanisms should ideally be permuted once, to obtain a total number of $2^3 = 8$ databases. For the reasons stated in section 3.1, only the pore structure and ionomer activation steps can be permuted. This has been carried out with the break-in process of a 5-cell GEN1 stack (P3 in TABLE 3.).

Ref.	Fuel cell Technology	Number of cells	Cell surface (cm^2)	Broken-in before test?	Activation mechanisms order of execution
P1	GEN1 (Symbio)	10	263	No	Ionomer/Pore structure/Catalyst
P2	GEN1 (Symbio)	**4**	263	No	Ionomer/Pore structure/Catalyst
P3	GEN1 (Symbio)	**5**	263	No	**Pore structure/Ionomer/Catalyst**
P4	GEN1 (Symbio)	5	263	**Yes**	Ionomer/Pore structure/Catalyst
P5	**Other (confidential)**	5	**190**	**Yes**	Ionomer/Pore structure/Catalyst

TABLE 3.1. TEST PLAN AND FUEL CELL SPECIFICATIONS

As stated in chapter 1 of this manuscript, PEMFC "conditioning" or "incubation" is related to the performance recovery of a fuel cell, which has not been used for a certain amount of time post-activation. In this test plan, a GEN1 fuel cell stack (5 cells) has been conditioned using this method. Its objective is to determine if stack "rejuvenation" has the same behaviour and signature characteristics as a stack during activation. Similar behaviour would confirm that the break-in and conditioning mechanisms are closely related, and activation protocols could be carried out periodically on a stack during its lifetime. Such a "rejuvenation" processes could consequently increase the overall fuel cell efficiency and lifetime. The final experiment within the scope of this test plan, consisted of conditioning a PEMFC from another manufacturer. This "edge case" test is applied to determine if it is still possible to identify similarities within experimental data provided by fully different stack technologies, and for different processes (break-in/conditioning).

As expected, for each test that has been carried out (break-in or conditioning), the stack performance gradually increased and converged. Additionally, the impact of the protocol on the final post break-in/conditioning stack performance has been evaluated for each test. For this, each stack has been subjected to a full PolCurve protocol (up to $1.9A.cm^{-2}$, using the TB07 test station), right after it had been broken-in or conditioned. This post-activation/conditioning PolCurve was compared to a refence curve of a fully activated stack (of the same technology). This comparison confirmed nominal losses in the reaction-rate region (superimposition of the PolCurves up to $\sim 0.2A.cm^{-2}$), but revealed a steeper slope in the ohmic region compared to the reference PolCurve. This difference of the slope (resulting in a 15 to 35mV lower voltage per cell at $1A.cm^{-2}$), is an indication of slightly incomplete ionomer activation. The N_2 hydration method (FIG. 3.7) may thus not be efficient enough to fully activate the ionomer. In this manuscript, the limitations of this method to activate the ionomer have been put forward in chapter 1 (section 3.2.3), considered in chapter 2 (ionomer break-in model) and will be confirmed in chapter 4.

Now that the essential experimental database, used for useful information extraction has been generated (and its limitations have been discussed), the break-in diagnosis tool development process may commence. The entire procedure to develop this diagnosis tool is detailed throughout the next section.

4 Break-in diagnosis tool development process

As previously stated, developing a diagnosis tool includes translating the raw experimental data (e.g., voltage, pressure, temperature) which is known to contain useful information, into clear exploitable useful information. In other words, characteristic features associated to each category of break-in morphological changes are determined, by identifying specific patterns in the experimental data [146]. As illustrated in Fig. 3.11, identifying these features is however only one step of the entire diagnosis tool development process.

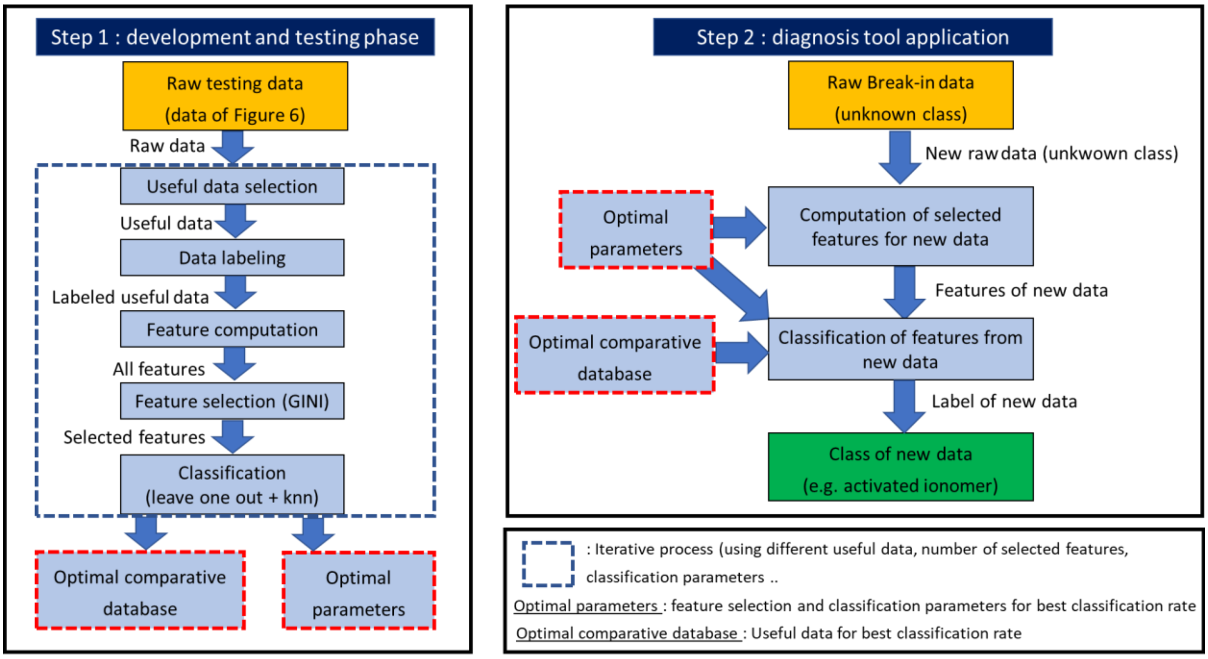

FIG. 3.11. FUEL CELL BREAK-IN DIAGNOSIS TOOL DEVELOPMENT PROCESS (STEP 1) AND APPLICATION (STEP 2)

As shown on Fig. 3.11, the development process of the fuel cell break-in diagnosis tool consists of (i) selecting the useful data within the measurements provided by the protocol presented in Fig. 3.6, (ii) labelling (activated/non-activated) the selected useful data, (iii) calculating a large number of statistical features from the labelled useful data, (iv) selecting only the best features from all the ones that have been computed (v) developing and testing a classification algorithm, capable of affecting labels (activated/non-activated) to new data, by comparing it with the features of the labelled data. Steps (i) to (v) are applied multiple times, using different data selection/feature selection/classification parameters (iterative process). Only the best parameters will be selected for the final fuel cell break-in diagnosis tool (step 2 on Fig. 3.11).

As for the ionomer activation model (presented in chapter 2), the break-in diagnosis tool has entirely been coded using Matlab™. This code has been developed with the help of Julie AUBRY, a PhD student affiliated to the FClab and to Symbio, specialized in PEMFC diagnosis methods. The detailed development procedure of the break-in diagnosis tool is further specified throughout the following subsections.

4.1 Selection and labelling of useful data

As previously stated, the development process of the break-in diagnosis tool starts with the selection of the useful data, following by the assignment of labels to this data. This step can typically be tedious (when detecting and identifying faults) [167], but not for the database dedicated to fuel cell break-in (presented in section 3). Indeed, the data to select (for all databases of TABLE 3.) as "useful data" are simply known to be the pseudo-PolCurves drawn before and after each activation step (FIG. 3.6). Furthermore, the "non-activated" and "activated" labels can simply be affected to the pseudo-PolCurves before and after each activation step, respectively (resulting in 5 total labels, see section 3.1).

The only parameter which is slightly more tricky to determine is the current density value(s) to choose for the useful data (which must ideally be at iso-current). Multiple iso-current values from the learning database (see pseudo-PolCurves) have been labelled and tested (using automated Matlab™ code). For each test, the same features have been calculated, and rated (using the process which is detailed in sections 4.2 to 4.3). Intuitively, one may expect the low current density region (reaction-rate losses) to be optimal to determine characteristic features of the catalyst activation, as it affects the ORR (see section 4.1.2 of chapter 1). Similarly, the ionomer activation and CL pore opening (reactant diffusion rate) features may theoretically stand out in the mid (ohmic) and high (mass transfer) current density regions, respectively. In practice however, one single current density region (corresponding to $I_{den} = 1 \pm 0.2$ A.cm^{-2}), has proven to provide the clearest, most useful experimental data, for all activation mechanisms. Consequently, for the rest of the diagnosis tool development process, only the useful data in this current density region is considered.

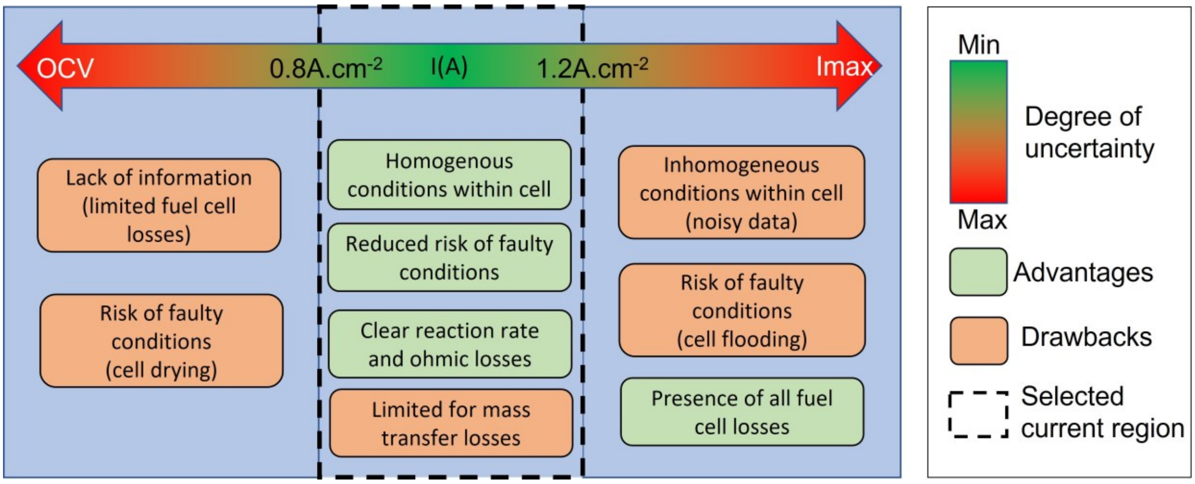

FIG. 3.12. ADVANTAGES AND DRAWBACKS OF DIFFERENT CURRENT INTERVALS, AS SELECTED USEFUL DATA

There are multiple reasons to explain why the 1 ± 0.2 A.cm^{-2} current interval provides the most useful data. As previously stated, when faults occur, the stack voltage signature is greatly affected, resulting in uninterpretable data (section 2.2). The risk of faulty conditions (e.g. flooding, starvations) increases with the current, as the conditions get more and more heterogenous within the cell. Similarly, a lower current (and consequently a reduced water production rate) increases the probability of stack drying. Additionally, at low current densities (near OCV), the fuel cell losses are limited, meaning that the effects of the break-in morphological changes are less pronounced. At elevated current densities, all losses are present, but the heterogenous conditions within the stack result in noisy data. Thus, the data at 1 ± 0.2 A.cm^{-2} provides the best compromise between data quality (noise, inhomogeneities…), and available information. FIG. 3.12 sums up the advantages and drawbacks of each current density region.

The final labeled useful data selection is stored as a matrix, containing all variable measurements (pressure, temperature, etc.). The following step, which is presented in the next subsection, consists of determining a certain number of features from this labeled useful data matrix.

4.2 Feature computation

As shown in FIG. 3.11, the process to determine characteristic features within the useful data consists of calculating a large number of features, to then select the ones that are related to the activation mechanisms. In many cases, the available variables to compute features is bound to a reduced number of metrics, as the number of sensors (e.g. pressure, temperature) are limited (e.g. in a fuel cell vehicle). This is not an issue on an activation bench (nor the TB07 test station of FIG. 3.10), where many cell operation parameters are monitored. The voltage of each individual cell/pack of cells can even be measured using a CVM (cell voltage monitoring) device. The main variables which are considered for the diagnosis tool are the anode and cathode (in/out) pressures, stack temperature (in/out), and the cell voltages. Other metrics (such as the gas input temperature, RH, etc.) are not used as they are not related to the stack behavior (only to the testbench control).

As stated in section 2.1, the features used to develop this break-in diagnosis tool are of a statistical nature. A number of frequential features have also been tested throughout this development process, without concluding results. This was to be expected, as the acquisition frequency of the TB07 test station (FIG. 3.10) is fixed to 0.66Hz. In other words, the available frequency band to analyse is limited from 0 to 0.33Hz, according to the Shannon sampling theorem [168]. Statistical feature computation is carried out on a temporal basis, but also between datasets at a fixed timestep (between cell voltages, between an/ca pressures, between in/out temperatures and pressures, etc.).

The statistical features computed between datasets can describe stack efficiency (dTstack), pressure losses (dPgas channels), membrane permeability, (dP an/ca), homogeneity between cells (dVcell), etc. More specific features of this nature have also been included. There is for example the standard deviation between the voltages of the cells located at the borders and the centre of the stack, to identify edge effects. Similarly, two features, which are the image of the pressure losses, but are independent of the flowrate, are computed. These features are the anode and cathode pressure losses, divided by their respective gas flowrates squared (as the pressure losses are proportional to this metric).

The statistical features which are calculated on a temporal basis describe the transient behaviour of a variable (or a combination of variables, such as for example dTstack). All the used time-dependent features, (which are computed for each data column), are listed below. The specific equation of each feature is not detailed in this section, but can be found in [169] :

- MEAN: Mean value of the signal/sample
- MEDIAN: Median value of the signal/sample
- STD: Standard deviation of the signal/sample
- VAR: Variance of the signal/sample
- RMS: Root mean square of the signal/sample
- MAX: Value of the maximum amplitude of the signal/sample
- MIN: Value of the minimum amplitude of the signal/sample
- PPV: Peak to peak value of the signal/sample

- SRA: Square root of amplitude of the signal/sample
- SKEW: Skewness of the signal/sample (measure of lack of symmetry)
- KURT: Kurtosis of the signal/sample (measure of the spikiness of the signal/sample)
- KURTF: Kurtosis Factor of the signal/sample
- CLF: Clearance factor of the signal/sample
- SF: Shape factor of the signal/sample (value of how much the shape of a signal is affected)
- IF: Impulse Factor of the signal/sample
- CF: Crest Factor of the signal/sample

To compute the time-dependent features for each variable, the "sliding window" process is used (see Fig. 3.13). This consist of selecting one data sample (also named window) of "n" values over a fixed time period, for which all time-dependent features are calculated. The "n" values for the window length (number of datapoints per sample) has been set to 5, as it has proven to provide the best results (iteratively tested using automated Matlab™ code). This window can also overlap to prevent outliers in the input data (see Fig. 3.13), but this did not provide better results (also tested through trial-and-error on Matlab™). Consequently, the sliding window process without overlap is used.

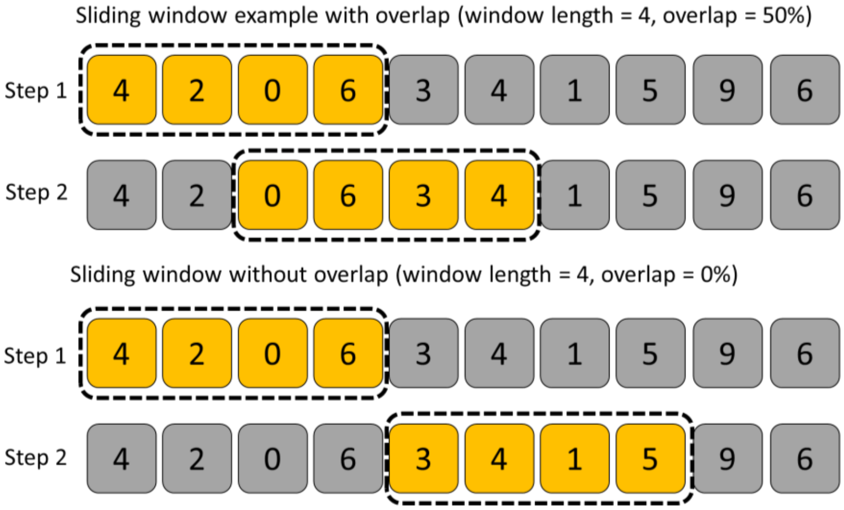

Fig. 3.13. Sliding window process, with and without overlap (for time-dependent feature computation)

Calculating all features (on a temporal basis and between variables at a fixed timestep) of the useful data results in a large feature data matrix (over 200 columns). Before selecting the best features from this matrix, all features are normalized so that each column has the same boundaries (between 0 and 1). Determining which features to select for the break-in diagnosis tool is the subject of the next subsection.

4.3 Feature ranking and selection

4.3.1 Presentation of feature ranking method

The main criterion according to which the data features will be selected, are their representativeness. In other words, the features must be the image of (and truly be related to) the morphological change(s) occurring during break-in. Only the "best" features (that fulfill this requirement at the finest level) must be considered.

Multiple methods exist to determine and select the greatest features [170]. Here, it is carried out using the GINI approach, which is used to quantify the impurity factor of a feature [151]. The feature impurity factor defines its level of representativeness (here of the break-in mechanism), and can vary from 0 (best case) to 1 (worst case). The GINI feature ranking method and associated equations are presented in FIG. 3.14.

	True class	
	Activated	Not activated
Feature on	True positive = TP	False positive = FP
Feature off	False negative = FN	True negative = TN

$$\boxed{\text{Impurity feature on} = 1 - \left(\frac{TP}{TP+FP}\right)^2 - \left(\frac{FP}{TP+FP}\right)^2}$$

$$\boxed{\text{Impurity feature off} = 1 - \left(\frac{FN}{FN+TN}\right)^2 - \left(\frac{TN}{FN+TN}\right)^2}$$

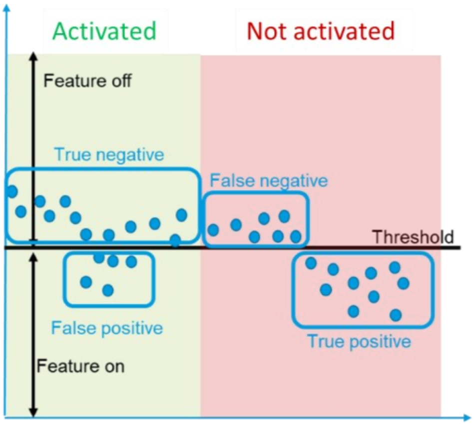

$$\boxed{GINI = \text{Impurity feature on} \times \frac{TP+FP}{TP+FP+FN+TN} + \text{Impurity feature off} \times \frac{TN+FN}{TP+FP+FN+TN}}$$

FIG. 3.14. EXPLANATION OF GINI CALCULATION METHOD TO DETERMINE FEATURE IMPURITY COEFFICIENT [151]

The GINI coefficients of the matrix of (200+) statistical features (section 4.2), that are based on multiple variables (time, cell voltage, pressure, temperature, etc.), are computed. By ranking the GINI results, the objective of the following subsection is to analyse and select the features that have the lowest impurity factor.

4.3.2 Feature ranking results and selection

As stated in section 3.1, there are 5 labels in total, related to the different possible combinations of "activation states" (e.g. non-activated ionomer/activated pore structure/non-activated catalyst). The impurity factor of a feature thus takes account for these 5 different labels. An additional analysis, consisting of determining the best features (lowest GINI scores) for each individual activation mechanism (2 labels) has also been carried out. This analysis has the sole purpose of determining if the morphological changes share the same greatest features (ideally they do not rely on the same features, for them to be easily dissociable from one another). From all the (200+) ranked features, a certain number of greatest features must be selected. For this, the classification rates (see next subsection), for different numbers of selected features has been computed (iteratively, using the developed Matlab™ code). According to these results, the "m" optimal number of chosen features is equal to 10. The best features, related to the 5 labels of the activation morphological changes, and for each dissociated activation mechanism, are presented in TABLE 3.2.

When analysing the feature ranking results of TABLE 3.2, one can distinguish an abundant presence of the cell voltage variable (good GINI coefficient). This was to be expected, as fuel cell performance evolves during break-in (and during conditioning). Another feature, which is the variance (or standard deviation) between cell voltages, also clearly reduces over time. Additionally, this feature is the most representative one for the ionomer activation process (better indicator than the mean cell voltage), as the proton conductivity of the cells converge. The cathode pressure losses (pressure difference divided by the flowrate squared) is also a characteristic feature. According to TABLE 3.2, this feature is also representative of the CL pore structure break-in. The pore opening effect may thus to a certain extent influence the overall pressure losses between the cathode gas inlet and outlet. A feature which is present in the catalyst activation ranking results, is the standard deviation between the anode and cathode input pressures. This may be caused by a more "stable" reactant consumption rate on the catalyst surface. This characteristic signature is however not present in the overall (5 labels) features, meaning that the catalyst activation measurements heavily depend on the absolute value of the cell voltage. This may result in poor classification rates (which will be analysed in the following section). Interestingly, the increase in stack efficiency (calory output reduction) does not have a sufficient impact on the cooling temperature gradient, to be identifiable through this metric.

Input useful data and labels	Top 10 selected features (with lowest GINI scores, among the 200+ features catalog)	Best GINI	Worst GINI	Mean GINI
All combinations of mechanisms (5 labels)	$Median \,\&\, Max(V_{cell\ max}), Mean \,\&\, Median(V_{cell\ mean}), Max \,\&\, Mean(V_{cell\ min}), Min(Std \,\&\, Var(V_{cell\ ext})), Max \,\&\, Median(dP_{ca}.Q_{ca}{}^{-2})$	0.191	0.373	0.246
Ionomer activation (2 labels)	$Min(Std \,\&\, Var(V_{cell\ ext})), Max \,\&\, Mean(V_{cell\ mean}), Max \,\&\, Mean(V_{cell\ min}), Min \,\&\, Max(V_{cell\ max}), Max(dP_{in\ an/ca}), Mean(dP_{an}.Q_{an}{}^{-2})$	0.227	0.379	0.307
Pore structure opening (2 labels)	$Sra \,\&\, Max(Std\ (V_{cell\ ext})), Max \,\&\, Median(V_{cell\ max}), Max \,\&\, Median(V_{cell\ min}), Max(V_{cell\ mean}), Max(dP_{ca}.Q_{ca}{}^{-2}), Std \,\&\, Ppv(dP_{out\ an/ca})$	0.326	0.387	0.361
Catalyst activation (2 labels)	$Max \,\&\, Min(V_{cell\ max}), Min \,\&\, Max(V_{cell\ mean}), Std \,\&\, Ppv(dP_{out\ an/ca}), Ppv \,\&\, Std(dP_{in\ an/ca}), Mean \,\&\, Median(V_{cell\ min})$	0.256	0.368	0.33

TABLE 3.2. BEST FEATURE RANKING RESULTS (10 SELECTED FEATURES), FOR ALL COMBINED MECHANISMS (5 LABELS) AND FOR EACH INDIVIDUAL ACTIVATION PROCESS (2 LABELS)

The resulting GINI coefficients clearly show patterns in the data, but their values are not ideal (close to 0). One must however note (section 3.2) that the used database is very diverse (with different number of cell stacks, different stack technologies, stack rejuvenation). To evaluate the impact of the diversity of the useful information database on feature impurity, an additional analysis has been carried out, by testing the same features for individual protocols (P1 to P5 of TABLE 3.). When applied to one single database (from one stack), lower GINI scores were generally obtained (mean GINI of ~0.1). This is explained by the fact that even if each individual stack shares the same representative features, they do not evolve at the same rate and amplitude (e.g. stack voltage during break-in versus rejuvenation). Consequently, using all stacks as input data inevitably results in a clear observable loss in feature representativity (higher GINI scores). What should also be noted is that the GINI is a feature-per-feature indicator. High individual GINI scores do not imply that the analysis of the combined features (carried out in the next subsection) cannot provide good results.

To further analyse features, matrixes of scatter plots are drawn by groups on XY curves, to obtain a general 2-dimensional translation of the combination of features. FIG. 3.15 illustrates this feature analysis procedure. In this example, two features (cell voltage standard deviation versus the mean cell voltage) are plotted for the ionomer activation step (2 labels) of a single database (P3, 5 cell GEN1 stack). This example provides a visual representation of what a good GINI coefficient (pure feature) looks like. Indeed, even though the STD feature contains two outlier data points (~0.78 and 1), the clear dissociation between the two labels is observable. One may thus rapidly conclude that the combination of these two features is very representative. As will be explained further in the next section, a classifier can view all features (along "n" features dimensions) at a time.

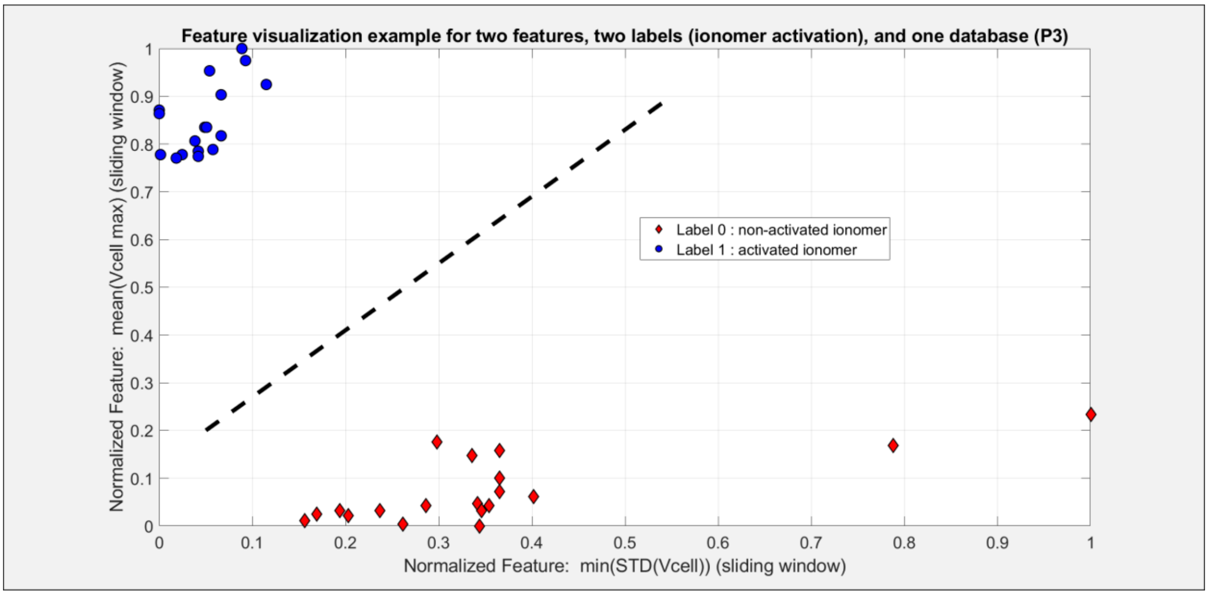

FIG. 3.15. VISUAL ANALYSIS EXAMPLE FOR TWO NORMALIZED FEATURES, TWO LABELS (IONOMER ACTIVATION) AND ONE DATABASE (P3 OF TABLE 1)

Now that a certain number of representative features have been selected, a classification algorithm may be developed. This algorithm is capable of affecting a label to new data, based on all the information provided by the representative features. This is the subject of the next subsection.

4.4 Classification using the k-nearest-neighbours method and cross validation using the leave-one-out approach

With the information provided by the final selected features, the diagnosis tool must be able to determine if a new point (unknown label) belongs to one class or another (here "activated" or "non-activated"). Making this decision is not a straightforward process, as it has to account for multiple dimensions (one dimension per feature). The procedure used to make this decision, and the verification that the correct decision is made (called cross validation), is presented in this section.

4.4.1 Presentation of k-nearest-neighbors algorithm

To affect a label to a new point, the decision making process is carried out through machine learning, and more specifically by using a classification algorithm [171]. A vast amount of classification algorithms (e.g. Gaussian Naïve Bayes, etc.) exist [172]. For this diagnosis tool, the KNN (k-nearest-neighbours) classifier method is used, for its simple operation and robustness [170]. FIG. 3.16 provides a simplified example of a KNN classification for a two-label problem, and for two features.

To classify a new datapoint (green octagram on FIG. 3.16), The KNN algorithm consists of calculating the distance between that point, and its neighbouring points (whose labels are known) [173]. The label (also named class) affected to the new datapoint corresponds to the most recurrent class of the points that are nearest to it. The number of neighbouring points to consider by the algorithm (which must be an odd number to avoid 50/50 cases) is represented by the letter "k" (hence the name k-nearest-neighbours). FIG. 3.16 displays two examples of the number of neighbours to consider (3 or 5), elucidating the decisive impact this coefficient can have regarding the classification results. For the break-in diagnosis tool, a k value of 3 has been chosen, as it provides the most accurate results (through trial-and-error on Matlab™).

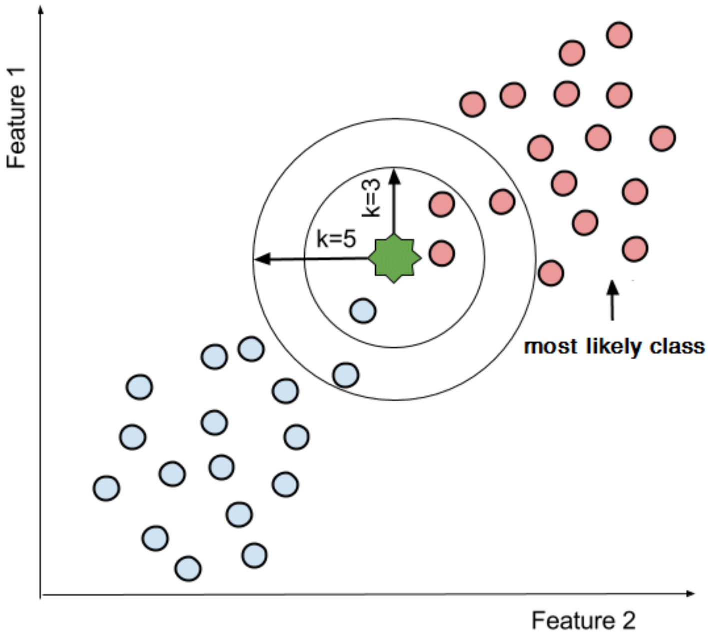

FIG. 3.16. TYPICAL EXAMPLE OF KNN CLASSIFICATION FOR A TWO CLASS PROBLEM [173]

One second parameter of the KNN classifier to consider is the formula on which to rely to calculate the distance between points. Indeed, different distance metrics can be applied (e.g. Manhattan, Euclidean, Cosine etc.), resulting in different classification decisions [174]. For this classifier, the Euclidean equation is used, as it is the most common distance metric, has been applied to an extensive range of studies, and is the most intuitive one. Its formula, here for two vectors of features (f_1 and f_2), is provided below.

$$d(f_1, f_2) = \sqrt{\sum_{i=1}^{n} (f_{1,i} - f_{2,i})^2} \tag{43}$$

For illustrative purposes, only two features are considered in the example of FIG. 3.16 and in (43). The KNN algorithm can however be applied for an unlimited number of features and thus determine the minimum distance throughout an unlimited number of dimensions. As in this case, the $m = 10$ best features (lowest GINI) have been considered, the KNN algorithm calculates the euclidean distance throughout 10 dimensions. The application of this algorithm to the break-in features, and the determination of a classification rate (to validate the diagnosis tool), is the subject of the next subsection.

4.4.2 Cross validation and classification results

To verify that the diagnosis tool is able to correctly classify data, a cross validation method is used. More specifically, the "leave-one-out" method is applied (chosen for its effectiveness in cases where the data samples have a limited number of elements) [175]. This iterative process, consists of removing one different single data point from the database for each iteration, and classifying this point (using the KNN algorithm). In other words, (for each iteration) one single data point is used as the validation data, and all remaining data is used as the training data. This is repeated until each data point in the sample is used once as the validation data. By comparing the decision of the algorithm for each of those points to the actual known labels, it provides the total good classification rate of the diagnosis tool (%).

As for the feature ranking and selection method (GINI), two classifications have been carried out. Firstly, there is the "traditional" classification, where the labels of all combinations of activation mechanisms are considered (5 labels). The second classification, consists of considering each category of morphological changes separately, by classifying their individual databases one by one (only 2 labels per analysis). additionally, the classifier has been tested for various input databases (for the combination of tests of TABLE 3., but also for each separate test). This is to elucidate the impact of the input useful data on the classification results. FIG. 3.17 shows the classification results for each individual activation mechanism (where only 2 labels, "non-activated" and "activated" are considered), and for different input data. A reference threshold value of "acceptable" classification rate at 95% has been added to this figure (arbitrarily chosen rate after which the model can be trusted).

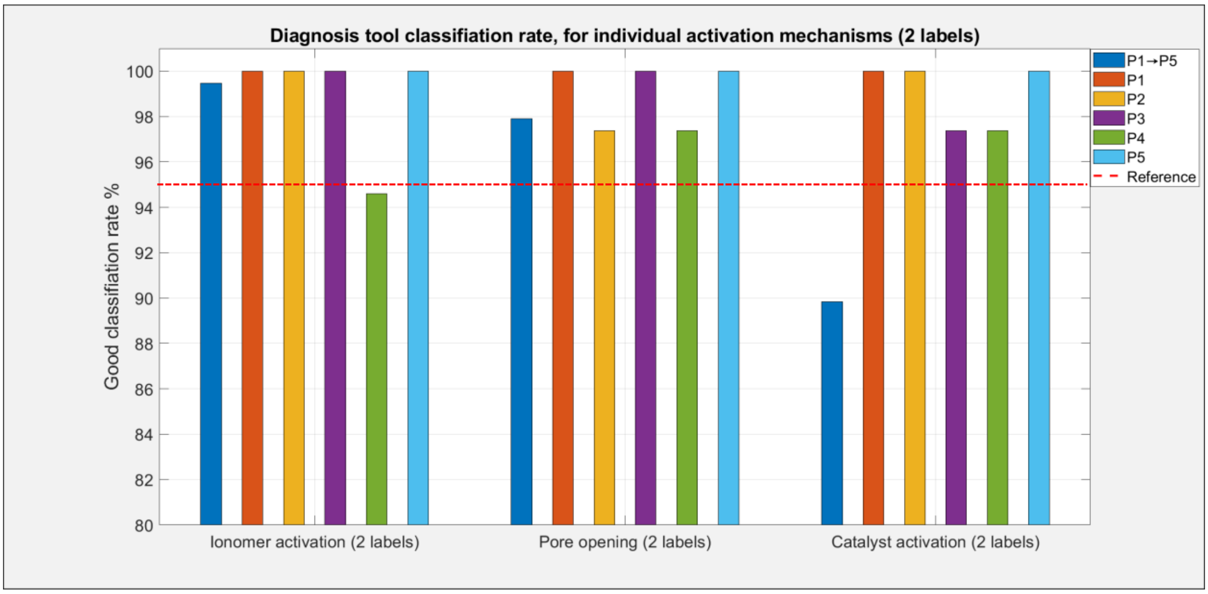

FIG. 3.17. CLASSIFICATION RATE RESULTS FOR VARIABLE INPUT DATA AND EACH INDIVIDUAL MECHANISM (2 LABELS)

The classification rates shown on FIG. 3.17 provide acceptable results, with an overall classification rate globally superior to (or near) 95% for all cases, except for the catalyst activation step. As the catalyst activation features strongly depend on the absolute value of the cell voltage (see section 4.3.2), the classification results worsen when combining the data from all stacks (see TABLE 3.). Indeed, the amplitude of the signature characteristics greatly varies from one stack to another (especially between a stack during activation and one during rejuvenation). Interestingly, no significant classification rate difference is observed for the different separate databases of the fuel cells that have been tested. Stack break-in, rejuvenation, etc. thus seem to share the same characteristic features (they just do not evolve at the same amplitude and rate).

As previously stated, data features must be representative, but also dissociable. The results in FIG. 3.17 do not consider this metric, as one separate analysis is made for each category of activation mechanisms. The true classification rate of the break-in diagnosis tool (for all data, and 5 labels) is shown in FIG. 3.18. Once again, the classification rates for the data of each individual stack has also been determined and shown in this figure (for 4 labels, one for each portion of data before and after the 3 steps of FIG. 3.6). Even though there are more labels, and thus a higher probability for the algorithm to choose a wrong class, FIG. 3.18 reveals classification rates that are as good as or better than the ones for 2 labels (FIG. 3.17). Indeed, a classification rate close to 99% is reached for the sum of all data (5 labels), and classification rates between 98 and 100% are obtained for each individual test (4 labels). This can be explained by the fact that the addition of labels comes with a larger training database. Consequently, when applying the leave-one-out method, the KNN algorithm has more reference information to classify each point (and so a better precision).

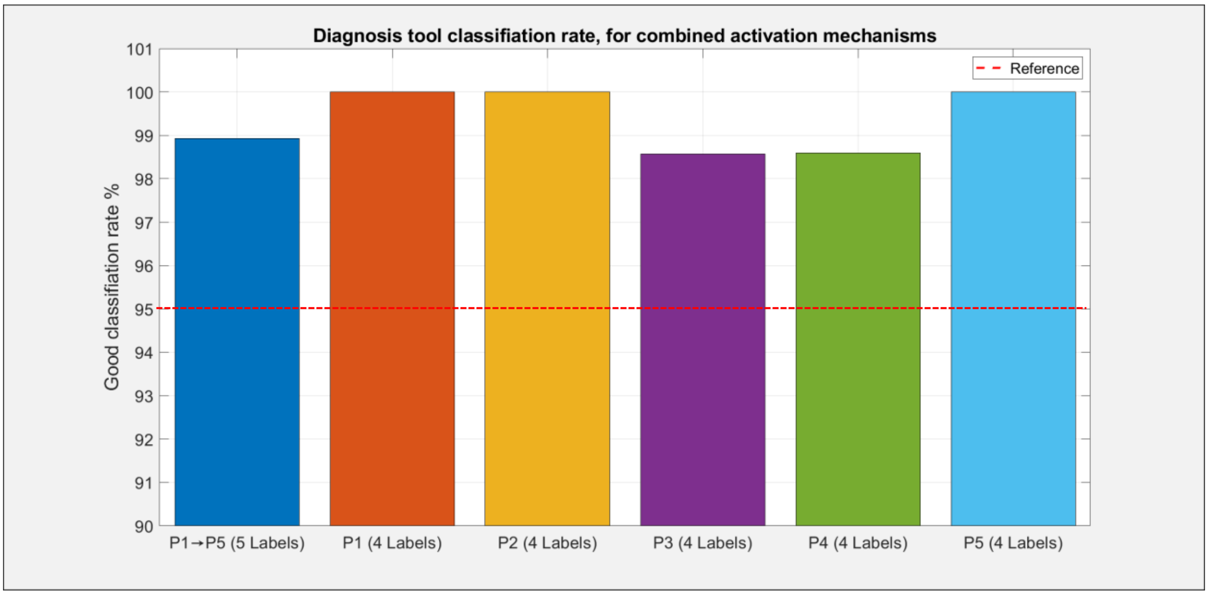

FIG. 3.18. CLASSIFICATION RATE RESULTS FOR VARIABLE INPUT DATA AND ALL COMBINED ACTIVATION MECHANISMS (5 LABELS FOR ALL DATA, AND 4 LABELS FOR OTHERS)

To further analyse the classification rate of the final data that will be conserved for the break-in diagnosis tool (5-label data containing all P1 to P5 databases), a confusion matrix is set up. This matrix (FIG. 3.19) provides additional information regarding the classified points, by specifying the label that has been affected to each point. As a reminder, the 5 labels are, for the ionomer, CL pore structure and catalyst activation, respectively: label 1 = 0/0/0, label 2 = 1/0/0, label 3 = 0/1/0, label 4 = 1/1/0, label 5 = 1/1/1. The numbers 0 and 1 correspond to “non-activated” and “fully activated”, respectively. As shown on FIG. 3.19, there are less data points for label 3 (corresponding to the case where only the CL pore structure is activated), as this data is only provided by a single stack (P3, see TABLE 3.). According to the confusion matrix, no case of false prediction between two labels stands out (the falsely predicted points are not all grouped in a single box). This confirms that the algorithm does not struggle to dissociate or make false decisions between two specific labels.

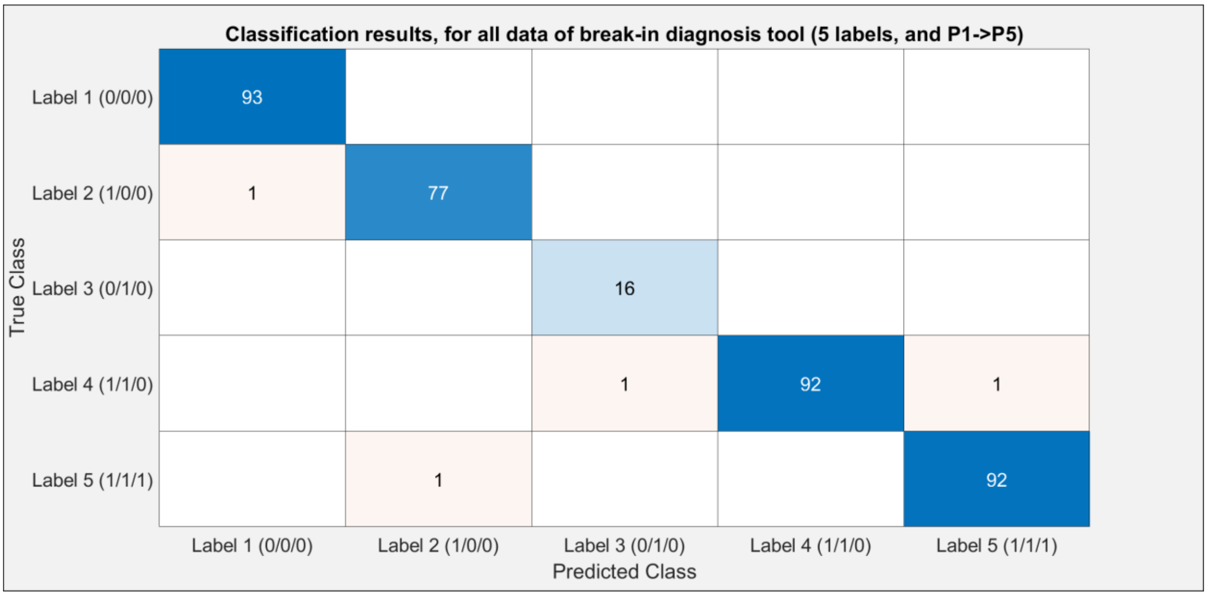

FIG. 3.19. CONFUSION MATRIX OF CLASSIFICATION RESULTS, FOR ALL DATA OF BREAK-IN DIAGNOSIS TOOL

Even though the break-in diagnosis tool provides promising results, the limitations involved in this classification strategy are worth noting. Indeed, to fully test the ability of the classifier to dissociate all morphological changes, one should ideally have one label per situation (non-activated/activated), for the 3 different categories of morphological changes, resulting in $2^3 = 8$ total possibilities. However, as stated in section 3, it is impossible to obtain the database for some hybrid labels (e.g. non-activated ionomer, non-activated pore structure, activated catalyst). Indeed, the catalyst activation protocol also acts on the pore opening effect, as well as the hydration of the ionomer. One can also note that there should ideally be intermediate labels (e.g. partly activated ionomer) to fully monitor the activation process. This is not possible with the protocol of FIG. 3.6, and would require much additional experimental data. Further analysis towards the quality of the input data may also be required (improvement of the test station control through software and hardware updates, verification of human errors, etc.) [176]. One must also be aware of the fact that the leave-one-out method only validates the break-in diagnosis tool, by testing the data of the training database. When truly applied to new break-in data (step 2 of FIG. 3.11), it will most likely be less precise. This will be tested in the fourth chapter of the manuscript.

5 Conclusion

In this chapter, a novel break-in diagnosis tool concept has been introduced and developed. The first layer of this tool (fault identification methods during break-in) has firstly been studied. More importantly however, its novel second layer, which consists of monitoring the “state of activation”, has been developed. To this aim, a test protocol has firstly been created, associated to an experimental campaign (using fuel cells having different proprieties, to diversify the database). In this campaign, three categories of break-in morphological changes have been dissociated. They are the activation of the ionomer, the CL pore structure, and the catalyst. The diagnosis tool development process firstly consisted of extracting the useful information out of the experimental data (in the 1A.cm^{-2} region), followed by the assignment of a label to each datapoint. In total, 5 different labels were specified. Secondly, many statistical features were computed from this useful data, from which a selection of most representative features has been made (GINI ranking method). The “brain” of the diagnosis tool is composed of a machine learning algorithm (KNN classifier). It is capable of allocating labels to new datapoints, based on the training dataset (features matrix). The precision (good classification rate) of the diagnosis tool has been tested using the leave-one-out cross validation method.

As for the development of an analytical model (chapter 2), there are less difficulties involved in the understanding and identification of the ionomer activation process, than for the other break-in mechanisms. Characteristic feature analysis of each dissociated activation process revealed a strong correlation between the ionomer activation process and the standard deviation between cell voltages. Even though the porous structure and catalyst activation datasets had less apparent information shown by their data features, a good overall classification rate (close to 99%) was reached. Additional cross validation tests on individual databases (datasets from individual stacks), and for individual activation mechanisms (2 labels) were carried out. The lower classification rate (90%) obtained for the catalyst activation step elucidated the limitations of this individual mechanism. This is caused by its dependence on the cell voltage feature, whose amplitude varies in the training dataset (especially between stacks during activation and rejuvenation). No significant classification rate difference is observed for the separate fuel cell datasets. Even though they do not evolve at the same amplitude and rate, stack break-in, rejuvenation, etc. thus share the same characteristic features.

Considering the large number of existing approaches to carry out fuel cell diagnosis, many decisions have been made early-on in the development process of this tool, to restrict the field of study. They concern the used methods (diagnosis method, type of features, feature selection method, type of classifier, etc..) and parameters (number of selected features, classifier parameters etc..). The perspectives associated with this study are therefore multiple and consist mainly of testing other diagnosis parameters and methods. There are also many possible improvements, related to the “useful information database”. They include the creation of an experimental database at a higher acquisition frequency. This would allow the identification of an entire new panel of frequential features, and may particularly be efficient to identify the data signature of rapid adsorption/desorption reactions on the catalyst surface. On a more general note, the diagnosis tool should be fed with more and better quality iso-current data, for multiple operating conditions. To more precisely quantify the evolution of the break-in process, intermediate labels may be added to the learning database.

To sum up, there are many challenges involved with the development of a signal-based diagnosis tool, dedicated to fuel cell break-in (to quantify the “state of activation”). Nonetheless, this chapter has introduced the novel break-in diagnosis concept and provided a detailed development process of such a tool. In the fourth and final chapter of this manuscript, which concerns the accelerated break-in experimental campaign, this diagnosis tool will be further tested, in an attempt to characterize the “state of activation”.

Chapter 4: Accelerated break-in experiments: Protocol creation, application, optimization, and performance/durability/cost analysis

1 Ambitions/Purpose

The first chapter of this manuscript was devoted to an in-depth state of the art concerning the activation mechanisms and procedures of PEM fuel cells. Armed with this knowledge, tools have been developed to simulate (analytical model, chapter 2) or monitor (break-in diagnosis, chapter 3) fuel cell activation. This research and associated tools all led to the final chapter, which is dedicated to the development, application, and iterative optimization of novel accelerated break-in protocols, for Symbio fuel cell stacks.

As seen throughout chapter 1, an important number of novel activation methods exist. To accelerate the break-in process, they act on a certain number of stressors (e.g. load, stack temperature, flow direction) to generate specific conditions (e.g. oxidation/reduction, condensation, uniform activation). Not all accelerated fuel cell activation methods (section 3 of chapter 1) have been considered for further testing. A selection of most promising methods has been made, with regards to their compatibility with large surface stacks, potential at accelerating the break-in process, guaranteeing durability, and overall cost. Among this selection, four different break-in protocols are proposed in this chapter, for a range of applications. Each proposed protocol follows a different order of priority regarding the following criteria: maintaining durability, accelerated activation, and material/reactant cost. In other words, each protocol has its own use case.

The protocols put forward in this chapter are based on or inspired from a selection of accelerated activation methods provided by the literature. The aim of the experimental test plan is one hand to adapt activation methods from the literature (often applied to small surface single cell PEMFCs [82]) to automotive grade size stacks. Its second objective is to evaluate and analyse their performance, impact on durability and cost for the Symbio stacks. Its third goal is to further develop and iteratively optimize these most promising methods for the stack technology in question. To develop and optimize this range of proposed break-in protocols, a certain number of activation tests have been carried out.

In this chapter, the used fuel cell testing equipment during this PhD is firstly presented. All following sections are dedicated to the presentation, testing and analysis of the four most promising accelerated break-in protocols. They are (presented in the following order), (i) the “Current stepping/controlled condensation activation” protocol (targeting durability), (ii) the “Cyclic voltammetry/passive N_2 hydration activation” protocol (targeting reactant cost), (iii) the “Pulsed current cycles activation” protocol (targeting break-in time), and finally (iv) the “Cathode starvation/reverse flow activation” protocol. This final procedure is the result of the main and best compromise found between all of the previously stated criteria and is considered as the flagship protocol of this thesis.

2 Fuel cell testing equipment

This section is dedicated to the presentation of the used test stations and fuel cell stacks, for all the experimental tests. In a first subsection, the characteristics of the test stations (provided by the FClab, Symbio and Sintef) are provided. Thereafter, the associated tested Symbio fuel cell stack prototypes are introduced.

2.1 Test stations

In this section, the characteristics of the three test stations (used during this PhD) are briefly presented. They are all adapted for fuel cell characterization, but each one has its own specifications and use cases.

2.1.1 FClab: In-house made test station (TB07)

The TB07 (20kW) test station (whose piping and instrumentation diagram has been presented in Fig. 3.10 of chapter 3), belongs to the FClab. This equipment has mostly been used to test break-in protocols, and to adapt them to the software/hardware constraints of a fuel cell testbench (e.g. humidifier response time).

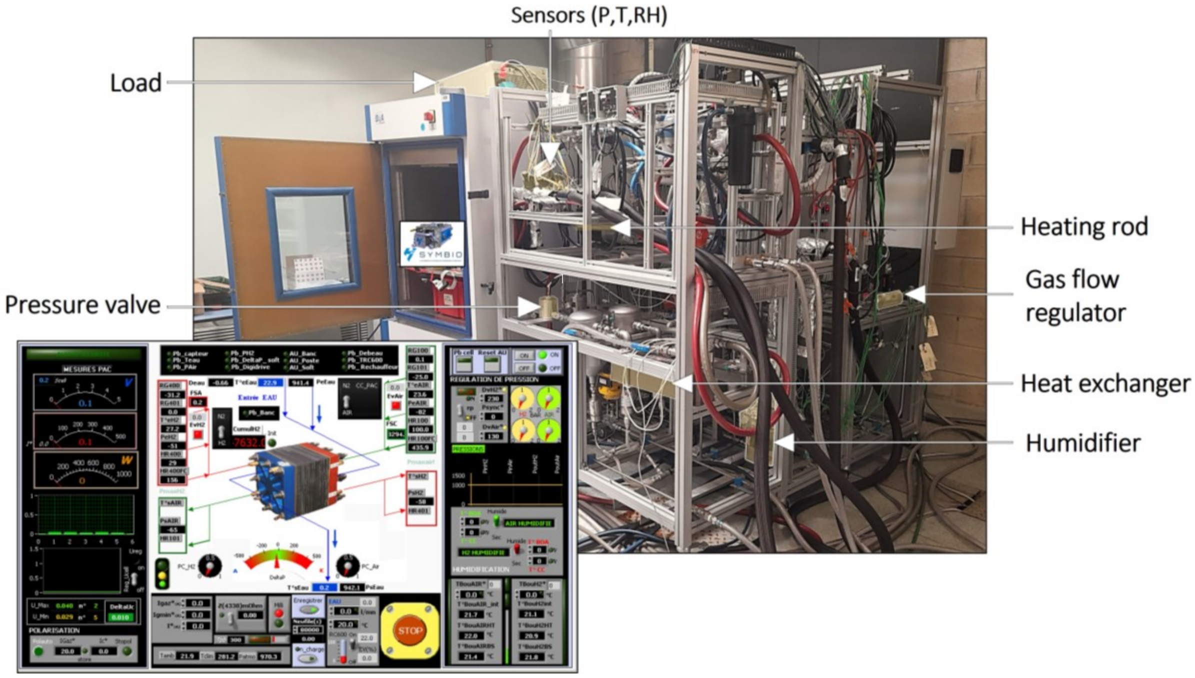

Fig. 4.1. FClab TB07 custom made 20kW test station with Labview™ interface

Fig. 4. shows the TB07 test station at the FClab with its associated Labview™ interface. The hardware and software of this testbench, mainly dedicated to fuel cell characterization, have been developed in-house by FClab employees, and used for over 10 years. The testbench gas channels are composed of: Swagelok tubing, H_2 and Air boilers (humidifiers), Brooks flowrate regulators and pneumatic pressure valves. The stack pressure at the anode and cathode input/output is measured, as well as the input RH and temperature (see P&ID of Fig. 3.10). The temperature of the internal stack cooling fluid is regulated using a heating rod, and a heat exchanger, which is connected to a secondary cooling circuit. This secondary cooling circuit is mixed with a controllable proportion of fresh/iced water at a fixed temperature. As shown on Fig. 4., the test station can also be coupled to a climatic chamber, to control the thermal conditions surrounding the stack.

All control parameters of the test station components (proportional integral derivative coefficients, or PID) have been selected in order to favour precision (with sacrifices in response time).

2.1.2 Symbio: In-house made test station (B057)

The novel B057 (5kW) fuel cell test station (FIG. 4.2) has been provided by Symbio, and has entirely been developed in-house by its employees. One of the objectives during this PhD consisted of helping in making this test station operational (finding components, electrical/gas connections, sensors/acquisition cards connections, pre-operation tests, etc.). It has therefore mostly served to gather a deeper understanding of the fuel cell testbench components, their control, and their integration into the test station. Additionally, a number of accelerated break-in protocols have subsequently successfully been applied on it.

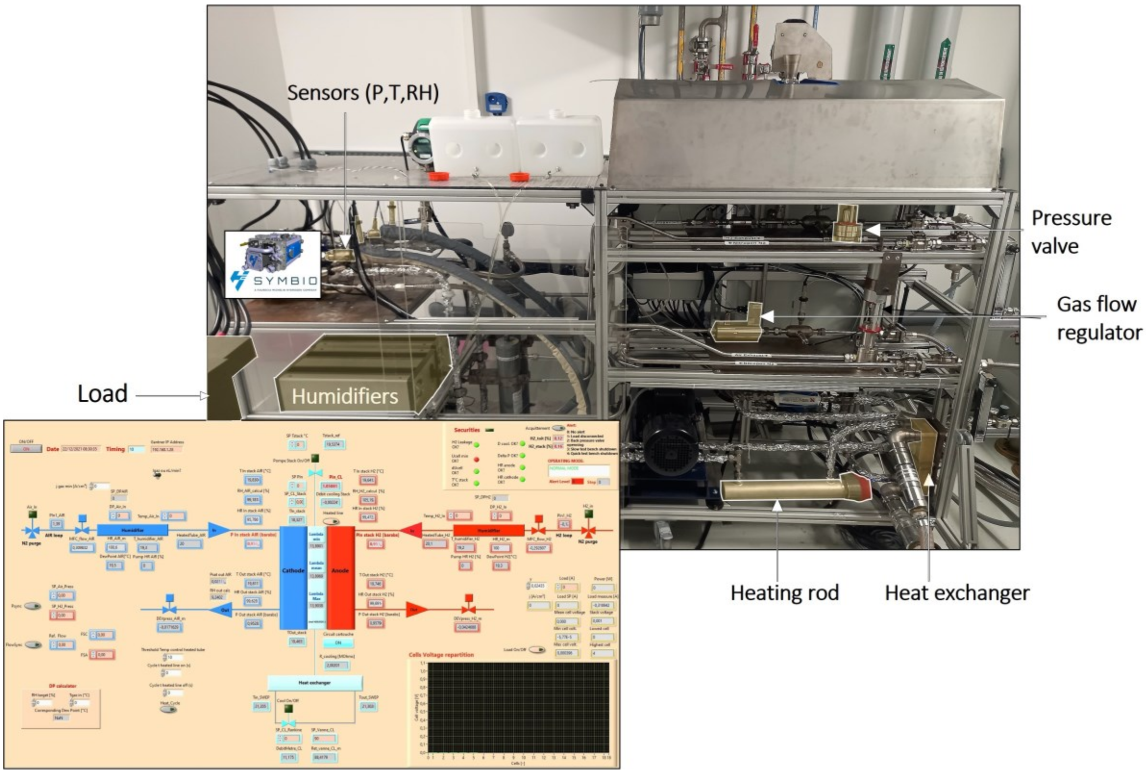

FIG. 4.2. SYMBIO B057 CUSTOM MADE 5KW TEST STATION WITH LABVIEW™ INTERFACE

The B057 testbench P&ID is very similar to the one of the TB07 test station (FIG. 3.10 of chapter 3). The main difference with this test station and the TB07 testbench are its dynamics (response time). For rapid humidity control, direct water spray humidifiers are used, which have the capacity to almost instantaneously impose a dew point temperature. Additionally, the PIDs of all components (pressure regulators, heating element, etc.) can directly be adjusted on the interface. The control can thus be optimized for a specific stack (specific gas flowrate, pressure losses, etc.) to reduce the response time whilst conserving precision.

2.1.3 Sintef: Commercial Greenlight test station (G400)

The Greenlight G400 (6kW) test station (FIG. 4.3) belongs to Sintef. This testing equipment was made available through a collaboration project between Sintef, UBFC, FEMTO-ST and Symbio, in the form of a one-month research stay in Trondheim, Norway. All experimental data provided by this test station was also used in the framework of the Virtual-FCS project [177], which financed the experimental costs. This test station differs from the TB07 and B057 as it is a commercial testbench (not manufactured in-house), developed by the Greenlight Innovation corporation. The G400 has been used to apply a break-in protocol with galvanostatic and potentiostatic operation, and a post-activation ageing campaign. For potential control and precise ageing characterization (e.g. CyV, EIS, output gas analysis), many additional devices have been hooked up to this testbench. The G400 was therefore mainly used to test and gain experience towards the use of several characterization methods and the configuration of an automated test bench control.

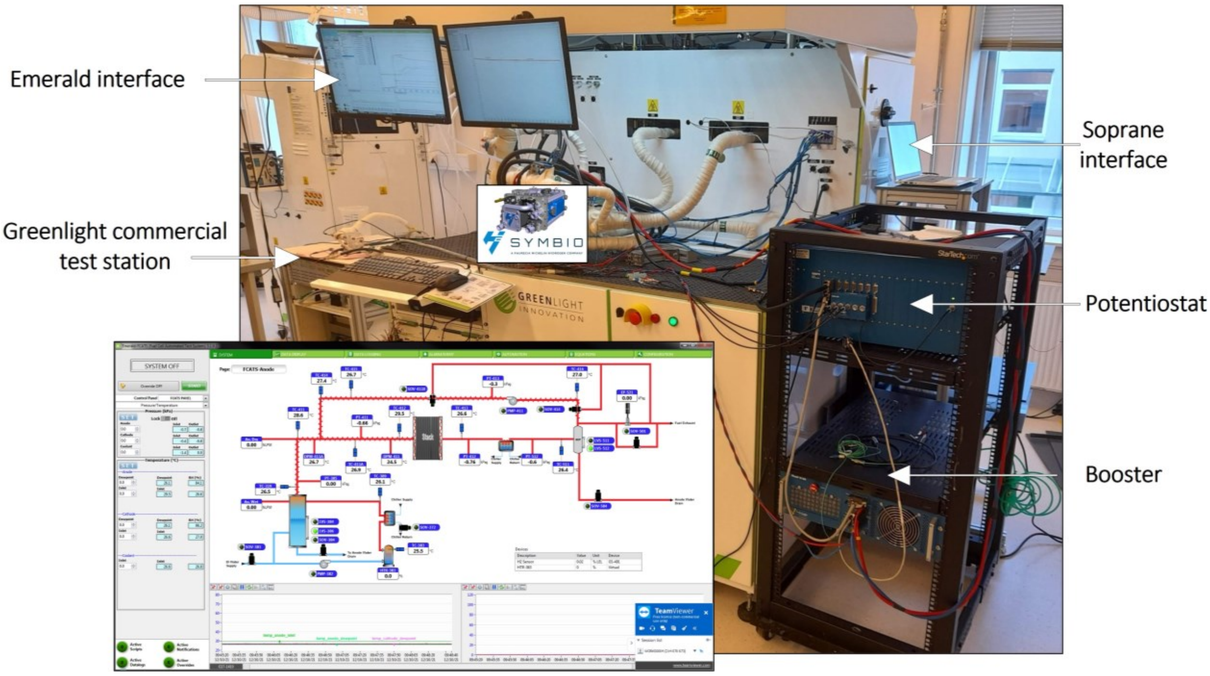

FIG. 4.3. GREENLIGHT G400 TEST STATION WITH EMERALD™ INTERFACE AND CHARACTERIZATION APPARATUS

The Emerald interface, used to control the G400, displays the test station P&IDs (anode, cathode and cooling circuits). The G400 can run in anode recirculation mode (or in dead end, as for the B057 and TB07). It also provides additional gas input and mixing channels (e.g. for test of CO-poisoned H_2). A detailed description of the Sintef G400 test station specifications and schematic of anode loop can be found in [178].

The equipment used for the EIS and Cyclic Voltammetry characterization is the Biologic WMP3 multi potentiostat, coupled to the Biologic Flex P0160 50A booster. This equipment is directly linked with the computer of the test station and is controlled through the ECLab software. When performing electrochemical measurements, the base load is supplied by the test station, and any additional load perturbations (e.g. for EIS analysis) are supplied by the booster, which is controlled by the potentiostat. All current responses are monitored and recorded by the potentiostat. The booster operating voltage range is 1 to 60V. An Agilent 990-PRO Micro-GC equipped is used to quantify the H_2, O_2, N_2, CO_2 and CH_4 content of the anode outlet gas stream. A bleed from the outlet, placed before the backpressure controller, is constantly flowing through the GC. Samples are passed through the column using Helium and Argon carrier gasses to achieve separation of components. The components are then quantified using a micro-machined thermal conductivity detector. The Micro GC is controlled using a separate computer, through the Soprane software. The final configuration of the Greenlight G400 test station with its additional components is shown on the scheme in FIG. 4.4.

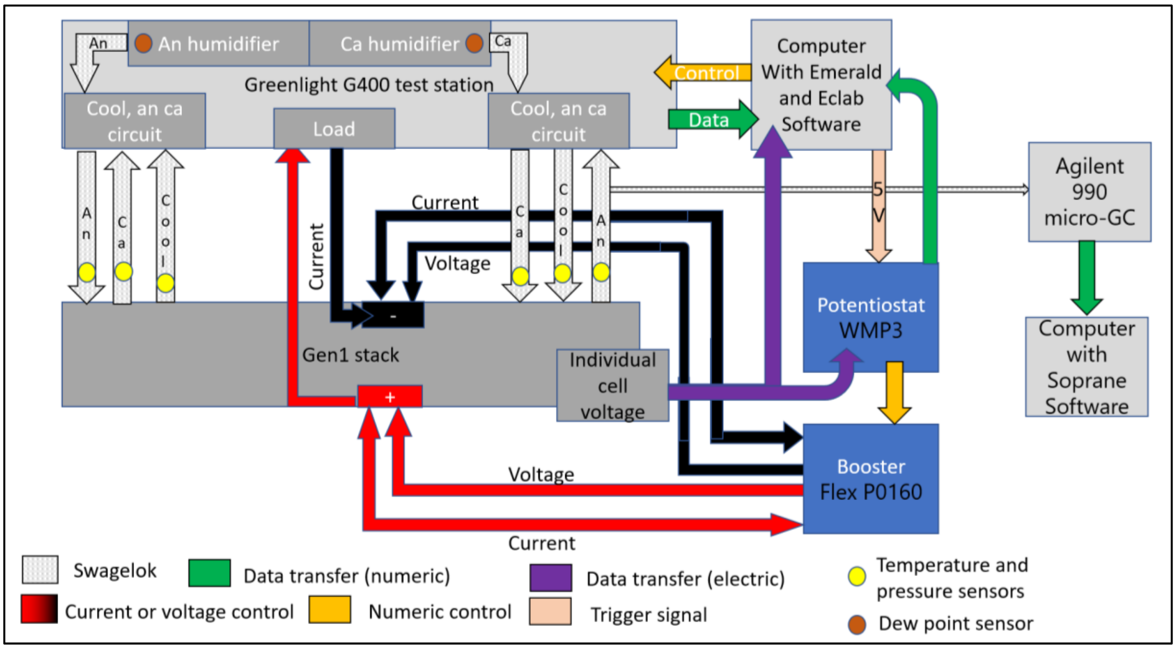

FIG. 4.4. GREENLIGHT G400 SETUP WITH CHARACTERIZATION EQUIPMENT (FOR CYV, EIS AND GAS ANALYSIS)

Now that all the test stations have been introduced, the characteristics of the used fuel cells are specified.

2.2 Fuel cell specimens

The fuel cells that have been tested during this PhD are prototype stacks built by Symbio, dedicated to the automotive sector. Their specifications (dimensions, materials and operating conditions) are listed below.

2.2.1 Symbio GEN1 prototype

The Symbio GEN1 prototype, is the focus technology of this workplan. For illustrative purposes, FIG. 4.5 provides the GEN1 stack structure. This fuel cell has an active surface of 263cm^2, rigid EndPlates (FIG. 4.5), and MEAs with Pt loadings of 0.1 and 0.4mg.cm^{-2} at the anode and cathode, respectively.

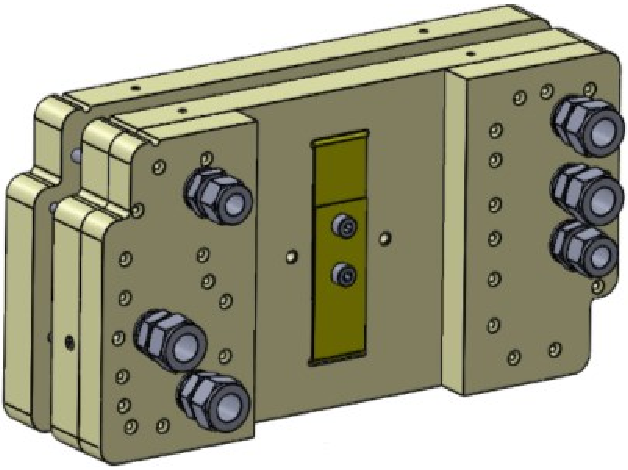

FIG. 4.5. SCHEMATIC REPRESENTATION OF SYMBIO GEN1 STACK PROTOTYPE STRUCTURE

The main stack operating conditions are summarized in TABLE 4..

Operating conditions for GEN1 fuel cell stack	
Maximum current density ($A.cm^{-2}$)	Up to $1.8A.cm^{-2}$ (above 0,6V per cell)
Anode / Cathode Pressure (barabs)	2 / 2
Anode / Cathode Stoichiometry	1.5 / 1.8
Anode / Cathode RH (%)	50 (at 82°C) / 30 (at 70°C)
Outlet Temperature (reference)	82 (reference temperature for control)
Inlet Temperature (measured)	70 (estimated value)

TABLE 4.1. OPERATING CONDITIONS FOR SYMBIO GEN1 STACK PROTOTYPE

The performance goal of this prototype is to reach $1.8A.cm^{-2}$ at 0.6V per cell for the conditions of TABLE 4. (entire PolCurve not provided in this manuscript). A single GEN1 stack dedicated to automotive applications is composed of ~250 to 300 cells, for a total volume of 25 to 30L. Mostly short-stacks (GEN1 fuel cell stacks with less cells) have been used during this PhD, for evident experimental cost related reasons.

2.2.2 Symbio NextGen prototype

As their names suggest, the NextGen technology is the successor to the GEN1 stack. This new prototype is based on the same architecture (same active surface and materials, very similar operating conditions, etc.). It however provides a list of improvements, mainly related to the type of MEA, EndPlate (now with springs), the BPP design (pressure losses, gas distribution) and production method (stamping versus hydroforming). The specific fuel cell characteristics (used materials, MEA technology, amount/type of catalyst) are not divulged for confidentiality reasons. Considering the numerous improvements this stack provides on its predecessor (GEN1), it can be considered as an entirely different fuel cell technology. In other words, the GEN1 and NextGen technologies do not necessarily share the same break-in characteristics.

Using the equipment that has been presented in this section, a certain number of break-in protocols have been developed, tested, and iteratively optimized in some cases. The main accelerated break-in protocols, which have provided the most promising results, are presented throughout the following sections. As previously stated, each of the 3 first accelerated activation protocols that have been put forward in this chapter have their own use case and are based on different priorities (durability/cost/activation rate). The fourth and final break-in protocol is considered as the best compromise between all criteria.

3 Break-in protocol: Current stepping/controlled condensation activation

The first accelerated break-in protocol put forward in this manuscript (current stepping/controlled condensation) prioritizes the conservation of stack durability. As all accelerated break-in protocols (section 3 of chapter 1), it acts on a certain number of stressors to enhance the activation kinetics. Simultaneously however, precautions are taken (e.g. incremental load variations, long stabilization times, OCV bypass) to limit faulty conditions (section 2.3 of chapter 3) and mitigate the risks of degradations. Additionally, this protocol has the specificity of having simultaneous characterization (PolCurves) during break-in, meaning that performance evolution and convergence may be monitored. For these aforementioned reasons, this protocol is strongly recommended for cases where a stack with unknown specifications nor break-in cycle instructions, must be activated. The detailed break-in process application and analysis is presented below.

3.1 Presentation of the protocol and its main objectives

The *current stepping/controlled condensation* protocol is divided into 4 steps, and has a current profile, similar to the one of a PolCurve [49] (FIG. 4.6). During the first 3 steps, the current stepping method is used (section 3.2.1 of chapter 1). The variable voltage imposed by the current cycles create oxidating/reducing conditions at the cathode which in turn induces Pt-oxides and other impurities desorption. Additionally, during step 2, the supersaturated operation technique is used, accompanied by the cooling after stop method before and after this step (sections 3.2.3 of chapter 1). This supersaturated environment promotes ionomer activation and the evacuation of desorbed species/unanchored particles. The last step (FIG. 4.6) has the sole purpose of determining if stack performance has stabilized (it does not activate it in an accelerated manner).

The first three steps of this protocol (FIG. 4.6) have mainly been inspired by the break-in process of Yang *et al.* [51], who applied similar techniques to accelerate the activation rate. As for most break-in methods presented in the literature, the procedure presented by Yang *et al.* has been applied on a small surface single cell (6.25cm^2). Consequently, the same operating conditions may not be applied on a large surface Symbio fuel cell stack (as the conditions are not as homogenous, more prone to faulty conditions, etc.). Similarly, the behaviour of the cell used by Yang *et al.* during break-in (duration and performance evolution rate) is not at all representative of automotive grade fuel cell stacks [82]. The peak current density, stabilization times, supersaturated operation and cooling after stop as presented by the literature have thus been adapted to the response time and performance characteristics of a large surface stack.

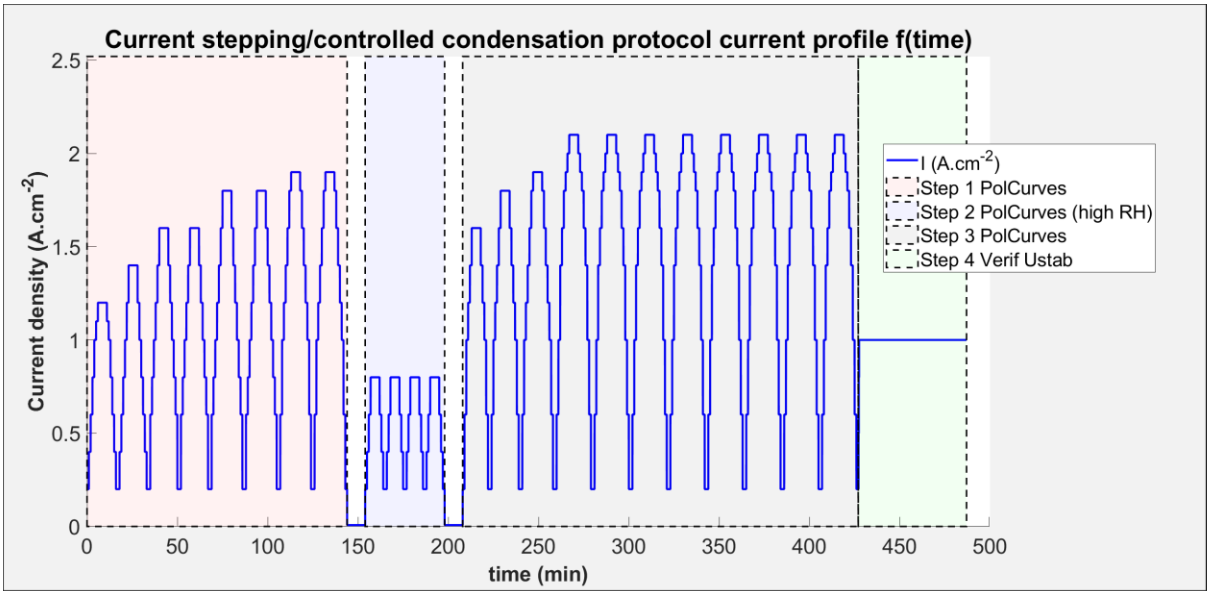

FIG. 4.6. CURRENT STEPPING/CONTROLLED CONDENSATION ACTIVATION PROTOCOL CURRENT PROFILE

To prevent flooding risks upon restart, the minimum temperature for the “cooling after stop" technique has been set to 60°C. To gain time, instead letting the stack passively dissipate heat, it is actively cooled using the cooling circuit. Additionally, the reactant flows are maintained (at high RH) to conserve the pressure setpoint within the anode/cathode gas channels, prior to the following PolCurves (TABLE 4.2). These operating conditions/method adjustments have been determined through an iterative process. One first attempt (first version of this protocol) for example consisted of passively heating the stack on the B057 test station (the only calories brought to the cooling circuit were provided by the stack). This forces condensation and suppresses the need for a heating component (heating rod). As could be expected, this resulted in rapid performance evolution as the ionomer is massively hydrated. This method does however not ensure that flooding will not lead to starvations. Consequently, it does not follow the main guideline of this protocol (guaranteeing durability). A more controlled condensation approach (with heating rod) is thus favourable.

Regarding the load profile (FIG. 4.6), the maximum current density is initially limited to 1.2A.cm^2 and progressively increased to its peak value of 2.1A.cm^2. In this configuration, the mass transport losses remain acceptable, thus preventing starvations. During supersaturated operation (step 2), the stack temperature is limited to 70°C and the current density is low to inhibit starvation risks (induced by flooding) once again. For the same reasons, the peak current of the 3 PolCurves following the cooling after stop phase is reduced.

Operating conditions during current stepping/controlled condensation activation protocol	
Anode / Cathode Pressure (barabs)	2 / 2
Anode / Cathode Stoichiometry	1.5 / 2
Anode RH (%)	92% for step 2 and 60 % for rest
Cathode RH (%)	94% for step 2 and 60 % for rest
Outlet Temperature (reference)	70 for step 2, 60 at 0A and 80 for rest (controlled values)
Inlet Temperature (measured)	60 for step 2, 60 at 0A and 70 for rest (estimated values)

TABLE 4.2. CURRENT STEPPING/CONTROLLED CONDENSATION ACTIVATION PROTOCOL OPERATING CONDITIONS

Additional precautions/improvements have been implemented to this protocol. High potential related degradations are for example mitigated by removing the OCV step from the PolCurves. The highest current step of each pseudo PolCurve is maintained for 5 minutes, to accelerate the ionomer activation kinetics.

3.2 Protocol application and data analysis

As previously stated, the *current stepping/controlled condensation* protocol has been applied multiple times. In this section, the break-in results for the latest version of the protocol (with active heating), using the TB07 testbench, and a 5-cell NextGen stack, is presented. Similar to the USFCC performance convergence criterion [15] (voltage deviation below 5mV.cell^{-1} between measurements at 0.8A.cm^{-2}), the performance convergence has here been monitored at a fixed iso-current value. FIG. 4.7 shows the progressive performance increase and convergence at 1A.cm^{-2} (to be identical to last step of protocol). This figure elucidates the convenience of having a current profile that simultaneously characterises (PolCurves) and activates the stack. Only the data of the first and third step of the protocol of FIG. 4.6 are considered, as during the second step the stack is flooded (reduced performance), and only downsized PolCurves are drawn.

The comparison of the mean cell voltage (at iso-current) of the beginning of step 3 to the end of step 1, shows no visible performance increase (see FIG. 4.7). One could thus argue that the supersaturated activation and cooling after stop methods had no effect on stack performance. One must however also keep in mind that the stack is initially oversaturated with water (at the beginning of step 3). These “reversible losses” (punctual performance loss due to the presence of a faulty condition) conceal the performance gain provided by step 2. During the 3 following PolCurves of step 3, as the water excess is removed from the stack, the benefits of step 2 become visible (rapid performance increase). This also confirms the necessity of having reduced PolCurves at the beginning of step 3 (to prevent flooding-induced starvations at elevated currents). The chosen peak current density of the PolCurves results in a mean cell voltage that never drops below 0.54V during the entire activation process. One may argue that stronger reducing conditions (mean cell voltages lower than 0.4-0.5V) are required to fully desorb the oxides from the catalyst [68]. This said, to maintain stack durability (which is the priority of this break-in process), and to prevent excessive H_2 consumption (already at 123g.cell^{-1} for a NextGen stack), the maximum current density must remain limited. Additionally, elevated and stable performance may be obtained even if the fuel cell voltage remains greater than 0.4V [63].

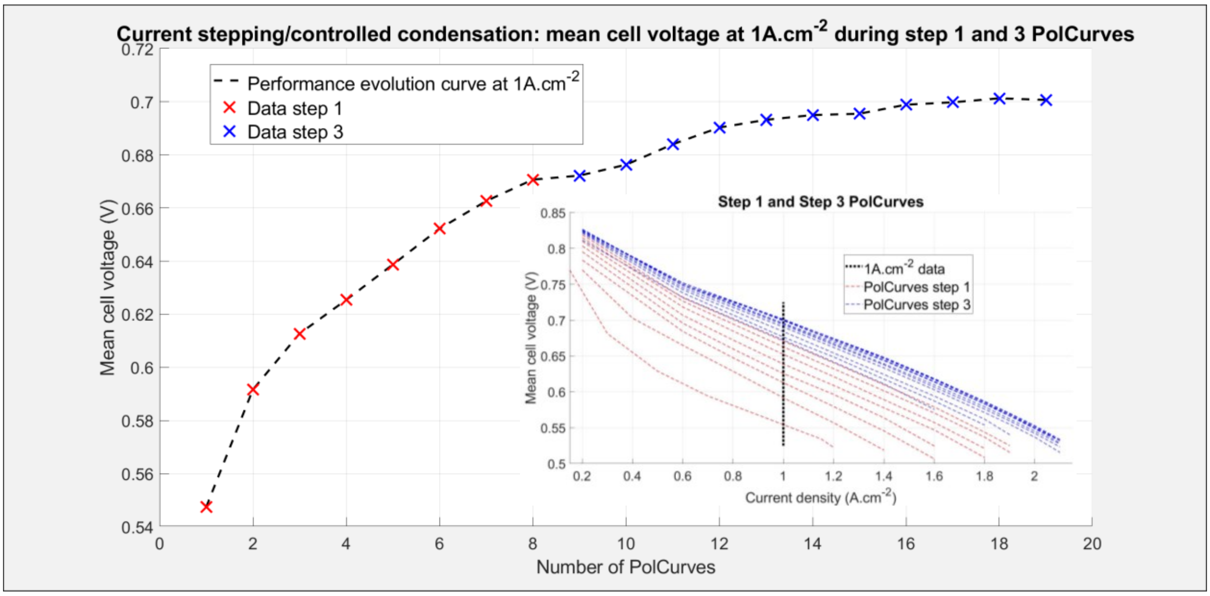

Fig. 4.7. Iso-current (1A.cm^{-2}) performance evolution during step 1 and 3 of the current stepping activation protocol

The measurements (Fig. 4.7) indicate that the USFCC performance deviation criterion (see section 4.1.1 of chapter 1) has been reached between the 12th and 13th PolCurve (~3mV.cell^{-1} at ~300min). Thereafter, full cell performance convergence (0.5mV deviation) is achieved between the two last PolCurves (mean cell voltages of 0.7013 and 0.7007V, respectively). Additionally, the fourth step of this protocol (1A.cm^{-2} for 1 hour) also indicates that peak performance has been reached. A slight performance decline of ~5mV.cell^{-1} is even recorded over this 1-hour period. This may be due to the gradual readsorption of oxides on the catalyst surface [24], or slight reduction of membrane water content. Similarly, the first post-activation PolCurve of this stack displays agreeable performance (>0.6V at 1.5A.cm^{-2}). Some slight residual activation (performance gain) was however observed on this fuel cell stack during other following post-break-in tests (tests not part of this PhD). This elucidates the difficulties involved regarding the definition of an end-of-break-in criterion (section 4.1 of chapter 1). Indeed, even two performance stabilization criteria (iso-current voltage evolution during PolCurves and step 4) were not sufficient to clearly determine if the stack had reached peak efficiency.

In the aim to further quantify the evolution and end-of break-in, the developed model (chapter 2) and diagnosis tool (chapter 3) are applied to each protocol put forward in this chapter. The feedback provided by testing these programs on accelerated break-in data may also elucidate perspectives for model improvements. The results from each model and the associated data analysis are presented in the following subsections.

3.2.1 Analysis with analytical ionomer activation model

For this analysis, the current profile of Fig. 4.6, the operating conditions of Table 4.2, and associated stack characteristics (NextGen) are used as input of the ionomer activation model (chapter 2). In this subsection, solely the evolution of the ionomer break-in coefficients is analysed, as they are the image of the "state of activation" of the ionomer. The evolution of each break-in coefficient over time is shown in Table 4.3.

Ionomer break-in model coefficients evolution for current stepping/controlled condensation protocol				
Coefficient convergence	$R_{skin\ \mathrm{an}}$ (time | value)	$R_{skin\ ca}$ (time | value)	R_{dspac} (time | value)	R_{cont} (time | value)
to 10% from final value	6.8min | 0.1	6.8min | 0.1	47.1min | 1.5×10^{-2}	184.3min | 1.7×10^{-3}
to 1% from final value	10min | 10^{-2}	10min | 10^{-2}	84.1min | 1.5×10^{-3}	216.9min | 8.3×10^{-4}
to 0.1% from final value	14.5min | 10^{-3}	21.5min | 10^{-3}	119.1min | 1.5×10^{-4}	218min | 7.4×10^{-4}
to final value	26min | 0	27.3min | 0	243.1min | 0	218.1min | 7.3×10^{-4}

TABLE 4.3. IONOMER BEAK-IN MODEL OUTPUT FOR CURRENT STEPPING/CONTROLLED CONDENSATION PROTOCOL

According to the analytical model, the first PolCurve (0 to 18min) successfully removes the initial barriers to water sorption (surface skin resistances, see section 6.1.1 of chapter 2). The domain spacing resistance follows a similar progressive trend, to reach 0.1% from its final value before the end of step 1 of the protocol (144 min). Full convergence is reached during step 3 (208 to 427min), thanks to the high load and supersaturated operation. The membrane contamination resistance fully converges in a similar time frame. As stated in section 6.1.3 of chapter 2, this contamination resistance does not necessarily converge to zero. Indeed, as the impurities migrate to the cathode CL and evacuate from the membrane, they can more or less severely contaminate the Pt and the surrounding polymer (whose effect is taken into account in R_{cont}). With this protocol, the final R_{cont} value is relatively low (7.3×10^{-4}, see Table 4.3) meaning that the humid gas flow has efficiently evacuated most impurities before they had a chance to contaminate the catalyst.

The evolution law of the break-in resistances (rapid drop followed by progressive convergence) concurs well with the general fuel cell performance evolution trend during this break-in protocol (Fig. 4.7). This accordance with the model indicates that equations used to describe ionomer activation (section 6.1 of chapter 2) fit with the experimental observations. This said, the time constant related to domain spacing and decontamination may have to be slightly recalibrated. Indeed, the slope of the PolCurves (Fig. 4.7) indicate a full convergence in the ohmic region after the 19th cycle (corresponding to ~350min). This is slightly longer than the domain spacing (243 min) and contamination (218min) resistances converge time. Regardless, the model and the experimental data agree on the fact that ionomer activation is finalized. Any residual post-activation performance increase may thus be related to activation mechanisms within the CL.

3.2.2 Analysis with break-in diagnosis tool

All the data at 1A.cm^{-2} presented in Fig. 4.6 (during step 1, 3 and 4 of the protocol) is extracted and used as input for the break-in diagnosis tool. This "validation database" (data with unknown labels) is classified by comparing it to the (labelled) training database, using the procedure illustrated in Fig. 3.11 of chapter 3. The output of the diagnosis tool (the class affected to each data sample) is summarized in Table 4.4.

The diagnosis tool has proven to present coherent as well as confident classification results. Indeed, it identified the stack as being fully non-activated initially, as well as the progressive transition to a fully activated stack. Distinctive intermediate steps between all break-in mechanisms (section 2.4 of chapter 3) are also visible. The break-in kinetics (duration of each activation mechanism to be completed) as shown by the diagnosis tool are however very optimistic. Indeed, it indicates full ionomer break-in after only 12.4min, followed by the CL pore structure activation, reached at 38.3min (both at a 100% confidence level). The program had more difficulties to distinctively identify the point at which the catalyst surface became fully activated. Indeed, between 38.3 and 141.5min, it mainly indicated that the stack already was entirely activated, with only 25% of the data showing that the catalyst was not broken-in yet. This lack of confidence towards the catalyst activation mechanism was to be expected as it also provided the worse cross validation classification results (see FIG. 3.17 of chapter 3). This said, the program is rather confident (at 96.4 %), that catalyst activation is finalized after 220min (corresponding to the beginning of step 3 of the protocol).

Break-in diagnosis tool results for current stepping/controlled condensation protocol in the 1A.cm^{-2} region				
Key time periods (min)	0 to 12.4	12.4 to 38.3	38.3 to 141.5	220 to 487.5
Labels (and % of data associated to each label)	Non-activated (100 %)	Ionomer (100 %)	Ionomer + CL (25 %), Fully activated (75 %)	Fully activated (96.4 %), Ionomer + CL (3.6 %)

TABLE 4.4. BREAK-IN DIAGNOSIS RESULTS FOR CURRENT STEPPING/CONTROLLED CONDENSATION PROTOCOL

The rather optimistic results of the model were to be expected considering the conditions at which the validation data measurements were made. Indeed, even if the training and validation databases share the same iso-current value (1A.cm^{-2}) the operating conditions (e.g. *RH,P,FSC*) of the validation data (TABLE 4.2) clearly favour stack performance. Additionally, the NextGen prototype is used for the validation database, which provides better baseline performance than its GEN1 predecessor (used for the training database). This affects the values of the features (e.g. $V_{cell\,mean}$, $STD(V_{cell})$) on which the diagnosis tool relies (see TABLE 3.2). In turn this impacts the classification decisions, therefore rapidly indicating full stack activation.

This has been proven by testing the validation data at a slightly higher current density (1.4A.cm^{-2}), to compensate the effects the operating conditions have on stack performance and behaviour. Indeed, this test provided similar classification results, but for more realistic time frames (non-activated stack from 0 to 75min, activated ionomer from 81.4 to 277.4 min, activated ionomer and CL from 297.4 to 424.3min). All classification intervals provided 97% to 100% confidence. This further proves that the diagnosis tool concept is functional, but that it requires training and validation databases that share the same operating conditions and equipment in order to be more precise. This said, even in its current form, the tool provides information towards the general evolution of break-in. For example, the increase of confidence towards full stack activation identified by the diagnosis tool after 220min indicates that supersaturated activation (step 2 on FIG. 4.6) beneficially affected break-in. The diagnosis tool will be further tested later in this chapter.

3.3 Protocol degradations and impact on durability

Few degradation risks exist with the *current stepping/controlled condensation* protocol, as it prioritizes the conservation of stack durability. The degradation risk of this process is therefore not further studied/quantified in this chapter. This will not be the case for the procedures presented in the following sections (sections 4, 5 and 6), which apply more "exotic" and possibly degrading conditions.

To conclude, among the protocols proposed in this chapter, this method does not degrade the stack, but is certainly not the most efficient one. Nevertheless, it has proven to reduce the activation time to some extent (whilst ensuring durability). Its duration depends on the stack characteristics and performance stabilization criterion (see section 4 of chapter 1). Using the aforementioned USFCC performance stabilization criterion, a break-in time of 300 minutes (~5 hours) is obtained. Perspectives with this protocol involve its application on a larger scale (more cells) fuel cell stack. This will be carried out on a 100-cell NextGen stack and on an associated 120kW test station (Hyban at FClab). Given the cost related to this test, it illustrates the confidence this protocol provides towards the preservation of stack durability.

4 Break-in protocol: Cyclic voltammetry/passive N_2 hydration activation

Among the proposed break-in protocols in this chapter, the *Cyclic voltammetry/passive N_2 hydration* activation process prioritizes the reduction of reactant consumption. According to the main references on which this protocol is based, it can divide the reactant consumption rate by up to 4 times (relative to traditional, non-accelerated break-in procedures) [58], [179]. Similar to the protocol presented in the previous section, this break-in procedure simultaneously characterises and activates the fuel cell. The nature of the characterization process however differs as it concerns the CyV measurements (voltammograms), instead of PolCurves. In other words, the active surface is characterized (not the overall cell performance).

4.1 Presentation of protocol and its main objectives

The *Cyclic voltammetry/passive N_2 hydration* protocol is comprised of 2 main steps (current/voltage profile provided in FIG. 4.8). As its name suggests, they are, the injection of humidified N_2 in the anode and cathode channels, followed by the application of multiple CV cycles (in this order). In between those two main steps, an additional "cooling after stop" step (section 3.2.3 chapter 1) has been added to the protocol. Pseudo Pol-Curves have also been implemented, for each 45min during N_2 hydration (step 1), and between each 20 CV cycles (~13m20s) during the last step, to provide an additional layer of characterization. Indeed, producing current is essential to monitor the cell performance evolution, which is impossible during N_2 hydration and CyV cycling due to the absence of hydrogen and/or oxygen. To evaluate the impact of CyV on stack ageing, this protocol will be followed by a complete ageing test campaign. Thus, contrary to the other protocols presented in this chapter, no final iso-current step (to verify stable performance) has been added.

The first step of humidified N_2 injection has one objective which is hydrating the polymer in the CL and in the membrane. This is the most time-consuming step of the protocol, but also the one where the stack performance increase is most noticeable (ohmic resistance reduction). The main purpose of using humidified N_2 to hydrate the ionomer is to reduce H_2 consumption (and thus the overall operating cost which is the main objective of this protocol). Cyclic voltammetry, the last step of this protocol, has one main goal which is desorbing impurities and oxides from the catalyst surface, at the cathode. As seen in section 4.1.4 of chapter 1, CyV consists of linearly sweeping the potential of the FC, in cycles (typically within a 0.05 to 1.2V range). These conditions are generated with a potentiostat that imposes a voltage on the stack terminals, meaning that the cell voltage and current are decorrelated (normally bound to a PolCurve). In other words, low cell voltage may be reached without having to draw much current, and the highest cell voltage is not limited to the OCV. In this configuration (electrical potential imposed by a potentiostat), the oxidation/reduction conditions of all Pt surface species (e.g. carbon monoxide, hydrocarbons, sulfur) are theoretically reachable.

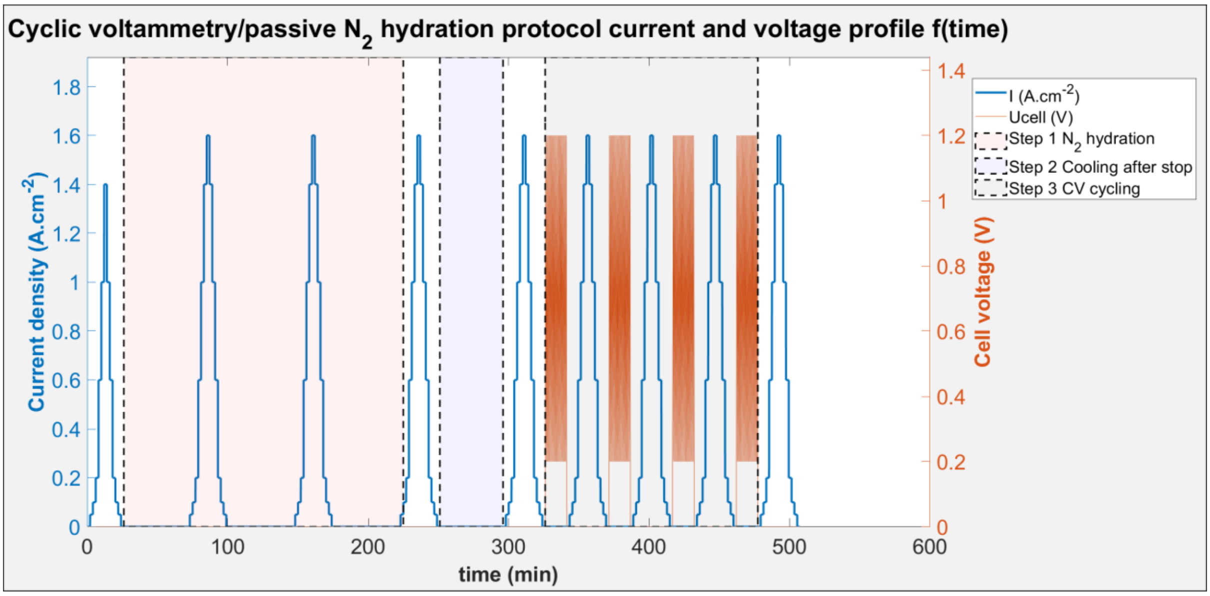

FIG. 4.8. CYCLIC VOLTAMMETRY/ PASSIVE N_2 HYDRATION ACTIVATION PROTOCOL CURRENT/VOLTAGE PROFILE

Similar to most protocols from the literature [58], [179], papers that present the CyV and/or N_2 hydration techniques use small single cell MEAs ($25cm^2$) to test the break-in procedure. It thus had to be adapted to the scale of a large surface stack [82]. This mostly consisted of adjusting the CyV hardware setup to a stack (traditionally applied to single cells), and limiting the RH during N_2 hydration to 90% (to prevent excessive condensation). Similarly, according to these papers, break-in is completed within two hours (whose duration is not valid for large surface stacks). FIG. 4.8 and TABLE 4.5 provide the current/voltage profile and the operating conditions of the final proposed break-in protocol, respectively. The CV cycles are composed of sets of 20 triangular waves (separated by PolCurves), swept between 0.2 and 1.2V, at a speed of $50mV.s^{-1}$ per cell. These criteria took into account the general cycling speed suggestions (5 to 100 $mV.s^{-1}$ per cell) [86], used parameters for similar break-in procedures [58], [77], and material limitations (see next section).

Operating conditions during cyclic voltammetry/passive N_2 hydration activation protocol	
Anode / Cathode Pressure (barabs)	2 / 2, except for stack shutdown (step 2) at ~Patm
Anode Stoichiometry (or flowrate)	1.5 for PolCurves, and 23 / 13.5 $Nl.min^{-1}$ for N_2 hydration / CyV
Cathode Stoichiometry (or flowrate)	1.8 for PolCurves, and 23 $Nl.min^{-1}$ for N_2 hydration / CyV
Anode RH (%)	50% for PolCurves / CyV and 90% for N_2 hydration
Cathode RH (%)	30% for PolCurves / CyV and 90% for N_2 hydration
Outlet Temperature (measured)	80°C (estimated value), except for stack shutdown (at ~20°C)
Inlet Temperature (reference)	77°C (controlled value), except for stack shutdown (at ~20°C)

TABLE 4.5. CYCLIC VOLTAMMETRY/N_2 HYDRATION ACTIVATION PROTOCOL OPERATING CONDITIONS

Additional material/time constraint related adjustments have been made to the protocol. The peak current density of the PolCurves is limited to $1.6A.cm^{-2}$, as the G400 test station automatically starts stepping the current downwards, once sub-0.5V cell voltage conditions are reached. Considering a GEN1 stack was used for this protocol (which has lower performance than the NextGen prototype), this condition was rapidly met. Apart from its ionomer hydration virtues, the aforementioned “cooling after stop” phase (step 2) has a second function. Indeed, this stack shutdown phase allows the (500min long) break-in protocol to be carried out over two days, and reduces the time during which the full potentiostat setup is required (FIG. 4.4).

4.2 Protocol application and data analysis

Adapting the break-in procedure to a large surface stack level (here a 5-cell GEN1 stack) posed many challenges. To achieve a mean voltage sweep of 50mV.s^{-1} per cell during CyV, a 250mV.s^{-1} sweep was imposed on the stack terminals. This method resulted in an uneven cell voltage distribution (see FIG. 4.9), leading to heterogeneous oxidation/reducing conditions between cells and consequently unbalanced activation rates. Much lower voltage distribution gradients are however shown in similar test of the literature, on activated stacks [180]. Wasterlain *et al.* for example measured a 6% ECSA difference between the voltammograms of each cell (also for a 5 cell stack) [86]. The observations of FIG. 4.9 may thus be caused by uneven cell performance (proton conductivity, ECSA, etc.) during stack activation. The used CyV method may thus have to be revisited (e.g. individual cell voltage control, instead of control over the stack terminals).

Other challenges with the setup of FIG. 4.4 included the Biologic Flex P0160 50A booster voltage range constraints. The minimum achievable voltage of 1V meant that the CyV voltage sweep could only go down to 0.2V (1V divided by 5 cells), instead of the traditionally used 0.05V limit. This distorted data in the low voltage zone resulted in uninterpretable voltammograms (which may also party be caused by the uneven cell voltage distribution). Consequently, the CyV characterization methodology cannot be used to further analyse the break-in results (see section 4.1.4 of chapter 1). Also, the concentration of the species that desorbed from the catalyst surface was too low to be identified by the Agilent Micro-GC (10ppm detection limit)

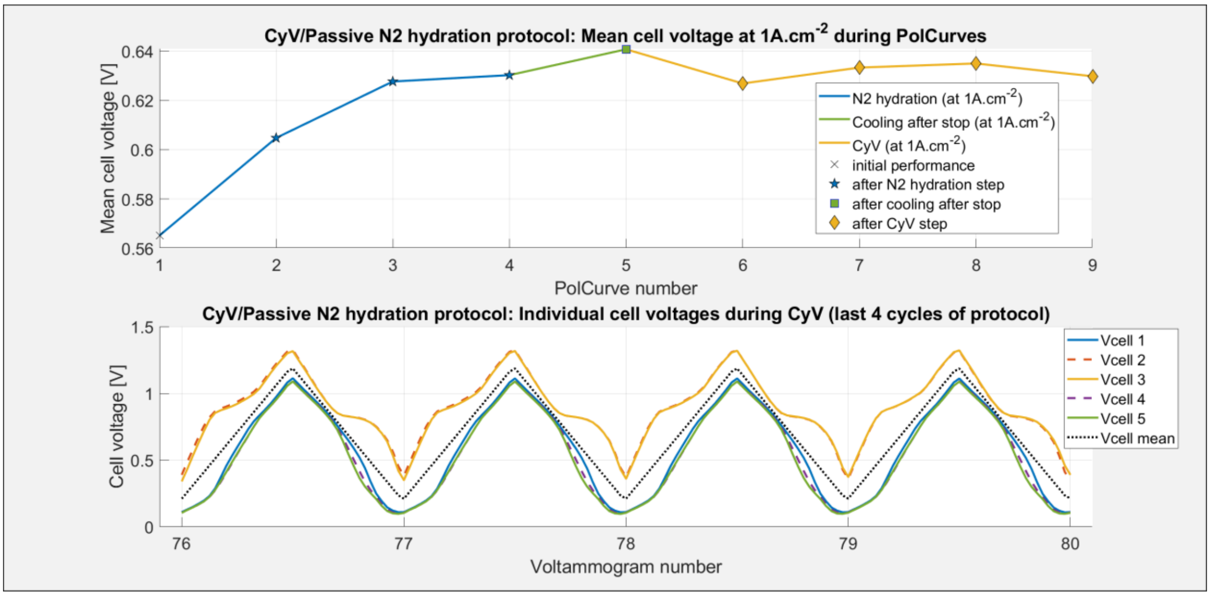

FIG. 4.9. CYV/N$_2$ HYDRATION BREAK-IN PROCESS: MEAN CELL VOLTAGE EVOLUTION (AT 1A.CM^{-2}) DURING POLCURVES, AND INDIVIDUAL CELL VOLTAGE EVOLUTION DURING CYV (LAST 4 CYCLES)

To analyse the general fuel cell performance evolution during break-in, the PolCurves are used (see Fig. 4.8). More specifically, as for the previous section, the data at 1A.cm^{-2} is analysed (see Fig. 4.9). One may first note that the absolute value of the mean cell voltage remains relatively low. This is due to the fact that an ancient GEN1 prototype was used, and that the control parameters of the G400 test station were not ideal for this stack (e.g. stack temperature control through cooling input). Therefore, the cell voltage evolution trend is mostly taken into account for this analysis, not its absolute value.

Fig. 4.9 shows the most drastic performance increase during the N_2 hydration step. This said, it was clearly not sufficient to fully activate the ionomer, as shown by the subsequent cooling after stop phase. As will be proven in section 4.3, ionomer activation remains incomplete post-break-in. Even though it may be efficient for a small cell (25cm^2 in literature), the N_2 hydration method is not adapted for large stacks. This confirms the comments towards passive hydration made in the three previous chapters of this manuscript.

The PolCurve measurements during CyV indicate a performance stabilization and/or decline (within the ~5mV.cell^{-1} range between points). From these results, one could presume that (i) CyV had a negligible effect on fuel cell break-in (ii) break-in is finalized (as the measurements meet most end-of-break-in criteria). Both these interpretations and resulting statements are however incorrect. Indeed, in this application, the CV cycles partly dried out the stack, prior to the pseudo PolCurves. The conditions of Table 4.5 (e.g. flowrate, RH) must thus be revisited (to take account for the absence of produced water during CyV). The beneficial impact of the CyV method is thus not seen through the PolCurves in Fig. 4.9, as it is hidden by the increase in ohmic losses. This elucidates the difficulties involved with stack characterization during break-in, and the definition of an end-of-break-in criterion. The benefits of CyV will be further studied in section 4.3.

4.2.1 Analysis with analytical ionomer activation model

As for the previous protocol, an additional break-in data analysis is carried out using the ionomer activation model (Table 4.6). For this, the current profile of Fig. 4.9, the operating conditions of Table 4.5, and associated stack characteristics (Gen1) are used as input of the ionomer activation model (chapter 2).

Ionomer break-in model coefficients evolution for cyclic voltammetry/passive N_2 hydration protocol

Coefficient convergence	$R_{skin\ \mathrm{an}}$ (time | value)	$R_{skin\ ca}$ (time | value)	R_{dspac} (time | value)	R_{cont} (time | value)
to 10% from final value	12.4min | 0.1	12.4min | 0.1	168min | 1.5×10^{-2}	/ (never reached)
to 1% from final value	15.6min | 10^{-2}	15.6min | 1×10^{-2}	359.4min | 1.5×10^{-3}	/
to 0.1% from final value	82.5min | 10^{-3}	/ (never reached)	493min | 1.5×10^{-4}	/
to final value	87.8min | 0	/	/ (never reached)	/

TABLE 4.6. IONOMER BEAK-IN MODEL OUTPUT FOR CYCLIC VOLTAMMETRY/PASSIVE N_2 HYDRATION PROTOCOL

The model clearly indicates that this protocol has not fully activated the ionomer, thus once again pointing to the ineffectiveness of the passive N_2 hydration method. Indeed, according to the model, over 28% of the contaminants are still located in the ionomer at the end of the break-in procedure, meaning that its decontamination process is not finalized. Additionally, the 72% of contaminants that did evacuate from the ionomer have partly redeposited on the catalyst surface, reducing stack performance (see section 6.1.3 of chapter 2). Indeed, the final post-activation R_{cont} value is 19% higher than its initial value, meaning that break-in has actually increased stack contamination. Additionally, the domain spacing resistance reduction is sluggish, and never fully converges to zero (see TABLE 4.6). The same goes for the cathode surface skin resistance. The uncomplete activation and catalyst contamination are mainly caused by the dry conditions during the CyV step and the absence of current during most of the break-in procedure (TABLE 4.5). The claim that ionomer activation is incomplete after break-in will be further proven in subsection 4.3.

This said, the model does not simulate all the benefits of the cooling after stop phase (as shown by the experimental data of FIG. 4.9). Indeed, during a prolonged stack shutdown phase, water condensation on/near the active sites, can slowly further hydrate the ionomer. Simulating the progressive water sorption in a stack that is shut down (isolated system, no flow) is thus part of the future work related to this model.

4.2.2 Analysis with break-in diagnosis tool

As for the procedure presented in section 3.2.2, the PolCurve data at 1A.cm^{-2} of FIG. 4.8 is used as input for the break-in diagnosis tool, to classify it using the training database presented in chapter 3. The output of the diagnosis tool (the class affected to each data point) is summarized in TABLE 4.7.

The diagnosis tool once again provides generally coherent and confident classification results. The same comments as for the application of this tool on the previous break-in protocol (see section 3.2.2) can however be made, regarding its optimistic results. This time however, this interference on the results is mainly related to the fact that the break-in data is provided by a vastly different test station (G400) than for the training dataset (TB07). According to the diagnosis tool, one N_2 hydration step (between 16 and 8N1min) is sufficient to fully activate the ionomer (100% confidence). Similarly, it is confident (at 100%) that the second N_2 hydration step is sufficient to reach full stack activation (which does not concur with FIG. 4.9).

Break-in diagnosis tool results for cyclic voltammetry/passive N_2 hydration protocol in the 1A.cm^{-2} region				
Key time periods (min)	0 to 16	81 to 91	156 to 316	351 to 507.4
Labels (and % of data associated to each label)	Non-activated (100 %)	Ionomer (100 %)	Fully activated (100%)	CL (38.1%), Fully activated (56.5 %), Ionomer (3.6 %), Ionomer + CL (1.8%)

TABLE 4.7. BREAK-IN DIAGNOSIS RESULTS FOR CYCLIC VOLTAMMETRY/PASSIVE N_2 HYDRATION PROTOCOL

Interestingly, after 316 minutes of break-in, as the CyV activation step starts (see FIG. 4.8), the classifier partly changes its mind regarding the full stack activation label. Indeed, for the following PolCurves (during the CyV activation step, between 351 to 507.4min), the diagnosis tool decided to affect another label to an important fraction of the data samples (38.1%). This label corresponds a scenario where the CL pore structure is activated, but where the ionomer is not (nor the catalyst surface). This classification decision strongly indicates that (i) during CyV, the stack dried out (as the ionomer is classified back to non-activated), and that (ii) part of the other break-in mechanism remain activated or are being activated by the voltammograms (as the CL pore structure remains activated). This confirms the observations made in section 4.2. Furthermore, a second piece of information indicates that stack drying occurs during CyV. Indeed, the diagnosis tool provides less confident classification results during the CyV step, shown by residual samples affected to ionomer activation (3.6 %), and CL + ionomer activation (1.8%). This may be assimilated to the presence of a faulty condition (stack drying), which is known to interfere with the results of the break-in diagnosis tool (section 2.2 of chapter 3). Now that the experimental data of the CyV/N_2 protocol on break-in kinetics has been fully analysed, its impact on fuel cell degradation may be evaluated.

4.3 Protocol degradations and impact on durability (Sintef collaboration)

As previously stated, this break-in protocol has been completed with a fuel cell ageing test plan (using the G400 test station). Indeed, during the application of CV cycles, the Pt catalyst electrochemical instability potential zone is reached (>1V) [181]. Higher potentials result in the creation of various oxide species on the Pt surface, and increase of Pt-O bond strength [38]. Potential cycling itself also remains one of the most damaging stressors for PEMFCs [181]. Its impact on stack performance must thus be determined.

To generate fuel cell degradation data, two test plans typically exist. One, known as "natural" ageing, consists of letting the stack go through a current profile, representing normalized driving cycles. This protocol typically requires up to 5,000 hours to be completed, depending on the stack degradation rate, and end of life criteria. The second type of protocol, categorized as "accelerated stress tests", or ASTs, uses operating parameters that are designed to increase the stack degradation rate. They often consist of cycling the stack voltage at a high amplitude and frequency. With these protocols, a fuel cell stack can reach its end-of-life performance in 500 hours or less. The issue with ASTs is however that they cannot be correlated with a natural degradation rate, as the current/voltage profile and thus degradation phenomena are vastly different.

Apart from the quantification of the degradation rate caused by CyV, the ageing test plan that is proposed in this manuscript has a second ambitious objective. This goal is to obtain an ageing protocol that can be more rapidly applied than a traditional protocol, whilst remaining representative of the natural ageing mechanisms (unlike ASTs). Obtaining such a protocol would drastically reduce the cost and time-consuming characters of a fuel cell ageing protocol, making it more accessible for post-activation characterization.

4.3.1 Presentation of ageing protocol: WLTC cycles and characterization methods

As the GEN1 fuel cell is dedicated to vehicular applications, the load profile and operating conditions used for the ageing protocol are based on WLTCs (Worldwide Harmonized Light Vehicles Test Cycles). This cycle (FIG. 4.10) is composed of city, extra-urban and highway driving, to represent the different current profiles that the stack would go through in a vehicle. In this scenario, the main vehicle power demand is supplied by the fuel cell, which is hybridized with a small battery (to smooth the current demand spikes).

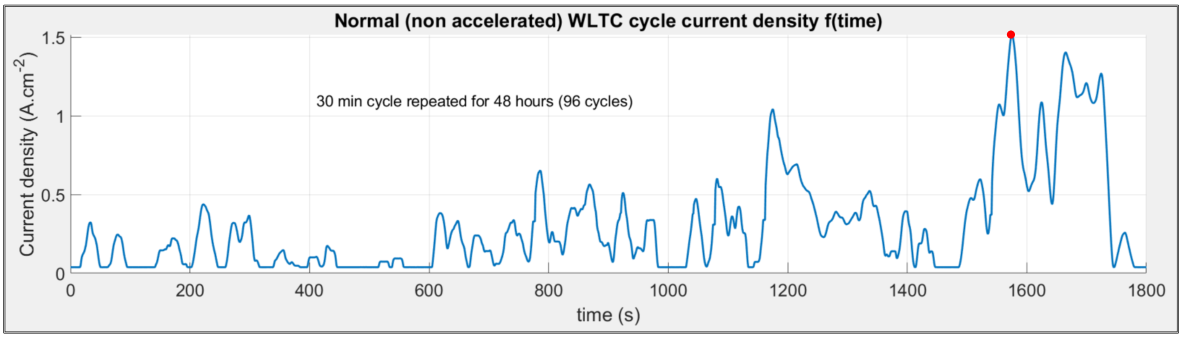

FIG. 4.10. NORMAL (NON-ACCELERATED) VERSION OF THE WLTC AGEING CYCLES CURRENT PROFILE

As previously stated, the objective of this ageing test plan, is to develop a "hybrid" AST/natural ageing protocol. For this, a mix of natural and accelerated ageing cycles are used. The natural and accelerated degradation steps are periodically switched, to better correlate the accelerated degradation rate with natural ageing. The natural fuel cell degradation step is based on the 30-minute normalized WLTC cycle (FIG. 4.10), which is repeated for 48 hours. The accelerated fuel cell degradation step is based on the exact same profile, also repeated for 48 hours. In this step however, the WLTC cycle time is reduced from 30 to 20 minutes. This increases the current variation kinetics and should thus theoretically accelerate degradation.

To further evaluate the efficiency of the "pseudo-AST" protocol, and to obtain additional useful information related to stack degradation, fuel cell characterization is also applied periodically. Fuel cell characterization consists of applying PolCurves, EIS and CyV. These methodologies have been presented throughout sections 4.1.2 to 4.1.4 of chapter 1. The entire characterization step is completed in ~7 hours and is carried out after each 48-hour degradation step. The entire experimental plan consists of repeating the following pattern: 48h natural ageing / characterization / 48h accelerated ageing / characterization.

The PolCurve profile corresponds to one upwards and one downwards current stepping cycle (330 sec per step with a $0.076A.cm^{-2}$ interval). The maximum current value of the PolCurve is automatically chosen by the Emerald software, depending on a minimum cell voltage threshold value (set to 0.4V). The EIS is carried out for three different current densities: 0.5, 1 and $1.5A.cm^{-2}$. The perturbation current corresponds to 5% of the total current density, and the signal frequency is swept between 0.1Hz and 6kHz, with a resolution of 10 points per decade. For the CyV, the stack potential is linearly swept between 1 and 4V (0.2 to 0.8V per cell). The 4V limit is imposed to prevent high-potential-related stack degradations (and the 1V limit is set by the booster). The stack scan rate is set at $250mV.s^{-1}$ (mean scan rate of $50mV.s^{-1}$ per cell). The operating conditions during the WLTC cycles, EIS, PolCurve and CyV are summarized in TABLE 4.8.

Operating conditions during WLTC cycles, EIS, PolCurve and CyV	
Anode / Cathode Pressure (barabs)	2 / 2 (and P_{atm} + pressure losses during CyV)
Anode / Cathode Stoichiometry (or flowrate)	1.5 / 1.8 (and 4 / $5NL.min^{-1}$ during CyV)
Anode / Cathode RH (%)	50 / 30
Outlet Temperature (measured)	80°C (estimated value)
Inlet Temperature (controlled)	77°C (controlled value)

TABLE 4.8. AGEING PROTOCOL OPERATING CONDITIONS (WLTC CYCLES, EIS, POLCURVE AND CYV)

4.3.2 Ageing data analysis

In this test plan, 4 normal and 4 accelerated ageing steps were carried out, accompanied by 9 characterization phases (one before and one after each ageing step), for a total duration of ~400h. The fourth and final accelerated ageing step however had to be prematurely terminated (after only 7h instead of 48h). This was due to the stack performance (progressively reducing with ageing) reaching a point where it became unable to follow the imposed current profile (FIG. 4.10). Consequently, its response to the dynamic cycle (voltage drop) kept triggering the G400 test station security (voltage threshold value).

An in depth ageing data analysis has been carried out by fitting the PolCurves to the Butler-Volmer model [11], and the EIS curves to a R+(R/C)+(R/C) model [182]. Using the Butler-Volmer model, the reaction-rate, ohmic and mass transfer losses are extracted from the PolCurves (at $1.6A.cm^{-2}$) and dissociated (see FIG. 4.11). Similarly, each set of parallel components of the EIS model (R+R/C+R/C) corresponds to one type of fuel cell losses. Here they are the ohmic (R), charge transfer (R/C) and mass transfer (R/C) losses (shown in FIG. 4.12). The EIS analysis is mainly based on the curves at $1.5A.cm^{-2}$, as they provided the clearest, least distorted results (compared to the curves drawn at 0.5 and 1A.cm^{-2}). The voltammograms are not used for this analysis as the CyV measurements are relatively uncertain (as explained in section 4.2).

What can firstly be noted, is that the initial PolCurve (at $t = 0$) displays a lower performance than the subsequent curve (after 48 hours of degradation). This may partly be due to the absence of a stabilization time before starting the PolCurves. Prior to the curve at $t = 0$, several CV cycles were carried out, which (as previously stated) partly dried out the stack. All the other PolCurves were preceded by the high current (high-water production) section of a WLTC cycle. The main reason behind this observation is however that residual break-in has occurred during ageing, and thus that the fuel cell activation was incomplete (at $t = 0$).

The EIS curve fitting shows that the high frequency resistance (HFR), which is an image of the ionomer resistance, is responsible for this reduced initial performance (higher at $t = 0$ than after ageing). The dissociated characteristics of the fitted PolCurves provide agreeable results, indicating a sharp reduction in ohmic resistance after break-in (FIG. 4.11). Both the characteristics of the fitted EIS data and PolCurves thus once again indicate that the humidified N_2 injection method is not efficient to activate the ionomer (section 4.3). This confirms that current must be drawn to fully activate the membrane, and comforts the more or less hypothetical processes (domain spacing, surface skin change, etc.) within the ionomer. Interestingly, both the PolCurves and EIS characteristics show that all other fuel cell losses (reaction-rate, charge transfer and mass transfer) are minimized post-activation (and subsequently increase with ageing). This indicates that the variable voltage during CyV successfully desorbed the species from the catalyst surface (ECSA increase). In other words, CyV successfully activated the catalyst, elucidating the beneficial aspect of this method.

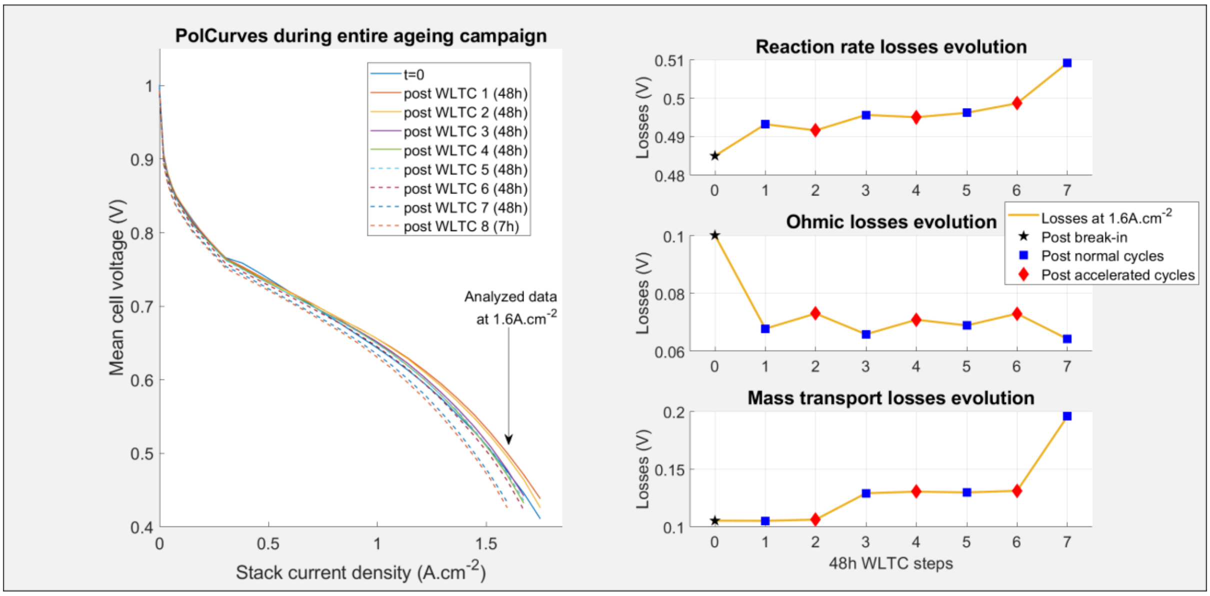

FIG. 4.11. POLCURVE MODEL (BUTLER VOLMER) CHARACTERISTICS EVOLUTION DURING FUEL CELL AGEING

As for analysis of stack ageing, a few first comments can be given regarding the overall degradation rate during this campaign. The total performance loss (measured on the PolCurves, see FIG. 4.11), is of 27.5 and 75mV.cell^{-1} at 1 and 1.6A.cm^{-2}, respectively (0.138 and 0.375V for the stack). This translates to degradation rates between 80 and 219µv.h^{-1}.cell^{-1} (over the ~343h long ageing period, assuming negligible impact of the PolCurves, CyV and EIS). According to the DOE recommendations, the EoL (end of life) is reached at a

10% total power loss within the 1 to 1.5A.cm^{-2} range (for a 5,000h durability target). The stack thus reached 42% of its EoL at 1A.cm^{-2} in only ~343h (this figure worsens at higher current densities). This elevated degradation rate may partly be due to the accelerated ageing cycles (pseudo-ASTs). The non-ideal control on the G400 (e.g. cooling input control) and the fact that the used stack (GEN1) is a prototype may however also be partly responsible. Considering these variables, it is complex to make a certain statement. It however clearly seems that the break-in protocol has degraded the fuel cell, and consequently reduced its lifetime.

With the characteristics of the EIS and PolCurves, the degradation rate of each individual fuel cell components can be analysed separately. For example, the absence of HFR (FIG. 4.12) and ohmic losses (FIG. 4.11) increase with ageing indicates little to no membrane degradation, nor BPP degradation (formation of oxides on its surface). In contrast, the EIS and PolCurves clearly indicate an important increase in mass transport losses with ageing. This corresponds to a reduction of the ion concentration and mobility between the membrane and the CLs. The mass transport capacity of the EIS circuit, (which can be attributed to stored oxygen in the cathode catalyst layer) [183] does however not change over the lifetime of the stack.

No decisive conclusions can be drawn regarding the charge transfer resistance variation during ageing. Indeed, the EIS curves show no charge transfer resistance variation during ageing, which contradicts the progressive increase in reaction-rate losses (slight CL degradation) shown by the PolCurves. Additionally, a slight pressure drop occurred on the lower gas flowrates zone of the PolCurves, possibly interfering with (amplifying) the reaction-rate losses measurements. Similarly, the increase of the charge transfer capacitor (double layer capacitance of the CL) measured on the EIS at 1.5A.cm^{-2} is also not fully reliable. Indeed, is the only metric whose trend is not in agreement with the other EIS curves at 0.5 and 1A.cm^{-2} (not presented in detail in this manuscript), which both show a decreasing tendency.

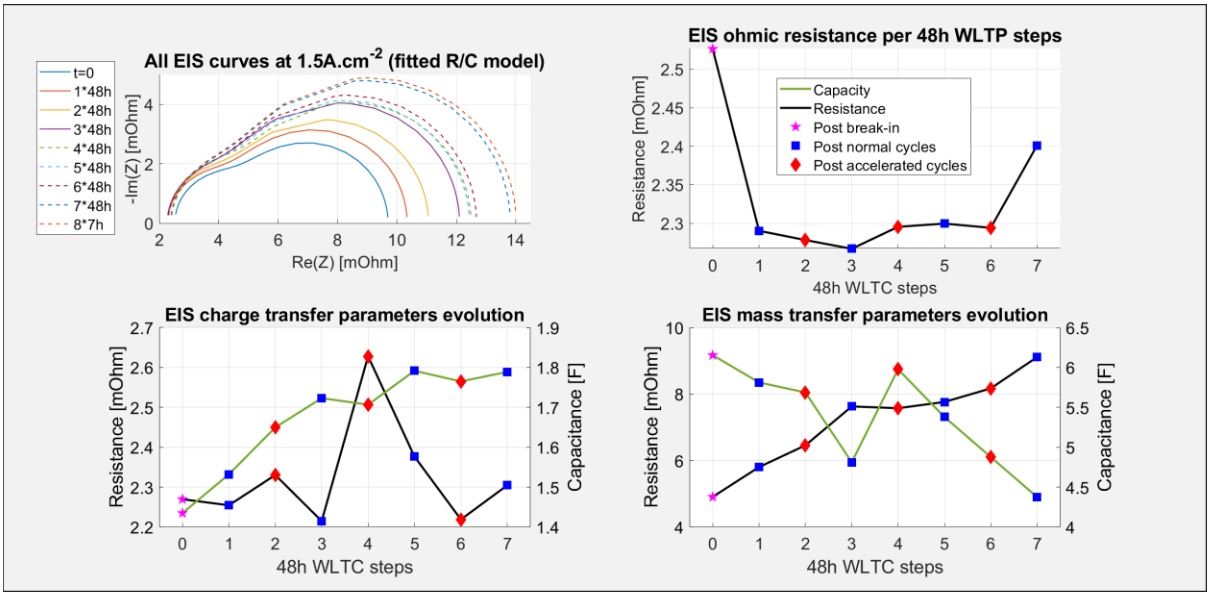

FIG. 4.12. EIS MODEL (RES/CAP) CHARACTERISTICS EVOLUTION AT 1.5A.CM^{-2} DURING FUEL CELL AGEING

As previously stated, the second objective of this ageing campaign is to be able to accelerate the stack degradation rate, whilst remaining representative of the natural ageing mechanisms (unlike ASTs). To determine if this objective has been reached or not by accelerating the WLTC cycling rate, various data analysis procedures have been carried out. Firstly, the stack degradation rate has been quantified by tracking its voltage evolution during the WLTC cycles at 1.5A.cm^{-2} (corresponding to the peak current value of each cycle, see red dot on FIG. 4.10). Interestingly, this resulted in an almost identical mean cell voltage loss per WLTC cycle (-0.234 mV for the 30min cycle, and -0.224mV for the 20min cycle, see TABLE 4.9). These results seem to indicate that it is possible to reduce the WLTC cycling time whilst preserving the same degradation rate per cycle. One must however keep in mind that these degradation measurements are carried out for non-stable (transient) conditions, and are composed of the sum of reversible and irreversible losses.

Indeed, the more precise stack performance measurements for stable (steady state) conditions (during PolCurves and EIS), do not provide the same results. Both characterization methods seem to indicate that stack degradation occurs at comparable rates for the normal and accelerated WLTC cycles. For example, the two highest mass transfer losses increase measured by the EIS and the PolCurves are related to the 3rd and 7th WLTC steps, which both correspond to 30min (non-accelerated) ageing cycles. Similarly, no pattern is identifiable in the reaction-rate (FIG. 4.11) and charge transfer (FIG. 4.12) losses evolution, to dissociate normal and accelerated WLTC cycles. In steady state conditions, the advantage of increasing the WLTC cycling rate thus seems to disappear. This said, unlike ASTs, when reducing WLTC cycling time, the degradation phenomena remain comparable as they affect the same stack components at proportional rates.

Number of ageing step (48h per step)	1 (a)	2 (b)	3 (a)	4 (b)	5 (a)	6 (b)	7 (a)
Total degradation (at 1.5A.cm^{-2}) during 48H WLTC step (mV.cell^{-1})	-27.98	-44.67	-24.71	-30.61	-15.04	-21.53	-19.35
Mean degradation (at 1.5A.cm^{-2}) per individual WLTC cycle (mV.cell^{-1})	-0.291	-0.31	-0.287	-0.213	-0.157	-0.15	-0.202

TABLE 4.9. DEGRADATION RATE MEASURED DURING WLTC CYCLES (A= 30 MIN CYCLES, B= 20 MIN CYCLES)

To conclude, the *N_2 hydration/CV cycling* break-in protocol (FIG. 4.8) it is not efficient in its current form. The N_2 hydration method should not be applied to break-in a stack, as it has proven to not fully activate the ionomer. The subsequent CyV step exacerbated the membrane hydration state by operating the stack at an elevated flowrate and reduced RH. This said, according to the fuel cell ageing campaign, this step rapidly and efficiently desorbed the surface-blocking species from the catalyst. Additionally, CyV is compatible with low H_2 flowrates (4.3g.h^{-1}.cell^{-1} in TABLE 4.8). The overall used stack voltage control method (potentiostat) also has many opportunities for improvement. Indeed, as more knowledge is gathered towards the catalyst desorption mechanisms (e.g. sulfur desorption > 0.8V [38], [184], [185]), a number of fixed optimal potentials may be reached to further accelerate break-in. The characterizing nature of CyV during break-in (not shown here, as booster voltage limitations resulted in unexploitable voltammograms) is also hugely advantageous.

According to the subsequent ageing campaign, the CyV method has its flaws with regards to stack durability, as rapid performance reduction rates were measured. Increase in mass transfer losses, significant CL porous structure degradations, and/or loss of GDL hydrophobic properties have occurred, for which the CyV method may partly be responsible. The membrane does however not seem to be affected, as no degradation is observed during the ageing procedure. The second objective of this ageing campaign (develop a hybrid pseudo-AST), is not obtainable by accelerating the WLTC cycling rate. It thus seems that to truly evaluate the impact of a break-in protocol on fuel cell ageing, going through a 5,000h long natural ageing protocol is required. Additional information regarding the used experimental data can be found in a joint publication, led by Aubry *et al.* [186], which used the ageing database to fuel a PEMFC prognosis program.

5 Break-in protocol: Pulsed current cycles activation

From the list of break-in protocols presented in this chapter, the *pulsed current cycles* break-in process targets rapid fuel cell activation (including performance increase and stabilization). This however comes to the expense of cell durability, which is not ensured. This protocol is therefore suitable for applications where a fuel cell with stable performance must rapidly be obtained, no matter the impact on stack durability.

5.1 Presentation of protocol and its main objectives

As its name suggests, the *pulsed current cycles* protocol consists of imposing frequent, periodic and high amplitude current fluctuations. More specifically, the current is alternated between near-short circuit and OCV conditions (FIG. 4.13). Permuting between these two states is supposedly capable of fully activating the fuel cell. Therefore, this protocol is solely based on that single step (repeated periodic switches between OCV and high current phases). For performance measurements reasons, a second and last iso-current step is added to the protocol. Similarly, due to the absence of simultaneous characterization and break-in (contrary to the previous protocols), pseudo PolCurves have been implemented each 45 minutes. This interval is a good compromise between the time required to draw a PolCurve, and the amount of information it provides.

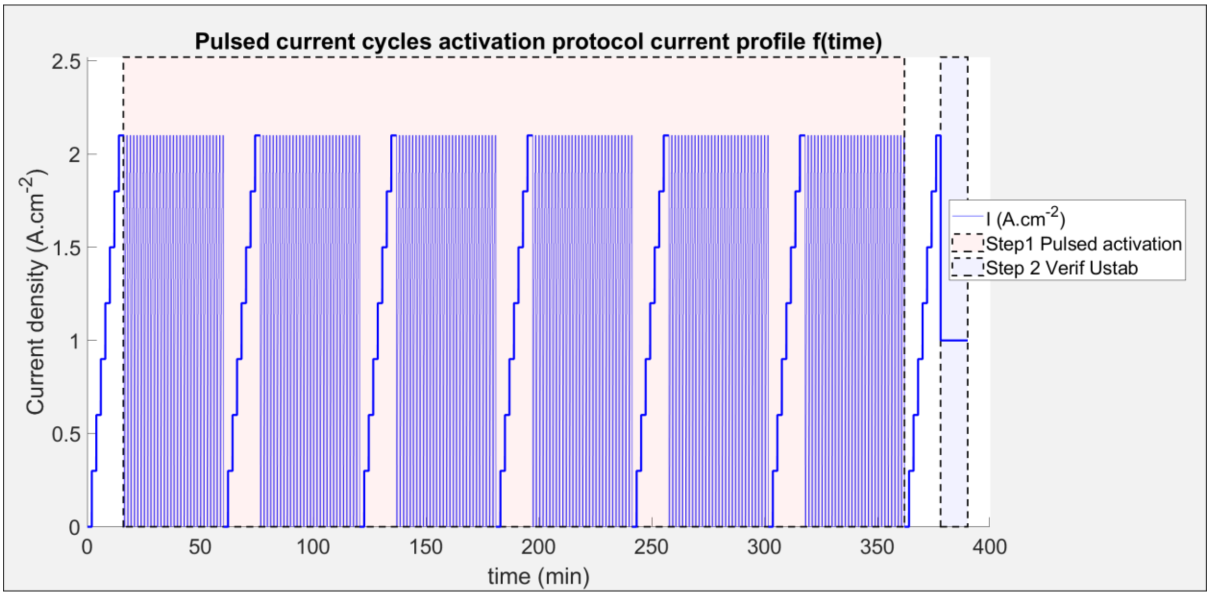

FIG. 4.13. PULSED CURRENT CYCLES ACTIVATION PROTOCOL CURRENT PROFILE

At extreme, near short-circuit conditions, every break-in morphological change occurs simultaneously, at an accelerated rate (section 3.2.4 of chapter 1). The maximized current (and water) production increases the ionomer activation kinetics, whilst the elevated reactant flow rapidly opens CL pores. Switching between OCV and high current conditions desorbs the catalyst surface-blocking-species, over a vast potential range. These species, along with other non-anchored particles, are evacuated by the elevated humid reactant flows. The OCV phase also mitigates fuel cell degradations, typically related to prolonged high current operation.

The fluctuating signature (between high/low potentials, flow rates, heat, water production, etc.) of this method further accelerates the break-in process. Indeed, periodic reduction/oxidation, along with dry/humid cycles may be required to fully activate the ionomer and "clean" the catalyst (see section 3.2.1 of chapter 1).

This protocol is mainly inspired by the work of Galitskaya *et al.*, among others [61], [62] (section 3.2.4 of chapter 1). The Galitskaya *et al* . method has been developed for (and demonstrated on) a single MEA of 1cm^2. It therefore required multiple adjustments to be suitable for an automotive grade stack. For example, in [23], the current is brought up to a value where the equivalent cell voltage equals 0.1V. On a large stack, non-equilibrium thermal and electrochemical conditions caused by near short-circuit operation are amplified. Imposing frequent "idle time" or "relaxation" (OCV) phases is therefore not sufficient to fully prevent degradations. Even though this protocol does not prioritize fuel cell durability, it must be adapted to prevent hazardous mechanical degradations such as pinholes in the membrane, or full corrosion of components. The main adjustment consisted of limiting the current to a peak value to 2.1A.cm^{-2} (regardless of the resulting voltage). Additionally, the stabilization time at high current is limited to 20s (and set to 20s at OCV), and the current increase rate to 43mA.cm^{-2}.s^{-1} (FIG. 4.13).

Additional precautions are taken during this protocol to prevent stack failure (performance drop) and excessive degradations. At 2.1A.cm^{-2}, the electrochemical water production at the cathode is maximized. This can prevent reactants from reaching the active sites, inducing local starvations and amplifying the non-equilibrium conditions. Therefore, an excessive amount of reactants (high stoichiometry) is supplied to partly drain the produced water. This high gas flow rate also favors catalyst impurity evacuation. Similarly, the anode and cathode RH are reduced to 70 and 40% respectively (instead of saturation in [23]). In addition to the current profile of FIG. 4.13, the specific used operating conditions are provided in TABLE 4.10.

Operating conditions during pulsed current cycles activation protocol	
Anode / Cathode Pressure (barabs)	2 / 2
Anode / Cathode Stoichiometry	1.5 / 2.2
Anode / Cathode RH (%)	70 / 40
Outlet Temperature (reference)	80°C (controlled value)
Inlet Temperature (measured)	70°C (estimated value)

TABLE 4.10. PULSED CURRENT CYCLES ACTIVATION PROTOCOL OPERATING CONDITIONS

The conditions of TABLE 4.10 remain identical during the last step of the protocol (>10min performance stabilization check), to avoid interference caused by the stack and/or test station response/stabilization times.

5.2 Protocol application and data analysis

In this subsection, the performance results of the *pulsed activation* method, applied on a 10-cell NextGen stack, using the TB07 testbench, are presented. In addition to the PolCurves, performance evolution monitoring has been carried out by tracking the mean cell voltage evolution at 2.1A.cm^{-2} (FIG. 4.14). This value is chosen as it corresponds to the zone where all fuel cell losses (reaction rate, ohmic and mass transfer) are combined for a NextGen stack. The protocol presented in FIG. 4.13, is of long duration (~6h30), meaning that break-in will probably be finalized before the procedure is completed. This duration has however been chosen, to provide a clear observation of performance convergence, stabilization, and possibly decline.

According to the PolCurve measurements (carried out each 45min, see FIG. 4.13), the USFCC performance convergence criterion [15] (see section 3.2) is reached between the second and third PolCurve. Residual performance increase and stabilization (to <1mV deviations) is observed during the subsequent PolCurves. The transient measurements at 2.1A.cm^{-2} (FIG. 4.14) fully agree with the PolCurve data. Indeed, the performance converges to less than 5mV from its final value (0.6075V) at ~105min (located between the second and third PolCurve). Additionally, residual performance increase and near-full convergence (at ~240min) are observed after the USFCC criterion has been reached. Similar to the protocol of section 3, the post-break-in PolCurve, and the iso-current performance verification step at the end of the break-in protocol both indicate that peak performance has been reached. A similar slight gradual performance decline of ~5mV/cell is even visible during the iso-current verification step. The results provided by this protocol thus prove that a high range variable load is a fundamental stressor to accelerate the break-in kinetics.

By following the USFCC guidelines, and by assuming that the PolCurves have a negligible impact on cell activation, 1h30 of pulsed current cycles are sufficient to reach the end-of-break-in criterion. Per cell (NextGen), this results in a hydrogen consumption of 28g (no recirculation). For a traditional protocol (e.g. 0.25A.cm^{-2} for 19 hours [16], [54]), 70g would be required (for a H_2 stoichiometry of 1.5).

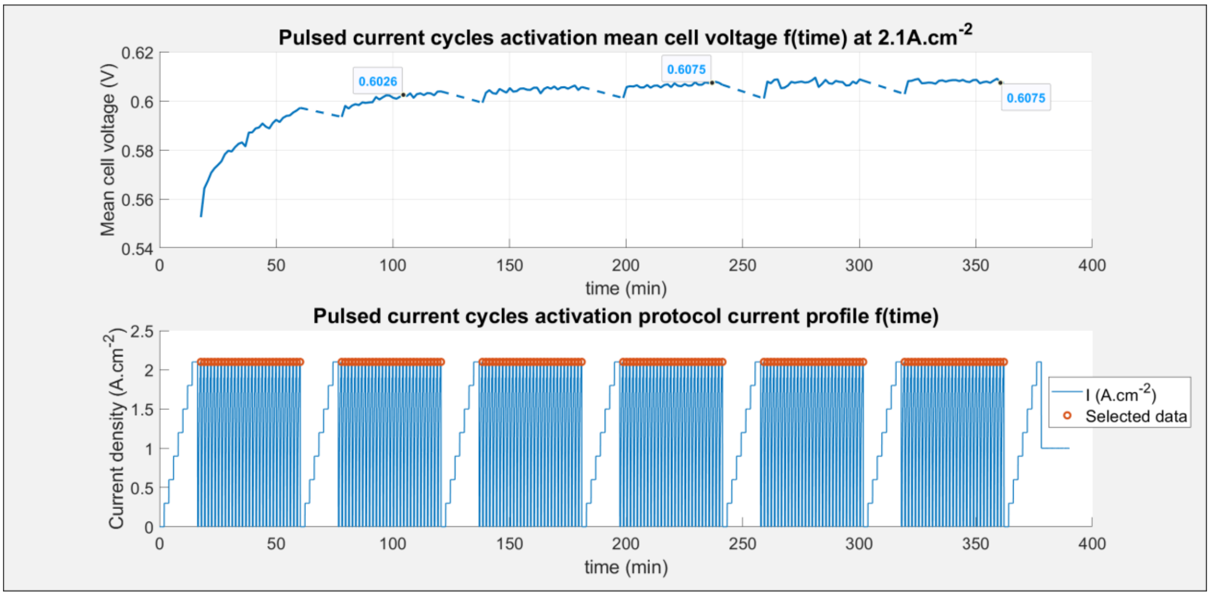

FIG. 4.14. PERFORMANCE EVOLUTION AT ISO-CURRENT (2.1A.CM^{-2}) DURING PULSED ACTIVATION

The duration of the break-in process may be further shortened by increasing the value of the peak current density (currently set to 2.1A.cm^{-2}). As previously stated, the high current steps in the literature aim at reaching voltages as low as 0.1V per cell [62] or even 0V (short-circuit) [61]. At these current values however, the effect of the mass transfer limitations become largely dominant. Consequently (among other safety concerns) the anode/cathode may periodically be starved, and the stack may locally overheat. The impact of pulsed/short-circuit operation on stack durability will be further discussed in subsection 5.3.

5.2.1 Analysis with analytical ionomer activation model

The results of the application of the ionomer activation model on the *pulsed current cycles* protocol (FIG. 4.13 and TABLE 4.10) are provided in TABLE 4.11.

As expected, the elevated, high humidity *pulsed current cycles* result in rapid ionomer activation. The initial barriers to sorption are almost entirely removed, before starting the first pulsed current cycle (16 min). According to the PolCurve measurements (carried out each 45min, see FIG. 4.13), the ohmic losses region has fully converged to a final value between the third and fourth curve (~135 to 180min). This concurs with the results of the model, indicating full domain spacing and ionomer contamination resistance convergence for similar durations (see TABLE 4.11). Only the final contamination resistance during this protocol is slightly more significant than for the current stepping/condensation procedure (see section 3.2.1). This is mainly due to the presence of "relaxation" phases (0A). Prolonged durations at the OCV must thus be prohibited.

Ionomer break-in model coefficients evolution for Pulsed current cycles protocol				
Coefficient convergence	$R_{skin\ \mathrm{an}}$ (time | value)	$R_{skin\ ca}$ (time | value)	R_{dspac} (time | value)	R_{cont} (time | value)
to 10% from final value	9.6min | 0.1	9.6min | 0.1	36.9min | 1.5×10^{-2}	151.2min | 4.4×10^{-3}
to 1% from final value	12.2min | 10^{-2}	13.4min | 10^{-2}	74.1min | 1.5×10^{-3}	165.6min | 3.8×10^{-3}
to 0.1% from final value	14.3min | 10^{-3}	15.3min | 10^{-3}	104.3min | 1.5×10^{-4}	167min | 3.7×10^{-3}
to final value	19.2min | 0	24.8min | 0	170.8min | 0	167.2min | 3.7×10^{-3}

TABLE 4.11. IONOMER BEAK-IN MODEL OUTPUT FOR PULSED CURRENT CYCLES PROTOCOL

The beneficial aspects of specific stressors such as hydration cycling (membrane swelling/shrinking effect) [24] on ionomer activation rates are also partly elucidated with this model. Indeed, the high current phases of the pulsed cycles display a water content profile with an important gradient between the anode and cathode (due to the elevated water production and electro-osmosis flow). The rapid drop to OCV removes the electroosmotic drag and rapidly diffuses the accumulated water at the cathode interface to the anode, therefore accelerating its local ionomer activation kinetics. Hydration cycling may thus result in more uniform ionomer activation between the anode and cathode interfaces. To experimentally confirm this observation, a number of additional tests have been carried out (on TB07 test station). These tests consisted of cycling the membrane water content (by adding "ripple" signals on stressors such as the flowrate and stack temperature), which effectively resulted in an increase of the ohmic resistance reduction rate.

5.2.2 Analysis with break-in diagnosis tool

As for the previous applications of the break-diagnosis tool, all the PolCurve data in the 1 ± 0.2A.cm^{-2} region is extracted (see FIG. 4.13) and classified using the procedure illustrated in FIG. 3.11 of chapter 3.

Break-in diagnosis tool results for pulsed current cycles protocol in the 1A.cm^{-2} region		
Key time periods (min)	0 to 10	68.4 to 390.1
Labels (and % of data associated to each label)	Ionomer (95%), Ionomer + CL (5%)	Fully activated (100 %)

TABLE 4.12. BREAK-IN DIAGNOSIS RESULTS FOR PULSED CURRENT CYCLES PROTOCOL

As previously stated, the operating conditions of this protocol (TABLE 4.10) have been adjusted to ensure that the stack could handle the frequent, high amplitude pulsed current profile (FIG. 4.13). These operating conditions (especially the cathode stoichiometry and anode RH) are therefore at even higher values than for the previous protocols (to maximize stack performance). Combined with the usage of a NextGen stack, these conditions create a drastic initial performance gap with the training database. Indeed, FIG. 4.14 shows a mean cell voltage beyond 0.55V at 2.1A.cm^{-2}, 20min into break-in. This performance is hard to reach with a GEN1 stack at nominal operating conditions (used for training database), even when it is fully activated. Consequently, the diagnosis tool directly classifies the data of the first PolCurve (0 to 10min) as partly activated (activated ionomer for the first 95% of samples, followed by 5% of activated ionomer and CL).

The impact of the operating conditions/used stack on the diagnosis tool results (see section 3.2.2) has once again been confirmed by applying the tool at a higher current (here at 1.5A.cm^{-2}). In this configuration, the results remained coherent (e.g. non-activated stack at beginning of process, smooth transition between activation steps). Full activation is however reached after 312 minutes (which fits with the measurement of FIG. 4.14). Despite the diagnosis tool duration issue, its classification results remain coherent and confident. Its absolute confidence in the fact that break-in fully completed, even for measurements at 1.5A.cm^{-2}, further indicates that pulsing the current in rapid cycles efficiently accelerates the break-in kinetics.

5.3 Protocol degradations and impact on durability

The literature has proven that rapid, variable load conditions, induces multiple degradation mechanisms [158]. Indeed, these conditions lead to thermal/humidity cycles, local starvations, and potential cycles. These factors may cause mechanical degradations (cracks in the ionomer and the CL), carbon corrosion, and dissolution/growth of Pt particles [131]. Therefore, ASTs (accelerated stress tests) are often based on rapid variable load profiles to increase the fuel cell degradation rate (see section 4.3.2) [54]. The *pulsed current activation* method thus presents major degradation risks. No additional ageing campaigns have however been applied to confirm and quantify its impact on fuel cell degradations, for duration and cost related reasons (which are significant, as seen in section 4.3.2). Unfortunately, the study of the impact of short-circuit/pulsed activation also lacks in the literature [82]. It therefore remains the main perspective for this procedure.

To sum up, the *pulsed current cycles* method has proven to be a protocol that ensures full stack activation, in a short time (~1h30 for the USFCC guidelines). This concurs with its main objective (accelerate the break-in kinetics). Additionally, the break-in kinetics may be further accelerated by increasing the current pulse rate and amplitude. Even though this procedure has proven to be efficient for rapid activation, this comes with a disregard to its impact of fuel cell lifetime (as performance is prioritized over durability). In its current state, this protocol is thus only adapted to scenarios where one solely rapidly needs stable performance.

6 Break-in protocol: Cathode starvation/reverse flow activation

The *cathode starvation/reverse flow* activation process, composed of a unique combination of break-in methods, is the main flagship protocol put forward for this PhD. From the list of break-in procedures in this chapter, it is the one which is considered to be the best compromise between speed, durability and cost. It is therefore also the protocol which has been optimized the most, through iterative experimental applications.

6.1 Presentation of protocol and its main objectives

The *cathode starvation/reverse flow* activation protocol is divided into 4 steps (FIG. 4.15). The first step includes gradually increasing the current drawn from the stack. The second and third step of this protocol consist of repeating the following cycle (i) rapidly increasing the current density to 1.9A.cm^{-2}, (ii) holding this current value for 5 minutes, (iii) instantaneously reducing the current to 0.3A.cm^{-2}, and holding this value for 3 minutes (iv) reducing the current between 0.01 to 0.02A.cm^{-2}, and simultaneously shutting off the air supply. As the lowest cell voltage drops below 0.2V, the air is resupplied, and the cycle is repeated. The difference between the second and third step of this protocol is that the third step takes place with inverted gas flow directions (H_2 an Air inputs/outputs inversion). The phases before and after step 3 (at 0A.cm^{-2}) are required to permute the gas channels inputs/outputs. As for the previously presented protocols, the last iso-current step has the sole purpose of determining if stack performance has stabilized. Unlike the previous protocols however, no additional PolCurves have been implemented. Indeed, the high current step (which has a stabilization time of 5min), already serves as a reference steady state performance measurement point.

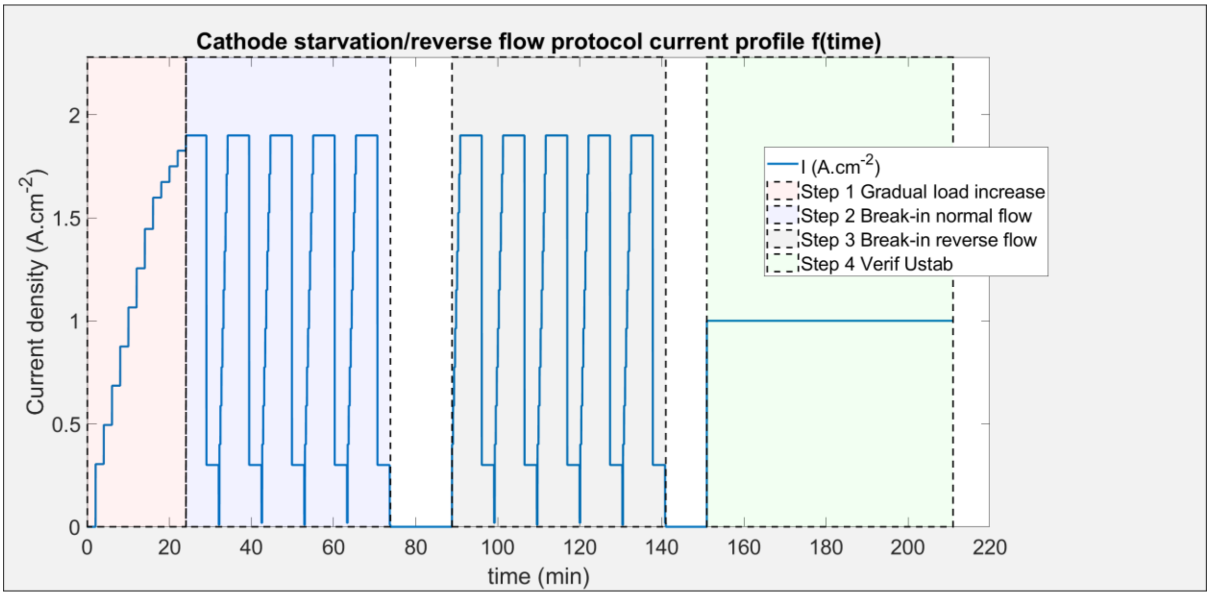

FIG. 4.15. CATHODE STARVATION / REVERSE FLOW ACTIVATION PROTOCOL CURRENT PROFILE

In this protocol, the first step (gradual current ramp at ~0.08A.cm^{-2}.min^{-1}) is of long duration (~24min) to ensure that the first post-assembly stack start-up phase is as smooth as possible (to prevent degradations). During steps 2 and 3, the oxidation/reducing conditions are partly generated by imposing current variations (consequently resulting in voltage drops/rises). The strongest reducing conditions are however generated by periodically starving the cathode. The control of air depletion can be assimilated to the control of the amplitude of the fuel cell mass transport losses, at any given current density. With this ingenious solution, the stack current and voltage are thus decorrelated (normally bound to a PolCurve). A low voltage may therefore be reached without having to impose an elevated current (similar to the CyV method of section 4). Apart from the reduction of Pt oxides, starving the cathode results in a hydrogen pumping effect. This accelerates CL pore opening, as well as the hydration of the ionomer (see section 3.2.5 of chapter 1).

Additionally, to further increase the reducing conditions, H_2 crossover is induced by imposing a pressure gradient between the anode and cathode (see section 3.2.8 of chapter 1). The presence of H_2 itself at the cathode (in addition to low potentials) further promotes the reduction of Pt oxides [187], as well as the enlargement of the triple phase boundary (TPB) [30]. The reverse Air and H_2 flow direction operation during step 3 allows for a more uniform stack activation (see section 3.2.6 of chapter 1) and is especially efficient when coupled to the cathode starvation technique. Indeed, it permutes the zone in which current (and water) is produced, with the zone in which hydrogen evolution occurs. This will be further discussed in the following sub-section, and is illustrated in FIG. 4.17.

The methods used for this protocol have mainly been inspired by the Balogun *et al.* [64] (cathode starvation), and the Park *et al.* [67] (reverse flow) methodologies. The Balogun *et al.* cathode starvation method, initially adapted for a 5cm^2 single cell, had to be vastly revisited to be suitable for an automotive grade stack. This mostly consisted of limiting the peak current density to 1.9A.cm^{-2}, as well as strongly reducing the current density and duration of the interval during which the cathode is starved of air. Similar to the implementation of a first gradual current increase (step 1 of FIG. 4.15), these adjustments are made to ensure fuel cell durability. In addition to the current profile of the final cathode starvation/reverse flow activation process (FIG. 4.15), the other final operating conditions of the protocol are provided in TABLE 4.13.

Operating conditions during cathode starvation/reverse flow activation protocol	
Anode Pressure (barabs)	P_{cat} + 0.5bar when at 0.3A.cm^{-2} for steps 2 and 3 and P_{cat} for rest
Cathode Pressure (barabs)	1.5 for step 4 and no regulation for rest (P_{atm} + pressure losses)
Anode Stoichiometry	1.5
Cathode Stoichiometry	2.3 for steps 1, 2, 3 (0 when starving) and 1.8 for step 4
Anode / Cathode RH (%)	70 / 40
Outlet Temperature (reference)	80°C (controlled value)
Inlet Temperature (measured)	70°C (estimated value)

TABLE 4.13. CATHODE STARVATION / REVERSE FLOW ACTIVATION PROTOCOL OPERATING CONDITIONS

As previously stated, the development process of this protocol has been carried out through a number of iterative experimental applications (on the TB07 and B057 test stations). Various durations of the peak and low current steps have for example been tested. The peak current step of at least 5 minutes, followed by a low current step of 3 minutes provided the best results. Additionally, different starvation ("air braking") current densities have been tested. The best values were in the 0.01 to 0.02A.cm^{-2} zone (resulting in best performance, and most convenient, as the slow voltage drop results in simpler control of air depletion).

Further (partly successful) attempts at reducing the activation time associated to this flagship protocol have been carried out. The addition of a MEA pre-activation step (prior to the cathode starvation break-in protocol), based on steam treatment (see section 3.1.1 of chapter 1), has for example been tested. It aims at obtaining a better initial (post-assembly) stack performance. This would reduce the need (and consequently the duration) of the first gradual current stepping phase of the break-in protocol (step 1 of FIG. 4.15). MEA steam treatment has firstly been carried out for various durations at 100°C, using a household pressure cooker (similar to [43] and [44]). In addition to untreated MEAs (used as reference), all steam treated MEAs have been assembled in one "rainbow stack", and broken-in using the cathode starvation method. The MEAs that were steam treated for 10 minutes, provided better initial performance (up to 32mV more than regular MEAs) during step 1 (FIG. 4.15). This performance gap however rapidly converged afterwards. Further attempts, at higher temperatures and pressures (118°C and 2bar) were carried out using the SA-232V autoclave, capable of enclosing the entire MEA (~35 × 17cm). This however resulted in multiple dimensional variability issues and gas leakages [24]. Additionally, as the entire 7-layer MEA was treated by steam, protecting the sub-gasket from the heat using isolating frames (e.g. PVC, cork), was challenging. For these reasons, the pre-treatment method has been abandoned for the latest attempts of the cathode starvation/reverse flow protocol.

6.2 Protocol application and data analysis

In this section, the break-in results for the latest version of the *cathode starvation/reverse flow* protocol (without MEA steaming), using a 10-cell GEN1 fuel cell stack, and the TB07 test station, are presented. Fig. 4.16 displays the stack performance evolution at 1.9A.cm^{-2} during break-in, for stable conditions (5 min stabilization before each measurement). This figure elucidates the effect of the reverse flow method on stack performance. Indeed, two dissociated activation processes are identifiable, as if the fuel cell is broken-in twice. One first activation (with gradual performance convergence) occurs in the conventional flow direction configuration. When reversing the flow (of air and H_2), and applying the same current cycles, a second activation process appears. Once again, a rapid initial performance increase, and subsequent convergence occurs. This concurs with the observations of Park *et al.*, who, using a segmented fuel cell, identified dissociable activation zones, whose local break-in kinetics depend on the direction of the flow [67].

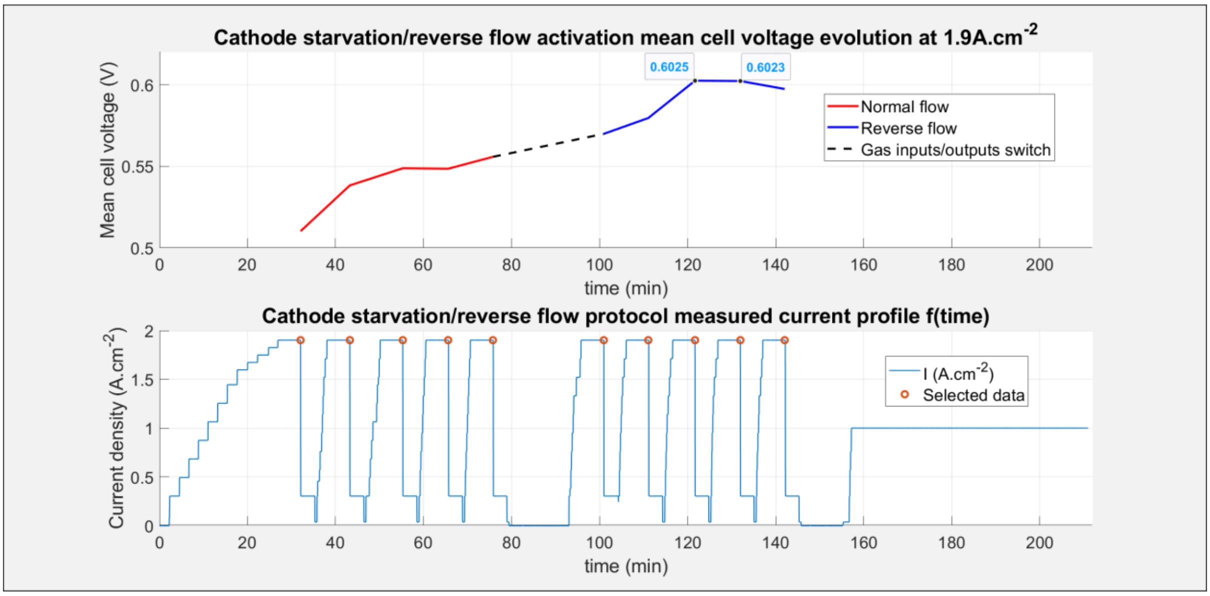

FIG. 4.16. MEAN CELL VOLTAGE EVOLUTION AT 1.9A.CM^{-2} DURING CATHODE STARVATION/REVERSE FLOW ACTIVATION

Fig. 4.16 also confirms the efficiency of the cathode starvation method, and its complementarity with the reverse flow technique (discussed in the previous subsection). The two zones generated during cathode starvation (one in which H_2 evolution occurs, and one in which water is produced) result in rapid stack performance increase and converge during step 2 (conventional flow). This beneficial effect on the stack (rapid performance increase/convergence) is once again proven when the zones are permuted (reverse flow). Fig. 4.17 illustrates the complementarity between the cathode starvation and reverse flow methodologies.

The rapid break-in kinetics measured during this protocol are also partly induced by the unique stack pressure control. Indeed, as previously stated, the cathode pressure is not regulated (depends on pressure losses). The anode pressure is controlled, but its control law depends on to the cathode pressure (see Table 4.13). The GEN1 fuel cell used for this application presents relatively high-pressure losses. Consequently, the variable current profile of FIG. 4.15 forces stack pressure fluctuations (between 1 and 2barabs). This causes internal RH cycles, resulting in improved ionomer activation [24]. The elevated pressure itself has also proven to accelerate the break-in kinetics (section 3.2.2 of chapter 1). The pressure control characteristic of the protocol is thus essential. If applied on stacks with lower pressure losses (e.g. NextGen), the cathode output pressure valve must remain partly closed to reproduce the elevated pressure environment of GEN1.

Once again, according to the USFCC guidelines, the voltage deviation criterion is reached after 120 minutes (FIG. 4.16). The performance stabilization test (step 4, between 150 and 210min) agrees with these results, in the form of a slight voltage drop (~2mV per cell). Additionally, in the protocol of FIG. 4.15, significant time (15min) is dedicated to the manual permutation of the gas inputs/outputs. This may be reduced to seconds by implementing 4-way-valves. Fundamentally, the USFCC criterion can thus be reached after only 105 minutes of break-in. This statement however remains debatable, due to the conditions in which the performance evolution is determined. Indeed, even though the measurements are carried for steady-state conditions (5min of stabilization), they are not each separated by a PolCurve (unlike the USFCC protocol). Additionally, a part of the measurements are carried out in reverse flow. In this unconventional layout, the baseline metrics (e.g. the measured stack voltage) may be influenced by water accumulation, pressure losses differences, etc. The performance stabilization measurements may therefore be less certain and precise.

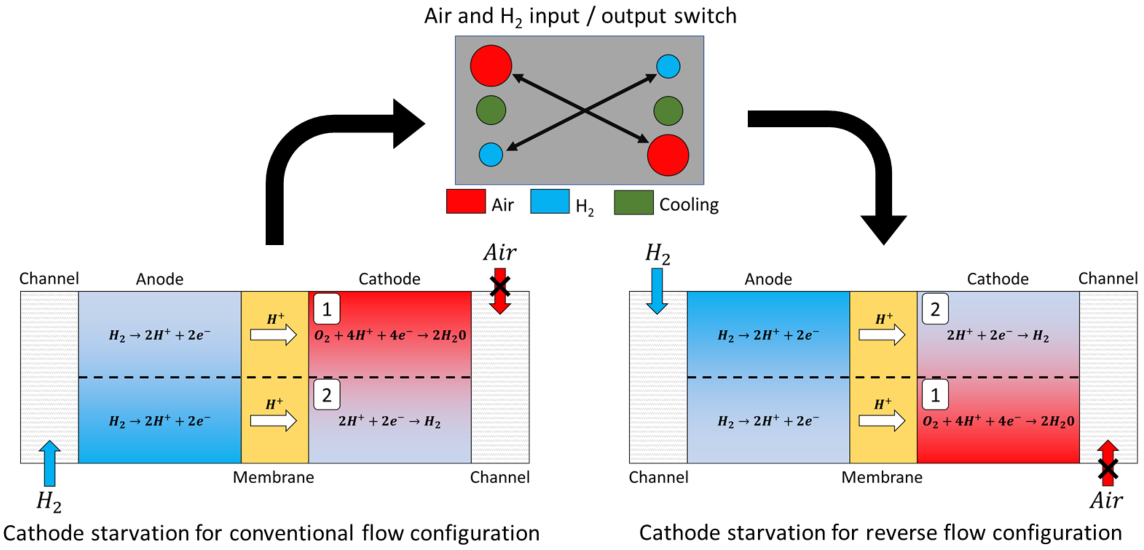

FIG. 4.17. SCHEMATIC ILLUSTRATION OF COMPLEMENTARITY BETWEEN CATHODE STARVATION (ACCELERATED) AND REVERSE FLOW (UNIFORM) ACTIVATION METHODS

Unfortunately, further conclusions cannot be drawn from the post-break-in PolCurve either. Indeed, a mechanical defect appeared with the GEN1 stack prototype, as it was being characterized. This said, the post-activation PolCurves provided by previous applications of this procedure (protocols with similar, less optimized operating conditions) can however be used as base. The most similar previous application (applied on the same test station and stack technology) provided a post-break-in PolCurve, with performances that exceeded the expectations. Indeed, it resulted in a stack with a significantly higher post-activation performance (up to 20mV per cell at $1A.cm^{-2}$), compared to identical stacks that have been broken-in using conventional methods. From these results, it thus seems that the hydrogen pumping effect, associated to the crossover and presence of H_2 at the cathode has directly affected the MEA morphology. This concurs with the literature, where MEAs activated by cathode starvation have been compared to ones activated using a conventional protocol. In this study, cathode starvation increased the CL thickness by up to 93% (by penetration into the membrane), consequently increasing the TPB, and reducing the ohmic resistance [30].

Even though multiple iterations of this protocol have already been tested, many additional break-in time reducing perspectives exist. Indeed, the protocol in its current configuration is developed using operating conditions margins that guarantee stack durability. Multiple adjustments, solely aiming at increasing the activation kinetics therefore exist. The current density during the cathode starvation step may for example be significantly increased. Similarly, the duration of the first step (gradual current increase) may be further reduced. Each of these adjustments do however require a subsequent ageing test, to determine their impact on fuel cell durability. The impact of this protocol on stack durability is further discussed in section 6.3.

6.2.1 Analysis with analytical ionomer activation model

TABLE 4.14 provides the results of the application of the ionomer activation model to *the cathode starvation/reverse flow* protocol (FIG. 4.15 and TABLE 4.13).

Ionomer break-in model coefficients evolution for cathode starvation/reverse flow protocol				
Coefficient convergence	$R_{skin\ \mathrm{an}}$ (time | value)	$R_{skin\ ca}$ (time | value)	R_{dspac} (time | value)	R_{cont} (time | value)
to 10% from final value	11.5min | 0.1	16.4min | 0.1	37.4min | 1.5×10^{-2}	177.7min | 9.5×10^{-3}
to 1% from final value	14.5min | 10^{-2}	22.9min | 10^{-2}	69.8min | 1.5×10^{-3}	195.7min | 1.1×10^{-2}
to 0.1% from final value	17.1min | 10^{-3}	25min | 10^{-3}	116.95min | 1.5×10^{-4}	197.5min | 1.1×10^{-2}
to final value	21.6min | 0	34.2min | 0	201.2min | 0	197.7min | 1.1×10^{-2}

TABLE 4.14. IONOMER BEAK-IN MODEL OUTPUT FOR CATHODE STARVATION/REVERSE FLOW PROTOCOL

The ionomer break-in model indicates complete ionomer break-in at the end of the procedure, but also elucidates multiples areas for improvement. As expected, the first progressive current increase step of the protocol (0 to 24min) has effectively removed the initial barriers to water sorption. The rate at which the skin surface resistances drop is however inferior to the previously presented break-in protocol (section 5.2.1). Similar observations can be made for the domain spacing and contamination resistances. They both fully converge before the end of the break-in protocol, but not before the last cathode starvation/reverse flow activation cycles (~140min). Additionally, during the last step of the protocol ($1\mathrm{A.cm}^{-2}$ at 1.5barabs) partial CL contamination has taken place, resulting in a final R_{cont} that is slightly superior to its initial value (TABLE 4.14). Thus, to increase the overall ionomer break-in kinetics and to mitigate CL contamination, the operating conditions (TABLE 4.13) should be adjusted to favor stack internal humidity increase (e.g. higher input RH).

This said, the *cathode starvation/reverse flow* may be more efficient to activate the ionomer than advertised by the model. Indeed, some possible benefits of the cathode starvation process are lacking, as the model does not allow stoichiometries below 1 (total consumption of reactants, no output flow). Similarly, as the model is one-dimensional, the benefits of reverse-flow operation are not shown. Future model improvements should therefore include enlarging the domain to 2 dimensions and allowing for stoichiometries below 1. The benefits of the pressure gradient cycles, resulting in a variable membrane water content distribution (similar to the pulsed current cycles effect of section 5.2.1) may also be further improved.

6.2.2 Analysis with break-in diagnosis tool

Unlike the three other protocols, no steady state data in the $1A.cm^{-2}$ region is available here, except for the first PolCurve and last performance stabilization step. Despite these limitations, the available data has been extracted, and classified using the procedure illustrated in Fig. 3.11 of chapter 3 (see Table 4.15). The data provided by this protocol dissociates itself from all the data used in the previous sections. Indeed, apart from a few operating conditions dissimilarities (Table 4.13) the data from the training and the validation datasets are generated for identical conditions (same stack technology and test station).

Break-in diagnosis tool results for cathode starvation/reverse flow protocol in the $1A.cm^{-2}$ region			
Key time periods (min)	0 to 13	14 to 159	160 to 210
Labels (and % of data associated to each label)	Non-activated (100 %)	*Absence of reference data at $1A.cm^{-2}$*	Ionomer/CL (100 %),

Table 4.15. Break-in diagnosis results for cathode starvation/reverse flow protocol

As expected, the data during the initial PolCurve (step 1 of Fig. 4.15), has been classified as non-activated (100% confidence). As previously stated, the absence of data near the $1A.cm^{-2}$ region prevents the diagnosis tool from being applied during the majority of the protocol. The last step of the protocol (160 to 210 min) however provides an interesting result. Indeed, it indicates that the ionomer and CL pore structure are fully broken-in but that the catalyst surface is not (100% confidence). It may thus be possible that the catalyst has not been fully activated during this protocol, or that starving the cathode has affected the voltage response by altering the CL morphology [82]. This said, other factors might have altered the results. These include the pressure conditions, in favour of the training database (0.5bar above the validation database), or the aforementioned classification uncertainties towards the catalyst cleaning break-in mechanism.

6.3 Protocol degradations and impact on durability

As previously stated, the *cathode starvation/reverse flow* activation protocol aims at being an optimum between break-in kinetics, operation cost and fuel cell durability. The choices and rationale behind the reasons why this method should, in theory, not affect cell durability are firstly detailed.

As stated in section 5.3, pulsed current variations are highly recommended to fully activate a stack but can also induce multiple degradations. The "pulsed" current signature of this protocol (Fig. 4.15) takes account of these risks, by limiting the amplitude of the current range, variation frequency and rate, as well as the addition of stabilization times. Its degradation risks are therefore largely mitigated. The initial gradual current increase step, and the elevated cathode stoichiometry, further reduce unwanted starvation risks.

The main stressor used for activation which is simultaneously considered as a stressor for degradations (see section 2.3 of chapter 3) is reactant starvation. During this break-in protocol, very specific conditions are however used to force, control, and manage the starvation procedure (to ensure fuel cell durability). Firstly, anode starvation is entirely prohibited, as it would inevitably lead to degradations [131], [188]. Secondly, the conditions in which the starvation is repeatably forced at the cathode, is of vast importance. Indeed, air is depleted by fully closing the supply of gas. This is vastly different from "partial" starvations that typically occur in a cell (during unwanted faulty conditions) and can lead to degradations. Fig. 4.18 illustrates the effects of a partial starvation and a total starvation on a stack voltage profile (at iso-current).

When partially starving the cathode of air, the uncontrollable voltage fluctuations have an obvious degrading impact on the fuel cell. These fluctuations also impact other metrics, leading to temperature, pressure, and humidity inhomogeneities, as well as hot points. When fully starving the cathode (air supply completely cut off), none of the aforementioned conditions occur. Indeed, only a gradual progressive voltage drop takes place, whose slope may be controlled by the amount of current drawn from the stack. Additionally, in the profile of FIG. 4.15, the cathode starvation is preceded by an iso-current stabilization step, meaning that the conditions within the stack (prior to starvation) are stable. Furthermore, air is resupplied as the lowest cell voltage reaches 0.2V which is simple to control at 0.01 to 0.02A.cm^{-2} (slow voltage drop at low currents).

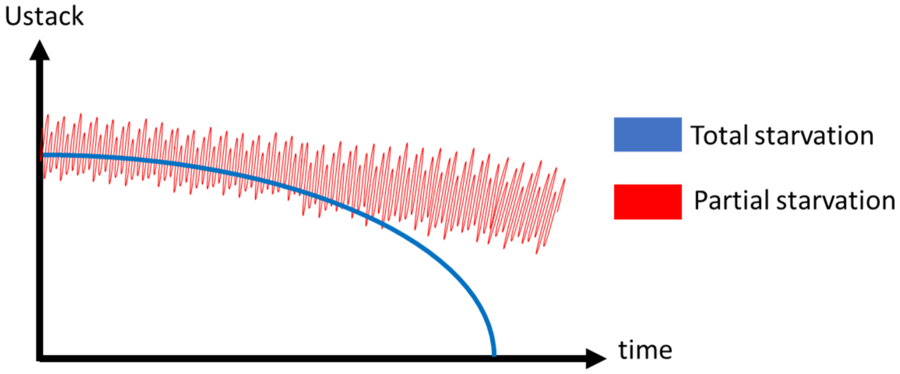

FIG. 4.18. EFFECTS OF A PARTIAL AND TOTAL STARVATION ON STACK VOLTAGE PROFILE (AT ISO-CURRENT)

In addition to the theoretical demonstration towards the negligible impact of cathode starvation on fuel cell durability, experimental ageing data provided by the literature is used to further confirm this statement. The impact of fuel cell break-in through cathode starvation on ageing has been determined by Balogun *et al.* [64], using an AST. As stated in section 5.3, an AST is not representative of ageing mechanisms occurring in a vehicle. It may therefore not be used to estimate a fuel cell lifespan. This said, the same ASTs can be applied on multiple cells/stacks to directly compare their relative degradations rates. This is the approach used by Balogun *et al.* For this, they activated one cell using the cathode starvation method, and several other reference cells using conventional break-in methods, and subsequently applied the same AST to them. The DOE procedure [50], the EU harmonized procedure [49], and a commonly used amperometric break-in method [64] are used as reference break-in protocols.

The used AST, originally provided by Taghiabadi *et al.* [54], is designed to make a FC reach its end of life in 9,000 rapid repeated cycles. Each cycle consists of (i) holding the cell at the OCV for 8s (ii) performing a voltage scan between OCV / 0.6V / OCV at a scan rate of 50mV.s^{-1}.cell^{-1} After each set of 3,000 ageing cycles, the relative performance loss (at the maximum power density), has been evaluated for each cell (see FIG. 4.19). As shown on this figure, the cell activated by cathode starvation provides the lowest relative performance loss at the end of the ageing cycles, compared to conventional methods. This once again indicates that starving the cathode of air may beneficially and irreversibly affect the MEA morphology [82]. One could thus consider that, if carried out correctly, starving the cathode of air during break-in even has a beneficial long-term effect on fuel cell lifetime. This said, the data of FIG. 4.19 only confirms that starving the cathode of air does not necessarily lead to degradations. It does not validate the entire break-in protocol (FIG. 4.15), and its numerous other methodologies (e.g. current profile, pressure variations, reverse flow).

The impact of reversing the direction of the Air and H_2 flow on stack durability has for example not been evaluated. During this protocol, to mitigate degradations risks (mainly uncontrolled partial starvations) the stack is shut down (no current) during the manual switch of Air and H_2 inputs/outputs. This said, when current is subsequently drawn from the stack, high pressure and local flooding risks appear, as it is not designed (e.g. BPP channels) for this unconventional operation mode. Similarly, the risk of water accumulation in the channels of the test station must also be considered as it is not configured for such a type of operation either. Additional analysis of the impact of reverse flow on the cell degradations should therefore be carried out (using for example local current distribution monitoring devices [189]).

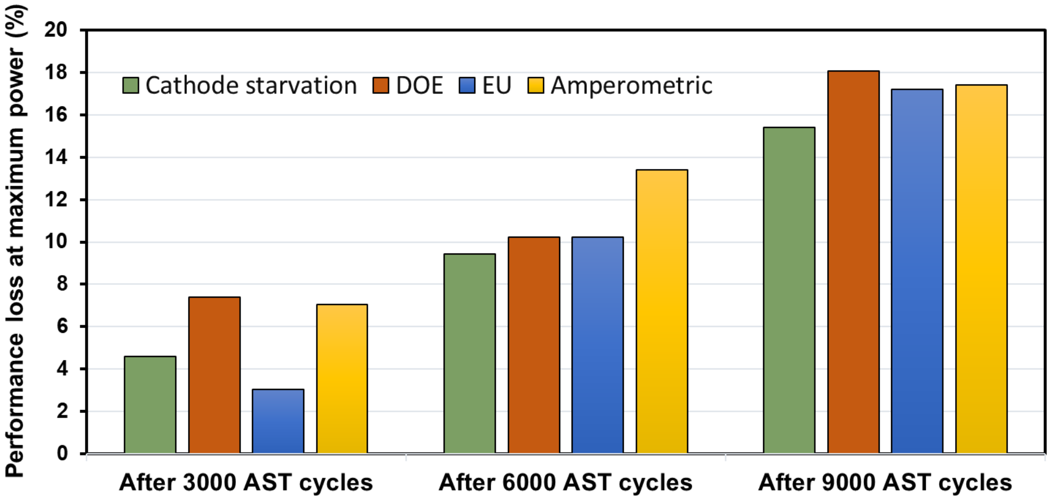

FIG. 4.19. RELATIVE DEGRADATION RATES OF CELLS ACTIVATED USING VARIOUS BREAK-IN METHODS [64]

To conclude, the *cathode starvation/reverse flow* protocol has proven to be efficient and versatile. It vastly reduces the duration of the activation process (~120min), fuel consumption (32g per cell for GEN1) and degradation risks. Compared to a conventional protocol, it may even improve initial cell performance and durability, by affecting the MEA morphology [82]. As previously stated, (section 6.1), much future work towards the optimization of this procedure may still be carried out. Indeed, this protocol has been developed to guarantee durability (e.g. by limiting the current peak values and variations). The true impact of more severe conditions (e.g. short-circuit starvation [61], [190], drawing current during flow switch [68]) on fuel cell lifetime still remain to be evaluated [82]. Future work also includes the reimplementation and optimization of the MEA steam treatment step (that has previously been abandoned due to dimensional variability and stacking issues). Steam treatment may for example be implemented before the full MEA assembly, on the CCM [43] (to prevent sub-gasket deformations), or even by steam injection in a fully assembled stack [45].

7 Conclusion

In this chapter, four main accelerated break-in protocols, adapted to Symbio automotive grade fuel cells, have been proposed. Each protocol has its use case and advantages, which has been illustrated though iterative experimental applications and associated detailed data analysis (see TABLE 4.16).

The ***current stepping/condensation*** protocol ensures stack durability, whilst moderately accelerating break-in (USFCC 5mV.cell^{-1} deviation criterion in ~300min). Simultaneously, its pseudo PolCurves provide a clear image of fuel cell performance evolution and convergence during break-in. It is therefore ideally adapted for scenarios, where the priority is to conserve stack durability whilst ensuring break-in is finalized (e.g. stacks dedicated to post-activation testing). The ***CyV/N$_2$ hydration*** protocol, optimized for the reduction of fuel cost, provided mixed results. On one hand, N_2 hydration has proven to be an inefficient ionomer activation method and must be prohibited. According to the post-activation EIS curves, the CyV method however successfully activated the catalyst. This procedure also provides significant room for improvement, as more knowledge is gained towards Pt impurities desorption potentials. The operating conditions used during CyV must however also be revisited to prevent degradations, as they currently reduce the CL lifetime. The ***pulsed current cycles*** protocol, aiming for maximized break-in kinetics, clearly demonstrated the efficiency of rapid, high frequency and high amplitude load fluctuations towards this goal. Indeed, 1h30 of break-in is sufficient to reach the 5mV.cell^{-1} deviation criterion. However, before considering implementing this protocol on a mass manufacturing scale, determining its impact on fuel cell degradation is mandatory.

The ***cathode starvation/reverse flow*** protocol has clearly proven to be versatile, and efficient. Among all the tested procedures, this unique combination of break-in methods is undoubtedly the most promising one. It provides many ingredients to accelerate break-in (e.g. H_2 pumping, uniform activation, pulsed current signature, temperature pressure and flowrate cycling), whilst still ensuring durability. This strongly reduces the break-in duration (to ~120min), and may even improve the MEA morphology. As the present strategy of most fuel cell manufacturers tends towards increasing the active surface, the impact of the reverse flow technique (used to uniformize activation) will only become more significant.

Protocol	Main advantage	Main drawback	Other comments
Current stepping /condensation	Durability	Break-in kinetics	- Simultaneous characterization (PolCurve) - Few prospects to further optimize protocol
CyV/N$_2$ hydration	Fuel cost	Durability	- Simultaneous characterization (CyV) - Must revisit hydration method & conditions
Pulsed current cycles	Break-in kinetics	Durability	- Must quantify current cycles effect on ageing - Few prospects to further optimize protocol
Cathode starvation /reverse flow	Best compromise	/	- Must quantify reverse flow effect on ageing - Many prospects to further optimize protocol

TABLE 4.16. COMPARATIVE SUMMARY OF FOUR MAIN ACCELERATED BREAK-IN PROTOCOLS

The applications of these procedures elucidated the difficulties involved with the determination of end-of-break-in conditions. Reaching the USFCC cell voltage deviation criterion does not necessarily imply that break-in is finalized (as demonstrated during the CyV/N_2 protocol). The only viable current solution is to track the (ideally stable) iso-current performance evolution during break-in, and to confirm the results through post-activation PolCurve and/or EIS characterizations. The duration of a break-in protocol has also proven to be highly dependent on the used stack technology (section 4.2.2 of chapter 1), even for fuel cells provided by the same manufacturer. As aforementioned, the used stack prototypes, have been subjected to various incremental changes. This disparity between stacks (no fixed characteristics) resulted in variable break-in times, and final stack performance. The developed break-in model (chapter 2) and diagnosis tool (chapter 3) have proven to provide complementary information towards the evolution/finalization of break-in. Given the number of assumptions that were required to develop these programs, and the disparity between stacks (e.g. GEN1 to NextGen), they can currently not be used to draw certain conclusions. They may however be further optimized as more knowledge towards the break-in mechanisms (chapter 1) is gathered.

Experimental perspectives mainly consist of further testing and improving the flagship protocol (cathode starvation/reverse flow). This includes testing the protocol on larger (>35kW) fuel cell stacks (currently carried out at Symbio), and for harsher conditions (higher current amplitude and variation rate). As the limitations towards the possible break-in time reduction on an activation bench will inevitably be reached, one should tend towards alternative solutions. They concern the optimization of the CL production method [40], among other manufacturing processes [41], or partly activating the stack during vehicle operation [8].

General conclusion and future work

General conclusion

As mentioned in the general introduction to this manuscript, the scientific study of the fuel cell break-in procedure remains a relatively new area of research. Efforts to optimize the activation process (such as this thesis) have only recently been driven by the goal of industry and laboratory partners to achieve low-cost mass manufacturing of fuel cells. Since the PEMFC break-in procedure is such a broad and recent research topic, this thesis was initially narrowed down to three main objectives. They were (i) to provide a state of the art of the fuel cell activation procedure (ii) to develop break-in monitoring and/or simulation tools (iii) to propose and test multiple optimized activation protocols, for automotive grade stacks.

All work carried out towards the **first objective of this thesis** has been presented in the first chapter of this manuscript. To achieve this goal, significant efforts were made to retrieve, combine, and summarize all the sparse information, and various theories regarding the PEMFC activation process. The main physical principles related to fuel cell break-in were firstly studied. This has elucidated that the break-in mechanisms are divided in a finite set of morphological changes, which mainly concern the components of the MEA. In the membrane, there is the polymer hydration and structural change, surface skin rearrangement and decontamination. In the CL, there is the pore structure change, polymer hydration and carbon support oxidation, as well as the catalyst decontamination and the Pt structure reorganization. The time constants associated with each break-in mechanism range from a few seconds to multiple hours (or even days).

In a second step, the different break-in methodologies and associated stressors for accelerated activation were reviewed. In summary, dynamic, high temperature/pressure and supersaturated operation promote the break-in kinetics. It is essential to generate oxidizing and reducing conditions during activation, and can be achieved by short circuit, CyV, cathode starvation or reactant switch. Uniform activation over the cell surface is attainable by reverse flow activation or hydrogen pumping. In this chapter, the absence of a standardized nor efficient processes to monitor break-in evolution, completion, and impact on ageing, was also elucidated. This need for such a process was emphasized, especially since the efficiency of an activation method strongly depends on fuel cell characteristics. This naturally led to the second objective of this thesis.

The work to achieve the **second goal of this thesis** (to provide break-in monitoring and/or simulation tools) was divided into two separate chapters. Chapter 2 focused solely on the development of a model dedicated to the simulation of the activation process. Its procedure consisted of (i) developing a dynamic two-phase MEA water transport model, based on the finite volume method, that can be resolved through implicit LU decomposition (ii) validating the model behaviour using ohmic resistance measurement tests on the Symbio test station (iii) adapting the functional water transport model, to fit to the activation process. For this final step, specific variables related to the break-in mechanisms were implemented into the water transport equations, based on the gathered knowledge of chapter 1. They were divided into three resistances, representing membrane domain spacing, surface skin change, and decontamination.

The simulation results (tested for different operating conditions) displayed the evolution of the water content profile of the membrane during its activation process. This elucidated the effect of the break-in mechanisms on the membrane water sorption trend, which initially has difficulty gaining momentum compared to an activated ionomer. The model output also clearly confirmed that drawing current during activation is mandatory for the ionomer to reach peak post-activation performance. The significant influence of the other operating conditions ($RH, FS, T, P\dots$) on the activation kinetics was also studied. During the model development process, certain uncertain points, due to absence of clear knowledge (assumptions used, mainly for the activation mechanisms) were also pointed out. Regardless, the model provided clear indications on the sensibility of different operating conditions on the ionomer activation kinetics. The model has also further been tested by comparing its output with experimental accelerated break-in data (in chapter 4), where it clearly proved to provide valuable complementary information. During these tests, perspectives to further improve the model were also highlighted.

Chapter 3 also focused on the second objective of this thesis. Indeed, this chapter was entirely devoted to the introduction and development of a novel break-in monitoring concept. The ambitious goal of this tool was to determine the “state of activation” of a stack, using the non-intrusive signal-based PEM fuel cell diagnosis methodology (traditionally used to identify faults). Moreover, it aimed at being capable to identify the separate evolution of the three main categories of break-in morphological changes (the activation of the ionomer, the CL pore structure, and the catalyst). To this end, a reference “useful information” database was firstly generated, by applying a novel test protocol on several stacks. Then, the diagnosis tool development process consisted of (i) extracting the useful information out of the experimental data, (ii) assigning a label to each datapoint (iii) calculating numerous statistical features from this useful data, (iv) selecting the most representative features using the GINI ranking method (v) developing a machine learning algorithm (KNN classifier) capable of assigning labels to new datapoints, based on the training database.

The proof of concept of such a novel tool was validated in this chapter, using a first layer of “leave-one-out” cross validation, providing excellent classification results (between 90 and 100%). Thereafter, the model was also tested on experimental accelerated break-in data (in chapter 4), to demonstrate the amount of “free information” (no additional sensors needed) such a tool can provide. Its results were consistent and coherent, if somewhat optimistic. The accuracy of this tool can be greatly improved by using one identical stack technology for the training and validation databases.

Finally, the **third ambition of this thesis**, which consisted in proposing an optimized break-in procedure (based on the theoretical knowledge and developed numerical tools), was the subject of the fourth chapter. The optimization criteria focused on accelerating the break-in kinetics, reducing the reactant cost, and guaranteeing post-activation stack durability. To this aim, not one, but several break-in procedures were proposed, tested, and analysed using various advanced characterization methodologies, and additional ageing test campaigns. These tests were performed using various Symbio automotive grade stacks and test stations from different entities with expertise in the PEMFC field (FEMTO-ST, Symbio, Sintef).

Three break-in protocols that were optimized along one specific criterion, were firstly proposed. These are (i) the *Current stepping/condensation* protocol (durability), (ii) the *CyV/ N_2 hydration* protocol, (reduced reactant cost), and (iii) the *Pulsed current cycles activation* protocol, (break-in kinetics). With the rapid, frequent and high amplitude load fluctuations of the *pulsed current cycles* protocol, the 5mV.cell^{-1} deviation criterion was reached in only 1h30 of break-in. On, the other hand, the *current stepping/condensation* process moderately accelerated the activation kinetics whilst guaranteeing stack durability. Despite the less than ideal results of the *CyV/N2 hydration* protocol, the potentiostatic control method on the stack terminals provided bright prospects for desorbing catalyst impurities at a reduced reactant cost.

Finally, a novel protocol which is the best compromise between all the above criteria (and the final flagship protocol of this thesis), has been developed. It has been named the *cathode starvation/reverse flow* activation process. This procedure was developed using a unique combination of break-in methods (e.g. H_2 pumping, reverse flow, pulsed current signature, temperature, pressure and flowrate cycling). It reduced the break-in duration to ~120min, whilst still ensuring durability, and possibly even improving the MEA morphology. The perfect alignment of the "uniform activation" characteristic of this protocol with future stack designs (trending towards increasingly larger active surfaces), has also been elucidated.

Overall, the objectives set for this thesis have been achieved. A review of the physical principles and mechanisms that affect fuel cell activation, as well as the existing break-in methods is provided. Numerical tools, that simulate and monitor the fuel cell activation process have been developed and tested. And finally, optimized (rapid, low cost) fuel cell break-in procedures for automotive grade fuel cell stacks have been proposed. The achievement of this final goal (and more specifically, the invention of the flagship cathode starvation/reverse flow protocol) is particularly important for the industrial partner of this thesis. Considering that Symbio wants to produce 200,000 fuel cell stacks by 2030, and that fuel cell activation accounts for over 5% of the manufacturing cost, applying this novel break-in protocol has a direct impact on their goal. Although all objectives of this work plan have been met, there are still many direct and indirect perspectives.

Future work

One of the main direct perspectives related to this thesis is to continue testing and improving the flagship protocol (cathode starvation/reverse flow). This includes experimenting the procedure on larger (multi-kW) fuel cell stacks, and for harsher conditions (higher current amplitude and variation rate). This future work will personally be conducted at Symbio, whose intentions to make use of the *cathode starvation/reverse flow* protocol are underlined by an ongoing patent filling attempt. Perhaps this protocol can be further improved by the addition of other break-in methodologies that have not been tested during this thesis due to lack of equipment and/or safety reasons. These include the CO stripping and cell/stack cyclic compression methods, as well as the laser or H_2SO_4 pre-treatment processes.

All other direct perspectives (continuity of this work) can be listed according to the various difficulties that have been encountered during this thesis. Among these difficulties, there is the significant lack of general knowledge about the physical principles of PEMFC break-in. This has complexified many tasks, such as the development of the break-in model (chapter 2) and diagnosis tool (chapter 3). Therefore, it is imperative to gain additional fundamental knowledge about the activation mechanisms to improve the accuracy and reliability of these models. This includes, for example, additional deeper studies in the fields of electrochemistry and material science (e.g. catalyst surface impurities desorption mechanisms, molecular structure and hydration mechanisms of the ionomer). Research and expertise in materials science and mechanics regarding contact surfaces between fuel cell elements and optimal clamping pressures is also needed. Acquiring this fundamental knowledge would also be helpful in further optimizing break-in methods such as CyV (e.g by briefly reaching specific previously unknown desorption voltage points).

Another difficulty encountered and therefore a direct prospect to this work is the lack of an effective break-in completion criterion in the literature. Elucidated in chapter 1, this issue has added a degree of uncertainty to all experimental break-in applications. Since the "end of break-in" criterion is still subject to debate, a more accurate universal solution must be defined.

A final difficulty and perspective encountered is related to the strong dependence of stack characteristics on the efficiency of a break-in protocol. Although the fuel cell prototypes used during this thesis were supplied by the same manufacturer, the heterogenous stack characteristics caused disparities in activation times, stack behaviour, and performance. This, for example, affected the break-in diagnosis tool results (which was developed and tested on the basis of data from various types of stacks). To improve the reliability of this tool for a specific type of stack (with fixed characteristics), a new experimental "training database" should be created, based solely on data from this exact PEMFC technology. More generally, future work should include further research into the impact of stack characteristics on the efficiency of a break-in process.

Although future knowledge of activation mechanisms and methodologies will undoubtedly further improve the break-in kinetics, there will inevitably be a limit to the reduction in activation time. To truly bring down the time spent on an activation bench to a few minutes, alternative solutions are needed. Fortunately, as mentioned above, break-in is still a relatively new topic, which means that many additional indirect perspectives (outsit the scope of this thesis) exist. These include optimizing of the MEA production method (to reduce the need for activation) and partial stack activation during vehicle operation (residual break-in). This thesis also focusses on the activation procedure itself. The post-break-in procedure, required to evaluate the operational readiness of the stack, must also be further studied to reduce its cost and duration.

As mentioned in the general introduction of this manuscript, climate change remains the main challenges society has to face and will remain a focus for attention for the years to come. It can only be solved through a collective effort throughout various fields. Albeit being insignificant compared to the total efforts required to fully solve climate change, this thesis brings one small contribution towards this goal. Hopefully, the main added value of this work will be to encourage others to provide contributions of their own, based on the information and perspectives provided by this manuscript.

References

[1] V. Thomas, *Climate Change and Natural Disasters: Transforming Economics and Policies for a Sustainable Future*, 1st ed. New York: Routledge, 2017. doi: 10.4324/9781315081045.

[2] V. Masson-Delmotte, *Climate change and land: an IPCC special report on climate change, desertification, land degradation, sustainable land management, food security, and greenhouse gas fluxes in terrestrial ecosystems : summary for policymakers*. Geneva: Intergovernmental Panel on Climate Change, 2019.

[3] M. Oppenheimer *et al.*, "Sea Level Rise and Implications for Low-Lying Islands, Coasts and Communities," p. 126.

[4] Ipcc, *Global Warming of 1.5°C: IPCC Special Report on impacts of global warming of 1.5°C above pre-industrial levels in context of strengthening response to climate change, sustainable development, and efforts to eradicate poverty*, 1st ed. Cambridge University Press, 2022. doi: 10.1017/9781009157940.

[5] J.-N. Kang, Y.-M. Wei, L.-C. Liu, R. Han, B.-Y. Yu, and J.-W. Wang, "Energy systems for climate change mitigation: A systematic review," *Applied Energy*, vol. 263, p. 114602, Apr. 2020, doi: 10.1016/j.apenergy.2020.114602.

[6] M. de las N. Camacho, D. Jurburg, and M. Tanco, "Hydrogen fuel cell heavy-duty trucks: Review of main research topics," *International Journal of Hydrogen Energy*, vol. 47, no. 68, pp. 29505–29525, Aug. 2022, doi: 10.1016/j.ijhydene.2022.06.271.

[7] T. Grube, S. Kraus, J. Reul, and D. Stolten, "Passenger car cost development through 2050," *Transportation Research Part D: Transport and Environment*, vol. 101, p. 103110, Dec. 2021, doi: 10.1016/j.trd.2021.103110.

[8] F. Van der Linden, E. Pahon, S. Morando, and D. Bouquain, "Optimizing Proton Exchange Membrane Fuel Cell manufacturing process to reduce break-in time," in *2020 IEEE Vehicle Power and Propulsion Conference (VPPC)*, Gijon, Spain, Nov. 2020, pp. 1–5. doi: 10.1109/VPPC49601.2020.9330846.

[9] B. D. James, J. Huya-Kouadio, C. Houchins, and D. Desantis, "Final SA 2018 Transportation Fuel Cell Cost Analysis -2020-01-23," 2018, doi: 10.13140/RG.2.2.12165.99049.

[10] Colleen Spiegel, "one-dimensional-heat-mass-and-charge-transfer-model-pem-fuel-cell-stack.pdf," 2020.

[11] R. P. O'Hayre, S.-W. Cha, W. G. Colella, and F. B. Prinz, *Fuel cell fundamentals*, Third edition. Hoboken, New Jersey: Wiley, 2016.

[12] F. Gao, B. Blunier, and A. Miraoui, *Proton exchange membrane fuel cells modeling*. London: ISTE, 2012.

[13] M. Chatenet, L. Dubau, N. Job, and F. Maillard, "The (electro)catalyst|membrane interface in the Proton Exchange Membrane Fuel Cell: Similarities and differences with non-electrochemical Catalytic Membrane Reactors," *Catalysis Today*, vol. 156, no. 3–4, pp. 76–86, Oct. 2010, doi: 10.1016/j.cattod.2010.02.028.

[14] A. Baroutaji, J. G. Carton, M. Sajjia, and A. G. Olabi, "Materials in PEM Fuel Cells," in *Reference Module in Materials Science and Materials Engineering*, Elsevier, 2016, p. B9780128035818040000. doi: 10.1016/B978-0-12-803581-8.04006-6.

[15] USFCC, "USFCC Single Cell Test Protocol # 05-014," Jul. 2006. [Online]. Available: http://www.members.fchea.org/core/import/PDFs/Technical%20Resources/MatComp%20Single%20Cell%20Test%20Protocol%2005-014RevB.2%20071306.pdf

[16] M. Zhiani, S. Majidi, and M. M. Taghiabadi, "Comparative Study of On-Line Membrane Electrode Assembly Activation Procedures in Proton Exchange Membrane Fuel Cell," *Fuel Cells*, p. n/a-n/a, Aug. 2013, doi: 10.1002/fuce.201200139.

[17] K. Christmann, K. A. Friedrich, and N. Zamel, "Activation mechanisms in the catalyst coated membrane of PEM fuel cells," *Progress in Energy and Combustion Science*, vol. 85, p. 100924, Jul. 2021, doi: 10.1016/j.pecs.2021.100924.

[18] X.-Z. Yuan, J. C. Sun, H. Wang, and H. Li, "Accelerated conditioning for a proton exchange membrane fuel cell," *Journal of Power Sources*, vol. 205, pp. 340–344, Jan. 2012, doi: https://doi.org/10.1016/j.jpowsour.2012.01.039.

[19] J.-M. Jang, G.-G. Park, Y.-J. Sohn, S.-D. Yim, C.-S. Kim, and T.-H. Yang, "The Analysis on the Activation Procedure of Polymer Electrolyte Fuel Cells," *J. Electrochem. Sci. Technol*, vol. 2, no. 3, pp. 131–135, Sep. 2011, doi: 10.33961/JECST.2011.2.3.131.

[20] A. Kusoglu and A. Z. Weber, "Water Transport and Sorption in Nafion Membrane," in *ACS Symposium Series*, vol. 1096, K. A. Page, C. L. Soles, and J. Runt, Eds. Washington, DC: American Chemical Society, 2012, pp. 175–199. doi: 10.1021/bk-2012-1096.ch011.

[21] S. Ueda, S. Koizumi, and Y. Tsutsumi, "Initial conditioning of a polymer electrolyte fuel cells: The relationship between microstructure development and cell performance, investigated by small-angle

neutron scattering," *Results in Physics*, vol. 12, pp. 1871–1879, Jan. 2019, doi: https://doi.org/10.1016/j.rinp.2019.01.066.

[22] N. Zhao, Z. Xie, and Z. Shi, "Understanding of Nafion Membrane Additive Behaviors in Proton Exchange Membrane Fuel Cell Conditioning," *Journal of Electrochemical Energy Conversion and Storage*, vol. 16, no. 1, p. 011011, Feb. 2019, doi: 10.1115/1.4040827.

[23] N. Zhao *et al.*, "Effects of Membrane Additives on PEMFC Conditioning," *ChemistrySelect*, vol. 4, no. 43, pp. 12649–12655, Nov. 2019, doi: 10.1002/slct.201903623.

[24] S. S. Kocha and B. G. Pollet, "Advances in rapid and effective break-in/conditioning/recovery of automotive PEMFC stacks," *Current Opinion in Electrochemistry*, vol. 31, p. 100843, Feb. 2022, doi: 10.1016/j.coelec.2021.100843.

[25] Z. Jingxin, "US20110195324A1 Methods and processes to recover voltage loss of pem fuel cell stack"

[26] V. Yarlagadda *et al.*, "Boosting Fuel Cell Performance with Accessible Carbon Mesopores," *ACS Energy Lett.*, vol. 3, no. 3, pp. 618–621, Mar. 2018, doi: 10.1021/acsenergylett.8b00186.

[27] M. S. Kim, J. H. Song, and D. K. Kim, "Development of Optimal Conditioning Method to Improve Economic Efficiency of Polymer Electrolyte Membrane (PEM) Fuel Cells," *Energies*, vol. 13, no. 11, p. 2831, Jun. 2020, doi: 10.3390/en13112831.

[28] S. Kabir *et al.*, "Elucidating the Dynamic Nature of Fuel Cell Electrodes as a Function of Conditioning: An ex Situ Material Characterization and in Situ Electrochemical Diagnostic Study," *ACS Appl. Mater. Interfaces*, vol. 11, no. 48, pp. 45016–45030, Dec. 2019, doi: 10.1021/acsami.9b11365.

[29] A. Kongkanand and M. F. Mathias, "The Priority and Challenge of High-Power Performance of Low-Platinum Proton-Exchange Membrane Fuel Cells," *J. Phys. Chem. Lett.*, vol. 7, no. 7, pp. 1127–1137, Apr. 2016, doi: 10.1021/acs.jpclett.6b00216.

[30] J. hee Song, M. soo Kim, Y. rim Kang, and D. kyu Kim, "Study on a drasitically hydrogen consumption saving conditioning method for Polymer electrolyte membrane fuel cell," *Journal of Energy Storage*, vol. 44, p. 103338, Dec. 2021, doi: 10.1016/j.est.2021.103338.

[31] I. Jiménez-Morales *et al.*, "Correlation between the surface characteristics of carbon supports and their electrochemical stability and performance in fuel cell cathodes," *Carbon Energy*, vol. 3, no. 4, pp. 654–665, Aug. 2021, doi: 10.1002/cey2.109.

[32] N. Job, M. Chatenet, S. Berthon-Fabry, S. Hermans, and F. Maillard, "Efficient Pt/carbon electrocatalysts for proton exchange membrane fuel cells: Avoid chloride-based Pt salts!," *Journal of Power Sources*, vol. 240, pp. 294–305, Oct. 2013, doi: 10.1016/j.jpowsour.2013.03.188.

[33] X. Cheng *et al.*, "A review of PEM hydrogen fuel cell contamination: Impacts, mechanisms, and mitigation," *Journal of Power Sources*, vol. 165, no. 2, pp. 739–756, Mar. 2007, doi: 10.1016/j.jpowsour.2006.12.012.

[34] K. Shinozaki, J. W. Zack, R. M. Richards, B. S. Pivovar, and S. S. Kocha, "Oxygen Reduction Reaction Measurements on Platinum Electrocatalysts Utilizing Rotating Disk Electrode Technique: I. Impact of Impurities, Measurement Protocols and Applied Corrections," *J. Electrochem. Soc.*, vol. 162, no. 10, pp. F1144–F1158, 2015, doi: 10.1149/2.1071509jes.

[35] J. Park and D. Kim, "Effect of cerium/18-crown-6-ether coordination complex OH quencher on the properties of sulfonated poly(ether ether ketone) fuel cell electrolyte membranes," *Journal of Membrane Science*, vol. 469, pp. 238–244, Nov. 2014, doi: 10.1016/j.memsci.2014.06.044.

[36] K. Palanichamy, A. Prasad, and S. Advani, "Off-Line Conditioning of PEM Fuel Cell Membrane," *ECS Meeting Abstracts*, Oct. 2008, [Online]. Available: http://ma.ecsdl.org/content/MA2008-02/11/1091.abstract

[37] J. M. Moore, P. L. Adcock, J. B. Lakeman, and G. O. Mepsted, "The effects of battlefield contaminants on PEMFC performance," p. 7, 2000.

[38] D. E. Ramaker, A. Korovina, V. Croze, J. Melke, and C. Roth, "Following ORR intermediates adsorbed on a Pt cathode catalyst during break-in of a PEM fuel cell by in operando X-ray absorption spectroscopy," *Phys. Chem. Chem. Phys.*, vol. 16, no. 27, pp. 13645–13653, 2014, doi: 10.1039/C4CP00192C.

[39] C. J. Netwall, B. D. Gould, J. A. Rodgers, N. J. Nasello, and K. E. Swider-Lyons, "Decreasing contact resistance in proton-exchange membrane fuel cells with metal bipolar plates," *Journal of Power Sources*, vol. 227, pp. 137–144, Apr. 2013, doi: 10.1016/j.jpowsour.2012.11.012.

[40] W. R. Chang, J. J. Hwang, F. B. Weng, and S. H. Chan, "Effect of clamping pressure on the performance of a PEM fuel cell," *Journal of Power Sources*, vol. 166, no. 1, pp. 149–154, Mar. 2007, doi: 10.1016/j.jpowsour.2007.01.015.

[41] A. Therdthianwong, P. Manomayidthikarn, and S. Therdthianwong, “Investigation of membrane electrode assembly (MEA) hot-pressing parameters for proton exchange membrane fuel cell,” *Energy*, vol. 32, no. 12, pp. 2401–2411, Dec. 2007, doi: 10.1016/j.energy.2007.07.005.

[42] V. Mehta and J. S. Cooper, “Review and analysis of PEM fuel cell design and manufacturing,” *Journal of Power Sources*, p. 22, 2003.

[43] Z. Qi and A. Kaufman, “Enhancement of PEM fuel cell performance by steaming or boiling the electrode,” *Journal of Power Sources*, vol. 109, no. 1, pp. 227–229, Jan. 2002, doi: https://doi.org/10.1016/S0378-7753(02)00060-5.

[44] S. Paul, “3M Innovative Properties Company Patent US7608118B2 – 2009 - Preconditioning Fuel cell membrane electrode asseblies,” p. 8.

[45] M. Zhiani, I. Mohammadi, and S. Majidi, “Membrane electrode assembly steaming as a novel pre-conditioning procedure in proton exchange membrane fuel cell,” *International Journal of Hydrogen Energy*, vol. 42, no. 7, pp. 4490–4500, Feb. 2017, doi: 10.1016/j.ijhydene.2017.01.103.

[46] J. Parrondo, M. Ortueta, and F. Mijangos, “SWELLING BEHAVIOUR OF PEMFC DURING CONDITIONING,” *Brazilian Journal of Chemical Engineering*, vol. 24, no. 03, p. 9, 2007.

[47] T. Van Nguyen, M. Vu Nguyen, K. J. Nordheden, and W. He, “Effect of Bulk and Surface Treatments on the Surface Ionic Activity of Nafion Membranes,” *J. Electrochem. Soc.*, vol. 154, no. 11, p. A1073, 2007, doi: 10.1149/1.2781247.

[48] R. Pinkhas, “US8415076 Preconditioning of gas diffusion layers for improved performance and operational stability of PEM fuel cells,” Nov. 2015

[49] G. Tsotridis, A. Pilenga, G. De Marco, T. Malkow, European Commission, and Joint Research Centre, *EU harmonised test protocols for PEMFC MEA testing in single cell configuration for automotive applications.* Luxembourg: Publications Office, 2015. Accessed: Nov. 12, 2019. [Online]. Available: http://bookshop.europa.eu/uri?target=EUB:NOTICE:LDNA27632:EN:HTML

[50] “U.S. Department of Energy, DoE Procedures for Performing PEM Single Cell Testing, 2009, p. 47. # DE-FC36-06GO16028 April 8.”

[51] C. Yang, M. Hu, C. Wang, and G. Cao, “A three-step activation method for proton exchange membrane fuel cells,” *Journal of Power Sources*, vol. 197, pp. 180–185, Sep. 2011, doi: https://doi.org/10.1016/j.jpowsour.2011.09.038.

[52] R. Cuccaro, M. Lucariello, A. Battaglia, and A. Graizzaro, “Research of a HySyLab internal standard procedure for single PEMFC,” *International Journal of Hydrogen Energy*, vol. 33, no. 12, pp. 3159–3166, Apr. 2008, doi: https://doi.org/10.1016/j.ijhydene.2008.04.016.

[53] T. Malkow, G. De Marco, A. Pilenga, M. Honselaar, and G. Tsotridis, “Testing the voltage and power as function of current density. Test Module PEFC SC 5-2,” JRC (Joint Research Centre, Institute for Energy), Petten, Apr. 2010. [Online]. Available: https://ec.europa.eu/jrc/sites/jrcsh/files/polarisation_curve_testprocedure.pdf

[54] M. M. Taghiabadi, M. Zhiani, and V. Silva, “Effect of MEA activation method on the long-term performance of PEM fuel cell,” *Applied Energy*, vol. 242, pp. 602–611, Mar. 2019, doi: https://doi.org/10.1016/j.apenergy.2019.03.157.

[55] F. A. de Bruijn, V. A. T. Dam, and G. J. M. Janssen, “Review: Durability and Degradation Issues of PEM Fuel Cell Components,” *Fuel Cells*, vol. 8, no. 1, pp. 3–22, Feb. 2008, doi: 10.1002/fuce.200700053.

[56] Z. Qi and A. Kaufman, “Quick and effective activation of proton-exchange membrane fuel cells,” *Journal of Power Sources*, vol. 114, no. 1, pp. 21–31, Oct. 2003, doi: https://doi.org/10.1016/S0378-7753(02)00587-6.

[57] Z. Qi and A. Kaufman, “Activation of low temperature PEM fuel cells,” *Journal of Power Sources*, vol. 111, no. 1, pp. 181–184, May 2002, doi: https://doi.org/10.1016/S0378-7753(02)00273-2.

[58] K.-Y. Cho and H.-Y. Jung, “Application of CV cycling to the activation of the polymer electrolyte membrane fuel cell,” vol. 23, pp. 445–449, 2012.

[59] N. Matsuoka and R. Shimoi, “Fuel cell conditioning system and related method,” 2005

[60] K. Kodama, “Method of running in operation of a fuel cell,” 2017

[61] S. Ik Jae *et al.*, “Apparatus and method for acceleratively activating fuel cell,” Sep. 2011

[62] E. Galitskaya *et al.*, “Pulsed Activation of a Fuel Cell on the Basis of a Proton-Exchange Polymer Membrane,” *Technical Physics Letters*, vol. 44, pp. 570–573, Aug. 2018, doi: 10.1134/S1063785018070064.

[63] R. H. Barton and U. S. Cl, “Conditioning and maintenance methods for fuel cells,” US 2003/0224227A1, 2003

[64] E. Balogun, A. O. Barnett, and S. Holdcroft, “Cathode starvation as an accelerated conditioning procedure for perfluorosulfonic acid ionomer fuel cells,” *Journal of Power Sources Advances*, vol. 3, p. 100012, Jun. 2020, doi: 10.1016/j.powera.2020.100012.

[65] M. Gerard, J.-P. Poirot-Crouvezier, D. Hissel, and M.-C. Pera, “Oxygen starvation analysis during air feeding faults in PEMFC,” *International Journal of Hydrogen Energy*, vol. 35, no. 22, pp. 12295–12307, Nov. 2010, doi: 10.1016/j.ijhydene.2010.08.028.

[66] D. Yang, “Rapid activation of a full-length proton exchange membrane fuel cell stack with a novel intermittent oxygen starvation method,” p. 9, 2022.

[67] J. Y. Park, I. S. Lim, E. J. Choi, Y. H. Lee, and M. S. Kim, “Comparative study of reverse flow activation and conventional activation with polymer electrolyte membrane fuel cell,” *Renewable Energy*, vol. 167, pp. 162–171, Apr. 2021, doi: 10.1016/j.renene.2020.11.069.

[68] B. Decoopman, “Compréhension des mécanismes de dégradation des cœurs de pile à combustible PEM en application automobile.”

[69] M. Gerard, J.-P. Poirot-Crouvezier, D. Hissel, and M.-C. Pe´ra, “Oxygen Starvation Effects on PEMFC Durability,” in *FUELCELL2010*, ASME 2010 8th International Fuel Cell Science, Engineering and Technology Conference: Volume 1, Jun. 2010, pp. 593–600. doi: 10.1115/FuelCell2010-33173.

[70] C. He, Z. Qi, M. Hollett, and A. Kaufman, “An Electrochemical Method to Improve the Performance of Air Cathodes and Methanol Anodes,” *Electrochem. Solid-State Lett.*, vol. 5, no. 8, p. A181, Jun. 2002, doi: 10.1149/1.1490715.

[71] Z. Qi and A. Kaufman, “Electrochemical Method to Improve the Performance of H2/Air PEM Fuel Cells and Direct Methanol Fuel Cells.,” p. 7, 2004.

[72] Z. Xu, Z. Qi, C. He, and A. Kaufman, “Combined activation methods for proton-exchange membrane fuel cells,” *Journal of Power Sources*, vol. 156, no. 2, pp. 315–320, May 2005, doi: https://doi.org/10.1016/j.jpowsour.2005.05.072.

[73] B. G. NengYou Jia, “Conditioning method for fuel cells,” May 2002

[74] J. H. L. Hyun Suk Choo, “Pre-activation method for fuel cell stack.pdf,” Feb. 2014

[75] H. S. Choo, “Method for activating Fuel cell stack without using electronic load,” US20160164132A1

[76] J. A. Schrooten, J. M. Marzullo, and M. L. Perry, “Performance enhancing Break-in method for a PEM fuel cell,” US 7,078,118B2

[77] K. Y. Cho, “Method of activating membrane electrode assembly (PEM) of polymerelectrolyte membrane fuel cell (PEMFC) using cyclic voltammetry (CV),” US 2009/0155635A1, Jun. 2009

[78] K. Masahito, “Ageing method of Fuel cell,” US 2020/0099071 A1

[79] H. Wang, “PEM Fuel Cell Diagnostic Tools,” p. 556.

[80] Z. Xu, Z. Qi, and A. Kaufman, “Activation of proton-exchange membrane fuel cells via CO oxidative stripping,” *Journal of Power Sources*, vol. 156, no. 2, pp. 281–283, Feb. 2005, doi: https://doi.org/10.1016/j.jpowsour.2005.02.094.

[81] S. Sugawara *et al.*, “Performance decay of proton-exchange membrane fuel cells under open circuit conditions induced by membrane decomposition,” *Journal of Power Sources*, vol. 187, no. 2, pp. 324–331, Feb. 2009, doi: 10.1016/j.jpowsour.2008.11.021.

[82] P. Pei, X. Fu, Z. Zhu, P. Ren, and D. Chen, “Activation of polymer electrolyte membrane fuel cells: Mechanisms, procedures, and evaluation,” *International Journal of Hydrogen Energy*, p. S0360319922023850, Jun. 2022, doi: 10.1016/j.ijhydene.2022.05.228.

[83] M. Zhiani and S. Majidi, “Effect of MEA conditioning on PEMFC performance and EIS response under steady state condition,” *International Journal of Hydrogen Energy*, vol. 38, no. 23, pp. 9819–9825, Aug. 2013, doi: 10.1016/j.ijhydene.2013.05.072.

[84] V. Silva, “Polymer electrolyte membrane fuel cells : activation analysis and operating conditions optimization,” University of Porto FEUP, Porto, 2009.

[85] V. B. Silva and A. Rouboa, “Hydrogen-fed PEMFC: Overvoltage analysis during an activation procedure,” *Journal of Electroanalytical Chemistry*, vol. 671, pp. 58–66, Feb. 2012, doi: https://doi.org/10.1016/j.jelechem.2012.02.013.

[86] S. Wasterlain, “Approches experimentales et analyse probabiliste pour le diagnostic de piles a combustible de type PEM,” 2010.

[87] X.-Z. Yuan, S. Zhang, J. C. Sun, and H. Wang, “A review of accelerated conditioning for a polymer electrolyte membrane fuel cell,” *Journal of Power Sources*, vol. 196, no. 22, pp. 9097–9106, Jun. 2011, doi: https://doi.org/10.1016/j.jpowsour.2011.06.098.

[88] S.-J. Shin, J.-K. Lee, H.-Y. Ha, S.-A. Hong, H.-S. Chun, and I.-H. Oh, "Effect of the catalytic ink preparation method on the performance of polymer electrolyte membrane fuel cells," *Journal of Power Sources*, vol. 106, no. 1–2, pp. 146–152, Apr. 2002, doi: 10.1016/S0378-7753(01)01045-X.

[89] V. B. Silva and A. Rouboa, "An activation procedure applied to fluorinated and non-fluorinated proton exchange membranes," *Fuel Processing Technology*, vol. 103, pp. 27–33, Mar. 2012, doi: https://doi.org/10.1016/j.fuproc.2011.12.042.

[90] I. Alaefour, S. Shahgaldi, A. Ozden, X. Li, and F. Hamdullahpur, "The role of flow-field layout on the conditioning of a proton exchange membrane fuel cell," *Fuel*, vol. 230, pp. 98–103, Oct. 2018, doi: 10.1016/j.fuel.2018.05.062.

[91] W. Dai *et al.*, "A review on water balance in the membrane electrode assembly of proton exchange membrane fuel cells," *International Journal of Hydrogen Energy*, vol. 34, no. 23, pp. 9461–9478, Dec. 2009, doi: 10.1016/j.ijhydene.2009.09.017.

[92] M. Andersson, S. B. Beale, M. Espinoza, Z. Wu, and W. Lehnert, "A review of cell-scale multiphase flow modeling, including water management, in polymer electrolyte fuel cells," *Applied Energy*, vol. 180, pp. 757–778, Oct. 2016, doi: 10.1016/j.apenergy.2016.08.010.

[93] D. Qiu, L. Peng, X. Lai, M. Ni, and W. Lehnert, "Mechanical failure and mitigation strategies for the membrane in a proton exchange membrane fuel cell," *Renewable and Sustainable Energy Reviews*, vol. 113, p. 109289, Oct. 2019, doi: 10.1016/j.rser.2019.109289.

[94] X.-Z. Yuan, H. Li, and H. H. Wang, "PEM Fuel Cell Failure Mode Analysis," p. 352.

[95] J. Wang, "System integration, durability and reliability of fuel cells: Challenges and solutions," *Applied Energy*, vol. 189, pp. 460–479, Mar. 2017, doi: 10.1016/j.apenergy.2016.12.083.

[96] S. Maharudrayya, S. Jayanti, and A. P. Deshpande, "Simplified Model to Predict Incipient Flooding/Dehydration in Proton Exchange Membrane Fuel Cells," *Journal of Fuel Cell Science and Technology*, vol. 4, no. 3, pp. 357–364, Aug. 2007, doi: 10.1115/1.2744055.

[97] T. E. Springer, "Polymer Electrolyte Fuel Cell Model," *J. Electrochem. Soc.*, vol. 138, no. 8, p. 2334, 1991, doi: 10.1149/1.2085971.

[98] H. Meng, "A three-dimensional PEM fuel cell model with consistent treatment of water transport in MEA," *Journal of Power Sources*, vol. 162, no. 1, pp. 426–435, Nov. 2006, doi: 10.1016/j.jpowsour.2006.07.022.

[99] T. Berning, M. Odgaard, and S. K. Kær, "Water balance simulations of a polymer-electrolyte membrane fuel cell using a two-fluid model," *Journal of Power Sources*, vol. 196, no. 15, pp. 6305–6317, Aug. 2011, doi: 10.1016/j.jpowsour.2011.03.068.

[100] S. Didierjean, O. Lottin, G. Maranzana, and T. Geneston, "PEM fuel cell voltage transient response to a thermal perturbation," *Electrochimica Acta*, vol. 53, no. 24, pp. 7313–7320, Oct. 2008, doi: 10.1016/j.electacta.2008.03.079.

[101] R. B. Ferreira, D. S. Falcão, V. B. Oliveira, and A. M. F. R. Pinto, "1D + 3D two-phase flow numerical model of a proton exchange membrane fuel cell," *Applied Energy*, vol. 203, pp. 474–495, Oct. 2017, doi: 10.1016/j.apenergy.2017.06.048.

[102] H. Wu, P. Berg, and X. Li, "Non-isothermal transient modeling of water transport in PEM fuel cells," *Journal of Power Sources*, vol. 165, no. 1, pp. 232–243, Feb. 2007, doi: 10.1016/j.jpowsour.2006.11.061.

[103] H. Guilin and F. Jianren, "Transient computation fluid dynamics modeling of a single proton exchange membrane fuel cell with serpentine channel," *Journal of Power Sources*, p. 14, 2007.

[104] G. Zhang and K. Jiao, "Multi-phase models for water and thermal management of proton exchange membrane fuel cell: A review," *Journal of Power Sources*, vol. 391, pp. 120–133, Jul. 2018, doi: 10.1016/j.jpowsour.2018.04.071.

[105] P. Massonnat, F. Gao, R. Roche, D. Paire, D. Bouquain, and A. Miraoui, "Multiphysical, multidimensional real-time PEM fuel cell modeling for embedded applications," *Energy Conversion and Management*, vol. 88, pp. 554–564, Dec. 2014, doi: 10.1016/j.enconman.2014.08.062.

[106] F. Moukalled, L. Mangani, and M. Darwish, *The finite volume method in computational fluid dynamics: an advanced introduction with OpenFOAM and Matlab*. Cham Heidelberg New York Dordrecht London: Springer, 2016.

[107] F. P. Incropera and F. P. Incropera, Eds., *Fundamentals of heat and mass transfer*, 6th ed. Hoboken, NJ: John Wiley, 2007.

[108] *Pem fuel cells theory and practice*.

[109] V. K. Mathur and J. Crawford, "Fundamentals of Gas Diffusion Layers in PEM Fuel Cells," in *Recent Trends in Fuel Cell Science and Technology*, S. Basu, Ed. New York, NY: Springer New York, 2007, pp. 116–128. doi: 10.1007/978-0-387-68815-2_4.

[110] X. Wang and T. V. Nguyen, "Modeling the Effects of Capillary Property of Porous Media on the Performance of the Cathode of a PEMFC," *J. Electrochem. Soc.*, vol. 155, no. 11, p. B1085, 2008, doi: 10.1149/1.2965512.

[111] J. C. Slattery and R. B. Bird, "Calculation of the diffusion coefficient of dilute gases and of the self-diffusion coefficient of dense gases," *AIChE J.*, vol. 4, no. 2, pp. 137–142, Jun. 1958, doi: 10.1002/aic.690040205.

[112] B. Ghanbarian, A. G. Hunt, R. P. Ewing, and M. Sahimi, "Tortuosity in Porous Media: A Critical Review," *Soil Science Society of America Journal*, vol. 77, no. 5, pp. 1461–1477, Sep. 2013, doi: 10.2136/sssaj2012.0435.

[113] Q. Ye and T. V. Nguyen, "Three-Dimensional Simulation of Liquid Water Distribution in a PEMFC with Experimentally Measured Capillary Functions," *J. Electrochem. Soc.*, vol. 154, no. 12, p. B1242, 2007, doi: 10.1149/1.2783775.

[114] H. Meng, "A two-phase non-isothermal mixed-domain PEM fuel cell model and its application to two-dimensional simulations," *Journal of Power Sources*, vol. 168, no. 1, pp. 218–228, May 2007, doi: 10.1016/j.jpowsour.2007.03.012.

[115] M. El Hannach, M. Prat, and J. Pauchet, "Pore network model of the cathode catalyst layer of proton exchange membrane fuel cells: Analysis of water management and electrical performance," *International Journal of Hydrogen Energy*, vol. 37, no. 24, pp. 18996–19006, Dec. 2012, doi: 10.1016/j.ijhydene.2012.09.139.

[116] K. Jiao and X. Li, "Water transport in polymer electrolyte membrane fuel cells," *Progress in Energy and Combustion Science*, vol. 37, no. 3, pp. 221–291, Jun. 2011, doi: 10.1016/j.pecs.2010.06.002.

[117] S. Didierjean, J.-C. Perrin, F. Xu, G. Maranzana, J. Mainka, and O. Lottin, "Influence of the Interfacial Water Transfer on the Analysis of Dynamic Sorption and Desorption Experiments in Nafion Membrane," *ECS Transactions*, vol. 69, no. 17, pp. 927–941, Sep. 2015, doi: 10.1149/06917.0927ecst.

[118] N. P. Siegel, M. W. Ellis, D. J. Nelson, and M. R. von Spakovsky, "Single domain PEMFC model based on agglomerate catalyst geometry," *Journal of Power Sources*, vol. 115, no. 1, pp. 81–89, Mar. 2003, doi: 10.1016/S0378-7753(02)00622-5.

[119] S.-K. Park and S.-Y. Choe, "Dynamic modeling and analysis of a 20-cell PEM fuel cell stack considering temperature and two-phase effects," *Journal of Power Sources*, p. 13, 2008.

[120] T. A. Zawodzinski, C. Derouin, S. Radzinski, R. Sherman, V. T. Smith, and T. E. Springer, "Water Uptake by and TransportThrough Nation| 117 Membranes," *J. Electrochem. Soc.*, vol. 140, no. 4, p. 7, 1993.

[121] J. T. Hinatsu, M. Mizuhata, and H. Takenaka, "Water Uptake of Perfluorosulfonic Acid Membranes from Liquid Water and Water Vapor," *J. Electrochem. Soc.*, vol. 141, no. 6, pp. 1493–1498, Jun. 1994, doi: 10.1149/1.2054951.

[122] Y. Wang, K. S. Chen, J. Mishler, S. C. Cho, and X. C. Adroher, "A review of polymer electrolyte membrane fuel cells: Technology, applications, and needs on fundamental research," *Applied Energy*, vol. 88, no. 4, pp. 981–1007, Apr. 2011, doi: 10.1016/j.apenergy.2010.09.030.

[123] T. Zawodzinskijr, T. Springer, F. Uribe, and S. Gottesfeld, "Characterization of polymer electrolytes for fuel cell applications," *Solid State Ionics*, vol. 60, no. 1–3, pp. 199–211, Mar. 1993, doi: 10.1016/0167-2738(93)90295-E.

[124] S. C. Yeo, "Physical properties and supermolecular structure of perfluorinated ion-containing (nafion) polymers," p. 24.

[125] S. Dutta, S. Shimpalee, and J. W. V. Zee, "Numerical prediction of mass-exchange between cathode and anode channels in a PEM fuel cell," *International Journal of Heat and Mass Transfer*, p. 15, 2001.

[126] J. T. Pukrushpan, A. G. Stefanopoulou, and H. Peng, *Control of Fuel Cell Power Systems: Principles, Modeling, Analysis and Feedback Design*. London: Springer London : Imprint : Springer, 2004. Accessed: Nov. 12, 2019. [Online]. Available: https://doi.org/10.1007/978-1-4471-3792-4

[127] S. K. Li, J. Hao, and M. Liddell, "Chapter 11 - Electrotransport Across Membranes in Biological Media: Electrokinetic Theories and Applications in Drug Delivery," in *Transport in Biological Media*, S. M. Becker and A. V. Kuznetsov, Eds. Boston: Elsevier, 2013, pp. 417–454. doi: 10.1016/B978-0-12-415824-5.00011-4.

[128] International Symposium on Proton Conducting Membrane Fuel Cells, S. Gottesfeld, G. Halpert, and A. Landgrebe, Eds., *Proceedings of the first International Symposium on Proton Conducting Membrane Fuel Cells I*. Pennington, NJ: Electrochemical Soc, 1995.

[129] D. M. Bernardi and M. W. Verbrugge, "Mathematical model of a gas diffusion electrode bonded to a polymer electrolyte," *AIChE J.*, vol. 37, no. 8, pp. 1151–1163, Aug. 1991, doi: 10.1002/aic.690370805.

[130] C. Bao, M. Ouyang, and B. Yi, “Modeling and control of air stream and hydrogen flow with recirculation in a PEM fuel cell system—I. Control-oriented modeling,” *International Journal of Hydrogen Energy*, vol. 31, no. 13, pp. 1879–1896, Oct. 2006, doi: 10.1016/j.ijhydene.2006.02.031.

[131] P. Ren, P. Pei, Y. Li, Z. Wu, D. Chen, and S. Huang, “Degradation mechanisms of proton exchange membrane fuel cell under typical automotive operating conditions,” *Progress in Energy and Combustion Science*, vol. 80, p. 100859, Sep. 2020, doi: 10.1016/j.pecs.2020.100859.

[132] P. Pei and H. Chen, “Main factors affecting the lifetime of Proton Exchange Membrane fuel cells in vehicle applications: A review,” *Applied Energy*, vol. 125, pp. 60–75, Jul. 2014, doi: 10.1016/j.apenergy.2014.03.048.

[133] J. O’Rourke, M. Ramani, and M. Arcak, “In situ detection of anode flooding of a PEM fuel cell,” *International Journal of Hydrogen Energy*, vol. 34, no. 16, pp. 6765–6770, Aug. 2009, doi: 10.1016/j.ijhydene.2009.06.029.

[134] W.-M. Yan, H.-S. Chu, J.-Y. Chen, C.-Y. Soong, and F. Chen, “Transient analysis of water transport in PEM fuel cells,” *Journal of Power Sources*, vol. 162, no. 2, pp. 1147–1156, Nov. 2006, doi: 10.1016/j.jpowsour.2006.07.047.

[135] E. J. F. Dickinson and G. Smith, “Modelling the Proton-Conductive Membrane in Practical Polymer Electrolyte Membrane Fuel Cell (PEMFC) Simulation: A Review,” *Membranes*, vol. 10, no. 11, p. 310, Oct. 2020, doi: 10.3390/membranes10110310.

[136] L. M. Sánchez, “Experimental characterization of water sorption and transport properties of polymer electrolyte membranes for fuel cells,” p. 179.

[137] V. Liso, S. Simon Araya, A. C. Olesen, M. P. Nielsen, and S. K. Kær, “Modeling and experimental validation of water mass balance in a PEM fuel cell stack,” *International Journal of Hydrogen Energy*, vol. 41, no. 4, pp. 3079–3092, Jan. 2016, doi: 10.1016/j.ijhydene.2015.10.095.

[138] A. Ferrara, P. Polverino, and C. Pianese, “Analytical calculation of electrolyte water content of a Proton Exchange Membrane Fuel Cell for on-board modelling applications,” *Journal of Power Sources*, vol. 390, pp. 197–207, Jun. 2018, doi: 10.1016/j.jpowsour.2018.04.005.

[139] D. S. Falcão, V. B. Oliveira, C. M. Rangel, C. Pinho, and A. M. F. R. Pinto, “Water transport through a PEM fuel cell: A one-dimensional model with heat transfer effects,” *Chemical Engineering Science*, vol. 64, no. 9, pp. 2216–2225, May 2009, doi: 10.1016/j.ces.2009.01.049.

[140] B. Tavakoli and R. Roshandel, “The effect of fuel cell operational conditions on the water content distribution in the polymer electrolyte membrane,” *Renewable Energy*, vol. 36, no. 12, pp. 3319–3331, Dec. 2011, doi: 10.1016/j.renene.2011.05.003.

[141] S. Ueda, S. Koizumi, and Y. Tsutsumi, “Flooding and performance of polymer electrolyte fuel cell, investigated by small-angle neutron scattering, neutron radiography and segmented electrode,” *Results in Physics*, vol. 12, pp. 504–511, Mar. 2019, doi: 10.1016/j.rinp.2018.11.082.

[142] C. Spiegel, *PEM fuel cell modeling and simulation using MATLAB®*. Amsterdam: Elsevier/Academic Press, 2008.

[143] D. Bezmalinović, J. Radošević, and F. Barbir, “Initial Conditioning of Polymer Eelectrolyte Membrane Fuel Cell by Temperature and Potential Cycling,” *Acta chimica Slovenica*, vol. 62, pp. 83–7, Mar. 2015, doi: 10.17344/acsi.2014.730.

[144] S. Goswami, S. Klaus, and J. Benziger, “Wetting and Absorption of Water Drops on Nafion Films,” *Langmuir*, vol. 24, no. 16, pp. 8627–8633, Aug. 2008, doi: 10.1021/la800799a.

[145] P. W. Majsztrik, M. B. Satterfield, A. B. Bocarsly, and J. B. Benziger, “Water sorption, desorption and transport in Nafion membranes,” *Journal of Membrane Science*, vol. 301, no. 1–2, pp. 93–106, Sep. 2007, doi: 10.1016/j.memsci.2007.06.022.

[146] Z. Zheng *et al.*, “A review on non-model based diagnosis methodologies for PEM fuel cell stacks and systems,” *International Journal of Hydrogen Energy*, vol. 38, no. 21, pp. 8914–8926, Jul. 2013, doi: 10.1016/j.ijhydene.2013.04.007.

[147] H. Wang, S. Morando, A. Gaillard, and D. Hissel, “Sensor development and optimization for a proton exchange membrane fuel cell system in automotive applications,” *Journal of Power Sources*, vol. 487, p. 229415, Mar. 2021, doi: 10.1016/j.jpowsour.2020.229415.

[148] E. Dijoux, N. Y. Steiner, M. Benne, M.-C. Péra, and B. G. Pérez, “A review of fault tolerant control strategies applied to proton exchange membrane fuel cell systems,” *Journal of Power Sources*, vol. 359, pp. 119–133, Aug. 2017, doi: 10.1016/j.jpowsour.2017.05.058.

[149] R. Petrone *et al.*, “A review on model-based diagnosis methodologies for PEMFCs,” *International Journal of Hydrogen Energy*, vol. 38, no. 17, pp. 7077–7091, Mar. 2013, doi: https://doi.org/10.1016/j.ijhydene.2013.03.106.

[150] W. Kun, "Ex-situ and in-situ diagnostic algorithms and methods for solid oxide fuel cell systems," Université de Franche-Comté, 2012.

[151] J. Aubry, N. Y. Steiner, S. Morando, N. Zerhouni, and D. Hissel, "Fuel cell diagnosis methods for embedded automotive applications," *Energy Reports*, vol. 8, pp. 6687–6706, Nov. 2022, doi: 10.1016/j.egyr.2022.05.036.

[152] R.-H. Lin, Z.-X. Pei, Z.-Z. Ye, C.-C. Guo, and B.-D. Wu, "Hydrogen fuel cell diagnostics using random forest and enhanced feature selection," *International Journal of Hydrogen Energy*, vol. 45, no. 17, pp. 10523–10535, Mar. 2020, doi: 10.1016/j.ijhydene.2019.10.127.

[153] A. Mohammadi, A. Djerdir, N. Yousfi Steiner, and D. Khaburi, "Advanced diagnosis based on temperature and current density distributions in a single PEMFC," *International Journal of Hydrogen Energy*, vol. 40, no. 45, pp. 15845–15855, Dec. 2015, doi: 10.1016/j.ijhydene.2015.04.157.

[154] D. Benouioua, D. Candusso, F. Harel, and L. Oukhellou, "Fuel cell diagnosis method based on multifractal analysis of stack voltage signal," *International Journal of Hydrogen Energy*, vol. 39, no. 5, pp. 2236–2245, Feb. 2014, doi: 10.1016/j.ijhydene.2013.11.066.

[155] D. Hissel and M. C. Pera, "Diagnostic & health management of fuel cell systems: Issues and solutions," *Annual Reviews in Control*, vol. 42, pp. 201–211, 2016, doi: 10.1016/j.arcontrol.2016.09.005.

[156] E. Dijoux, N. Y. Steiner, M. Benne, M.-C. Péra, and B. Grondin-Perez, "Fault Structural Analysis Applied to Proton Exchange Membrane Fuel Cell Water Management Issues," *Electrochem*, vol. 2, no. 4, pp. 604–630, Nov. 2021, doi: 10.3390/electrochem2040038.

[157] A. Sorrentino, K. Sundmacher, and T. Vidakovic-Koch, "Polymer Electrolyte Fuel Cell Degradation Mechanisms and Their Diagnosis by Frequency Response Analysis Methods: A Review," *Energies*, vol. 13, no. 21, p. 5825, Nov. 2020, doi: 10.3390/en13215825.

[158] J. Wu *et al.*, "A review of PEM fuel cell durability: Degradation mechanisms and mitigation strategies," *Journal of Power Sources*, vol. 184, no. 1, pp. 104–119, Sep. 2008, doi: 10.1016/j.jpowsour.2008.06.006.

[159] M. Chandesris, R. Vincent, L. Guetaz, J.-S. Roch, D. Thoby, and M. Quinaud, "Membrane degradation in PEM fuel cells: From experimental results to semi-empirical degradation laws," *International Journal of Hydrogen Energy*, vol. 42, no. 12, pp. 8139–8149, Mar. 2017, doi: 10.1016/j.ijhydene.2017.02.116.

[160] M. Kim *et al.*, "Effects of anode flooding on the performance degradation of polymer electrolyte membrane fuel cells," *Journal of Power Sources*, vol. 266, pp. 332–340, Nov. 2014, doi: 10.1016/j.jpowsour.2014.04.092.

[161] C. Damour, M. Benne, B. Grondin-Perez, M. Bessafi, D. Hissel, and J.-P. Chabriat, "Polymer electrolyte membrane fuel cell fault diagnosis based on empirical mode decomposition," *Journal of Power Sources*, vol. 299, pp. 596–603, Dec. 2015, doi: 10.1016/j.jpowsour.2015.09.041.

[162] Q. Li, Z. Liu, Y. Sun, S. Yang, and C. Deng, "A Review on Temperature Control of Proton Exchange Membrane Fuel Cells," *Processes*, vol. 9, no. 2, p. 235, Jan. 2021, doi: 10.3390/pr9020235.

[163] K. Chen, Y. Hou, C. Jiang, X. Pan, and D. Hao, "Experimental investigation on statistical characteristics of cell voltage distribution for a PEMFC stack under dynamic driving cycle," *International Journal of Hydrogen Energy*, vol. 46, no. 77, pp. 38469–38481, Nov. 2021, doi: 10.1016/j.ijhydene.2021.09.092.

[164] N. Yousfi Steiner, D. Hissel, Ph. Moçotéguy, and D. Candusso, "Diagnosis of polymer electrolyte fuel cells failure modes (flooding & drying out) by neural networks modeling," *International Journal of Hydrogen Energy*, vol. 36, no. 4, pp. 3067–3075, Feb. 2011, doi: 10.1016/j.ijhydene.2010.10.077.

[165] Z. Liu, L. Yang, Z. Mao, W. Zhuge, Y. Zhang, and L. Wang, "Behavior of PEMFC in starvation," *Journal of Power Sources*, vol. 157, no. 1, pp. 166–176, Jun. 2006, doi: 10.1016/j.jpowsour.2005.08.006.

[166] N. Fouquet, C. Doulet, C. Nouillant, G. Dauphin-Tanguy, and B. Ould-Bouamama, "Model based PEM fuel cell state-of-health monitoring via ac impedance measurements," *Journal of Power Sources*, vol. 159, no. 2, pp. 905–913, Sep. 2006, doi: 10.1016/j.jpowsour.2005.11.035.

[167] E. Pahon, D. Hissel, S. Jemei, and N. Y. Steiner, "Signal-based diagnostic approach to enhance fuel cell durability," *Journal of Power Sources*, vol. 506, p. 230223, Sep. 2021, doi: 10.1016/j.jpowsour.2021.230223.

[168] L. Tan and J. Jiang, "Signal Sampling and Quantization," in *Digital Signal Processing*, Elsevier, 2019, pp. 13–58. doi: 10.1016/B978-0-12-815071-9.00002-6.

[169] S. Shukla, R. N. Yadav, J. Sharma, and S. Khare, "Analysis of statistical features for fault detection in ball bearing," in *2015 IEEE International Conference on Computational Intelligence and Computing Research (ICCIC)*, Madurai, India, Dec. 2015, pp. 1–7. doi: 10.1109/ICCIC.2015.7435755.

[170] Z. Li, R. Outbib, D. Hissel, and S. Giurgea, "Data-driven diagnosis of PEM fuel cell: A comparative study," *Control Engineering Practice*, vol. 28, pp. 1–12, Jul. 2014, doi: 10.1016/j.conengprac.2014.02.019.

[171] P. Mccaffrey, “Introduction to machine learning: Regression, classification, and important concepts,” in *An Introduction to Healthcare Informatics*, Elsevier, 2020, pp. 191–210. doi: 10.1016/B978-0-12-814915-7.00014-4.

[172] C. M. Bishop, *Pattern recognition and machine learning*. New York: Springer, 2006.

[173] M. R. H. Samadi, “Eye Tracking with EEG life-style,” p. 153.

[174] S. Feng, J. Keung, P. Zhang, Y. Xiao, and M. Zhang, “The impact of the distance metric and measure on SMOTE-based techniques in software defect prediction,” *Information and Software Technology*, vol. 142, p. 106742, Feb. 2022, doi: 10.1016/j.infsof.2021.106742.

[175] M. Rafało, “Cross validation methods: Analysis based on diagnostics of thyroid cancer metastasis,” *ICT Express*, vol. 8, no. 2, pp. 183–188, Jun. 2022, doi: 10.1016/j.icte.2021.05.001.

[176] C. Cadet, S. Jemeï, F. Druart, and D. Hissel, “Diagnostic tools for PEMFCs: from conception to implementation,” *International Journal of Hydrogen Energy*, vol. 39, no. 20, pp. 10613–10626, Jul. 2014, doi: 10.1016/j.ijhydene.2014.04.163.

[177] SINTEF AS, “VIRTUAL & physical platform for Fuel Cell System development. Grant agreement ID: 875087.” doi: 10.3030/875087.

[178] J. Ihonen *et al.*, “HYDRAITE – Hydrogen Delivery Risk Assessment and Impurity Tolerance. D2.2 A summary report of FC measurements for the first half of the project.”

[179] H.-Y. J. Ki-Yun Cho, “Application of CV Cycling to the Activation of fuel cells,” Aug. 2012.

[180] S. Wasterlain, D. Candusso, F. Harel, D. Hissel, and X. François, “Development of new test instruments and protocols for the diagnostic of fuel cell stacks,” *Journal of Power Sources*, vol. 196, no. 12, pp. 5325–5333, Jun. 2011, doi: 10.1016/j.jpowsour.2010.08.029.

[181] H. Zhang, H. Haas, J. Hu, S. Kundu, M. Davis, and C. Chuy, “The Impact of Potential Cycling on PEMFC Durability,” *J. Electrochem. Soc.*, vol. 160, no. 8, pp. F840–F847, 2013, doi: 10.1149/2.083308jes.

[182] D. Qu *et al.*, “Electrochemical Impedance and its Applications in Energy-Storage Systems,” *Small Methods*, vol. 2, no. 8, p. 1700342, Aug. 2018, doi: 10.1002/smtd.201700342.

[183] I. Pivac, D. Bezmalinović, and F. Barbir, “Catalyst degradation diagnostics of proton exchange membrane fuel cells using electrochemical impedance spectroscopy,” *International Journal of Hydrogen Energy*, vol. 43, no. 29, pp. 13512–13520, Jul. 2018, doi: 10.1016/j.ijhydene.2018.05.095.

[184] J. Fu, M. Hou, C. Du, Z. Shao, and B. Yi, “Potential dependence of sulfur dioxide poisoning and oxidation at the cathode of proton exchange membrane fuel cells,” *Journal of Power Sources*, vol. 187, no. 1, pp. 32–38, Feb. 2009, doi: 10.1016/j.jpowsour.2008.10.103.

[185] D. E. Ramaker, D. Gatewood, A. Korovina, Y. Garsany, and K. E. Swider-Lyons, “Resolving Sulfur Oxidation and Removal from Pt and Pt_3Co Electrocatalysts Using in Situ X-ray Absorption Spectroscopy,” *J. Phys. Chem. C*, vol. 114, no. 27, pp. 11886–11897, Jul. 2010, doi: 10.1021/jp101977g.

[186] J. Aubry, N. Yousfi Steiner, S. Morando, N. Zerhouni, F. Van Der Linden, and D. Hissel, “Fuel Cell prognosis using particle filter: application to the automotive sector,” p. 6.

[187] J. Mitzel, Q. Zhang, P. Gazdzicki, and K. A. Friedrich, “Review on mechanisms and recovery procedures for reversible performance losses in polymer electrolyte membrane fuel cells,” *Journal of Power Sources*, vol. 488, p. 229375, Mar. 2021, doi: 10.1016/j.jpowsour.2020.229375.

[188] J. Zhao, Z. Tu, and S. H. Chan, “Carbon corrosion mechanism and mitigation strategies in a proton exchange membrane fuel cell (PEMFC): A review,” *Journal of Power Sources*, vol. 488, p. 229434, Mar. 2021, doi: 10.1016/j.jpowsour.2020.229434.

[189] I. Alaefour, G. Karimi, K. Jiao, and X. Li, “Measurement of current distribution in a proton exchange membrane fuel cell with various flow arrangements – A parametric study,” *Applied Energy*, vol. 93, pp. 80–89, May 2012, doi: 10.1016/j.apenergy.2011.05.033.

[190] L. Jae Hyuk, “Method for activating stack of fuel cell,” US2017040624A1